

Universidad de Málaga

Escuela Técnica Superior de Ingeniería de Telecomunicación

Programa de Doctorado en Ingeniería de Telecomunicación



UNIVERSIDAD DE MÁLAGA

TESIS DOCTORAL

Experimental Channel Modeling and Performance Analysis of
Underwater Optical Wireless Communication Systems

Autor:

PEDRO SALCEDO SERRANO

Directores:

JOSÉ MARÍA GARRIDO BALSELLS

RUBÉN BOLUDA RUIZ

2025



DECLARACIÓN DE AUTORÍA Y ORIGINALIDAD DE LA TESIS PRESENTADA PARA OBTENER EL TÍTULO DE DOCTOR

D./Dña PEDRO SALCEDO SERRANO

Estudiante del programa de doctorado EN INGENIERÍA DE TELECOMUNICACIÓN de la Universidad de Málaga, autor/a de la tesis, presentada para la obtención del título de doctor por la Universidad de Málaga, titulada: EXPERIMENTAL CHANNEL MODELING AND PERFORMANCE ANALYSIS OF UNDERWATER OPTICAL WIRELESS COMMUNICATION SYSTEMS.

Realizada bajo la tutorización de JOSÉ MARÍA GARRIDO BALSELLS y dirección de JOSÉ MARÍA GARRIDO BALSELLS Y RUBÉN BOLUDA RUIZ.

DECLARO QUE:

La tesis presentada es una obra original que no infringe los derechos de propiedad intelectual ni los derechos de propiedad industrial u otros, conforme al ordenamiento jurídico vigente (Real Decreto Legislativo 1/1996, de 12 de abril, por el que se aprueba el texto refundido de la Ley de Propiedad Intelectual, regularizando, aclarando y armonizando las disposiciones legales vigentes sobre la materia), modificado por la Ley 2/2019, de 1 de marzo.

Igualmente asumo, ante a la Universidad de Málaga y ante cualquier otra instancia, la responsabilidad que pudiera derivarse en caso de plagio de contenidos en la tesis presentada, conforme al ordenamiento jurídico vigente.

En Málaga, a 28 de ENERO de 2025.

Fdo.: PEDRO SALCEDO SERRANO Doctorando/a	Fdo.: JOSÉ MARÍA GARRIDO BALSELLS Tutor/a
Fdo.: JOSÉ MARÍA GARRIDO BALSELLS Y RUBÉN BOLUDA RUIZ Director/es de tesis	



Autorización para la lectura de la Tesis Doctoral.

Por la presente, Dr. D. José María Garrido Balsells y Dr. D. Rubén Boluda Ruiz, profesores doctores del Departamento de Ingeniería de Comunicaciones de la Universidad de Málaga, certifican que el doctorando Pedro Salcedo Serrano ha realizado en el Departamento de Ingeniería de Comunicaciones de la Universidad de Málaga, bajo su dirección, el trabajo de investigación correspondiente a su TESIS DOCTORAL titulada:

“Experimental Channel Modeling and Performance Analysis of Underwater Optical Wireless Communication Systems”

Los resultados expuestos han dado lugar a las siguientes publicaciones en revistas y congresos que no han sido utilizadas en tesis anteriores:

1. P. Salcedo-Serrano, C. Gómez-García, J. Iamaguti-Debessa, R. Boluda-Ruiz, J. M. Garrido-Balsells, B. Castillo-Vázquez, A. Puerta-Notario, A. García-Zambrana, “On the effect of air bubbles-induced scattering on turbid waters: an experimental UOWC channel modeling approach,” *IEEE Access* **12**, pp. 75888-75898 (2024).
2. P. Salcedo-Serrano, R. Boluda-Ruiz, J. M. Garrido-Balsells, B. Castillo-Vázquez, A. Puerta-Notario, A. García-Zambrana, “Performance evaluation of UOWC systems from an empirical channel model approach for air bubble-induced scattering,” *Sensors* **24**(16), pp. 5232 (2024).
3. P. Salcedo-Serrano, R. Boluda-Ruiz, J. M. Garrido-Balsells, B. Castillo-Vázquez, A. Puerta-Notario, A. García-Zambrana, and S. Hranilovic “UOWC spatial diversity techniques over hostile maritime environments: a new approach under imperfect CSI and per-source power constraints,” *Opt. Express* **32**(24), 42347-42367 (2024).
4. P. Salcedo-Serrano, R. Boluda-Ruiz, J. M. Garrido-Balsells, A. García-Zambrana and S. Hranilovic, “Underwater optical wireless channel capacity under oceanic turbulence using spatial diversity techniques,” *IEEE International Conference on Communications (ICC)*, Rome, Italy, 2023, pp. 1162-1168
5. C. Gómez-García, J. Iamaguti-Debessa, P. Salcedo-Serrano, R. Boluda-Ruiz, J.M. Garrido-Balsells, B. Castillo-Vázquez, A. Puerta-Notario, A. García-Zambrana, “Modelado estadístico del efecto de burbujas de aire en sistemas de comunicaciones ópticas inalámbricas submarinos”, XXXVIII Simposio Nacional URSI Spain, September 13-15, 2023, Cáceres, Spain.
6. P. Salcedo-Serrano, J.M. Garrido-Balsells, A. García-Zambrana, A. Puerta-Notario, B. Castillo-Vázquez, R. Boluda-Ruiz, “Análisis de técnicas de diversidad espacial adaptadas al canal óptico submarino en presencia de dispersión y turbulencia oceánica,” XXXVIII Simposio Nacional URSI Spain, September 13-15, 2023, Cáceres, Spain.

Por todo ello, consideran que esta Tesis es apta para su presentación al Tribunal que ha de juzgarla. Y para que conste a efectos de lo establecido, AUTORIZAN la presentación de esta Tesis en la Universidad de Málaga.

En Málaga, a 28 de enero del 2025

Fdo.: Dr. D. José María Garrido Balsells

Fdo.: Dr. D. Rubén Boluda Ruiz

UNIVERSIDAD DE MÁLAGA
ESCUELA TÉCNICA SUPERIOR DE INGENIERÍA DE
TELECOMUNICACIÓN

Reunido el tribunal examinador en el día de la fecha, constituido por:

Presidente: Dr. D. _____

Secretario: Dr. D. _____

Vocal: Dr. D. _____

para juzgar la Tesis Doctoral titulada *Experimental Channel Modeling and Performance Analysis of Underwater Optical Wireless Communication Systems* realizada por D. Pedro Salcedo Serrano y dirigida por el Prof. Dr. D. José María Garrido Balsells y Prof. Dr. D. Rubén Boluda Ruiz, acordó por

_____ otorgar la calificación de

_____ y para que conste,

se extiende firmada por los componentes del tribunal la presente diligencia.

Málaga a _____ de _____ del _____

El Presidente:

El Secretario:

El Vocal:

Fdo.: _____

Fdo.: _____

Fdo.: _____

To my family and Alicia

“Bursting forth at last is the ower of truth, whose calyx usually opens after a long and profound sleep at dawn—in those placid hours of the morning that Goethe and so many others consider especially favorable for discovery.”

(“Y al fin surgirá la flor de la verdad, que, por lo común, abrirá su cáliz, al rayar el alba, tras largo y profundo sueño, durante esas horas plácidas de la mañana que Goethe y tantos otros consideraron propicias a la invención.”)

Santiago Ramón y Cajal

Acknowledgments

I would first like to thank my thesis advisors, Dr. José María Garrido-Balsells and Dr. Rubén Boluda-Ruiz, who believed in me and guided me during this project. Their support has allowed me to discover the research and laboratory work, inspiring me with their passion for learning and overcoming any challenge that comes our way. I am also deeply grateful to the entire team of the Wireless Optical Communication (WOC) Lab at the TELMA Institute of the University of Málaga, with a special mention to Prof. Antonio García-Zambrana for his insightful comments, which have significantly improved this work.

I wish to extend my sincere gratitude to Prof. Steve Hranilovic for hosting my research stay, for sharing his technical expertise with me, and for the many helpful discussions during my time at McMaster University.

I would like to thank all my colleagues who have shared with me countless hours of discussions, both professional and otherwise, over these years. In particular, I would like to mention Carlos Gómez-García and Jacqueline Iamaguti Debessa for their efforts in assembling and fine-tuning the UOWC test-bed.

I would like to sincerely thank Alicia for so many reasons that it would take countless pages to list them all. Her patience, advices, and warm love have been essential in helping me navigate this adventure and remain standing despite the challenges we have faced together. I would also like to thank my parents and my brother for their unconditional support in every decision I have made and for giving me the confidence to embark on a path filled with uncertainty.

Finally, but no less importantly, I would like to thank my friends who have accompanied me on this journey. Thank you for pulling me away from the whirlwind of academia and reminding me of where I come from and where I want to go.

I also wish to acknowledge the financial support provided by the University of Málaga, the Spanish Ministry of Science, Innovation, and Universities under the grant FPU22/02183 and the research project PID2019-107792GB-I00, the Programa Operativo I+D+i FEDER Andalucía 2014-2020 under the research project P18-RTJ-3343, and the Plan Andaluz de Investigación, Desarrollo e Innovación under the research project P21_00390.

Contents

List of Figures	vii
List of Tables	xi
Abstract	xiii
Resumen	xv
Acronyms	xvii
1 Introduction	1
1.1 A brief overview of underwater communication	1
1.2 Underwater optical wireless communications	5
1.2.1 Historical context of optical wireless communication	5
1.2.2 Current state of UOWC technology and challenges	7
1.2.3 State of the art	7
1.3 Research challenges and objectives	9
1.4 Thesis outline	10
1.5 Thesis contributions	11
2 Fundamentals of UOWC	15
2.1 General overview of UOWC systems	15
2.1.1 Transmitter block	15
2.1.2 Receiver block	17
2.2 Underwater channel impairments	20
2.2.1 Absorption and scattering	20
2.2.2 Oceanic turbulence	29
2.2.3 Air bubbles	34
2.3 UOWC channel modeling	37
2.3.1 Optical power fluctuations	38
2.4 UOWC systems	41
2.4.1 Performance of UOWC systems	43
2.5 Summary	46

3	Experimental UOWC channel model	49
3.1	Introduction	49
3.1.1	Motivation and related work	49
3.1.2	Structure	52
3.2	UOWC channel emulator	52
3.2.1	Experimental set-up	52
3.3	Emulated underwater channel effects	56
3.3.1	Absorption and scattering	57
3.3.2	Air bubbles generation	58
3.4	Bubbles-induced fading analysis	60
3.4.1	Estimated UOWC channel parameters	60
3.4.2	Channel measurements and calibration	66
3.4.3	Numerical results and discussion	67
3.5	UOWC system performance under proposed channel	77
3.5.1	System and channel models	78
3.5.2	Bit error rate	79
3.5.3	Outage probability	80
3.5.4	Diversity order	82
3.5.5	Numerical results and discussion	82
3.6	Summary	87
4	MISO UOWC systems	91
4.1	Introduction	91
4.1.1	Motivation and related work	91
4.1.2	Structure	94
4.2	MISO systems	95
4.2.1	Eye safety considerations	95
4.3	System and channel models	96
4.3.1	Underwater channel model	96
4.3.2	Proposed MISO system models	98
4.4	Performance analysis	104
4.4.1	Spatial repetition coding performance	105
4.4.2	Generalized transmit laser selection performance	106
4.5	Numerical results and discussions	107
4.5.1	Impact of power constraint in SRC schemes	107
4.5.2	Impact of imperfect CSI in GTLS scheme	111
4.6	Summary	116
5	Conclusions and Future Work	119
5.1	Conclusions	119
5.2	Future Work	121

Appendices	125
A Special Functions	127
A.1 Gamma Function	127
A.2 Incomplete Gamma Function	127
A.3 Meijer's G-Function	128
A.3.1 Relation to Other Functions	128
A.4 H-Fox Function	129
A.5 Other Definite Integrals	129
B Publications and Projects	131
B.1 Publications	131
B.2 Funding and projects	133
B.3 Research Fellowship	133
C Summary (Spanish)	135
C.1 Introducción a las comunicaciones inalámbricas ópticas submarinas	135
C.1.1 Antecedentes y motivación	135
C.1.2 Objetivos	138
C.2 Fundamentos de las comunicaciones inalámbricas ópticas submarinas	138
C.2.1 Absorción y dispersión	138
C.2.2 Turbulencia oceánica	140
C.2.3 Burbujas de aire	140
C.2.4 Modelo de sistema UOWC	141
C.3 Modelado de canal UOWC experimental	141
C.3.1 Motivación	142
C.3.2 Emulador de canal UOWC	142
C.3.3 Análisis de las fluctuaciones inducidas por las burbujas de aire	144
C.3.4 Rendimiento de sistemas UOWC bajo el canal empírico propuesto	146
C.4 Análisis de sistemas MISO UOWC	150
C.4.1 Motivación	150
C.4.2 Consideraciones de seguridad ocular	151
C.4.3 Modelo de canal óptico submarino	152
C.4.4 Esquema SRC	153
C.4.5 Esquema TLS	154
C.4.6 Resultados numéricos	156
C.5 Conclusiones y líneas futuras	159
C.5.1 Conclusiones	159
C.5.2 Líneas futuras	160
References	161

List of Figures

1.1	Absorption coefficient of pure seawater.	4
1.2	Example of an underwater wireless network in the presence of air bubbles and particles.	6
1.3	Thesis flowchart.	11
2.1	UOWC system model.	16
2.2	Relative response curve of different photodetector materials.	19
2.3	Angular distribution of (a) Rayleigh scattering, and (b) Mie scattering.	22
2.4	Graphical representation of the interaction between a collimated light beam and a small volume of water.	24
2.5	Phytoplankton concentration in the Bay of Biscay captured at two different times by the Moderate Resolution Imaging Spectroradiometer aboard NASA's Terra satellite.	25
2.6	Relationships among the main IOPs used in UOWC.	29
2.7	Blurred visual effect due to a geothermally heated water discharge from a hydrothermal vent which induce temperature-induced oceanic turbulence.	30
2.8	Representation of Kolmogorov cascade theory of turbulence.	31
2.9	Different scenarios for light interaction at an interface when transitioning from a medium with a higher refractive index to one with a lower refractive index.	36
2.10	Reflection and refraction effect due to the water-air bubble interface.	37
2.11	Scintillation index as a function of the link distance for different receiver aperture under Nikishov oceanic turbulence with a temperature-salinity ratio of $w = -1$	39
2.12	Diagram block of mathematical model of a UOWC system with IM/DD modulation.	41
3.1	(1) Current controller (CC). (2) Temperature controller (TC). (3) Pigtailed laser diode mount. (4) Fiber Collimator. (5) Water tank. (6) Propellers (PP). (7) Diffusers. (8) Air pump (AP). (9) Dielectric mirror. (10) Beamsplitter (BS). (11) Plano-convex lens (L). (12) Photodetector (PD). (13) Camera CMOS. (14) RedPitaya STEMLab.	53

3.2	Measured optical power curve versus operating current for the LD LP520-SF15. Data obtained from Thorlabs.	54
3.3	Experimental setup of a UOWC link with a link distance of 4.5 meters achieved by two mirrors placed at both ends of the water tank.	56
3.4	A green laser beam propagating through the water tank filled with tap water with (a) no antacid, and (b) 7.3 mg/L of Maalox antacid.	58
3.5	Proposed air bubbles scenarios: (a) small bubbles with low density (b) small bubbles with high density, (c) large bubbles with low density, and (d) large bubbles with high density.	59
3.6	Polynomial fit of the optical power as a function of the injection current with the manufacturer-provided data for the LD LP520-SF15.	61
3.7	Responsivity curve of the PDA10A2 photodetector.	62
3.8	Histograms of channel fluctuations due to (a) small and (b) large air bubbles.	68
3.9	Received footprints of (a) small bubbles, and (b) large bubbles in consecutive frames at high density scenarios.	69
3.10	Normalized autocovariance of channel fluctuations when (a) small bubbles, and (b) large bubbles in high density scenario are considered.	70
3.11	Normalized power fluctuations exclusively due to small air bubbles at different time scales.	71
3.12	Received voltage when tap water and tap water with (a) small air bubbles and (b) large air bubbles are considered.	73
3.13	Statistical distribution model fitting under different levels of water turbidity when small air bubbles are considered.	74
3.14	Statistical distribution model fitting under different levels of water turbidity when large air bubbles are considered.	75
3.15	Scintillation index of small and large air bubbles under different levels of water turbidity.	77
3.16	(a) Average outage duration and (b) coherence time of small and large air bubbles under different levels of water turbidity.	78
3.17	Diversity order when considering small air bubbles and large air bubbles for different levels of antacid in the experimental UOWC link.	83
3.18	Average BER performance when considering an empirical UOWC channel in the presence of small air bubbles-induced fading under different levels of antacid concentration at a link distance of 3 m and a wavelength of 520 nm.	84
3.19	Outage performance when considering an empirical UOWC channel in the presence of small air bubbles-induced fading under different levels of antacid concentration at a link distance of 3 m and a wavelength of 520 nm.	84
3.20	Average BER performance when considering an empirical UOWC channel in the presence of large air bubbles-induced fading under different levels of antacid concentration at a link distance of 3 m and a wavelength of 520 nm.	86

3.21	Outage performance when considering an empirical UOWC channel in the presence of large air bubbles-induced fading under different levels of antacid concentration at a link distance of 3 m and a wavelength of 520 nm.	86
4.1	Geometric representation of a MISO system that guarantees the eye safety regulations when two emitters are simultaneously operating under a <i>per-source</i> power constraint.	97
4.2	Scintillation index fitted function of Eq. (4.6) as a function of the link distance for different temperature-salinity ratios.	99
4.3	Diagram of the proposed underwater MISO system.	99
4.4	Block diagram of the proposed SRC system.	100
4.5	Block diagram of the proposed TLS system.	102
4.6	Probability mass function of r with 4 laser sources.	105
4.7	Average BER in UOWC links in clear ocean (a), and coastal waters (b), under oceanic turbulence, assuming a salinity-balance of $w = -1$ and several link distances when the SRC and GTLS schemes are used with 4 emitters when perfect CSIT is assumed.	109
4.8	The gain G as a function of (a) the link span, and (b) the total number of transmitter sources M , assuming $\rho = M$ when different severity of oceanic turbulence are considered.	110
4.9	Average BER in UOWC links in clear ocean (a), and coastal waters (b), under ocean turbulence, assuming a salinity-balance of $w = -1$ when an imperfect TLS scheme transmits through the r -th smallest channel gain.	113
4.10	Average BER in UOWC links in clear ocean (a), and coastal waters (b) when a GTLS scheme are used with 4 source lasers for several imperfect CSI at the transmitter scenarios, under salinity-induced turbulence with a salinity-balance of $w = -1$	114
4.11	Diversity order of BER when a GTLS scheme are used with 4 source lasers for several imperfect CSI at the transmitter scenarios in clear ocean (a), and coastal waters (b), under salinity-induced turbulence, assuming a link distance of 35 m and a salinity-balance of $w = -1$	115
C.1	(1) Controlador de corriente (CC). (2) Controlador de temperatura (TC). (3) Diodo láser. (4) Colimador. (5) Tanque de agua. (6) Ventiladores (PP). (7) Difusores de aire. (8) Bomba de aire (AP). (9)Espejo dieléctrico. (10) Beamsplitter (BS). (11) Lente plano-convexa (L). (12) Fotodetector (PD). (13) Cámara CMOS. (14) RedPitaya STEMLab.	143
C.2	Ajuste del modelo de distribución estadística propuesto bajo diferentes niveles de turbidez cuando se consideran burbujas de aire pequeñas.	146
C.3	Ajuste del modelo de distribución estadística propuesto bajo diferentes niveles de turbidez cuando se consideran burbujas de aire grandes.	147

C.4	Índice de centelleo, AOD, y tiempo de coherencia de las fluctuaciones bajo diferentes niveles de turbidez cuando se consideran burbujas de aire pequeñas y grandes.	148
C.5	BER promedio cuando se considera un modelo de canal UOWC empírico en presencia de burbujas de aire pequeñas para diferentes niveles de turbidez a una distancia de enlace de 3 metros y $\lambda = 520$ nm.	149
C.6	BER promedio cuando se considera un modelo de canal UOWC empírico en presencia de burbujas de aire pequeñas para diferentes niveles de turbidez a una distancia de enlace de 3 metros y $\lambda = 520$ nm.	149
C.7	Representación geométrica de un sistema MISO que cumple con las regulaciones de seguridad ocular cuando dos emisores operan simultáneamente bajo una restricción de potencia por fuente.	152
C.8	Diagrama de bloques del sistema SRC propuesto.	153
C.9	Diagrama de bloques del sistema TLS propuesto.	154
C.10	Función de densidad de probabilidad de r para 4 emisores.	156
C.11	BER promedio de sistemas MISO UOWC en océano claro (a) y agua de costa (b) en presencia de turbulencias oceánicas con $w = -1$ y varias distancias de enlace, utilizando los esquemas SRC y GTLS con 4 emisores y CSI en el transmisor perfecto.	157
C.12	BER promedio de sistemas GTLS UOWC en océano claro (a), y agua de costa (b), en presencia de turbulencias oceánicas con $w = -1$ para diferentes escenarios de CSI imperfecto en el transmisor.	158

List of Tables

1.1	Comparison of underwater wireless communication technologies.	5
2.1	Comparison between LED and LD characteristics.	18
2.2	Summary of absorption, scattering, and extinction coefficient for different water types when considering a green wavelength.	26
2.3	Summary of chlorophyll concentration for different Jerlov water types.	26
2.4	Oceanic turbulence parameters assumed in Fig. 2.11.	39
3.1	Commercial models of the experimental UOWC system.	54
3.2	Experimental results of the propagation losses, attenuation coefficient, coherence time, and AOD of the histograms in high density scenarios of small and large bubbles in Fig. 3.8(a) and Fig. 3.8(b), respectively.	69
3.3	Experiment results of the losses due to particles and air bubbles in high density scenarios of small and large bubbles.	72
3.4	Experiment results of losses due to particles, attenuation coefficient, losses due to air bubbles, fitting parameters for generalized Gamma and R^2 of the histograms in Fig. 3.13.	76
3.5	Experiment results of losses due to particles, attenuation coefficient, losses due to air bubbles, fitting parameters for the mixture of generalized Gamma and R^2 of the histograms in Fig. 3.14.	76
4.1	Values of fitted parameters of Eq. (4.6) for different strengths of oceanic turbulence	98
4.2	Numerical values of oceanic turbulence parameters.	98
4.3	UOWC system and channel parameters.	107
4.4	Values of scintillation index of Eq. (4.6) for different strengths of oceanic turbulence and link distances.	108
C.1	Coefficientes de absorción, dispersión y extinción para diferentes tipos de agua considerando una longitud de onda $\lambda = 532$ nm.	139

Abstract

In recent years, the growing demand for oceanic applications such as offshore exploration, aquaculture, and environmental monitoring has driven interest in underwater wireless communication systems. Particularly, these systems provide greater flexibility and lower installation and maintenance costs compared to traditional wired alternatives. Although underwater acoustic wireless communication (UAWC) systems have dominated this technology, they fall short in applications which requires high data rates and low latency, such as real-time video transmission for autonomous underwater vehicles (AUVs) and remotely operated vehicles (ROVs), among others. Hence, underwater optical wireless communication (UOWC) systems offer a promising alternative, providing data rates up to Gbps with minimal latency and a lower power consumption. However, UOWC systems present significant challenges due to the inherent absorption and scattering effect of the underwater medium, which limits the communication link distance to tens of meters. Both effects are increased in turbid environments, such as coastal waters, where scattering intensifies and causes temporal and spatial beam dispersion. Additional factors like air bubbles and oceanic turbulence can deteriorate the performance considerably. This work investigates the underwater optical channel through experimental measurements in various turbidity conditions. It aims to develop statistical models and mathematical tools to characterize the stochastic behavior of light propagation and its impairments, providing insights for the interaction of absorption and scattering effects with the rest of the channel impairments.

On the one hand, a statistical framework is developed to describe scattering-related phenomena and their interaction with other underwater effects, such as air bubbles, and ocean currents, based on experimental measurements. Firstly, an experimental UOWC test-bed is designed and built to emulate diverse underwater environments under controlled laboratory conditions. This includes scenarios with varying turbidity levels and the presence of air bubbles of different diameters, focusing on underwater scenarios that remain unexplored in the literature. The statistical behavior of the UOWC test-bed is characterized through the derivation of an empirical probability density function (PDF), along with other parameters related to the stochastic behavior of the signal, based on several channel measurements for small and large air bubbles. Furthermore, the impact of scattering and other emulated underwater impairments on UOWC system performance is analyzed in terms of bit error rate (BER) and outage probability, providing novel closed-form and asymptotic expressions.

On the other hand, two multiple-input/single-output (MISO) techniques are introduced to mitigate the impact of oceanic turbulence, as well as absorption, and scattering on the UOWC system performance in practical underwater environments. The first MISO system model employs a spatial repetition coding (SRC) scheme by considering both a *per-source* power constraint, maximizing the optical power of each laser diode, as well as a *per-transmitter*, optimizing the energy limitations of battery-powered systems. The second MISO system is based on a generalized transmit laser selection (GTLS) scheme that account for imperfect channel state information at the transmitter. Analytical and asymptotic expressions are derived to evaluate bit error rate performance under practical oceanic turbulence scenarios and various water types, demonstrating the adaptability and effectiveness of these MISO techniques in enhancing UOWC system reliability.

Resumen

En los últimos años, el desarrollo de actividades relacionadas con la exploración oceánica, la acuicultura, o la obtención de fuentes de energía en entornos marinos ha impulsado el interés en los sistemas de comunicación inalámbricos submarinos. Los actuales sistemas de comunicación inalámbricos submarinos basados en la tecnología acústica presentan limitaciones en aplicaciones como la transmisión de video en tiempo real para vehículos autónomos submarinos y vehículos operados de forma remota por su baja tasa de transmisión de datos y alta latencia. Por ello, los sistemas de comunicación óptica inalámbrica submarina (UOWC, *Underwater Optical Wireless Communication*) representan una alternativa muy interesante, ya que permiten velocidades de transmisión de hasta Gbps con muy baja latencia y un menor consumo energético. Sin embargo, los sistemas UOWC se ven afectados por los efectos inherentes de absorción y dispersión del medio submarino, los cuales limitan la distancia máxima de enlace en torno a las decenas de metros. Estos efectos se intensifican en entornos turbios, como las aguas costeras, donde la dispersión aumenta y provoca un esparcimiento temporal y espacial del haz transmitido. Además, otros efectos derivados del entorno submarino como las burbujas de aire y las turbulencias oceánicas pueden deteriorar considerablemente las prestaciones de estos sistemas. En esta tesis se investiga el canal óptico submarino a través de mediciones experimentales en diversas condiciones de turbidez. El objetivo principal de este trabajo es desarrollar modelos estadísticos y expresiones matemáticas para caracterizar el comportamiento estocástico de la luz tras su propagación en un medio submarino y su impacto en las prestaciones de un sistema UOWC, proporcionando información sobre la interacción de los efectos de absorción y dispersión con el resto de efectos del canal oceánico.

Por un lado, se desarrolla un marco estadístico para describir los fenómenos relacionados con la dispersión y su interacción con otros efectos submarinos, como burbujas de aire y corrientes oceánicas, basado en mediciones experimentales. Para ello, se diseña y construye una plataforma experimental para emular diversos entornos submarinos en condiciones controladas de laboratorio. Dicha plataforma permite el estudio de un amplio espectro de escenarios submarinos en referencia a su nivel turbidez, así como por la presencia de burbujas de aire de diferentes diámetros, analizando de manera experimental la propagación de un haz de luz en escenarios submarinos que no han sido explorados previamente en la literatura. La fluctuación aleatoria de la potencia óptica recibida derivada de los efectos del canal controlados a través del banco de pruebas se caracteriza mediante una función

de densidad de probabilidad (PDF, *Probability Density Function*) empírica, junto con otros parámetros relacionados con el comportamiento estocástico de la señal, basados en mediciones del canal para burbujas de aire pequeñas y grandes y diferentes niveles de turbidez. Además, se analiza el impacto de la dispersión y el resto de efectos emulados en el banco de pruebas mediante un análisis teórico del rendimiento de un sistema UOWC en términos de la tasa de error de bit (BER, *Bit Error Rate*) y probabilidad de *outage* en base al modelo de canal empírico, proporcionando expresiones novedosas en forma cerrada y asintótica.

Por otro lado, se presentan dos técnicas de transmisión de sistemas MISO (*Multiple-Input/Single-Output*) con el objetivo de mitigar el impacto de la turbulencia oceánica, así como la absorción y la dispersión en el rendimiento de un sistema UOWC en entornos submarinos prácticos y realistas. El primer modelo de sistema MISO emplea un esquema de codificación por repetición espacial (SRC, *Spatial Repetition Coding*) que permite considerar una restricción de potencia máxima por fuente o emisor, maximizando la potencia óptica de cada diodo láser, así como una restricción de potencia máxima por transmisor, optimizando las limitaciones energéticas de los sistemas alimentados por batería. El segundo modelo de sistema MISO se basa en un esquema generalizado de selección de láser transmisor (GTLS, *Generalized Transmit Laser Selection*), que considera la casuística de que el transmisor posea una información de estado del canal imperfecta. Se derivan expresiones analíticas y asintóticas para evaluar el rendimiento en términos de BER bajo diferentes escenarios prácticos de turbulencia oceánica y diversos tipos de agua, comparando la capacidad de mitigación de los efectos del canal submarino de ambas técnicas MISO.

Acronyms

AOD	<i>Average Outage Duration</i>
AOP	<i>Apparent Optical Property</i>
APD	<i>Avalanche Photodiode</i>
AUV	<i>Autonomous Underwater Vehicle</i>
AWGN	<i>Additive White Gaussian Noise</i>
BER	<i>Bit Error-Rate</i>
CDOM	<i>Colored Dissolved Organic Matter</i>
CDF	<i>Cumulative Density Function</i>
CSI	<i>Channel State Information</i>
CSIT	<i>Channel State Information at the Transmitter</i>
CW	<i>Continuous Wave</i>
DD	<i>Direct Detection</i>
ELF	<i>Extremely Low Frequency</i>
EU	<i>European Union</i>
FPGA	<i>Field Programmable Gate Array</i>
FOV	<i>Field of View</i>
FSO	<i>Free-Space Optical</i>
GTLS	<i>Generalized Transmit Laser Selection</i>
GVA	<i>Gross Value Added</i>
HG	<i>Henry-Greenstein</i>
IDOE	<i>International Decade of Ocean Exploration</i>
IEC	<i>International Electrotechnical Commission</i>
IM	<i>Intensity Modulation</i>
IOP	<i>Inherent Optical Property</i>
ISI	<i>Inter-Symbol Interference</i>
IoUT	<i>Internet of Underwater Things</i>
LD	<i>Laser Diode</i>
LED	<i>Light-Emitting Diode</i>
LOS	<i>Line-of-Sight</i>

M-PAM	<i>M-ary Pulse Amplitude Modulation</i>
MGF	<i>Moment Generating Function</i>
ML	<i>Maximum Likelihood</i>
MPE	<i>Maximum Permissible Exposure</i>
MIMO	<i>Multiple-Input/Multiple-Output</i>
MISO	<i>Multiple-Input/Single-Output</i>
NLOS	<i>Non-Line-of-Sight</i>
OAM	<i>Orbital Angular Momentum</i>
OOK	<i>On-Off Keying</i>
OP	<i>Outage Probability</i>
OTOPS	<i>Oceanic Turbulence Optical Power Spectrum</i>
OWC	<i>Optical Wireless Communication</i>
PDF	<i>Probability Density Function</i>
PSD	<i>Power Spectral Density</i>
ROV	<i>Remotely Operated Vehicles</i>
RF	<i>Radio Frequency</i>
SIMO	<i>Single-Input/Multiple-Output</i>
SISO	<i>Single-Input/Single-Output</i>
SNR	<i>Signal-to-Noise Ratio</i>
SPF	<i>Scattering Phase Function</i>
SRC	<i>Spatial Repetition Coding</i>
TLS	<i>Transmit Laser Selection</i>
TTHG	<i>Two-Term Henyey-Greenstein</i>
UAWC	<i>Underwater Acoustic Wireless Communication</i>
UHF	<i>Ultra High Frequency</i>
USPL	<i>Ultrashort Pulse Lasers</i>
UOWC	<i>Underwater Optical Wireless Communication</i>
UWSNs	<i>Underwater Wireless Sensor Networks</i>
VHF	<i>Very High Frequency</i>
VLf	<i>Very Low Frequency</i>
VLC	<i>Visible Light Communication</i>
VSF	<i>Volume Scattering Function</i>

Chapter 1

Introduction

1.1 A brief overview of underwater communication

The development of humankind has been intimately connected to ocean exploration. The ocean has long served as a vital source of food, minerals, energy, and transport, supporting the livelihoods of hundreds of millions of people across different historical periods. Nowadays, the maritime industry that constitutes the “blue economy” is highly diverse, encompassing sectors such as fisheries, aquaculture, shipping, submarine cables, port activities, offshore wind farms, offshore oil and natural gas production, maritime manufacturing and construction, and tourism. In economic terms, according to preliminary data from the Organization for Economic Co-operation and Development, the contribution of the ocean economy in 2010 —measured by the contribution of maritime industries to economic production and employment — represented approximately 2.5% of global gross value added (GVA) [1]. In the European Union (EU), the blue economy remains a vital component of economic activity. In 2021, the established sectors of the EU blue economy directly employed approximately 3.59 million people and generated a GVA of €171.1 billion, accounting for 1.3% of the EU economy [2]. However, this contribution varies across the different member states. For instance, Spain leads the employment related to the blue economy, accounting for 17% of total jobs and ranking among the top contributors to its economic output. Notably, the marine renewable energy and shipbuilding industries are experiencing significant growth, underscoring the increasing importance of innovation and sustainability in the EU’s economy. Despite the ocean’s significant impact on human life, the vast majority of natural water bodies — covering 71% of the Earth’s surface — remain largely unexplored¹ [1, 3, 4].

¹A well-known statement, often attributed to the renowned oceanographer Jacques Cousteau, claims that only about 5% of the ocean floor has been mapped with high-resolution maps, leaving over 95% of the underwater world unexplored. However, more recent data indicates that approximately 15% of the ocean floor has been mapped in detail. Despite this progress, only 0.0001% of the deep-ocean floor, those below 200 meters, have been thoroughly explored. [3].

In the 1970s, UNESCO developed the first International Decade of Ocean Exploration (IDOE), a long-term and comprehensive program for oceanographic research that aimed at the rational use of the oceans [5]. The main purpose of the IDOE was to increase the knowledge of the ocean and its composition, to optimize the sustainable use of the ocean and its resources for the progress of humanity [6]. Over the past decades, research and technological advancements have made more remote parts of the ocean accessible. This progress has fueled a growing interest in the ocean’s resources such as food, materials, and space, a trend known as “blue acceleration” [7]. Therefore, in alignment with the 2030 Agenda, in 2017, the United Nations General Assembly proclaimed the Decade of Ocean Science for Sustainable Development (2021-2030), also known as Ocean Decade, aiming to stimulate ocean science and knowledge generation to reverse the decline of the ocean system and catalyze new opportunities for the sustainable development against the global warming [8]. These initiatives also drive the growth of emerging ocean applications, including industries such as offshore wind, tidal and wave energy generation, ultra-deep-water oil and gas exploration, offshore aquaculture, seabed mining, and marine biotechnology [1]. These emerging oceanic industries usually employ devices that require underwater communication systems capable of real-time data collection to monitor the ocean environment and interconnect underwater devices and sensors. Furthermore, the integration of the Internet of Underwater Things (IoUT) into the technological ecosystem of underwater communication networks has significantly increased the volume of data that such devices can produce [9–11]. Consequently, to support this increased data generation, it is crucial to develop communication systems that ensure robust and high data-rate links capable of supporting the demands of these novel underwater applications. Wired communication systems, such as fiber optics and copper cables, can offer high-speed and reliable communication links, but they come with high installation and maintenance costs. Additionally, mobile platforms, such as autonomous underwater vehicles (AUVs) or remotely operated vehicles (ROVs), cannot utilize cables because their constant movement makes it impractical. Another example is the underwater wireless sensor networks (UWSNs), consisted of seabed sensors and relay buoys, typically deployed in remote locations where wired communication systems cannot be implemented. To overcome these issues, wireless communication systems are adopted to facilitate data transmission, thereby ensuring effective communication even in dynamic and remote underwater environments.

Historically, advancements in underwater wireless communication have been primarily driven by military needs, particularly those related to submarine operations [12]. However, the need for these systems is now rapidly expanding for the aforementioned applications, as they offer greater flexibility and have the potential to reduce deployment complexities and costs. At present, there are three types of underwater wireless communication: acoustic, radio frequency (RF), and optical communications. Underwater acoustic wireless communication (UAWC) is the most widely used and well-established physical layer technology in underwater environments. The acoustic method allows for data transmission over long distances, reaching up to tens of kilometers. However, acoustic waves have a propagation

speed of approximately 1500 m/s, which results in significant communication delays over long link distances [13]. In addition, long-range systems capable of operating over several tens of kilometers may offer a bandwidth of a few kHz, whereas short-range systems operating over several tens of meters can barely achieve bandwidths of hundreds kHz [14]. In both scenarios, these characteristics lead to low bit rates, typically in the range of tens of kbps for current devices [15]. Lastly, acoustic wave power absorption increases in proportion to the square of the frequency, which results in bulky and high-powered antennas for practical UAWC links. Secondly, RF communication has very few applications in underwater scenarios because seawater is a good conductor at very- and ultra-high frequency (VHF and UHF, respectively) ranges and limits the underwater RF communications links to ultra-short ranges, in the order of centimeters [13, 16]. Hence, the severe underwater absorption to electromagnetic waves only enables practical underwater RF communications links to short ranges at extremely- and very-low frequencies (ELF and VLF, respectively) with the consequent low bandwidth and low data rate [17]. The short distances of RF communication systems and the limited bandwidth of acoustic systems led researchers to explore other communication systems. In light of the implementation of atmospheric free-space optical (FSO) links, the deployment of communication systems operating within the optical spectrum is also proposed in underwater environments, particularly within the green and blue optical range between 400 and 700 nm, due to the optical transmission “window” present in natural waters [18, 19]. To graphically illustrate this transmission window, the absorption coefficient of pure seawater for different transmission wavelengths is shown in Fig. 1.1. In terms of the overall link performance, underwater optical wireless communications (UOWC) links offer high data transmission rates up to tens of Mbps with a very low latency. In fact, experimental results have demonstrated that, under controlled laboratory conditions, UOWC systems can achieve data rates up to Gbps [20–22]. In addition, the smaller size of light transmitters and receivers allows for more compact transceivers, which are particularly useful in small-scale underwater devices, such as mobile sensors or small AUVs or ROVs. Regarding power consumption and economic cost, light sources are generally more energy-efficient and cost-effective, enabling the deployment of transmission systems in low-cost, battery-operated underwater devices.

Despite the aforementioned advantages, UOWC also presents some notable challenges related to the underwater channel. Firstly, UOWC systems experience significant absorption compared to UAWC systems, which limits the link range to short and moderate distances, typically up to tens or hundreds of meters. Secondly, natural waters exhibit a significantly higher concentration of suspended particles such as organic and inorganic matter, resulting in light scattering due to interactions with these particles, known as scattering agents. The optical beam may undergo multiple scattering events along its propagation path, leading to temporal and spatial beam dispersion, which results in inter-symbol interference (ISI) at high data rates and in beam widening and blurring [24–26]. Absorption and scattering effects are particularly pronounced in coastal and turbid waters, where higher concentrations of in-suspension particles limit the achievable link distance to tens of meters. In contrast,

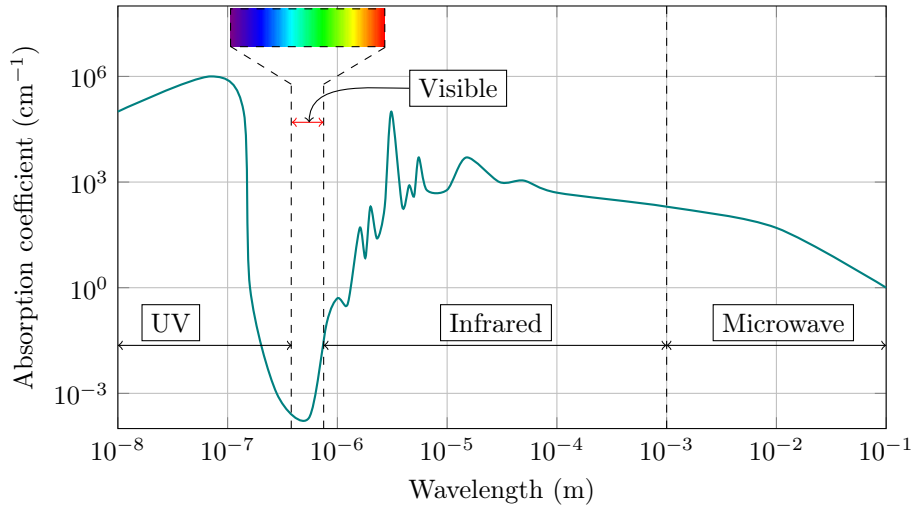


Figure 1.1: Absorption coefficient of pure seawater (adapted from [23]).

clearer ocean waters tend to exhibit less scattering, allowing longer link distances. Another challenge for UOWC systems is the oceanic turbulence induced by temperature and salinity fluctuations, which causes random variations in the refractive index along the propagation path [27–29]. Similar to the effect of atmospheric turbulence, these variations can lead to fluctuations in the received optical power at the receiver [30]. In addition, air bubbles generated by biological processes and artificial activities represent another potential challenge, as bubbles can induce random partial or total blockages of the transmitted light beam [31–33].

Moreover, UOWC systems require a strict line-of-sight (LOS) link, which implies no physical obstructions along the propagation path, i.e., the receiver must see the transmitter. In order to address this limitation, some authors have proposed leveraging the water-air surface to reflect the optical beam, thereby deploying a non-line-of-sight (NLOS) link [34, 35]. Lastly, in dynamic underwater environments with random movement of seawater due to ocean currents, link misalignment, and pointing errors are inevitable phenomena that reduce the UOWC system performance [36].

In Table 1.1, a comparison between UAWC, RF, and UOWC technologies with their benefits and limitations is shown. In summary, each wireless technology has different strengths and limitations, depending on the specific scenarios and applications. As a result, UOWC systems should be considered for their ability to satisfy application requirements that current UAWC and RF systems are unable to address. Currently, UOWC systems are particularly suitable for real-time, bandwidth-hungry applications, such as the remote control and video streaming of underwater vehicles.

In Fig. 1.2, various applications of UOWC systems are depicted. As shown, UOWC systems can be employed for many purposes, such as communication between UWSNs, remote

Table 1.1: Comparison of underwater wireless communication technologies [19, 37].

Parameters	Acoustic	RF	Optical
Speed (m/s)	1500 m/s	$\approx 2.3 \times 10^8$	$\approx 2.3 \times 10^8$
Frequency band	10–15 kHz	30–300 MHz	10^{12} – 10^{15} Hz
Data rate	\sim kbps	\sim Mbps	Up to Gbps
Latency	High	Low	Low
Distance	Several km	\approx 1 - 10 m (at ELF)	\approx 10–100 m
Transmission power	Tens of watts [W]	mW - W	mW - W
Benefits	Long link range	High data rate Low propagation delay	High data rate Low cost Low propagation delay Compact transceiver
Limitations	High delay latency Costly and bulky transceiver Energy consuming	Short link range Bulky transceiver	Severe absorption and scattering Turbulence and air bubbles

control of ROVs from a surface ship, as well as diver-to-diver communication. Furthermore, an example of an NLOS link utilizing the water surface to dodge a physical obstacle is illustrated. These applications are illustrated in the presence of underwater impairments, including air bubbles, represented as opaque gray spheres, and suspended particles, shown as smaller green spheres. It can be observed that water bubbles generated by cavitation effects from motors and propellers of submarine vehicles, along with suspended particles, disrupt beam propagation, leading to the previously discussed effects.

1.2 Underwater optical wireless communications

1.2.1 Historical context of optical wireless communication

Sending information via light beams is not a new idea. The earliest known illustrations of optical wireless communication (OWC) can be found in the ancient Chinese, Greek, and Roman Empires, which employed beacon towers to convey military information. More recently, in the 1880s, Alexander Graham Bell introduced the “photophone,” an instrument capable of transmitting an audio signal (human voice) through a wireless optical system that reflected sunlight on a mirror, which moves according to the vibrations of the audio signal [38].

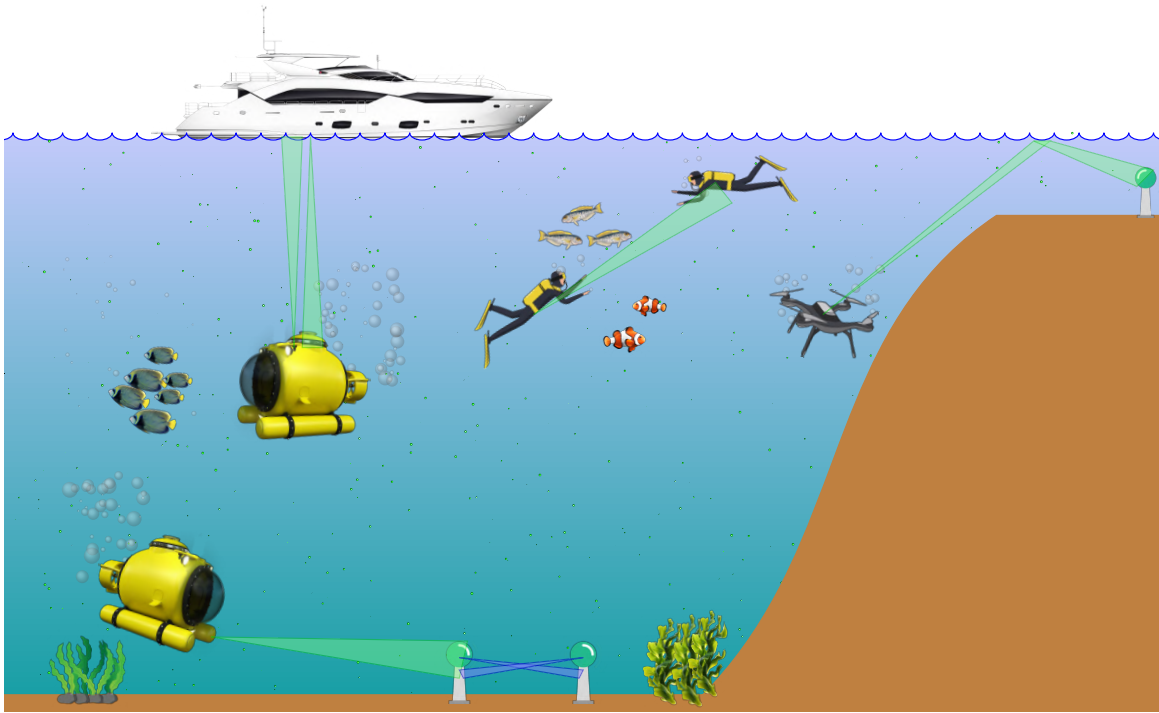


Figure 1.2: Example of an underwater wireless network in the presence of air bubbles and in-suspension particles. [19].

During the 20th century, OWC were traditionally confined to military applications. However, in the latter half of the century, numerous demonstrations of OWC were conducted using infrared laser systems for many applications, including space communication [39]. Since then, academic and industry research have considered the development of OWC technologies across heterogeneous fields and applications. Significant progress has been made in short-range systems, commonly referred to as visible light communication (VLC) for indoor wireless access, as well as in moderate- and long-range systems for outdoor terrestrial or underwater optical wireless communication, also known as FSO communication [40–44].

To the author’s knowledge, the first work that proposes using light emitters for underwater communications dates back to 1980 [45]. This pioneering work proposes using blue and green light sources for military submarine communications because the use of bulky antennas associated with RF communication systems at VLF could increase the risk of detection by enemy surveillance systems. Since that time, there has been a steady expansion of UOWC due to the growing scientific interest in improving its performance and robustness [46].

1.2.2 Current state of UOWC technology and challenges

From a commercial perspective, numerous private companies offer commercial UOWC systems. Numerous examples include the MC500 from Shimadzu Corporation, which supports data rates of 1 Mbps, 10 Mbps, and 20 Mbps with a link distance up to 80 meters; the LUMA X from Hydromea, which provides up to 10 Mbps with a range of 75 meters; and the BlueComm 200 from Sonardyne, which offers up to 10 Mbps over a distance of 150 meters [47–49]. Both the LUMA X and BlueComm 200 models also present ultraviolet versions, LUMA X-UV and BlueComm 200 UV, that offer increased resilience to interference from artificial lights and sunlight and operate at ranges up to 30 and 75 meters, respectively.

On a regional level, the Andalusian company DatLight SL stands out for its focus on designing high-speed transmission solutions based on optical wireless technology, further contributing to advancements in the field of the UOWC systems [50]. The development of these communication systems aligns with the interests of regional maritime companies such as Andalusí Sea Robótica Submarina, an Andalusian company dedicated to underwater exploration and the maintenance of submerged installations using ROVs [51]. Additionally, companies like BlueFloat, a Spanish firm located in Madrid that focuses on offshore wind generation, could also benefit from UOWC systems for reduce assembly and maintenance costs in offshore platforms [52].

Despite the development of UOWC systems and its positive impact on the maritime industry, the current state of optical technology does not yet allow its immediate implementation in practical underwater communication systems. Although UOWC systems offer higher transmission data rates than UAWC technology, the underwater environment as a transmission medium presents critical challenges, particularly regarding communication reliability due to oceanic conditions. For UOWC links, the maximum link span is primarily limited by oceanic attenuation, which is mainly influenced by water scattering, i.e., the turbidity of water. For instance, the Sonardyne BlueComm 200 and the LUMA X solely offer the above transmission speeds in clear water environments, i.e., in low dispersive environments. In addition, the transmission speed of current commercial systems are far from the potential of optical technology.

1.2.3 State of the art

Current limitations of available UOWC systems have pushed both industry and research institutions to continue exploring the UOWC technology to make it reliable and practical for the next generation of underwater wireless communications systems. Part of this research has focused on analyzing the underwater optical channel, hereafter referred to simply as the underwater channel. In line with research on FSO communication about atmospheric turbulence, some studies have applied similar analytical models to examine the effects of oceanic turbulence on underwater channels. This approach enhances understanding of how oceanic

turbulence impacts light propagation, aiming to optimize the performance of underwater optical communication systems. In [53], a comprehensive underwater channel emulator incorporating random temperature and salinity fluctuations, along with air bubbles, was used to analyze received optical power fluctuations for various transmitter and receiver configurations. More recently, a study indicated that river environments exhibit low turbulence, while nearshore ocean waters show moderate levels of turbulence [54]. In [55], an experimental UOWC link was proposed considering the combined effects of thermohaline gradients and air bubbles and introducing a unified model to characterize random optical power fluctuations. These findings advance understanding of the marine channel's behavior, facilitating the development of analytical channel models for designing UOWC systems suited to challenging marine conditions [56–58].

Although numerous studies focus on the effects of oceanic turbulence and air bubbles on underwater light propagation, few have addressed experimentally how both effects interact with scattering, i.e., on different types of waters. This research gap is significant, as the primary limiting factor for deploying UOWC systems is the short link distance, making it challenging to establish practical links in non-ideal underwater environments, such as coastal or turbid waters with a high presence of underwater organic matter. As mentioned above, these scenarios not only present extremely high attenuation levels, but also they are subject to other detrimental effects resulting from scattering, such as pulse and beam spreading. Therefore, any study that focuses solely on oceanic turbulence or the presence of air bubbles without considering the effects of absorption and scattering could be considered as incomplete, as it overlooks the most limiting factor of current UOWC systems. It is crucial to analyze the behavior of underwater channels over different degrees of water impurities to develop more accurate models and optimize communication systems, particularly in challenging environments where scattering plays a significant role.

Moreover, some statistical models employed to analyze the performance of UOWC systems under oceanic turbulence and air bubbles are derived from simulation tools [59, 60]. While simulations offer advantages in terms of accessibility and cost, the absence of experimental channel models reduces the practical applicability of the models, especially in situations where accuracy is essential, such as in the design of UOWC system adapted to hostile marine environments in the presence of the combined effect of oceanic turbulence or air bubbles with particle-induced scattering. Simulations may simplify complex environmental aspects, potentially leading to less precise representations of real oceanic conditions. Therefore, it is essential to conduct an experimental analysis of the impact of oceanic impairments and their variation with different levels of water turbidity. Understanding these interactions and their impact on UOWC system performance is key to designing transceivers that are robust and reliable in highly turbid environments.

1.3 Research challenges and objectives

As previously stated, UOWC systems offer a promising alternative for addressing the current limitations in data rate and security of underwater communication links. However, despite the advantages and applications of UOWC systems, this technology also exhibits several critical shortcomings and constraints that have yet to be addressed.

In the last few years, the advancement of underwater optical channel modeling has been significant. However, there is still a lack of knowledge, particularly with regard to the integration of scattering effects in conjunction with other underwater phenomena, such as oceanic turbulence and the presence of air bubbles. Only a limited number of studies have examined experimentally the influence of the water turbidity on this degradation, with few considering the impact of absorption and scattering effects on the UOWC system performance [61,62]. Furthermore, it is essential to investigate novel transmission schemes that can not only mitigate the impact of oceanic turbulence, but also reduce the significant levels of attenuation caused by scattering. This complex interplay of challenges necessitates the development of innovative approaches to enhance the performance of underwater optical communication systems in challenging environments.

The main purpose of this thesis is to provide a comprehensive study of the underwater channel based on experimental measurements, with the aim of accurately evaluating the behavior of light propagation across different underwater environments. This work intend to propose new statistical models and mathematical tools to describe the stochastic behavior of several effects that influence light propagation in underwater media and, hence, the overall performance of UOWC systems. Therefore, in addition to a comprehensive understanding of the channel itself, the thesis aims to investigate the performance of UOWC systems under the proposed underwater channel models, analyzing their advantages and limitations from a practical perspective.

The study of the scattering process in underwater light propagation represents the cornerstone of this work, which aims to explore the diverse scattering-induced phenomena and evaluate their impact on the performance of UOWC systems. Furthermore, the study considers the impact of other underwater phenomena, including the influence of air bubbles and oceanic turbulence. Hence, the objective of this research is twofold. Firstly, the development of a statistical framework that can independently describe scattering-related phenomena and their interplay with other underwater effects such as air bubbles and ocean currents based on experimental measurements. Secondly, the study of a more sophisticated transmitter designs such as multiple-input/single-output (MISO) schemes that focused on the mitigation of the underwater absorption and scattering, as well as oceanic turbulence by employing novel approaches adapted to the underwater environment.

In order to address the aforementioned issues, the following objectives have been established:

- O1.** Design an experimental UOWC test-bed capable of emulating accurately different underwater environments and evaluate the UOWC system performance over the proposed experimental channel.
 - O1.1** Emulate different scattering conditions as well as other representative oceanic effects such as air bubbles and ocean currents under controlled laboratory conditions for scenarios that has not been considered yet in the literature.
 - O1.2** Characterize the statistical behavior of the empirical UOWC channel under different scattering conditions and model the probability density function (PDF) of the measured channel fluctuations.
 - O1.3** Analyze the impact of scattering on the UOWC system performance under the empirical UOWC channel model by deriving novel closed-form analytic and asymptotic expressions.
- O2.** Propose MISO techniques specially adapted to underwater environments in order to mitigate the effects of absorption, scattering, and oceanic turbulence.
 - O2.1** Design and analyze MISO schemes in underwater channels that mitigate the impact of absorption and scattering in UOWC systems.
 - O2.2** Derive novel closed-form analytical and asymptotic expressions to evaluate the performance of MISO techniques under oceanic turbulence and different scattering conditions.

1.4 Thesis outline

The work is structured into six chapters, with their content and interconnections summarized in the flowchart, as shown in Fig. 1.3. Apart from this initial chapter, the remainder of the thesis is organized as follows.

Chapter 2 provides an overview of the fundamental principles of UOWC systems, as well as the underwater channel. This chapter starts by reviewing the most common effects that influence the propagation of a light beam through the underwater medium, including absorption, scattering, oceanic turbulence, and air bubbles. This is followed by the mathematical modeling of the underwater channel through the radiative transfer equation and the different PDFs typically employed to describe random power fluctuations, depending on the nature of the fading effect. Finally, the chapter defines the diverse performance metrics for UOWC systems adopted in this thesis.

Chapter 3 presents an experimental UOWC channel emulator designed to model the impact of air bubbles on system performance across several turbidity levels. In order to model the PDF of the received optical power fluctuations, empirical measurements

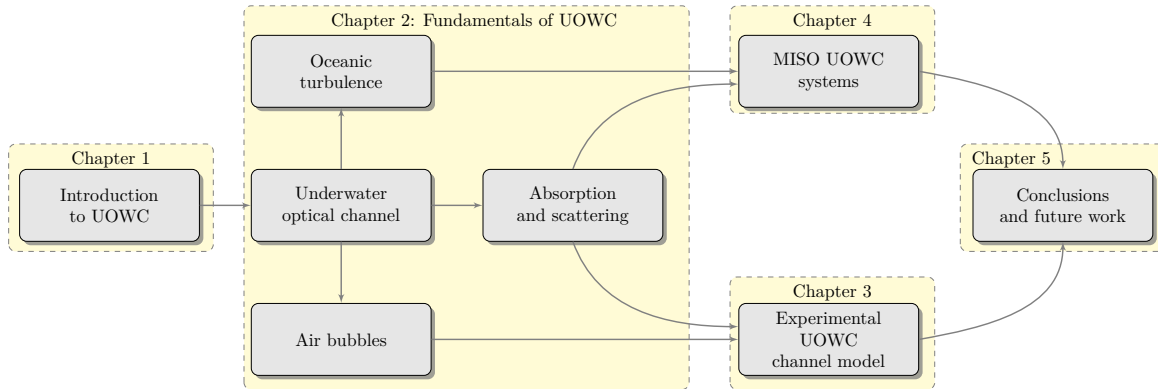


Figure 1.3: Thesis flowchart.

are utilized, taking into account various air bubble sizes and levels of particle-induced scattering. The fitted PDF is then applied to obtain the analytical and asymptotic BER and outage performance of a single-input/single-output (SISO) UOWC system under the proposed empirical channel model.

Chapter 4 proposes a novel approach for the design of practical MISO UOWC systems to mitigate the impact of oceanic turbulence, and the attenuation due to absorption and scattering effects. The novel premise underlying this analysis is that each light emitter operates at the maximum optical power allowed by the international safety standard. A comparative analysis of a spatial repetition coding (SRC) and a generalized transmit laser selection (GTLS) scheme is presented over different link distances and types of water.

Chapter 5 draws the main conclusions of this thesis and directions for further study in UOWC channel modeling and UOWC system designs.

1.5 Thesis contributions

The main contributions of this thesis have been disseminated in indexed journals and international conference proceedings. A list of all these publications is presented as follows

Journal publications

- [63] **P. Salcedo-Serrano**, C. Gómez-García, J. Iamaguti-Debessa, R. Boluda-Ruiz, J. M. Garrido-Balsells, B. Castillo-Vázquez, A. Puerta-Notario, A. García-Zambrana, “On the effect of air bubbles-induced scattering on turbid waters: an experimental UOWC channel modeling approach,” *IEEE Access* **12**, pp. 75888-75898 (2024).

- [64] **P. Salcedo-Serrano**, R. Boluda-Ruiz, J. M. Garrido-Balsells, B. Castillo-Vázquez, A. Puerta-Notario, A. García-Zambrana, “Performance evaluation of UOWC systems from an empirical channel model approach for air bubble-induced scattering,” *Sensors* **24**(16), pp. 5232 (2024).
- [65] **P. Salcedo-Serrano**, R. Boluda-Ruiz, J. M. Garrido-Balsells, B. Castillo-Vázquez, A. Puerta-Notario, A. García-Zambrana, and S. Hranilovic “UOWC spatial diversity techniques over hostile maritime environments: a new approach under imperfect CSI and per-source power constraints,” *Opt. Express* **32**(24), 42347-42367 (2024).

Conference proceedings

- [66] **P. Salcedo-Serrano**, R. Boluda-Ruiz, J. M. Garrido-Balsells, A. García-Zambrana and S. Hranilovic, “Underwater optical wireless channel capacity under oceanic turbulence using spatial diversity techniques,” *IEEE International Conference on Communications (ICC)*, Rome, Italy, 2023, pp. 1162-1168
- C. Gómez-García, J. Iamaguti-Debessa, **P. Salcedo-Serrano**, R. Boluda-Ruiz, J.M. Garrido-Balsells, B. Castillo-Vázquez, A. Puerta-Notario, A. García-Zambrana, ”Modelado estadístico del efecto de burbujas de aire en sistemas de comunicaciones ópticos inalámbricos submarinos”, XXXVIII Simposio Nacional URSI Spain, September 13-15, 2023, Cáceres, Spain.
- **P. Salcedo-Serrano**, J.M. Garrido-Balsells, A. García-Zambrana, A. Puerta-Notario, B. Castillo-Vázquez, R. Boluda-Ruiz, “Análisis de técnicas de diversidad espacial adaptadas al canal óptico submarino en presencia de dispersión y turbulencia oceánica,” XXXVIII Simposio Nacional URSI Spain, September 13-15, 2023, Cáceres, Spain.

The author of this thesis has also authored and co-authored the following publications in the context of UOWC systems and underwater channel modeling

Related journal publications

- [67] **P. Salcedo-Serrano**, R. Boluda-Ruiz, J. M. Garrido-Balsells, and A. García-Zambrana, “On the scattering-induced fading for optical wireless links through seawater: statistical characterization and its applications,” *Opt. Express* **29**(23), 37101-37116 (2021).
- [68] R. Boluda-Ruiz, **P. Salcedo-Serrano**, B. Castillo-Vázquez, A. García-Zambrana, and J.M. Garrido-Balsells, ”Capacity of underwater optical wireless communication systems over salinity-induced oceanic turbulence channels with ISI,” *Opt. Express* **29**(15), 23142-23158, 2021.

- [69] R. Boluda-Ruiz, **P. Salcedo-Serrano**, B. Castillo-Vázquez, A. García-Zambrana and J.M. Garrido-Balsells, "Impact of scattering on secrecy outage probability of underwater optical wireless links," in IEEE Journal of Oceanic Engineering, **48**(4), pp. 1362-1372, 2023.

Related conference proceedings

- [70] **P. Salcedo-Serrano**, R. Boluda-Ruiz, J. M. Garrido-Balsells, and A. García-Zambrana, "On scattering-induced fading in underwater FSO links for clear ocean and coastal waters," in Conference on Lasers and Electro-Optics (CLEO), OSA Technical Digest (Optical Society of America, 2021), paper JTu3A.166.
- [71] R. Boluda-Ruiz, **P. Salcedo-Serrano**, B. Castillo-Vázquez, A. García-Zambrana and J.M. Garrido-Balsells, "On the effect of inter-symbol interference on mutual information of undersea optical wireless links," 2021 IEEE Photonics Conference (IPC), 2021.
- [72] **P. Salcedo-Serrano**, R. Boluda-Ruiz, J. M. Garrido-Balsells, and A. García-Zambrana, "Outage capacity of underwater FSO systems over scattering-induced fading channels," in OSA Imaging and Applied Optics Congress 2021 (3D, COSI, DH, ISA, pcAOP), OSA Technical Digest (Optical Society of America, 2021), paper PM2G.2.
- [73] **P. Salcedo-Serrano**, R. Boluda-Ruiz, J. M. Garrido-Balsells, and A. García-Zambrana, "Ergodic capacity analysis of underwater FSO systems over scattering-induced fading channels in the presence of Weibull oceanic turbulence," IEEE International Conference on Communications (ICC), Seoul, Republic of Korea, 2022, pp. 3814-3819

Chapter 2

Fundamentals of UOWC

2.1 General overview of UOWC systems

UOWC systems are designed to transmit information between two points by propagating a light beam through the underwater medium. Basically, a UOWC system can be explained by the three blocks shown in Fig. 2.1: the transmitter, the receiver, and the underwater channel. The design of the first two mentioned blocks depends on the purpose of the link and the specific characteristics of the underwater channel where the link is deployed.

In this thesis, we consider an intensity modulation and direct detection (IM/DD) scheme due to its lower complexity and cost than those required in coherent schemes [74]. In IM/DD technique, the information is transmitted at base-band and directly demodulated at the receiver back into the transmitted signal. It should be noted that information can also be encoded in the amplitude and phase of the optical carrier, as in quadrature amplitude modulation (QAM) and phase shift keying (PSK) schemes [75, 76]. Coherent detection schemes enable background noise rejection, enhance receiver sensitivity, and improve system spectral efficiency. Nevertheless, the expense of higher implementation complexity and higher cost limit its implementation in commercial UOWC transceivers.

2.1.1 Transmitter block

Regarding the transmitter side, the most commonly used modulation type in commercial optical wireless transmitters is intensity modulation, which involves modulating the instantaneous power of the optical transmitted carrier $P_{tx}(t)$, based on an electrical input signal $i_{tx}(t)$. In other words, the intensity of the emitted light is employed to convey the information. This electro-optical conversion process is usually accomplished by a light-emitting diode (LED) or a laser diode (LD) [77]. An appropriate light source selection depends

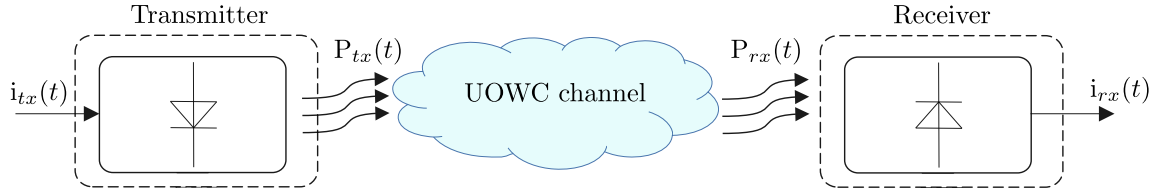


Figure 2.1: UOWC system model.

primarily on the specific applications and their characteristics, including the optical power versus current profile, operational speed, and the beam profile.

Light generation typically occurs when an electron transitions from an excited state to a lower energy state. This energy difference can lead to either a radiative process, which produces light and serves as the basis for optical sources, or a non-radiative process, which generates heat. In LED devices, an external electric excitation such as the electrical input signal $i_{tx}(t)$ causes electrons in the conduction band (high energy state) to spontaneously return to the valence band (low energy state), releasing a photon in the process. This process is known as spontaneous emission. Since the emitted photons are radiated in arbitrary directions, only a small fraction of them contribute to light in the desired direction. The emission process in planar LEDs is characterized by emitting light from all surfaces, which describes a Lambertian emitted light pattern distribution [74].

The emission process of an LD is more complex. Electrons are also excited by an external electric signal, which allows them to transition to a lower energy state, releasing photons in the process. Unlike spontaneous emission, the emitted photons induce the emission of new photons, a process known as stimulated emission. The stimulated emission process is repeated within an optical cavity with mirrors on both sides, which acts as a resonator, where photons are reflected and amplified. One mirror provides nearly total reflection, while the other allows the emission of some photons. In the case of the stimulated emission, emitted photons present the same direction, energy, frequency, and phase as the incident photon. Hence, the output light from this reaction is said to be coherent. In contrast, LED emitters radiate incoherent light.

The differences in the light generation processes of LDs and LEDs lead to significant discrepancies in their technical characteristics. Generally, LED is more cost-effective compared to LD sources. Furthermore, the light emission process in LDs is more sensitive to external factors, such as temperature. As a result, LD emitters often require specialized control circuits to maintain stable operating conditions, which also increases the total cost of the emitter. The electro-optical conversion efficiency of LDs is notably higher than that of LEDs. For example, to emit 1 mW of output optical power, an LED requires up to 150 mA of current, while an LD only needs 10 mA or less to produce the same amount of power [74].

Regarding the operational speed, i.e., the modulation bandwidth, LDs are also superior to LEDs. LDs can be modulated at gigahertz frequencies, whereas LEDs are typically limited to the megahertz range, which may be insufficient for high-speed applications. Additionally, the emission pattern of LEDs is broader and spreading quickly, while the beam generated by an LD is highly collimated¹.

In the design of optical wireless transmitters, it is essential to consider safety standards. The light emitted by a UOWC system could potentially reach human-populated areas such as beaches or marinas. Furthermore, such systems are often deployed in oceanographic research zones, which increases the risk of accidental exposure for divers or oceanographic researchers working in the vicinity. More generally, concerns regarding human-eye safety should also extend to marine life to minimize the human impact on ocean biodiversity, aligning with broader environmental and ecological principles. Hence, the International Electrotechnical Commission (IEC) has established guidelines, as outlined in IEC60825-1 standard, which define permissible optical power thresholds based on the considered wavelength and the type of technology used [78]. These limits are essential to prevent an excessive exposure to optical power which can cause damage to the eyes or skin, particularly in the case of LD sources, due to the coherence and high intensity of the emitted laser beam [79]. Typically, permissible optical power thresholds are less restrictive when applied to light sources that emit less concentrated and incoherent light, such as LED emissions [77].

The selection of the appropriate light source for UOWC systems depends on the specific characteristics of the link and the underwater environment. In general, LDs are preferable for applications requiring high optical power, as they produce high-intensity light with a narrower optical linewidth compared to LEDs. This advantage is due to the stimulated emission process, making them particularly efficient and suitable for communication systems in turbid waters and long-distance links. Additionally, LDs support much higher modulation bandwidth, which is essential for real-time and bandwidth-hungry applications such as remote control and video streaming of underwater vehicles. However, LEDs can be more advantageous for short-distance links due to their broader emission pattern, which reduces the system's sensitivity to link misalignment and pointing errors. In Table 2.1, a comparison of the features of LEDs and LDs for UOWC systems are summarized.

2.1.2 Receiver block

At the receiver side, as shown in Fig. 2.1, a photodetector generates a current $i_{rx}(t)$ that is proportional to the instantaneous power of the received optical signal $P_{rx}(t)$, and, therefore, proportional to the square of the received electric field. Specifically, the relationship between $i_{rx}(t)$ and $P_{rx}(t)$ is given by

$$i_{rx}(t) = R \cdot P_{rx}(t), \quad (2.1)$$

¹A collimated beam is defined as a beam of light in which the light rays travel in parallel, thereby minimizing beam spreading as it propagates.

Characteristic	LED	LD
Modulation Bandwidth	Up to hundreds of MHz	Up to tens of GHz
Conversion efficiency	10-20%	30-70%
Control circuitry	None	Temperature and threshold compensation
Eye Safety	Low restrictive	High restrictive
Directionality	Broad beam	Collimated beam
Cost	Low	Moderate to high

Table 2.1: Comparison between LED and LD characteristics [74, 77].

where R is the responsivity of the photodetector.

The fundamental physical principle behind the operation of a photodetector is the photoelectric effect, which takes place within a p - n junction. A photodetector consists of a junction formed by a p -type semiconductor (rich in positive charge carriers) and an n -type semiconductor (rich in negative charge carriers). The creation of p -type and n -type semiconductors is achieved through the doping of the same base semiconductor, such as silicon, with specific impurities. This doping process introduces atoms that either reduce or increase the number of free electrons. Due to charge redistribution, the p - n junction forms a depletion region at the interface, where a natural electric field is established.

When incident photons are absorbed by the depletion region, and their energy exceeds the bandgap energy of the material, electrons in the valence band gain sufficient energy to move to the conduction band, leaving behind positive charges in the valence band. The electric field in the depletion region drives these free electrons toward the n -type region and the positive charges toward the p -type region. The movement of released electrons charges creates an electrical current proportional to the intensity of the incident light.

The material composition of a photodetector determines the wavelengths of light to which it responds and its efficiency, i.e., the responsivity of the photodetector. Different semiconductor materials are used to create photodetectors, each offering unique properties suitable for specific applications. In Fig. 2.2, the relative response of different photodetector materials is shown. Silicon (Si) photodetector is commonly used for its low cost and high efficiency in the visible and near-infrared range (780-950 nm). Other materials, such as gallium arsenide (GaAs), germanium (Ge), and indium gallium arsenide (InGaAs), are also used for specialized applications requiring detection in different spectral ranges such as infrared in fiber optics transmissions. As mentioned in Chapter 1, in underwater environments, the optical transmission window primarily covers the blue-green spectrum, with lower absorption in the blue range. In that sense, the opto-electrical conversion in UOWC systems is typically performed by a silicon photodetector, due to its much higher responsivity in the optical spectrum of interest compared to the rest of technologies. However, although silicon

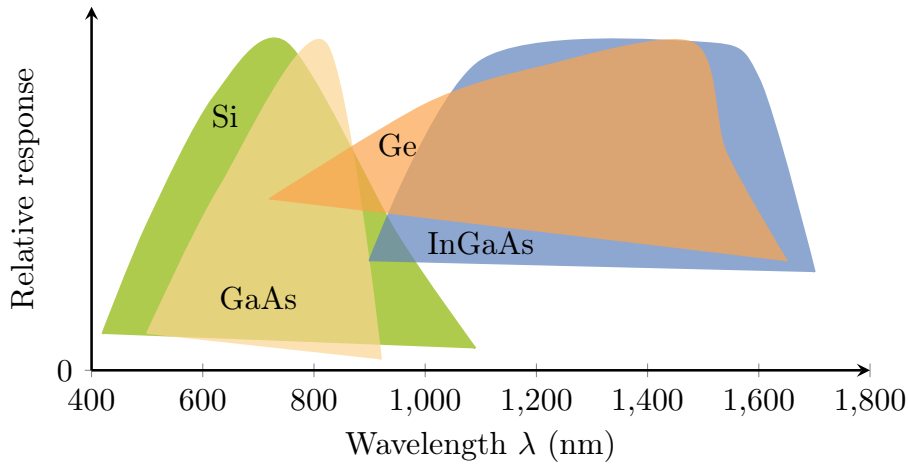


Figure 2.2: Relative responsivity curve of photodetector for different materials composition (adapted from [74]).

photodetectors offer good responsiveness in the visible range, their efficiency in detecting blue wavelengths remains limited. For this reason, despite the slightly higher underwater attenuation of green wavelengths, light emitters in the green range are preferred, as silicon photodetectors are more sensitive to this wavelength, improving system efficiency.

Concerning photodiode technology, *p-i-n* (PIN) and avalanche photodiodes (APD) are two practical examples of photodetectors used in optical wireless systems [41, 77]. In a PIN photodetector, the inclusion of an intrinsic region between the *p*-type and *n*-type layers increases the width of the depletion region. This expansion of the depletion region allows a larger number of photons to be absorbed than in a *p-n* junction. An APD photodetector shares the basic operating principle of PIN photodetectors, but it applies a high bias voltage, close to the reverse breakdown voltage. This allows the electrons released by incoming photons to gain high kinetic energy, causing collisions with the atoms of the material and releasing additional electrons. This chain reaction, known as the avalanche effect, results in internal signal amplification and gives the APD higher sensitivity.

The higher sensitivity of the APD makes it more suitable for long-range links such as fiber-optics links between continents or optical satellite communications, compared to PIN photodetectors [80]. However, the avalanche process in APDs photodetectors introduces an additional noise component proportional to the generated photocurrent due to the multiplication electron in the avalanche process, which can potentially degrade the performance of the detected signal. Furthermore, the avalanche process is highly sensitive to temperature variations.

2.2 Underwater channel impairments

As described in Chapter 1, most commercial UOWC systems are capable of providing data rates of up to tens of Mbps over distances of up to 150 meters. However, it is important to note that manufacturers specify that these performance specifications are measured under conditions of clear water as well as deep-water environments [47–49]. While this highlights the potential capabilities of UOWC systems, it also underscores that the performance can vary significantly in less favorable underwater channel conditions. The underwater optical channel has unique characteristics and differs in several critical aspects from atmospheric FSO channels, which have been extensively discussed in the literature [40–42].

In UOWC, light propagation is greatly influenced by the properties of the aquatic medium. In [81], the optical properties of natural waters are classified into inherent optical properties (IOPs) and apparent optical properties (AOPs). An inherent property is one that does not depend on the ambient light field; an apparent property is one for which this is not the case. Accordingly, the IOPs depend mainly on the composition and concentration of the subsea particulates and dissolved substances in the medium. The IOPs usually employed in UOWC are the absorption and scattering coefficients, which are used to describe the underwater medium and its composition. For that reason, both IOPs are usually used to describe different types of water. Understanding the impact of IOPs on UOWC systems performance helps us to propose a UOWC system customized explicitly for particular scenarios.

Furthermore, light propagation in the underwater medium is also affected by other phenomena such as oceanic turbulence, which causes small changes in the index of refraction, due to temperature and salinity fluctuations. As will be discussed in the following sections, the relative impact of refractive index fluctuations due to ocean turbulence is typically negligible in certain scenarios and does not significantly affect light propagation. However, their effects can be noticeable in high-quality imaging systems, as well as in UOWC systems that use coherent and narrow light beams, such as those provided by LD sources. In addition to these effects, the optical beam is also disturbed and blocked by the presence of air bubbles, which also causes random fluctuations in the refractive index owe to the interface between water and air bubbles [82].

The following sections discuss the optical properties of the above mentioned impairments, and examine the impact of each one on the light beam propagation.

2.2.1 Absorption and scattering

The absorption process occurs when propagating photons interact with molecules of a medium along their path. During this interaction, the energy state of the molecules is elevated to a higher energy level, whereby the photons' energy is converted to another form, such as heat. This process results in a reduction in the number of photons traveling through

the medium. In underwater environments, light absorption is affected not only by water molecules but also by particles and organisms suspended in the water, such as phytoplankton. For instance, the absorbed photon energy is used by these organisms for oxygenic photosynthesis, which converts light energy into chemical energy. It is important to note that water salinity, i.e., the presence of dissolved salt particles, has a negligible impact on light absorption, as demonstrated by various experimental studies [83, 84].

The absorption characteristic in a given underwater medium highly depends on the type of the particles in suspension, their chemical composition, and their concentration. For instance, pure water, which has a chemical composition of H_2O , exhibits lower absorption than coastal water. Coastal waters contain higher concentrations of particles, organic matter, sediment, and other contaminants that contribute to increased light absorption. These additional contaminants in the water limit the light that can penetrate and propagate through the medium.

In order to define the coefficients that describe the absorption and scattering properties of a water body, it is necessary to define the concept of absorptance. The absorptance is defined as the fraction of incident optical power by a collimated beam at a wavelength λ that is absorbed by a small volume of water ΔV along a distance Δl , given by

$$A(\lambda) \triangleq \frac{\Phi_a(\lambda)}{\Phi_i(\lambda)}, \quad (2.2)$$

where $\Phi_i(\lambda)$ is the incident power, and $\Phi_a(\lambda)$ is the absorbed optical power.

The absorption coefficient, $a(\lambda)$, is defined as the absorptance *per unit distance*, i.e., when Δl tends to zero. Hence, the absorption coefficient is defined as follows

$$a(\lambda) \triangleq \lim_{\Delta l \rightarrow 0} \frac{\Delta A(\lambda)}{\Delta l} \quad (\text{m}^{-1}). \quad (2.3)$$

As the absorption effect, the scattering process results from the interaction of a light beam with a molecule or a particle. The interaction causes an angular redistribution of the optical field, but there is no loss of beam energy like in the absorption effect. At this point, it is possible to differentiate between two types of scattering: elastic scattering and inelastic scattering. In elastic scattering, only the direction of the light beam changes, whereas in inelastic scattering, there is an associated change in wavelength. In this thesis, we primarily focus on elastic scattering.

The result of the interaction depends on the geometry of the particle and its relationship with the wavelength of the incident light. In the case of spherical and homogeneous particles that are smaller than the wavelength of the transmitted beam, the phenomenon of Rayleigh scattering occurs. In this scattering process, no interference phenomenon cancels out the radiation in any direction, therefore the intensity of the scattered light is the same in all directions. This type of scattering is evidenced in the interaction of light with water molecules.

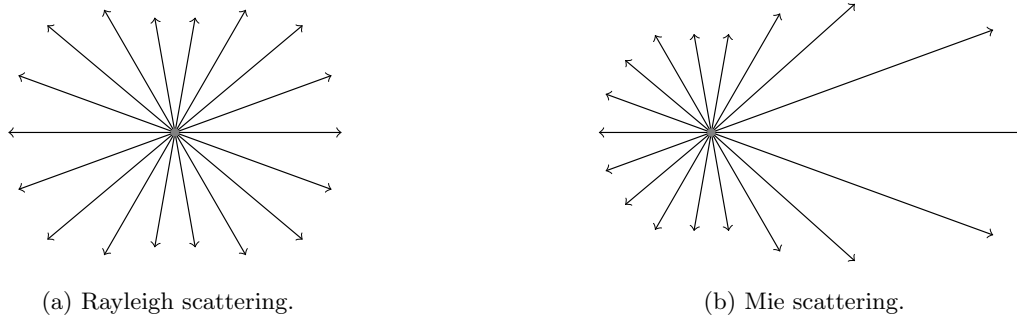


Figure 2.3: Angular distribution of (a) Rayleigh scattering, and (b) Mie scattering.

When light interacts with particles of similar or slightly larger size than the optical wavelength, Mie scattering is produced. In this case, the particle absorbs part of the transmitted light while the remaining portion is reflected, resulting in greater forward scattering [42]. A graphical representation of the angular distribution of Rayleigh and Mie scattering is shown in Fig. 2.3. The effects of particle sizes significantly larger than the wavelength are analyzed using diffraction theory or through the simplified approach of geometrical optics, which describes light propagation in terms of rays. This simplification is particularly useful when the wavelength is much smaller than the dimensions of the structures with which the light interacts.

Nevertheless, the theory of Rayleigh and Mie scattering is not applicable to underwater scattering by oceanic particles, such as phytoplankton or minerals, which are too large and not spherical. In such cases, the behavior of the scattered light follows more complex expressions that depend on the geometry and nature of the subsea particles [85].

The dispersive properties of the underwater medium are characterized by its volume scattering function (VSF), which describes the angular distribution of scattered power. It is important to note that the VSF is applicable only to an isotropic medium, i.e., its influence on light is the same in all directions at a specific point. This is a reasonable assumption for natural waters bodies, where particles are randomly oriented due to ocean currents and turbulence [85]. Mathematically speaking, the VSF provides the probability of light being scattered at an angle θ around a solid angle $\Delta\Omega$ relative to its angle of incidence. Thus, by integrating the VSF over all possible scattering angles and assuming that scattering is azimuthally symmetrical around the direction of incidence, the scattering coefficient is obtained as follows

$$b(\lambda) = \int \beta(\theta) d\Omega = 2\pi \int_0^\pi \beta(\theta) \sin(\theta) d\theta, \quad (2.4)$$

where $\beta(\theta)$ is the volume scattering function. This integration is often divided into forward scattering and backward scattering parts. The corresponding forward and backward

scattering coefficients are, respectively, as follows

$$b_f(\lambda) = 2\pi \int_0^{\pi/2} \beta(\theta) \sin(\theta) d\theta. \quad (2.5a)$$

$$b_b(\lambda) = 2\pi \int_{\pi/2}^{\pi} \beta(\theta) \sin(\theta) d\theta. \quad (2.5b)$$

For simplicity, throughout this work, the forward scattering coefficient $b_f(\lambda)$ will be referred to as scattering and will be denoted as b due to the negligible impact of the backward scattering. A measure that characterizes the shape of the VSF regardless of the magnitude of the intensity of the scattered light is the scattering phase function (SPF), which is obtained by normalizing the VSF to the scattering coefficient as follows

$$\bar{\beta}(\theta) \triangleq \frac{\beta(\theta)}{b}. \quad (2.6)$$

Similarly to the absorption coefficient, the scattering coefficient can be also defined by the scatterance, which represents the fraction of incident optical power that is scattered out of the propagation direction into other directions by a small volume of water, ΔV , over a distance Δl . given by

$$B(\lambda) \triangleq \frac{\Phi_s(\lambda)}{\Phi_i(\lambda)}, \quad (2.7)$$

where $\Phi_s(\lambda)$ is the scattered optical power. Hence, the scattering coefficient, $b(\lambda)$, is defined as the scatterance *per unit distance* as follows

$$b(\lambda) \triangleq \lim_{\Delta l \rightarrow 0} \frac{\Delta B(\lambda)}{\Delta l} \quad (\text{m}^{-1}). \quad (2.8)$$

Fig. 2.4 illustrates the interaction of a light beam with a water body, depicting the fractions of optical power that are transmitted, absorbed, and scattered through an angle θ , also known as scattering angle, around a solid angle $\Delta\Omega$. It is important to note that a similar process occurs when the light beam encounters a subsea particle during its propagation through the underwater medium. By conservation of energy, the transmitted optical power can be described as follows

$$\Phi_t(\lambda) = \Phi_i(\lambda) - \Phi_a(\lambda) - \Phi_s(\lambda). \quad (2.9)$$

Based on the definitions of the absorption and scattering coefficients presented above, another useful parameter known as the total attenuation coefficient is defined as follows

$$c(\lambda) = a(\lambda) + b(\lambda) \quad (\text{m}^{-1}). \quad (2.10)$$

It should be noted that the attenuation coefficient is also defined as the extinction coefficient, which describes how a light beam can traverse a volume of material. In UOWC channel

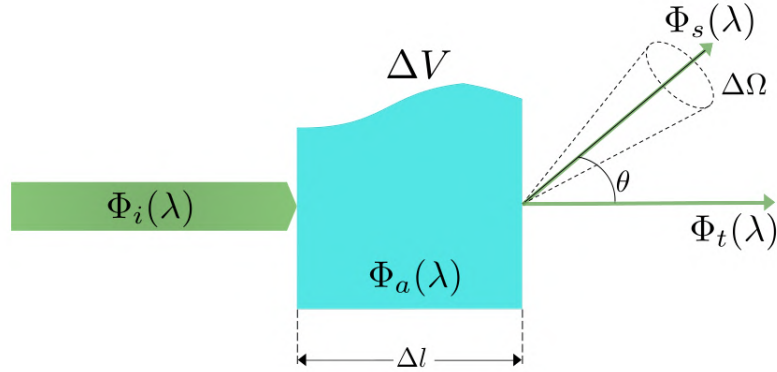


Figure 2.4: Graphical representation of the interaction between a collimated light beam and a small volume of water.

modeling, another common IOP is the scattering albedo, which is defined as follows

$$w(\lambda) = \frac{b(\lambda)}{c(\lambda)}. \quad (2.11)$$

The scattering albedo represents the fraction of scattered power within the total power that has not been transmitted. A scattering albedo value close to 1 indicates that the medium under study is highly dispersive, whereas a value close to 0 indicates that the medium is minimally dispersive.

Water classification

As mentioned before, the absorption and scattering coefficients are primarily influenced by the composition, morphology, and concentration of particles and dissolved substances in a specific water body. A key challenge in oceanography is understanding how the diverse constituents of the ocean determine the variability in IOPs, as well as its impact on the light beam propagation. The variability can be observed in the different textures and colors exhibited by the same body of water at different times. For example, in Fig. 2.5, the yellow and green swirls indicate the presence of extensive phytoplankton populations. The duration of sunlight, the variability of nutrient influx from ocean currents and freshwater rivers, and changing water temperatures result in varying concentrations of phytoplankton that are even observable from space. From the optics radiation perspective, the color of the water provides information about the wavelength with the lowest absorption coefficient for that particular water body.

In accordance with the oceanography literature, natural waters can be classified into distinct standard optical water types according to light transmittance [85]. In this thesis, we consider the three major water types used in UOWC literature, as presented in Table 2.2 with

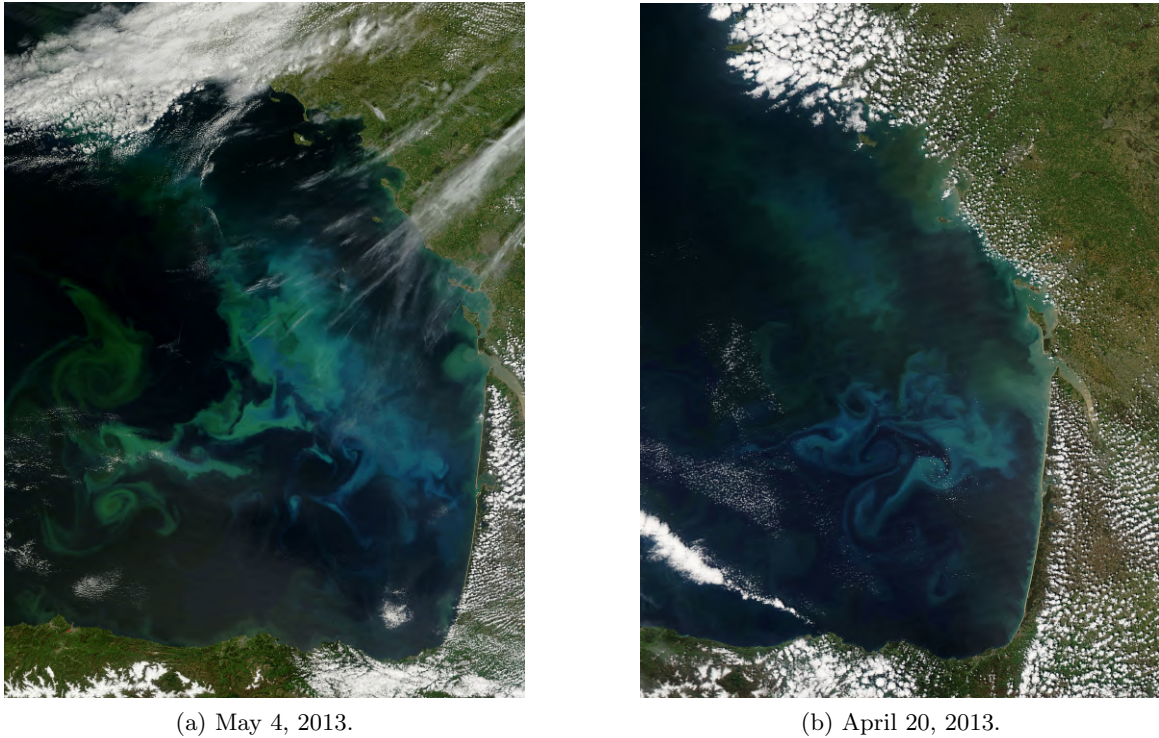


Figure 2.5: Phytoplankton concentration in the Bay of Biscay captured at two different times by the Moderate Resolution Imaging Spectroradiometer aboard NASA’s Terra satellite [86].

their respective absorption, scattering, and extinction coefficients [19]. It should be mentioned that these coefficient are measured when considering a green wavelength of $\lambda = 532$ nm. However, an alternative classification system, known as the Jerlov water types, is also commonly used in UOWC literature and is presented in Table 2.3 [87]. On the one hand, Jerlov water classification categorizes open ocean waters into types I, IA, IB, II, and III, with type I being the clearest one and type III the most turbid one. On the other hand, coastal waters are classified from type 1C (clearest) to type 9C (most turbid). Types I-III typically correspond to waters bodies dominated by phytoplankton, while types 1C-9C correspond to those dominated by yellow matter and terrigenous particles. This is reflected in the chlorophyll concentration associated with each type of water, as shown in Table 2.3.

IOPs such as absorption and scattering coefficients can be estimated from a chlorophyll concentration based on bio-optical models [88, 89]. In [88], the correlation between the average value of the absorption coefficient and the concentration of phytoplankton and other underwater organic elements in different water samples is analysed. While this method allows for the estimation of water absorption based on its composition, it does not enable the estimation of the scattering coefficient. In [89], a bio-optical model based on *in situ* measurements in different waters and oceans is proposed. This model allows for the esti-

Table 2.2: Summary of absorption, scattering, and extinction coefficient for different water types when considering a green wavelength [19].

Water type	a [m^{-1}]	b [m^{-1}]	c [m^{-1}]
Clear ocean water	0.114	0.037	0.151
Coastal ocean water	0.179	0.219	0.398
Turbid harbor water	0.295	1.875	2.17

mation of the absorption coefficient, the scattering coefficient, and the VSF using only the chlorophyll concentration and the wavelength employed. Although these bio-optical models are useful for estimating water properties from chlorophyll concentration, their results lack the precision required for high-accuracy applications. The substantial discrepancies between model predictions and empirical measurements are likely due to absorption and scattering being influenced not only by particle concentration (typically parameterized by chlorophyll concentration) but also by the particle index of refraction and the specifics of the particle size distribution, which are inadequately represented by chlorophyll concentration alone.

Table 2.3: Summary of chorophyll concentration for different Jerlov water types [87].

Water type	Concentration of Chlorophyll (mg/m^3)
I	0.010
IA	0.027
IB	0.037
II	0.044
III	0.177
1C	1
3C	1.28
5C	3.95
7C	8.4
9C	9.1

The SPF is also approximated by statistical models fitted to experimental measurements in various oceanic environments. Among the numerous measurement campaigns conducted to characterize the VSF in different locations worldwide, it should be highlighted the one by Theodore J. Petzold in 1972 in the coast of California and the Bahamas, which considers a wide range of water types, from very clear to turbid waters [90]. While it is preferable to use an VSF measured at the exact location and time of the study when modeling a specific water body, obtaining these measurements can be technically challenging and expensive. Consequently, generic phase functions, such as the Henyey-Greenstein (HG), are usually assumed. The HG phase function was initially proposed to study scattering by interstellar

dust in astrophysics. However, it has gained renown due to its mathematical simplicity and extensive use in various fields, including oceanography [85, 91]. The HG phase function is expressed as

$$\bar{\beta}_{\text{HG}}(\theta, g) = \frac{1 - g^2}{2(1 + g^2 - 2g \cos \theta)^{3/2}}, \quad (2.12)$$

where g is the HG asymmetry parameter that depends on the characteristics of the medium and represents the average cosine of θ across all scattering directions. In [92], the parameter g was calculated for clear ocean, coastal, and turbid harbor waters. However, in [93], it is verified that small variations in g have a negligible effect on the underwater optical channel characteristics. With the aim of improving the fit of the HG model at small and large scattering angles, a linear combination of Henyey-Greenstein functions is often employed to enhance accuracy. This approach, known as the Two-Term Henyey-Greenstein (TTHG) phase function, is expressed as follows [94]

$$\bar{\beta}_{\text{TTHG}}(\theta, g_1, g_2, \alpha) = \alpha \bar{\beta}_{\text{HG}}(\theta, g_1) + (1 - \alpha) \bar{\beta}_{\text{HG}}(\theta, g_2), \quad (2.13)$$

where $\alpha \in [0, 1]$ is a weighting factor.

Radiative transfer equation

As can be observed, the propagation of a light wave in water can be complex and challenging for theoretical treatments due to the intrinsic phenomena of the aquatic medium, primarily scattering. This complexity is reflected in the radiative transfer equation (RTE), which describes the propagation of a light wave through the underwater medium in terms of its IOPs [95]. Let us denote by $\Psi(z, \theta, \phi)$ the light radiance, z the distance between the transmitter and receiver, and θ and ϕ the polar and azimuthal angles, respectively. Hence, the RTE is defined as follows [93]

$$\frac{d\Psi}{dr} = -c\Psi + \Psi^E + \Psi^I, \quad (2.14)$$

where $r = z / \cos(\theta)$ is the link distance, Ψ^E and Ψ^I are the path functions for elastic and inelastic scattering, respectively. Due to its minimal impact on the solution of the RTE, inelastic scattering is typically neglected [93]. Hence, Ψ^I can be ignored in Eq. (2.14). By assuming a situation of horizontally homogeneous water and time independence, the RTE can be expressed as follows [95]

$$\begin{aligned} \frac{d\Psi(r, \theta, \phi, \lambda)}{dr} = & -c(r, \lambda)\Psi(r, \theta, \phi, \lambda) + \\ & \int_0^{2\pi} \int_0^\pi \Psi(r, \theta', \phi', \lambda) \beta(r, \theta', \phi' \rightarrow \theta, \phi, \lambda) \sin(\theta') d\theta' d\phi'. \end{aligned} \quad (2.15)$$

To the best of the author's knowledge, a closed-form solution of the RTE can be obtained only under certain assumptions and simplifications. The most commonly used approximation in the literature includes two implicit assumptions: the transmitter and receiver are

perfectly aligned and all scattered photons are lost. Both of these assumptions are reflected mathematically in Eq. (2.14) by neglecting the term Ψ^E . In this case, Eq. (2.15) can be simplified as follows

$$\frac{d\Psi(r, \theta, \phi, \lambda)}{dr} = -c(r, \lambda)\Psi(r, \theta, \phi, \lambda), \quad (2.16)$$

which can be easily solved as follows

$$\Psi(r, \lambda) = \Psi(0)e^{-c(\lambda) \cdot r}, \quad (2.17)$$

where $\Psi(0)$ is the transmitted radiance by the emitter. This result is known as the Beer-Lambert's law, which is also assumed in atmospheric FSO channel modeling [42]. The Beer-Lambert model provides some insight into the attenuation that suffer the optical beam propagated a link distance d through the underwater medium. Fundamentally, this model describe the path loss between the transmitter and the receiver, which can be obtained as follows

$$L = \frac{\Psi(d, \lambda)}{\Psi(0)} = e^{-c(\lambda) \cdot d}. \quad (2.18)$$

Note that the product $-c(\lambda) \cdot d$ is usually called as optical depth or attenuation length in optical wireless literature [74, Eq. (3.50)]. Therefore, the Eq. (2.18) can be expressed as follows

$$L = e^{-\tau}, \quad (2.19)$$

where τ is the optical depth.

However, Beer-Lambert's model is inadequate to give an accurate path loss estimation in practical underwater scenarios since in practice underestimates the received optical power, especially in turbid environments, where scattering is the dominant inherent optical property. The assumption of Eq. (2.16) neglects all the scattered photons. Nevertheless, a considerable proportion of the scattered photons are deviated at small angles, resulting in the scattered photons traveling in a direction that is similar to that of the unscattered photons. Consequently, photons scattered at small angles would be reached in the photodetector, thereby increasing the received optical power. Although more advanced analytical or quasi-analytical approximations exist beyond Beer-Lambert's law, they all rely on various simplifying assumptions, often leading to results that can deviate by an order of magnitude [96–98].

A strategy to overcome this problem is applying numerical methods commonly employed in light propagation problems [99]. The Monte Carlo ray tracing method, known for its simplicity and versatility, is extensively applied to solve the RTE across various disciplines, including oceanography and atmospheric sciences [100, 101]. The Monte Carlo method simulates the trajectories of emitted rays under an absorptive and dispersive medium by considering the multiple interactions of a ray with underwater particles. Although this approach often requires lengthy computational times for complex problems, some mathematical strategies can reduce the computational process.

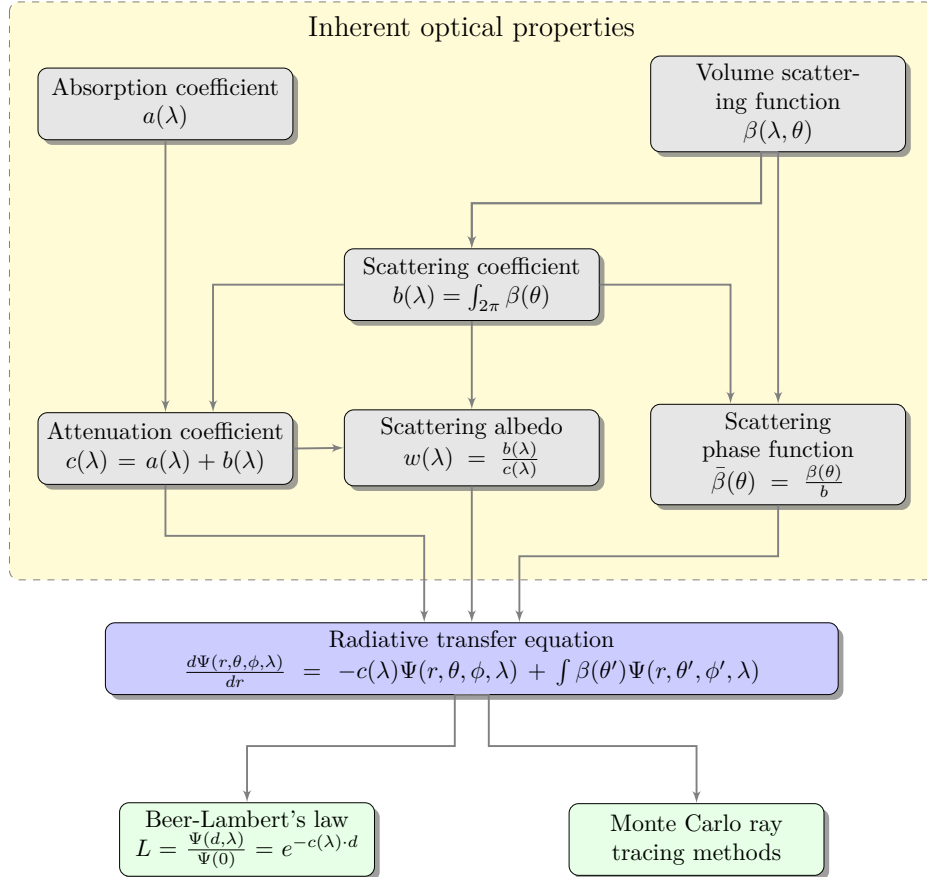


Figure 2.6: Relationships among the main IOPs used in UOWC.

In Fig. 2.6, the most common IOPs employed in UOWC, along with their interrelationships with the RTE and its solutions are illustrated. In this figure, the importance of considering the light scattering phenomenon not only through the attenuation coefficient but also through the VSF is highlighted. This approach is crucial for accurately capturing the overall effects of scattering. Therefore, it is imperative to develop channel models that represent both the attenuation phenomenon and the spreading associated with scattering in detail, allowing for a more comprehensive and precise characterization of light transmission in aquatic environments.

2.2.2 Oceanic turbulence

Oceanic turbulence is a complex phenomenon that is part of the overall behavior of the oceans and is related to larger-scale processes. Firstly, solar energy heats the Earth's surface, generating atmospheric winds that drive the majority of surface currents and waves in the ocean. Additionally, variations in solar radiation induce pressure and density differences

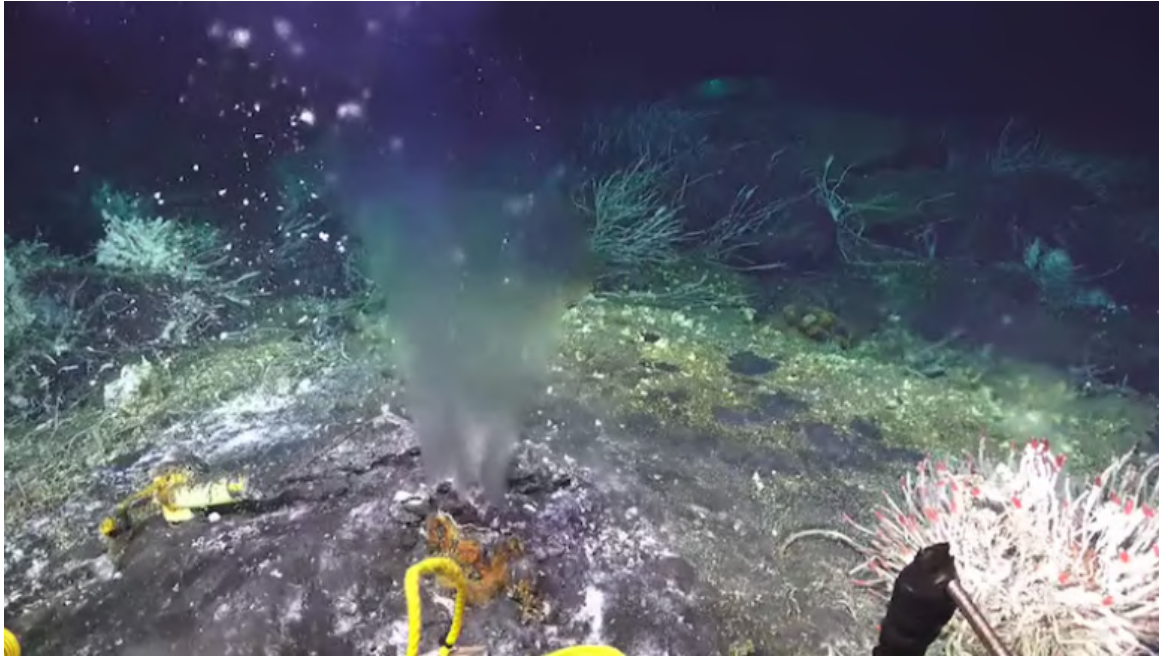


Figure 2.7: Blurred visual effect due to a geothermally heated water discharge from a hydrothermal vent which induce temperature-induced oceanic turbulence.

that produce deep and vertical underwater currents. Although these density fluctuations are typically minor, they are sufficient to cause denser waters to sink, by generating a process known as thermohaline circulation, driven by temperature and salinity variations at the surface [102]. While these currents are usually analyzed such as slow movements of large volumes of water, small-scale variations in salinity and temperature also produce turbulent phenomena that can affect the transmission of a light beam over moderate and long distances. Specifically, temperature and salinity fluctuations due to the thermohaline circulation generate small-scale but spatially continuous changes in the index of refraction, causing small-angle deviations in the direction of light propagation. These effects are referred to as oceanic turbulence. In specific circumstances, these fluctuations can reach large magnitudes, with temperature differentials of several degrees and salinity differentials of many practical salinity units, particularly where cold or freshwater mixes with warm or salty water. Rainfall on the sea surface, river inflows into the ocean, and near hydrothermal vents on the seabed are examples of scenarios where differences in temperature and salinity cause extreme oceanic turbulence. Under such extreme conditions, optical turbulence near these boundaries can produce unique visual effects even for the human eye, like visual perception of blurred objects seen through the water, as shown in Fig. 2.7.

Generally speaking, oceanic turbulence is similar to atmospheric turbulence, which has been extensively studied in the literature on FSO systems [40,42,103]. According to these studies,

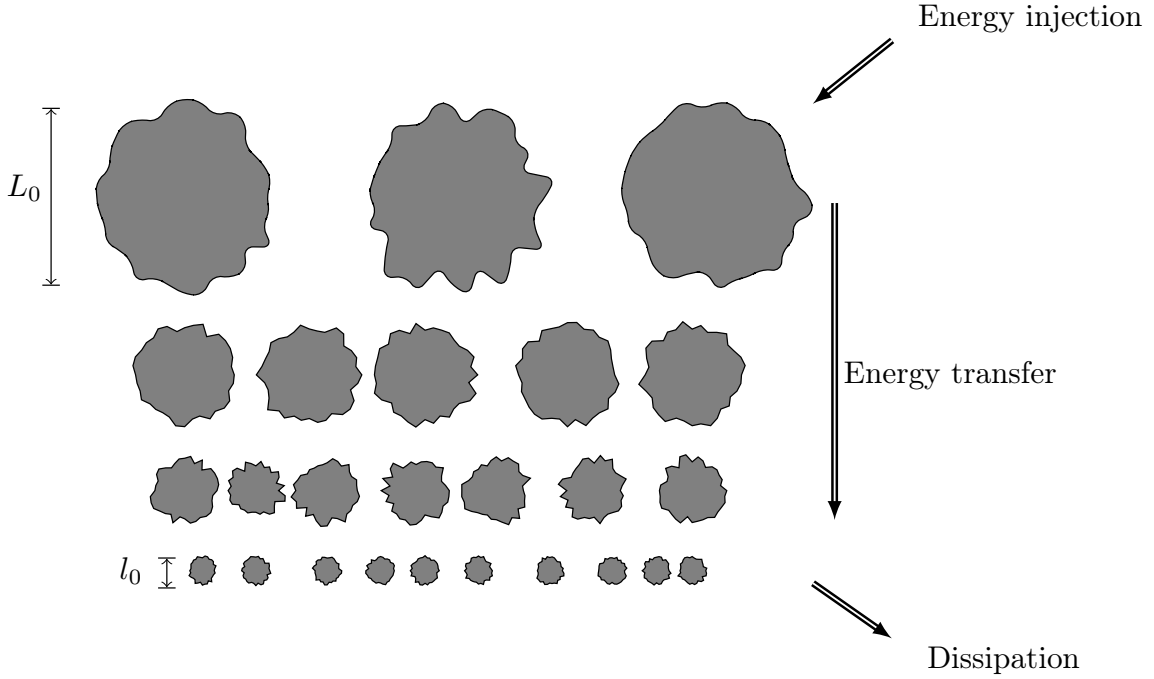


Figure 2.8: Representation of Kolmogorov cascade theory of turbulence.

turbulent air motion represents a set of eddies (air masses) of various scale sizes. By their nature, turbulent media are challenging to be described mathematically due to the non-linear physical processes intrinsic to the turbulent process in a fluid. To avoid the difficulty associated with using the Navier-Stokes equations that govern the behavior of turbulent fluid, Kolmogorov developed the cascade theory of turbulence [104, 105]. According to this theory, large eddies break down into smaller ones under the influence of inertial forces, initiating a continuous cascade of eddies with decreasing sizes between L_0 and l_0 . This process, illustrated in Fig. 2.8, represents the cascade of eddies, assuming a vertical time axis for a fixed spatial point. The sizes of these eddies range from a macroscale L_0 , known as the outer scale of turbulence, which corresponds to the characteristic size of the largest eddies, to a microscale, l_0 , referred to as the inner scale of turbulence. Scales smaller than l_0 fall within the viscous dissipation range, where turbulent eddies vanish, and the remaining energy in the fluid motion is dissipated as heat. In atmospheric turbulence, L_0 and l_0 are typically on the order of several meters and a few millimeters, respectively [42].

Without going into details, it is possible to calculate the expression for the spatial power spectral density (PSD) of refractive index fluctuations defined by Kolmogorov, which is examined in greater detail in [42, Chapter 3], as follows

$$\Phi_n(\kappa) = 0.033C_n^2\kappa^{-11/3}, \quad 1/L_0 \ll \kappa \ll 1/l_0, \quad (2.20)$$

where κ is the scalar spatial frequency (in units of rad/m), and C_n^2 is the refractive index

structure parameter, which depends on local conditions and characterizes the intensity of the atmospheric refractive index fluctuations. The Kolmogorov spectrum is commonly applied in theoretical analyses in FSO, but its applicability is restricted with respect to wavelength. As can be observed, this spectrum is valid only over the range $1/L_0 \ll \kappa \ll 1/l_0$, also known as the inertial subrange. It is generally assumed that the outer scale is infinite ($L_0 \rightarrow \infty$) and the inner scale is negligible ($l_0 = 0$). However, alternative models for refractive index fluctuations, such as the Tatarskii and Von Kármán models, become necessary when the effects of the outer and inner scales are significant and cannot be overlooked [42].

The generation processes of oceanic turbulence are quite different from those of atmospheric turbulence because atmospheric turbulence are primarily induced by temperature fluctuations, while oceanic turbulence are induced by temperature and salinity fluctuations. Therefore, it is not possible to adopt the power spectral density for refractive index fluctuations of Eq. (2.20) for oceanic scenarios. To analyze these phenomena independently, scalar spatial PSD² were developed to model temperature and salinity fluctuations separately as follows [27, 28]

$$\phi_T(\kappa) = C_0 \epsilon^{-1/3} \chi_T \kappa^{-5/3} \left[1 + C_1 (\kappa \eta)^{2/3} \right] \exp[-A_T \delta], \quad (2.21a)$$

$$\phi_S(\kappa) = C_0 \epsilon^{-1/3} \chi_S \kappa^{-5/3} \left[1 + C_1 (\kappa \eta)^{2/3} \right] \exp[-A_S \delta], \quad (2.21b)$$

where $C_0 = 0.72$ is the Obukhov-Corrsin constant, $C_1 = 2.35$ is a fitted constant, ϵ is the rate of loss of turbulent kinetic energy per unit mass of fluid, χ_T is the rate of loss of temperature variance, χ_S is the rate of loss of salinity variance, η is the Kolmogorov length scale, $\delta = 1.5C_1^2(\kappa\eta)^{4/3} + C_1^3(\kappa\eta)^2$, $A_T = C_0 C_1^2 / Pr_T$, and $A_S = C_0 C_1^2 / Pr_S$. Coefficient Pr_T , and Pr_S are the *Prandtl* numbers defined as $Pr_T = \nu / \chi_T$, and $Pr_S = \nu / \chi_S$, where ν is the kinematic viscosity. On the one hand, the inner scale is assumed as the Kolmogorov length scale is assumed as, i.e., $l_0 = \eta$. On the other hand, it is assumed that outer scale is infinite ($L_0 \rightarrow \infty$).

In the year 2000, both temperature and salinity PSD were integrated into a single linearized polynomial power spectrum [29]. The combination of the two scalar spectra in a single expression is obtained from the relation between the refractive index and the normalized fluctuations of temperature and salinity described in [107]. Hence, the scalar spatial PSD of refractive index fluctuations is obtained as follows

$$\phi_n(\kappa) = C_0 \epsilon^{-1/3} \kappa^{-5/3} \left[1 + C_1 (\kappa \eta)^{2/3} \right] [G_T(\kappa) + G_S(\kappa) - 2G_{TS}(\kappa)], \quad (2.22)$$

where

$$G_T(\kappa) = \alpha_T^2 \chi_T \exp[-A_T \delta], \quad (2.23a)$$

$$G_S(\kappa) = \alpha_S^2 \chi_S \exp[-A_S \delta], \quad (2.23b)$$

²Scalar, or one-dimensional, spatial PSD (denoted by the symbol ϕ) are related to the three-dimensional spatial PSD (denoted by the symbol Φ) as described in [42, Eq. 2.53]. Specifically, temperature and salinity scalar spatial PSD are related to the three-dimensional spatial PSD as $\Phi(\kappa) = \frac{1}{4\pi} \kappa^2 \phi(\kappa)$ [106].

$$G_{TS}(\kappa) = \alpha_T \alpha_S \chi_{TS} \exp[-A_{TS}\delta], \quad (2.23c)$$

where $A_{TS} = 0.5C_0C_1^{-2}(\frac{1}{P_{rT}} + \frac{1}{P_{rS}})$. In order to tune the strength of the temperature and salinity fluctuations, both rates of dissipation are related to the temperature gradient, T_0 , and salinity gradient, S_0 , as follows

$$\chi_T = K_T T_0^2, \quad (2.24a)$$

$$\chi_S = K_S S_0^2, \quad (2.24b)$$

where K_T and K_S are the coefficients of the eddy thermal diffusivity and diffusion of the salt. Furthermore, it is defined the temperature-salinity balance parameter as follows

$$w = \frac{\alpha_T T_0}{\alpha_S S_0}, \quad (2.25)$$

where $\alpha_T = 2.6 \times 10^{-4}$ L/°C, $\alpha_S = 1.7 \times 10^{-4}$ L/g. The temperature-salinity balance parameter w represents the ratio of temperature and salinity contributions to the spatial PSD for refractive-index fluctuations. Experimental data limit the range of w to the interval $[-5, 0]$ [107]. A larger value of this ratio ($w \rightarrow 0$) indicates that turbulence is predominantly influenced by salinity fluctuations, leading to a strong turbulence regime. Conversely, a smaller ratio ($w \rightarrow -5$) indicates that turbulence is predominantly induced by temperature fluctuations, resulting in a weak turbulence regime [30]. Thus, by considering isotropic and homogeneous waters concerning temperature and salinity, and after performing some algebraic manipulations, $\Phi_n(\kappa)$ is derived as in [29, 30]

$$\Phi_n(\kappa) = \frac{C_0 \alpha_T^2}{4\pi} \kappa^{-11/3} \epsilon^{-1/3} \left[1 + C_1(\kappa\eta)^{2/3} \right] \times \frac{\chi_T}{w^2} \left(w^2 e^{-A_T\delta} + e^{-A_S\delta} - 2w e^{-A_{TS}\delta} \right), \quad (2.26)$$

This unified model, also known as Nikishov's spatial PSD, has become the predominant power spectrum used in underwater optical turbulence. Due to its simplicity and adaptability, it is widely employed in theoretical predictions of light behavior in underwater turbulence [30]. In an effort to more precisely characterize various oceanic turbulence conditions, several spatial PSD have been proposed to consider more specific environmental parameters [108, 109]. It should be mentioned the OTOPS (*Oceanic Turbulence Optical Power Spectrum*) model, which has recently been introduced in [110]. This model allows for the consideration of average water temperature and salinity concentration [111].

Another noteworthy aspect is the dependence of oceanic turbulence on water depth. Although both salinity and temperature vary significantly with water depth, it is important to note that at great depths (below 1000 meters), both physical parameters remain practically constant down to the ocean floor [112, Chapter 5]. This implies that the effect of oceanic turbulence can be ignored in deep-water scenarios. In this regard, the OTOPS PSD stands out for its ability to incorporate specific average temperature and salinity concentration values into the Prandtl numbers and the eddy diffusivity ratio calculations [111]. This feature allows for a more accurate adjustment of the natural water conditions on Earth, reflecting

the variation of temperature and salinity with depth. Although this approach results in a mathematically more complex final form of the spectrum, it offers the advantage of enabling more precise calculations, thereby improving the representation of the optical characteristics of water in natural contexts. However, it can also be seen as more cumbersome due to the large number of constants and physical parameters it involves, making the Nikishov spatial PSD approach more practical in this regard. The Nikishov model has, in fact, gained broader acceptance and has consolidated itself as the reference power spectrum for modeling oceanic turbulence [113].

2.2.3 Air bubbles

Air bubbles in the oceanic environment result from various independent phenomena, increasing the heterogeneity of bubble types and their effects on a UOWC system. Numerous studies have explored the role of air bubbles in the air-sea gas transfer process [114, 115]. Bubble clouds are formed when wind-driven waves break in the open ocean, entraining air into the water body [32]. These clouds initially comprise a broad spectrum of bubble sizes with diameters between 0.8 mm and 8 mm [116]. Larger bubbles, due to their significant buoyancy, ascend rapidly and burst at the surface, while smaller bubbles disperse laterally or sink deeper. The shape and penetration depth of bubble clouds are influenced by the turbulent dynamics within the water. The spatial and temporal distribution of these subsurface bubble clouds manifests as whitecaps on the ocean surface, which randomly form, evolve, and eventually dissipate over time. Aquatic organisms, such as phytoplankton, also generate and release gas bubbles to modulate their buoyancy, enabling them to position themselves optimally for photosynthesis or move to locations with varying oxygen concentrations [31, 117, 118]. Additionally, human activities, such as the cavitation effect of underwater vehicle propellers and the breathing systems of scuba divers, also contribute to generating air bubbles [119].

In terms of light propagation, an air bubble submerged in water represents an element with a refractive index that differs from that of the underwater medium. In other words, an air bubble can be treated as a local water-to-air interface. Depending on the bubble size relative to the wavelength of light, its interaction with incident rays can be described using different optical frameworks. When the bubble is assumed as spherical and its diameter is smaller or comparable to the wavelength, Rayleigh and Mie scattering theory are commonly applied to evaluate their optical properties, respectively, as described in Fig. 2.3 [120, 121]. For macroscopic bubbles relative to the wavelength, each point on the bubble can be approximated as a small segment of a flat surface for the incident light [85]. This approximation is valid because, locally, the curvature of the bubble is negligible compared to the wavelength scale for a light ray. Although the bubble has a spherical shape, a light ray interacts only with a small flat region of its surface. In this case, the interaction of light with the air bubble is governed by the law of refraction along with the Fresnel equations, which describe the

reflection and transmission of light at the interface between different media with different refraction indices.

Law of refraction

Consider a light ray traveling through a homogeneous medium characterized by a refractive index n_1 , which strikes the interface separating this medium from another homogeneous medium with a refractive index n_2 . At the interface between two media, the angle of incidence θ_i and the angle of transmission θ_t are related by the law of refraction, commonly referred to as *Snell's law*, as follows [122]

$$n_1 \sin \theta_i = n_2 \sin \theta_t. \quad (2.27)$$

In addition to the refraction phenomenon, the interaction of the light ray with the interface results in the reflection of a ray back into the original medium with a reflection angle θ_r . According to the law of reflection, the angle of reflection is equal to the angle of incidence, i.e., $\theta_i = \theta_r$ [122]. It should be noted that all angles involved in both the law of reflection and Snell's law of refraction are measured with respect to the normal to the surface at the point of incidence.

It is worth highlighting a particularly important case. According to Eq. 2.27, when a light ray transitions from a medium with a higher refractive index to one with a lower refractive index, $n_1 > n_2$, no transmission occurs if the angle of incidence satisfies $\sin(\theta_i) > \frac{n_2}{n_1}$. This is because, under these conditions, there is no real value of the transmission angle θ_t that satisfies Snell's law (the value of $\sin \theta_t$ is $\frac{\pi}{2}$ as maximum). The angle of incidence for which $\sin(\theta_i) = \frac{n_2}{n_1}$ is called the critical angle θ_c . When $\theta_i > \theta_c$ all the light energy is reflected back into the original medium. This phenomenon, known as *total internal reflection*, is crucial in applications such as light guidance in optical fibers and NLOS communication links [34,123].

In Fig. 2.9, various practical cases of light transmission and reflection at the interface of two different media are illustrated for different incidence angles relative to the critical angle. When $\theta_i < \theta_c$, the light undergoes partial transmission and reflection, with a portion of the light passing into the second medium. $\theta_i = \theta_c$, the transmitted ray propagates along the interface, marking the transition between refraction and total internal reflection. Finally, for $\theta_i > \theta_c$, total internal reflection occurs, where all the light energy is reflected back into the original medium.

In the context of light transmission between water ($n_1 = 1.33$) and an air bubble ($n_2 = 1$), the critical angle can be calculated from Eq. (2.27) as follows

$$\theta_c = \arcsin \frac{n_2}{n_1} = \arcsin \frac{1}{1.33} \approx 48.75^\circ. \quad (2.28)$$

Thus, for angles of incidence θ_i less than 48.7° , partial transmission and reflection occur at the interface. When $\theta_i = 48.75^\circ$, the transmitted ray travels along the boundary between

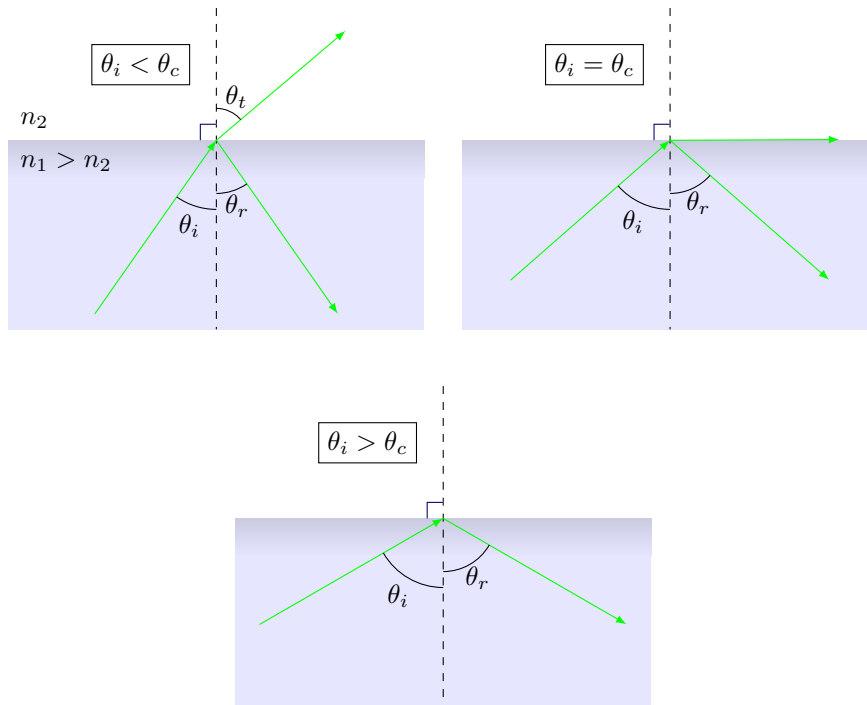


Figure 2.9: Different scenarios for light interaction at an interface when transitioning from a medium with a higher refractive index to one with a lower refractive index.

water and air. For θ_i greater than 48.7° , total internal reflection takes place, with all light being reflected back into the underwater medium.

In Fig. 2.10, the interaction of light rays parallel to the optical axis with an air bubble in an underwater medium is shown as a function of the incident angle. When the light ray reaches the water-air interface, part of the light is refracted, i.e., transmitted, into the bubble, while the rest is reflected into the underwater medium. A similar phenomenon occurs when light transitions from the air bubble to the underwater medium. Specifically, part of the light is transmitted into the underwater medium, while part is reflected inside the air bubble. The reflected light within the air bubble undergoes successive internal reflections, with the intensity gradually decreasing after each iteration due to energy loss. Light rays with an incident angle greater than 48.75° are reflected to the underwater medium, effectively blocking it by the air bubble. Light rays that strike along the optical axis are transmitted without any reflection.

Power losses caused by the change of medium—specifically, the reflection and transmission coefficients when a light ray interacts with an air bubble—can be calculated using the Fresnel equations [34]. Furthermore, the reflectivity and transmission coefficients can be influenced by organic films that coat the clean surface of air bubbles. However, experimental

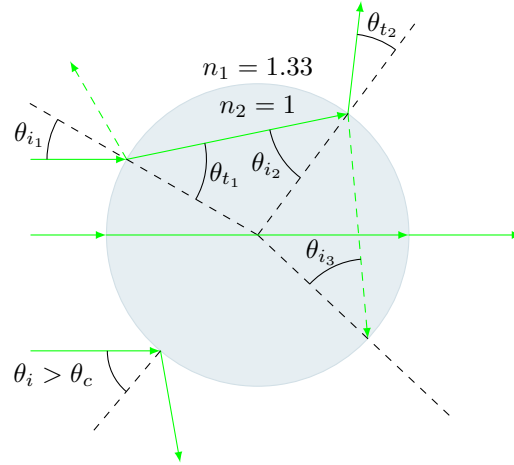


Figure 2.10: Reflection and refraction effect due to the water-air bubble interface.

measurements conducted with air bubbles of varying diameters and in different types of water have shown that the optical properties of coated bubbles do not significantly differ from those of a clean bubble with a mean diameter greater than $2 \mu\text{m}$ [82].

However, the geometrical optical framework described in this section does not account for the stochastic nature of bubble generation or the erratic motion induced by ocean currents and turbulence. Random spatial distribution of bubbles along the link span induces random scattering events during the light propagation path. This random fluctuation in the refractive index can cause a twinkling effect similar to that caused by oceanic turbulence. To derive expressions for the statistical properties of an optical beam traveling through the underwater medium in the presence of air bubbles, it is essential to simplify the problem by making certain assumptions. These assumptions help reduce the complexity inherent in the movement and generation of air bubbles, making the analysis more manageable [59]. Alternatively, empirical measurements in controlled laboratory environments can be conducted, enabling the extraction of mathematical expressions based on experimental results [124].

2.3 UOWC channel modeling

Before designing a communication system, it is essential to comprehend the environment and specific conditions in which it will operate. This requires a thorough study of the properties of the communication channel, that is, the development of a channel model. A theoretical channel model should be capable of detailing the physical medium and include the main characteristics and physical parameters. The following sections provide an overview of the most commonly used mathematical tools for describing the underwater optical channel in the UOWC bibliography.

2.3.1 Optical power fluctuations

The random fluctuations of the refractive index due to oceanic turbulence and air bubbles causes random phase and amplitude variations (scintillation) of the optical beam which ultimately results in fading of the received optical power, thus leading to the system performance degradation.

The optical power fluctuations are usually quantified by the scintillation index, defined as the variance of the received normalized received optical power as follows [42]

$$\sigma^2 = \frac{\mathbb{E}[P_{rx}^2] - \mathbb{E}^2[P_{rx}]}{\mathbb{E}^2[P_{rx}]}, \quad (2.29)$$

where $\mathbb{E}[\cdot]$ is the expected value.

In the context of oceanic turbulence, the scintillation index can be directly derived from the spatial PSD. For the specific case of plane-wave propagation, the scintillation index is given by [42]

$$\sigma^2 = 8\pi^2 k^2 d \int_0^1 \int_0^\infty \kappa \Phi_n(\kappa) \exp\left(-\frac{D^2 \kappa^2}{16}\right) \left(1 - \cos\left(\frac{d\kappa^2 \xi}{k}\right)\right) d\kappa d\xi, \quad (2.30)$$

where $k = 2\pi/\lambda$ is the wavenumber, D is the receiver aperture, i.e., the lens diameter at the receiver or photodetector surface diameter, and d is the link distance. While Eq. (2.30) might be mathematically intractable, numerical methods can be employed to calculate the scintillation index effectively as a function the spatial PSD and the rest of the propagation parameters. Although a Gaussian-beam wave model is more convenient for characterizing the propagation of optical waves, most theoretical treatments of scintillation index due to oceanic turbulence in UOWC bibliography that consider the Nikishov spatial PSD focus on plane waves and spherical waves [30, 125]. In fact, when the Gaussian beam exhibits relatively large divergence, plane wave approximations are perfectly applicable to FSO communication systems. We consider plane wave propagation in this thesis for simplicity in scintillation index modeling.

The parameter D in Eq. (2.30) reflects the influence of the receiver aperture on the scintillation index, highlighting the phenomenon known as *aperture averaging* [126]. When the aperture is small, the receiver detects intensity fluctuations from a single region. However, as the aperture size increases the receiver begins to capture light from multiple areas of the received optical wavefront. This results in a decrease in the scintillation level measured by the receiver, as the larger aperture *averages* the spatial turbulent optical power variations. Hence, it is possible to optimize the design of UOWC systems under oceanic turbulence in order to reduce the fading effect. Several studies have analyzed the impact of the aperture averaging effect on the performance of a UOWC system under oceanic turbulence [127–130]. In Fig. 2.11, the scintillation index numerically obtained in Eq. (2.30) is plotted as a function of the link distance under different values of receiver aperture diameter in order to

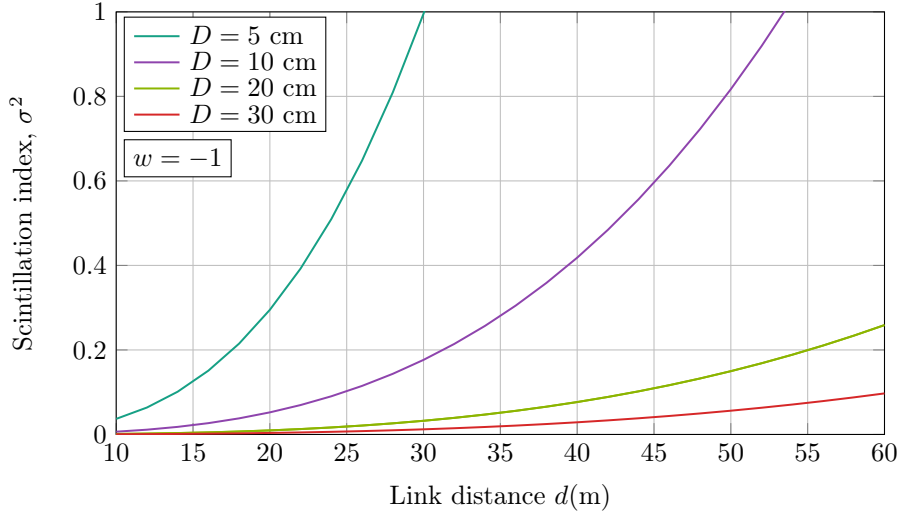


Figure 2.11: Scintillation index as a function of the link distance for different receiver aperture under Nikishov oceanic turbulence with a temperature-salinity ratio of $w = -1$.

Table 2.4: Oceanic turbulence parameters assumed in Fig. 2.11.

Parameter	Value
Dissipation of turbulent kinetic energy (ϵ)	$10^{-6} \text{ m}^2/\text{s}^3$
Dissipation of temperature (χ_T)	$10^{-4} \text{ K}^2/\text{s}$
Kolmogorov length scale (η)	10^{-3} m
A_T	1.863×10^{-2}
A_S	1.9×10^{-4}
A_{TS}	9.41×10^{-3}

represent the mitigation of oceanic turbulence by aperture averaging effect for a wavelength of $\lambda = 532 \text{ nm}$. The assumed spatial PSD is the Nikishov spatial PSD described in Eq. 2.26. A temperature-salinity balance ratio of $w = -1$ is assumed, which described a moderate-to-strong salinity-induced oceanic turbulence. The rest of oceanic turbulence parameters are described in Table 2.4.

The behavior of random power fluctuations, as well as the scintillation index, are defined by the probability density function (PDF), which describes the statistical behavior of the received signal intensity under such fluctuations. There is no universal model valid for all power fluctuations in a UOWC link, as the PDF heavily depends on the nature of these fluctuations. Different statistical models can validate empirical measurements of different natural processes that induced optical power fluctuations in UOWC links. The probability density functions used in this thesis are shown below.

Weibull distribution

A commonly used model for salinity-induced turbulence is the Weibull distribution, which provides a good agreement with experimental measurement data for a wide range of turbulence scenarios as presented in several saltwater bodies [131]. The PDF of the Weibull distribution is expressed as follows

$$f_{H_W}(h) = \frac{\beta_1}{\beta_2} \left(\frac{h}{\beta_2} \right)^{\beta_1-1} \times e^{-\left(\frac{h}{\beta_2}\right)^{\beta_1}}, \quad h \geq 0, \quad (2.31)$$

where H_W is a Weibull distributed random variable, $\beta_1 > 0$ is the shape parameter related to the scintillation index of the fading effect, and $\beta_2 > 0$ is the scale parameter related to the mean value of the optical power. The mean and variance of the Weibull distribution are given by

$$\mathbb{E}[H_W] = \beta_2 \Gamma \left(1 + \frac{1}{\beta_1} \right), \quad (2.32a)$$

$$\sigma_{H_W}^2 = \beta_2^2 \left(\Gamma \left(1 + \frac{2}{\beta_1} \right) - \left(\Gamma \left(1 + \frac{1}{\beta_1} \right) \right)^2 \right). \quad (2.32b)$$

Generalized Gamma distribution

The generalized Gamma distribution is usually proposed for modeling turbulence-induced fading as it encompasses the characteristics of several statistical distributions. The PDF of the generalized Gamma distribution is defined as follows [53]

$$f_{H_G}(h) = \frac{p}{a^d \Gamma(d/p)} h^{d-1} e^{-(h/a)^p}, \quad (2.33)$$

where H_G is a generalized Gamma distributed random variable, a is the scale parameter, and d and p are the shape parameters. The mean and variance of the generalized Gamma distribution are given by

$$\mathbb{E}[H_G] = a \frac{\Gamma \left(\frac{d+1}{p} \right)}{\Gamma(d/p)}, \quad (2.34a)$$

$$\sigma_{H_G}^2 = a^2 \left(\frac{\Gamma \left(\frac{d+2}{p} \right)}{\Gamma(d/p)} - \left(\frac{\Gamma \left(\frac{d+1}{p} \right)}{\Gamma(d/p)} \right)^2 \right). \quad (2.34b)$$

As mentioned above, the generalized Gamma distribution is a general case of important statistical distributions, such as the Gamma distribution when $d = p$, the Weibull distribution when $p = 1$, and the exponential distribution when $d = p = 1$.

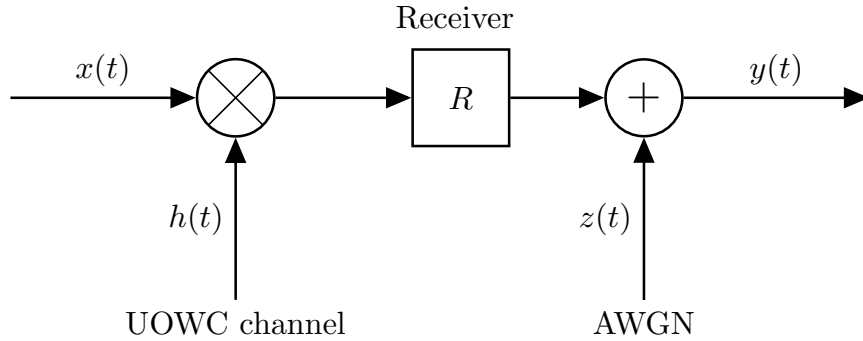


Figure 2.12: Diagram block of mathematical model of a UOWC system with IM/DD modulation.

In order to clarify the analytical UOWC model under optical power fluctuations caused by oceanic turbulence or air bubbles, the PDF is normalized with respect to its mean value. This normalization separates the optical power fluctuations, represented by the normalized PDF with a mean of $\mathbb{E}[H] = 1$, from the overall power losses introduced by these phenomena, which are incorporated into the underwater path loss term L .

2.4 UOWC systems

In Fig. 2.12, a basic model of a UOWC channel based on IM/DD is presented. Mathematically, the channel model is given by

$$y(t) = R \cdot x(t) \cdot h(t) + z(t), \quad (2.35)$$

where $x(t) \triangleq X$ is the transmitted optical power, $h(t) \triangleq H$ is the underwater channel gain that represents the impairments of scattering, oceanic turbulence, and air bubbles, R is the photodetector responsivity, $z(t) \triangleq Z$ is an additive noise, and $y(t) \triangleq Y$ is the received electrical signal. Without loss of generality, the photodetector responsivity is assumed hereinafter to be the unity.

It is important to note that Eq. (2.35) does not explicitly account for potential ISI effect caused by scattering. This phenomenon, which arises due to the multipath nature of the underwater channel, can introduce a low-pass filtering effect that becomes more pronounced at higher transmission rates, particularly above the Gbps range. Previous studies have shown that this effect can limit the achievable data rates by causing temporal overlap of consecutive symbols [24]. However, a detailed temporal analysis of the UOWC channel and the potential degrading impact of ISI is not included in this thesis, as this specific topic

has already been thoroughly explored in the literature for scenarios comparable to those examined in this work [68, 69].

Here, it is used that X , Y , Z , and H represent random variables, and $x(t)$, $y(t)$, $h(t)$, and $z(t)$ their corresponding realizations. In this case, a simple discrete representation for an UOWC system is given by

$$Y = X H + Z. \quad (2.36)$$

In this model, H represent the optical fluctuations of the underwater channel gain, which include the underwater path loss, L , and the normalized optical power fluctuations due to fluctuations of the refractive index, H_i as follows

$$H = L \cdot H_i, \quad (2.37)$$

where H_i is the received optical fluctuations due to air bubbles (H_b) or oceanic turbulence (H_o).

The noise at the receiver in UOWC systems can be originated from multiple sources. Firstly, the receiver collects background light, such as sunlight or blackbody radiation. Although this noise source can be filtered, any residual contribution is typically treated as additive noise. In underwater scenarios, background radiations are practically negligible except in very shallow waters due to the high absorption effect, especially in turbid waters [132]. As demonstrated in [133], water acts as a natural filter by absorbing and scattering solar radiation, which significantly reduces background noise from solar radiation. Secondly, the inherent noise to the photodetection process, commonly referred to as shot noise, is due to the quantum nature of light. When the received signal is low in the photon-counting regime, a Poisson distribution describes accurately the random noise when other noise sources are negligible [77]. With large signal photoelectron counts, the intensity shot noise results from the summation of many independent Poisson distributed random variables. Hence, under the condition of high signal intensity, i.e., the number of photons at the receiver becomes large, as the number of random variables summed approaches infinity, the noise probability density function approaches a Gaussian distribution by the central limit theorem [41, 42]. Lastly, thermal noise, which is independent of the received optical signal and arises from the electronic of the pre amplifier at the receiver due to resistive elements, is generally modeled as a Gaussian distribution [77]. Given that both high-intensity shot noise and thermal noise can be accurately approximated as a Gaussian distribution, as well as the negligible effect of solar background noise at moderate depths, it is common to simplify the overall receiver noise as an AWGN source. Hence, Z is modeled as an additive white Gaussian noise (AWGN) with zero mean and variance $\sigma_Z^2 = N_0/2$, where N_0 is the power spectral density of the additive noise.

Given that the system input represents power, not amplitude, $x(t)$ must be positive. Furthermore, the average power of the transmitted signal, P_t , is constrained to an average power limitation, P_{\max} , due to power-consumption and eye safety regulations [41]. Hence,

the average transmitted optical power is given by

$$P_t = \lim_{T \rightarrow \infty} \frac{1}{2T} \int_{-T}^T x(t) dt \leq P_{\max}. \quad (2.38)$$

The simplest modulation scheme applied in IM/DD systems is On-Off Keying (OOK) modulation, where a $\langle 0 \rangle$ bit is represented by the absence of optical signal (zero intensity), and a $\langle 1 \rangle$ bit is represented by the presence of optical signal (positive intensity). OOK modulation is considered a special case of the M -ary Pulse Amplitude Modulation (M -PAM), with $M = 2$ possible amplitudes [134]. Hence, assuming that ones and zeros are equally likely, and an average transmitted power of P_t during the transmission, the average transmitted optical power during a $\langle 1 \rangle$ bit is $2P_t$.

The waveform of the transmitted signal, and consequently, the spectrum of the transmitted signal, depends on the chosen signal pulse shape. In this thesis, we assume an OOK scheme with a rectangular pulse shape and a duty cycle of 100%, which is commonly used as a benchmark for comparison with more complex pulse shapes [41]. Hence, the transmitted pulse shape is given by

$$p(t) = \begin{cases} 1 & \text{for } t \in [0, T_b), \\ 0 & \text{elsewhere,} \end{cases} \quad (2.39)$$

where T_b is the bit period. The transmitted symbols are represented by the unit-energy signal waveform $\Phi(t)$, also known as basis function, defined as $\Phi(t) = p(t)/\sqrt{T_b}$. In this way, the transmitted optical signal can be expressed as follows

$$x(t) = \sum_{k=-\infty}^{\infty} a_k 2P_t \sqrt{T_b} \Phi(t - kT_b), \quad (2.40)$$

where a_k is the discrete-time sequence of transmitted symbols that follows a equiprobable Bernoulli distribution, taking values of 0 for the $\langle 0 \rangle$ bit and 1 for the $\langle 1 \rangle$ bit. By defining a constellation of these two equiprobable points, the Euclidean distance can be expressed as $d_E = 2P_t \sqrt{T_b}$.

2.4.1 Performance of UOWC systems

Theoretical and numerical results of UOWC systems performance provide valuable insights for system engineers into design reliable and robust communication systems that fulfill the requirements of emerging applications under complex underwater channels. Furthermore, analytical and asymptotic performance expressions allow us for a deep analysis of the impact of the underwater channel parameters, such as the level of turbidity or the turbulence strength, on the UOWC system performance.

Among the various performance metrics that are usually used in wireless communications, one of the most popular indicators in the literature is the bit error rate (BER). In addition

to the BER, other standard performance measurements of optical wireless channels such as the outage probability and the channel capacity also provide information for the impact of the oceanic channel on the overall system design. Outage probability is defined as the probability that the output SNR falls below a certain specified threshold. Ergodic capacity defines the maximum data rate that can be transmitted over a concrete channel with a negligible error probability. In this thesis, we primarily focus on the BER and outage probability.

Next, formal definitions of BER and outage probability performance metrics are presented.

Bit error rate

A bit error occurs whenever the transmitted bit and the corresponding received bit do not match. This error is a stochastic event since the underwater channel presents random characteristics such as random scattering events, oceanic turbulence-induced fluctuations, or the air bubbles movement. Therefore, the BER is the average fraction of bits in error at the decision point to the total number of transmitted bit. Mathematically, the bit error rate is defined as follows

$$P_b(e|i) = P_b(0)P_b(e|0) + P_b(1)P_b(e|1), \quad (2.41)$$

where $P_b(0)$ and $P_b(1)$ are the probabilities of symbols 0 and 1, respectively, and $P_b(e|0)$ and $P_b(e|1)$ are the conditional bit error probability when transmitting 0 and 1 symbols, respectively. Consider equiprobable symbols, i.e., $P_b(0) = P_b(1) = 1/2$ and $P_b(e|0) = P_b(e|1)$. The conditional bit error probability of a UOWC system under AWGN with zero mean and variance σ_n^2 noise can be determined by the Euclidean distance as follows [41]

$$P_b(e) = Q\left(\frac{d_E/2}{\sigma_n}\right) = Q\left(\frac{P_t\sqrt{T_b}}{\sqrt{N_0/2}}\right), \quad (2.42)$$

where $Q(\cdot)$ is the Gaussian Q -function defined as $Q(x) = (1/\sqrt{2\pi}) \int_x^\infty \exp(-t^2/2) dt$, and $d_E/2$ is the decision threshold. However, UOWC systems suffer from the impairments described in Section 2.2 in the form of a random channel gain h . Thus, the bit error probability can be expressed as follows

$$P_b(e|H) = Q\left(\frac{P_t\sqrt{T_b}}{\sqrt{N_0/2}}H\right) = Q\left(\sqrt{\frac{2P_t^2T_b}{N_0}}H\right) = Q\left(\sqrt{2\gamma}H\right), \quad (2.43)$$

where $\gamma = P_t^2T_b/N_0$ is a normalized electrical SNR. Hence, the average BER can be obtained by averaging $P_b(e|H)$ over the PDF of H , $f_H(h)$, as follows

$$P_b = \int_0^\infty Q\left(\sqrt{2\gamma}h\right) f_H(h) dh. \quad (2.44)$$

In some cases, obtaining a closed-form analytical expression for P_b is mathematically complex or even impossible due to the intractability of $f_H(h)$. In such cases, it is common to study the asymptotic behavior of P_b , which provides information about system performance at high SNR. Additionally, the asymptotic behavior contributes to a deeper conceptual understanding of the factors that limit the performance of communication systems over a specific fading channel. According to [134, 135], the asymptotic BER at high SNR is expressed as follows

$$P_b \doteq (G_c \gamma)^{-G_d}, \quad (2.45)$$

where G_c is the coding gain, G_d is the diversity order, and \doteq is the asymptotic equality sign. Firstly, G_c (in decibels) specifies a relative horizontal shift in the asymptotic regime versus the average SNR curve on a log-log scale. Secondly, G_d determines the slope of the average BER in the asymptotic regime versus the average SNR curve on a log-log scale. Furthermore, based on [135, Proposition 1], the asymptotic BER can be derived from the behavior of the PDF of the considered random variable near the origin. Thus, it is possible to characterize the average error probability at high SNR through the parameters G_c and G_d from the behavior of $f_H(h)$ when $h \rightarrow 0^+$ [135].

Outage probability

The outage probability (OP) is defined as the probability that the instantaneous combined SNR falls below a certain specified, γ_{th} , that is

$$\text{OP} = P(\text{SNR} \leq \gamma_{th}), \quad (2.46)$$

where the resulting electrical SNR at the receiver is given by

$$\text{SNR}(h) = \frac{1}{2} \frac{d_E^2}{N_0/2} h^2 = \frac{4P_t^2 T_b}{N_0} h^2 = 4\gamma h^2. \quad (2.47)$$

By using Eq. (2.47), the outage probability can be written as

$$\text{OP} = P(4\gamma h^2 \leq \gamma_{th}) = \int_0^{\sqrt{\gamma_{th}/4\gamma}} f_H(h) dh = F_H \left(\sqrt{\frac{1}{4\bar{\gamma}}} \right), \quad (2.48)$$

where $F_H(\cdot)$ is the cumulative density function (CDF) of h , and $\bar{\gamma} = \frac{\gamma}{\gamma_{th}}$ is the normalized SNR. The definition of the normalized SNR allows for the extrapolation of outage probability results to any predefined threshold value.

Similarly to the asymptotic behavior of the average error probability, the high SNR behavior of the outage probability can be also expressed as

$$\text{OP} \doteq (O_c \bar{\gamma})^{-O_d}, \quad (2.49)$$

where O_c is the coding gain, and O_d is the outage diversity. As stated in [135], the average BER and outage performance exhibit identical diversity orders for sufficiently large SNR, i.e., $G_d = O_d$.

Monte Carlo simulation performance

For the sake of validating the analytical and asymptotic expressions derived in the following chapters, Monte Carlo simulation results have consistently been included. For this purpose, numerical simulation tools have been developed based on the random number generation of all input random variables to estimate system performance. A quasi-analytical Monte Carlo method has been considered to reduce the generation of large numbers of samples and, consequently, enhance the computational efficiency of the simulation tool. This method reduces simulation time by not explicitly simulating all input processes into the system. As shown in Fig. 2.12, the proposed Monte Carlo simulation employs a scheme based on an equivalent noise source to provide an overall performance curve, such as BER and outage probability, as a function of the signal-to-noise ratio.

Regarding the Monte Carlo simulation of the BER performance, the size of the transmitted bits chain is carefully chosen to ensure statistical reliability for the presented simulation results. According to [136], achieving an error probability measurement of the order $p = 10^{-v}$ requires simulating the system with $10/p = 10^{v+1}$ samples to attain a 95% confidence interval for the error probability estimation. Furthermore, the random binary source followed a Bernoulli distribution, with each bit occurring with a probability of 0.5. As mentioned above, OOK modulation is employed with a rectangular pulse shape. The output waveform takes predefined values corresponding to a 1 or 0. It should be noted that no channel coding scheme was incorporated. At the receiver side, the transmitted signal is detected using a matched filter, whose impulse response matches the considered pulse shape in Eq. (2.39). This filter maximizes the sampled SNR, and a maximum likelihood (ML) detector is employed to minimize symbol error probability.

2.5 Summary

In this chapter, an approach to UOWC systems and the underwater environment has been presented, along with the mathematical tools that will be utilized in the performance analysis in subsequent chapters.

Firstly, a review of optical wireless communication technology has been conducted. Key features that make UOWC systems suitable for underwater environments have been highlighted. While LED emitters reduce system sensitivity to alignment errors due to their broad emission pattern, LD emitters provide higher modulation speeds, essential for high data-rate and real-time applications. Furthermore, LDs enable longer link distances in turbid waters, thanks to their higher output optical power and narrower optical linewidth. At the receiver side, APD photodetectors are well-suited for long-range optical links due to their high sensitivity, but their performance can be affected by the additional noise introduced

by the avalanche process and their higher sensitivity to temperature variations compared to PIN photodetectors.

Secondly, the physical theory of the most critical underwater impairments affecting light beam propagation in oceanic environments has been reviewed. Accordingly, the absorption and scattering properties have been mathematically characterized by the absorption and scattering coefficients. Both coefficient be used to derive other practical channel parameters, such as the extinction coefficient and the scattering albedo. Different classifications of optical water types have been presented to describe the turbidity, absorption, and scattering conditions of the most common ocean environments. A closed-form solution of the RTE, obtained by assuming that the transmitter and receiver are perfectly aligned and all scattered photons are lost, known as Beer-Lambert's law, has been presented. The processes causing oceanic turbulence have also been described, and Nikishov's spatial PSD, which describes the refractive index fluctuation induced by oceanic turbulence based on temperature and salinity gradients, has been introduced. Lastly, the generation of air bubbles and their impact on light beam propagation based on the law of refraction has been analytically described.

Thirdly, various tools used to statistically model the received optical power fluctuations due to the underwater impairments such as the scintillation index have been described. Statistical models utilized in this thesis to characterize the random behavior of oceanic turbulence and air bubbles have been defined.

Lastly, a comprehensive description of the UOWC system model employed throughout this thesis is provided. Performance metrics such as BER, and outage probability have been mathematically defined for a UOWC system under OOK modulation over a generic random medium. The asymptotic performance analysis tools and their characteristic parameters for the performance metrics at high SNR have also been presented.

Chapter 3

Experimental UOWC channel model

This chapter provides a comprehensive overview of an experimental UOWC link designed to model and analyze the impact of air bubbles on system performance across several levels of scattering. An underwater optical channel emulator is developed to obtain reliable measurements under laboratory conditions, simulating realistic underwater phenomena across a wide range of channel states. Empirical measurements are utilized to assess the statistical behavior of the received optical power fluctuations, considering various air bubble sizes and levels of particle-induced scattering. Performance parameters and statistics of the experimental UOWC channel, such as the probability density function, scintillation index, average outage duration, and coherence time, are described. Additionally, novel closed-form analytical and asymptotic expressions are derived to compute the BER and outage performance of a SISO UOWC system operating over the emulated channel, using an analytical framework fitted to the experimental measurements under various scattering conditions.

3.1 Introduction

3.1.1 Motivation and related work

Underwater channel modeling is the first step in the design of efficient, reliable and robust UOWC systems. It allows accurate prediction of the effect of natural water constituents on light propagation without the need to deploy physical links. This approach offers effective tools to tackle theoretical designs of novel transmission and reception techniques that enhance the robustness and overall performance of UOWC systems. The development of an accurate statistical modeling requires experimental measurement campaigns to ensure a strong correlation between physical reality and numerical results. Nevertheless, the

high cost of conducting measurement campaigns in open ocean limits the acquisition of a wide variety of scenarios and water conditions. As a result, stochastic channel simulators are frequently employed in UOWC channel modeling. These simulators provide a valuable tool for investigating the properties of specific effects in isolation, such as the impact of scattering on light beam propagation. However, they often fail to capture the behavior of the medium when two or more effects interact simultaneously or collectively influence the light beam propagation. Consequently, experimental test-beds are commonly developed to analyze the behavior of open waters across a wide range of underwater conditions. The empirical approach provides a more accurate and realistic representation of the underwater optical channel, integrating realistic environmental conditions rather than relying on simplified theoretical assumptions. Furthermore, underwater channel emulators enable the generation of extensive databases of experimental samples while maintaining precise control over the measurement process, significantly reducing costs and deployment time compared to open ocean measurement campaigns.

Many studies have focused on the experimental modeling of UOWC channels under different phenomena, such as random temperature and salinity variations or air bubbles [53–55, 131, 137–139] (and references therein). These works have concentrated on measuring and analyzing optical power fluctuations for different UOWC link configurations under temperature and salinity gradients, air bubbles, or both simultaneously. In [131], the Weibull distribution is proposed to characterize the received intensity fluctuations in UOWC channels due to the presence of salinity-induced turbulence. The impact of air bubbles on a UOWC link, based on their size, is investigated in [137]. In that study, it is concluded that the received optical power and the light obstruction of a UOWC link in the presence of air bubbles depends on the density and size of the bubbles. In [53], several statistical distributions of intensity fluctuations generated in an underwater channel emulator with random temperature and salinity variations, as well as the presence of air bubbles, are experimentally evaluated for different transmitter and receiver configurations. In [138], the mixture of Exponential–generalized Gamma distribution is proposed for underwater channels under the influence of air bubbles and temperature gradients, in both fresh and salty waters, under various channel conditions ranging from weak to strong turbulence. In [139], the Burr distribution is shown to outperform the log-normal and Weibull distributions in describing random power fluctuations generated in a water tank with temperature gradients. In [54], light intensity fluctuations are measured and analyzed under different water flow speeds in two natural rivers. In [55], the mixture of Weibull–generalized Gamma distribution is proposed to characterize the received optical power fluctuations induced by thermohaline channels, i.e., in the presence of temperature and salinity gradients, as well as air bubbles.

Although these models comply with current data of optical power fluctuations due to the joint effect of thermohaline gradient and air bubbles, neither of them has been evaluated under different turbidity levels, i.e., in various types of water with distinct absorption and scattering coefficients. To our knowledge, there is a lack of experimental research on thor-

oroughly analyzing the dependence of the scintillation index in different underwater environments and its changing nature with the water turbidity. In fact, it should be highlighted that the majority of literature uses tap water. Regarding the combined impact of air bubbles and marine particles, as far as we know, only one study in terms of simulation has been published [61]. In this work, they calculated the increase in the delay spread of the channel due to air bubbles in different types of water. This is quite remarkable since, as commented in Section 2.2.3, the generation of air bubbles is directly related with some of important scattering agents such as phytoplankton and zooplankton [31, 33]. Additionally, it should be noted that the experimental insights which have been gained about the impact of air bubbles on intensity fluctuations of UOWC systems are usually analyzed along with other turbulent phenomena such as temperature gradients that obscured its analysis. However, thermohaline currents induced in UOWC channel emulator under laboratory conditions can obscure the true impact of air bubbles on the perturbed wavefront at the receiver, since at such short link distances, the required temperature and salinity gradients to observe distortions in the received light beam are much larger than those found in natural water environments.

Based on the previous studies, the optical community has concentrated on analyzing UOWC systems under the distributions mentioned above, such as the Weibull distribution [140–142], the Exponential-Generalized Gamma distribution [143, 144], and the Gamma-Gamma distribution [145]. As described above, these models comply with current data of measured optical power fluctuations due to the exclusively oceanic turbulence or joint effect of thermohaline gradient and air bubbles. To the best of our knowledge, only a few investigations have demonstrated that the performance degradation in UOWC links can be due solely to air bubbles [59, 124]. In [124], an experimental analysis is conducted to investigate the dependence of the BER in UOWC systems, employing pulse position modulation, on bubble density and size. In [59], closed-form expressions for the ergodic capacity and the BER were obtained over a composite channel model considering the bubble-obstruction and turbulence effect. However, the proposed statistical model is purely mathematical and numerically obtained by using statistics of the generation, size, and horizontal movement of air bubbles. As mentioned above, statistical channel models derived from theoretical simulations often require simplifying and assuming specific channel parameters. This can result in significant discrepancies between the simulated results and the current behavior of underwater environments.

In light of the demonstrated impact of air bubbles on UOWC performance and the scattering-induced distortion of the light beam in underwater environments, it is crucial to experimentally analyze the effect of bubbles-induced fluctuations and their variability with water turbidity. Understanding these interactions and their influence on UOWC system performance is essential to design robust and reliable transceivers adapted for turbid environments.

3.1.2 Structure

The remainder of this chapter is organized as follows. In Section 3.2, the experimental underwater channel emulator, as well as the proposed transmitter and receiver used in this work, are described. In Section 3.3, the emulation of absorption and scattering effects in the water tank using a commercial antacid is detailed, along with the generation of different air bubbles scenarios using an air pump and two brushless motors with propellers. In Section 3.4, the statistical characterization of air bubbles-induced fading is obtained from experimental measurements considering two different bubble diameters across various turbidity levels. In Section 3.5, UOWC system performance in terms of BER and outage is evaluated using the proposed statistical channel model for small and large air bubbles under different scattering conditions. Finally, the chapter is concluded in Section 3.6.

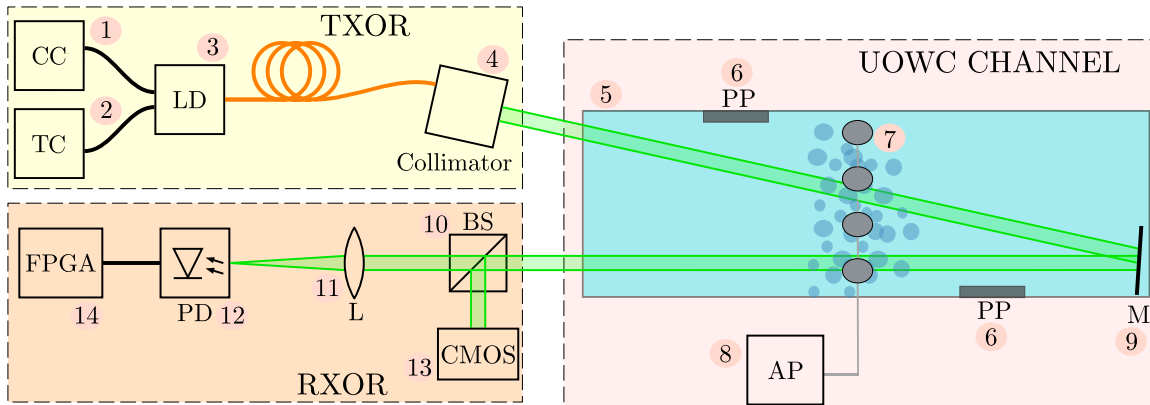
3.2 UOWC channel emulator

As mentioned in Section 3.1, the cost of conducting experiments in open water is significantly high. Moreover, due to its inherent complexity and instability, the limited control over the underwater medium often impedes the acquisition of reliable and replicable measurements. Consequently, there is a need for a test-bed that can reliably simulate a broad spectrum of marine environments while ensuring precise control throughout the measurement process. In this section, we provide a more detailed description of the experimental UOWC link and the developed underwater channel emulator.

3.2.1 Experimental set-up

For illustration purposes, a block diagram of the experimental UOWC system configuration, as well as the final implementation during the experiments are depicted in Fig. 3.1. Commercial models of the experimental UOWC system instrumentation are summarized in Table 3.1. The following paragraphs provide a detailed account of the configuration and characteristic of the test bench devices.

At the transmitter side, the light source is a green LD with a central wavelength of 520 nm coupled with a single-mode optical fiber. The LD is mounted on a compact housing which protects the pigtail from physical damage, and provides access to a Bias-T circuit for RF modulation, as well as temperature and current control. During the experiment, the LD operates in constant current mode, driven by an injection current, or operating current, i_{tx} . The value of the injection current determines the operating point of the LD, which defines the LD output optical power. In this thesis, the output optical power corresponds to the transmitted optical power by the UOWC system, P_{tx} . The relationship between P_{tx} and



(a) Block diagram of the UOWC experimental system setup.



(b) Actual implementation of the UOWC experimental system setup.

Figure 3.1: (1) Current controller (CC). (2) Temperature controller (TC). (3) Pigtailed laser diode mount. (4) Fiber Collimator. (5) Water tank. (6) Propellers (PP). (7) Diffusers. (8) Air pump (AP). (9) Dielectric mirror. (10) Beamsplitter (BS). (11) Plano-convex lens (L). (12) Photodetector (PD). (13) Camera CMOS. (14) RedPitaya STEMLab.

i_{tx} is obtained from the current–power diagram of the LD provided by the manufacturer, shown in Fig. 3.2.

As can be observed in Fig. 3.2, the optical transmission of the LD begins at a threshold current of 30 mA. Below the threshold current, the LD operates in spontaneous emission mode, similar to an LED. When the injection current exceeds the threshold, the LD transitions to stimulated emission, generating coherent light and resulting in a rapid increase in output

Table 3.1: Commercial models of the experimental UOWC system instrumentation.

Instrumentation	Commercial model
Laser diode	LP520-SF15 (Thorlabs)
Current controller	LDC205C (Thorlabs)
Temperature controller	TED200C (Thorlabs)
LD mount	LDM9LP (Thorlabs)
Aspheric collimator	CFC5-A (Thorlabs)
Plano convex lens	KPX100 (Newport)
Photodetector	PDA10A2 (Thorlabs)
Camera	DFK 38UX253 (The Imaging Source)
CMOS sensor	IMX253 (Sony)
FPGA	Xilinx Zynq 7010 (AMD)
Dielectric mirror	BBSQ2-E02 (Thorlabs)
Propellers	Vortech MP10WQD (Ecotech Marine)

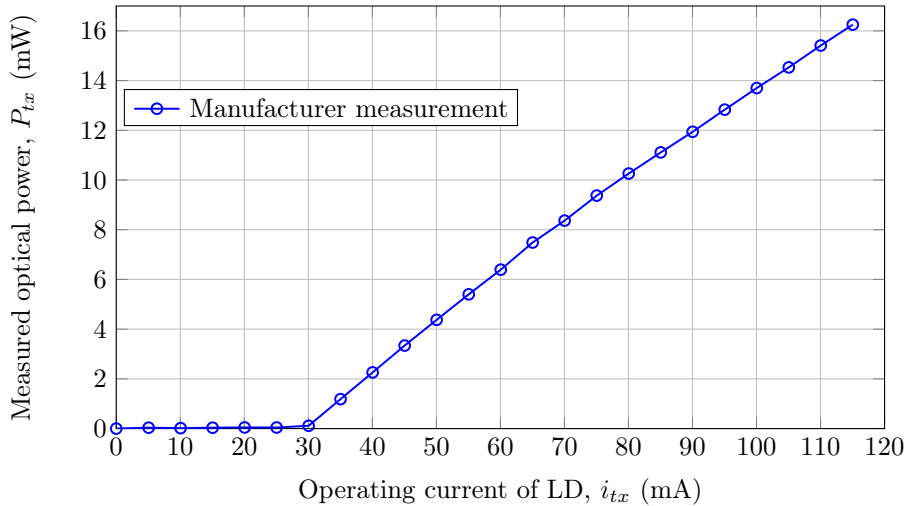


Figure 3.2: Measured optical power curve versus operating current for the LD LP520-SF15. Data obtained from Thorlabs [146].

power as a function of the injection current. The relationship between the injection current and the output optical power is very sensitive to the operating temperature. At ambient temperature, the maximum injection current the LD can withstand before sustaining damage is 115 mA. To ensure the stable operation of the LD, a temperature controller maintains the LD operating temperature at 25°C. Hence, without loss of generality, the transmitted optical power of the LD is assumed as a constant value during the experiment. Finally, the light exiting of the fiber is collimated to free space by an adjustable aspheric collimator.

On the receiver side, a beamsplitter with a 50:50 splitting ratio is used to divide the received light after passing the underwater channel between a high-resolution camera equipped with a CMOS image sensor, which captures the received footprint, and a converging plano convex lens. Although the light beam emitted by the LD during the experiment is narrow and collimated, beam spreading caused by scattering results in a footprint at the receiver that is significantly larger than the photosensitive area of the photodiode. To address this, a lens is used to focus the light onto the photodiode. Specifically, a lens with a focal length of 15 cm is employed, with the photodetector placed at this distance. As a result, the equivalent detection area of the receiver corresponds to the diameter of the lens, which is 2.5 cm. The considered photodetector presents a silicon reverse-biased PIN photodiode. The photodiode is mounted in an amplified photodetector, which includes a transimpedance amplifier with a gain of $G = 10 \text{ kV/A}$.

The output electrical signal from the photodetector is acquired by a Red Pitaya STEMLab development board, which is powered by an ARM Cortex-A9 and a Field Programmable Gate Array (FPGA) [147]. The received samples are transmitted via IP from the FPGA to an external computer and then processed offline using MATLAB R2022b and Wolfram Mathematica to compute different evaluation metrics and arise the statistical characterization.

The underwater channel emulator consists of a glass tank of $1.5 \times 0.2 \times 0.3 \text{ m}$ filled with tap water. Although the total capacity of the water tank is 90 liters, measurements are performed with 55 liters of water, which results in a water height within the tank of 0.2 m. Marine and wind-generated currents are produced by two brushless DC motors, which drive propellers with adjustable speed and several flow patterns. Furthermore, a broadband dielectric mirror is placed on the side of the water tank to extend the range of the UOWC link. In Fig. 3.3, an experimental UOWC link with a link distance of 4.5 meters is demonstrated in the developed test-bed. This configuration is achieved by utilizing two mirrors placed at both ends of the water tank to extend the optical path through mirror reflections. During the test-bed setup, measurements were conducted for distances ranging from the tank's physical length of 1.5 meters, without the use of mirrors, to a maximum effective link distance of 7.5 meters, achieved with the assistance of four mirrors. In this thesis, numerical results are presented for a link distance of 3 meters, as will be justified later.

Air bubbles are generated by an external air pump and four porous stones that modify its characteristics in a controlled way. Lastly, different turbid levels, i.e., types of water, are emulated by adding antacid solutions to the tap water. The following section provides a comprehensive overview of the process of bubble generation and the emulation of different levels of water turbidity.

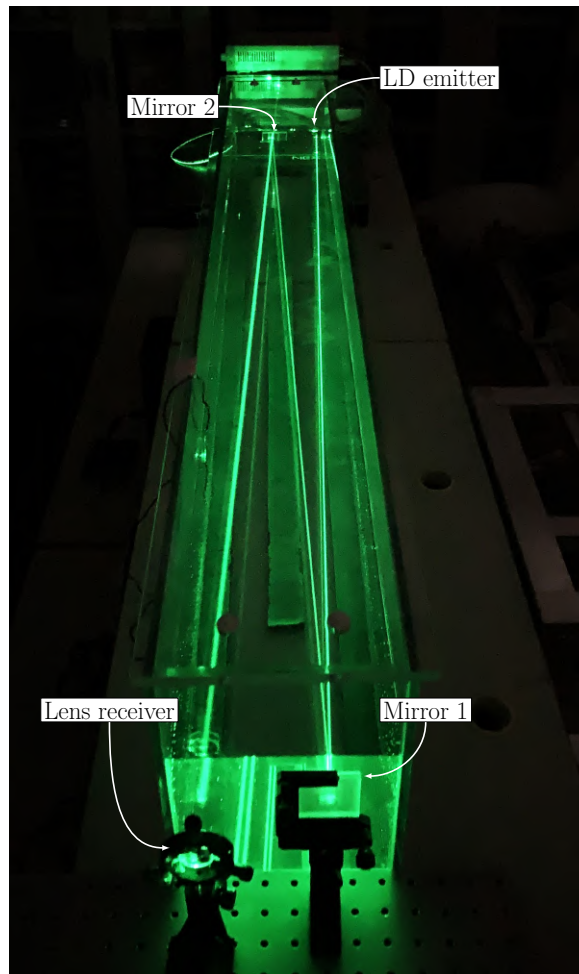


Figure 3.3: Experimental setup of a UOWC link with a link distance of 4.5 meters achieved by two mirrors placed at both ends of the water tank.

3.3 Emulated underwater channel effects

As discussed in Section 2.2, underwater light propagation depends significantly on attenuation due to particle-induced absorption and scattering, as well as on oceanic turbulence and air bubbles. As mentioned in Section 2.2.2, oceanic turbulence typically causes small-angle deviations in the direction of light propagation due to the random fluctuations of the refractive index, which can induce a scintillation effect. However, at short link distances, this scintillation effect is barely noticeable in underwater environments due to the small temperature and salinity gradients typically present in natural waters. Emulating oceanic turbulence with a meaningful impact on a UOWC link within the confined dimensions of an experimental water tank poses significant challenges. Firstly, the temperature and salinity gradients required to accurately replicate such turbulence for short link distances in a

UOWC test-bed would need to be exceedingly large. This approach is not only unrealistic but also costly and impractical under laboratory conditions. Secondly, from an experimental standpoint, maintaining the physical conditions necessary to simulate turbulence phenomena with precise salinity and temperature gradients over extended periods is inherently challenging. Reproducing these conditions accurately in consecutive experiments adds further complexity, limiting the feasibility of such experiments. Therefore, in this chapter, we assume a negligible oceanic turbulence impact, and focus on the impact of water turbidity on the air bubbles-induced fading, for different air bubbles sizes and water types. It should be noted that the absence of oceanic turbulence holds for UOWC systems operating at great depths, such as below 1000 meters, where salinity and temperature remain constant due to their dependence on water depth [112, Chapter 5].

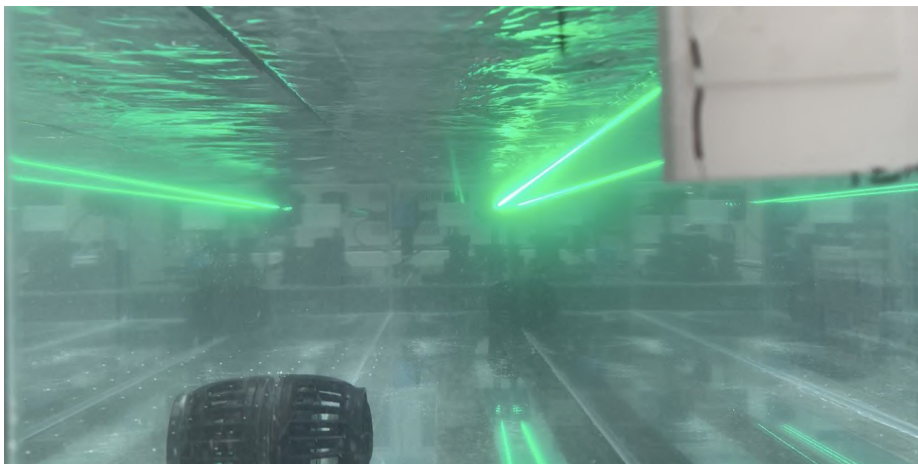
3.3.1 Absorption and scattering

The absorption and scattering levels of a water body depends on its chemical composition and the concentration of other ocean constituents such as colored dissolved organic matter (CDOM), phytoplankton, and detritus [81]. However, the use of biological particles in laboratory experiments is impractical due to the variability of their properties over time, as well as the complexity associated with their acquisition and storage. Therefore, it is common to use alternative compounds to emulate the effects of these water constituents. Specifically, the underwater optics community has proposed various scattering agents such as magnesium hydroxide and aluminum hydroxide with similar phase functions to natural scattering agents. Both of the mentioned chemical components are the primary components of Maalox, a commercial antacid commonly used to treat the symptoms of excess stomach acid. Consequently, Maalox antacid is also frequently employed to simulate different types of marine environments due to its similarity in the volume scattering function to those observed in realistic oceanic water samples [148–150]. In this thesis, we use commercial Maalox tablets as main scattering agent to emulate different levels of turbidity and types of water.

In order to guarantee the reproducibility of turbidity levels, the amount of Maalox used in each experiment is accurately determined using a precision scale with a resolution of 0.01 g. By way of example, Fig. 3.4 visually shows the impact of the antacid solution in terms of visibility in the water tank with 7.3 mg/L of Maalox dissolved in tap water, which in 60 liters of water is an amount of 0.44 g of Maalox. As can be observed, the visibility is drastically reduced, indicating a higher absorption coefficient. Furthermore, noticeable blurring of the edges of the light beam on the right is evident, showing beam broadening.



(a) Tap water.



(b) Tap water with 7.3 mg/L of Maalox antacid.

Figure 3.4: A green laser beam propagating through the water tank filled with tap water with (a) no antacid, and (b) 7.3 mg/L of Maalox antacid.

3.3.2 Air bubbles generation

The generation of air bubbles is directly controlled by an air pump that injects external air into the water through four air outlets at the bottom of the tank. Although the generation process appears straightforward, creating different scenarios of interest for underwater channel modeling requires identifying the key characteristics of a channel in the presence of air bubbles. In this work, two key aspects of air bubble characteristics are considered: the bubble population and their size.

Firstly, the bubble population, or density of air bubbles, is controlled by adjusting the airflow rate of the air pump with flow regulator valves. The air pump used in this experiment has

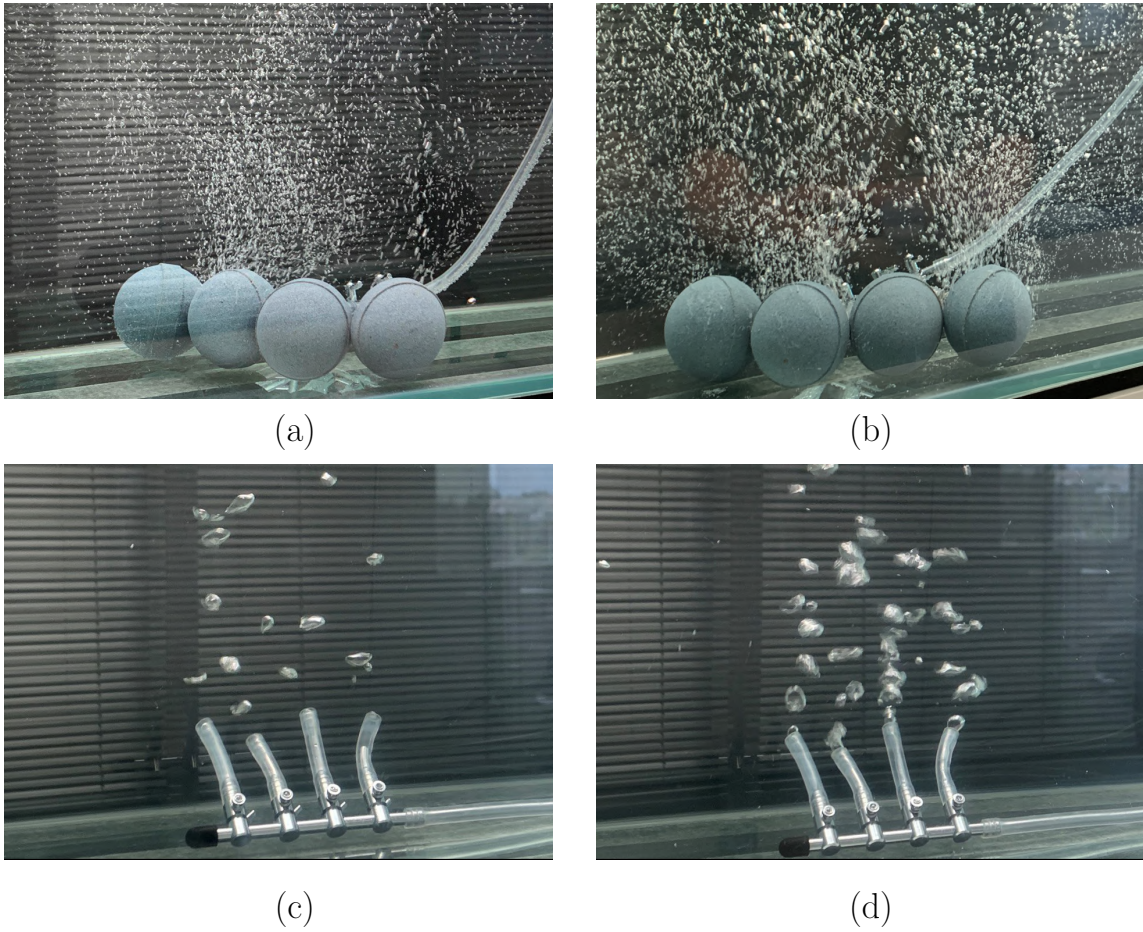


Figure 3.5: Proposed air bubbles scenarios: (a) small bubbles with low density (b) small bubbles with high density, (c) large bubbles with low density, and (d) large bubbles with high density.

a maximum capacity of 16 L/min. To manually regulate the total airflow inside the water tank, flow valves of each air outlet are slightly adjusted to accurately control its airflow.

Secondly, the size of the air bubble is determined by four porous stones connected to each air outlet, which function as air diffusers. Due to the heterogeneity of the porous stones, the diameter of small air bubbles ranges from 1 to 4 mm. In order to produce larger bubbles, the porous stones are removed from the air outlets, leaving the air outlet unobstructed, and generating bubbles with a diameter of approximately 1 cm.

The two considered density levels of air bubbles, as well as both sizes of air bubbles, are shown in Fig. 3.5. It is important to note that the diameter measurements were conducted using digital image processing techniques. Photographic images of bubbles with a resolution of 4032×3024 pixels, taken at a distance of 5 cm, were acquired during the experiment and

analyzed using software such as GIMP to determine their diameter in pixels. A reference distance between identifiable landmarks within the image was necessary to translate the pixel measurements into physical distances. In this study, the reference was the distance of the metal pipe connected to the experimental setup.

Air outlets are positioned to simulate realistic clusters of air bubbles that tend towards the surface in the form of column, typically generated by biological processes of marine organisms. Furthermore, the bubble column is randomly distributed throughout the water tank using two propeller pumps which also emulate natural wind-generated currents. At the same time, the interactions among bubbles and the propellers lead to a random division and merging of bubbles. As a result, this process promotes increased diversity in the bubble size and shape across the medium. This emulation captures imperfections and variations in bubbles characteristic of realistic underwater environments with natural air bubbles sources.

3.4 Bubbles-induced fading analysis

The random process generated by the proposed UOWC channel emulator results in optical power fluctuations at the receiver during an optical transmission. Therefore, it is essential to conduct a statistical analysis and develop a set of mathematical tools that not only accurately model the stochastic behavior of the received optical power but also provide insights into the impact of turbidity and air bubbles on the propagation of the transmitted beam. Furthermore, understanding the combined effect of both impairments on light beam transmission is crucial for accurately predicting UOWC system performance under different environmental conditions.

To that end, we derive key parameters of the emulated underwater channel from the proposed experiments, including the water attenuation coefficient, i.e., the extinction coefficient, the scintillation index, and the PDF of the optical power fluctuations. Additionally, other critical parameters, such as the coherence time of the fluctuations and the average outage duration, are also directly estimated from experimental measurements.

3.4.1 Estimated UOWC channel parameters

Underwater path loss

The most limiting factor of current UOWC systems is the short link distance due to the strong absorption and scattering of the underwater environment. Therefore, any experimental study of underwater channel must include an analysis of the empirical path loss obtained for different scattering conditions. The path loss is defined as the mean of the ratio between

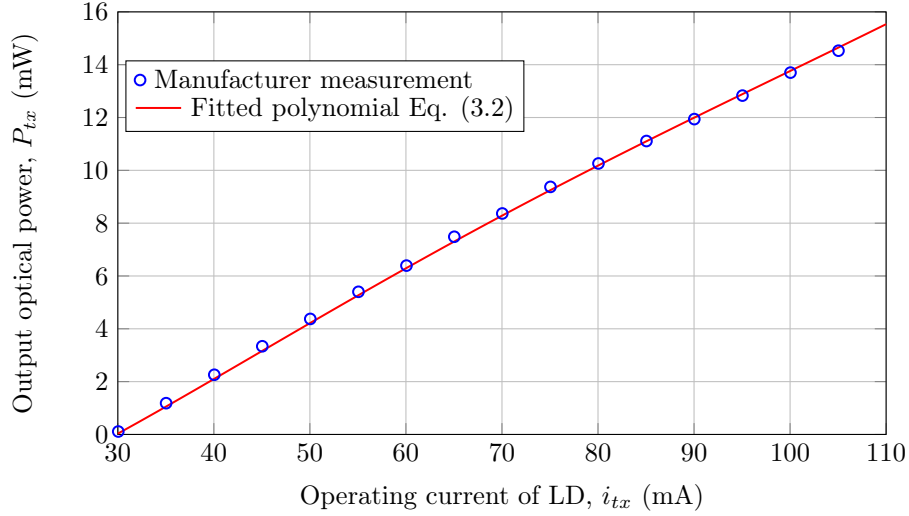


Figure 3.6: Polynomial fit of the optical power as a function of the injection current with the manufacturer-provided data for the LD LP520-SF15.

the received optical power and the transmitted optical power as follows

$$L = \mathbb{E} \left[\frac{P_{rx}}{P_{tx}} \right]. \quad (3.1)$$

As mentioned before, the transmitted optical power is determined based on the operating current of the LD, which is set using the current controller LDC205C. To facilitate the computation of optical power values corresponding to operating currents not explicitly included in the manufacturer's calibration measurements, a polynomial fit is applied to the data points from the provided curve. The fitted polynomial is given by

$$P_{tx} = 0.005 i_{tx}^2 + 0.051 i_{tx} - 4.29. \quad (3.2)$$

In Fig. 3.6, the fitted polynomial of Eq. (3.2) is presented alongside the values provided by the manufacturer.

The LD operating current is set to ensure that the received signal is sufficiently greater than the noise floor of the photodetector to allow correct reception of the optical signal. As mentioned before, the LD used in this thesis supports a maximum operating current of 115 mA. This hardware limitation prevents experiments from being conducted at turbidity levels so high that they would result in an insufficient signal for subsequent signal processing.

The received optical power is derived from the sampled electrical intensity, $i_{rx}[n]$, which is calculated from the output voltage at the photodetector sampled by the FPGA and the transimpedance gain of the photodetector as follows

$$i_{rx}[n] = \frac{V_{rx}[n]}{G}, \quad (3.3)$$

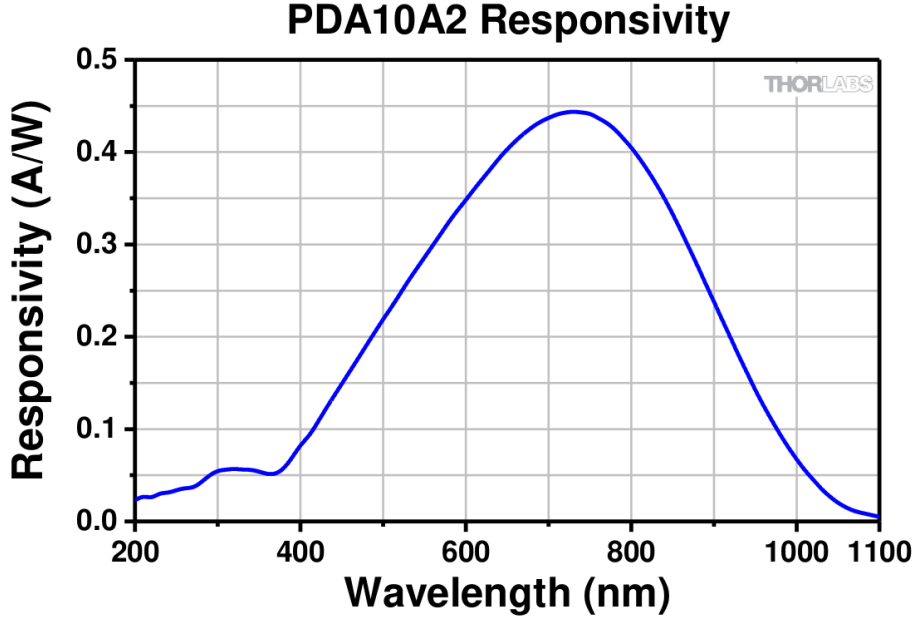


Figure 3.7: Responsivity curve of the PDA10A2 photodetector [151].

where $V_{rx}[n]$ is the n -th sample of the output voltage signal sampled by the FPGA. Afterwards, the received optical power is obtained from the above intensity and the responsivity of the photodetector as follows

$$P_{rx}[n] = \frac{i_{rx}[n]}{R}, \quad (3.4)$$

where R is the responsivity provided by the manufacturer. As illustrated in Fig. 3.7, the responsivity is $R = 0.25$ A/W for a wavelength of 520 nm.

At this point, it is important to distinguish between losses that occur within the underwater channel and those introduced by external factors in the experimental setup. The underwater path loss must account exclusively for the losses due to the underwater environment. However, Eq. (3.4) includes additional losses that arise from changes in propagation channel which are unrelated to the underwater channel itself. These external losses include refraction effects at the medium boundaries such as air-glass and glass-water transitions, reflectivity of mirrors used to extend the link distance, and the transmittance of the lens employed in the setup. To isolate the losses associated with the underwater channel, the received optical power calculated from Eq. (3.4) must be corrected by compensating for these external factors.

The transmittance coefficients for the medium changes are calculated using the Fresnel equations, assuming normal incidence as follows

$$T_{a-g} = \frac{4n_a n_g}{(n_a + n_g)^2}, \quad (3.5a)$$

$$T_{g-w} = \frac{4n_g n_w}{(n_g + n_w)^2}, \quad (3.5b)$$

where T_{a-g} is the transmittance coefficient due to air-glass transition, T_{g-w} is the transmittance coefficient due to glass-water transition, $n_a = 1$ is the air refractive index, $n_w = 1.33$ is the water refractive index, and $n_g = 1.5$ is the glass refractive index. Additionally, the transmittance of the lens $T_l = 0.91$, and the reflectivity coefficient of mirrors $R_m = (0.99)^N$, where N is the number of mirrors used in the link, must be also considered.

Thus, by substituting Eq. (3.3) into Eq. (3.4) and compensating for the external losses introduced by the experimental configuration, the corrected received optical power can be expressed as follows

$$P_{rx_u}[n] = \frac{V_{rx}[n]}{G R} \frac{1}{(T_{a-g})^2 \cdot (T_{g-w})^2 \cdot T_l \cdot R_m}, \quad (3.6)$$

Finally, by assuming a constant P_{tx} , the underwater path loss is obtained by substituting Eq. (3.6) into (3.1) as follows

$$L_u = \frac{\mathbb{E}[P_{rx_u}[n]]}{P_{tx}}. \quad (3.7)$$

To further analyze the contributions of suspended particles and air bubbles to underwater losses, the total path loss is decomposed based on its origins as follows

$$L_u[dB] = L_b[dB] + L_p[dB], \quad (3.8)$$

where L_b is the loss coefficient attributable to air bubbles, and L_p is the loss coefficient caused by in-suspension particles, such as Maalox antacid and tap water molecules. This decomposition provides a clearer understanding of how different physical factors contribute to overall underwater path loss.

Attenuation coefficient

As stated in Section 3.1, the main focus of the proposed experimental UOWC test-bed is to analyze light propagation through different underwater environments, with a particular emphasis on characterizing the impact of water turbidity on beam degradation. To accomplish this, it is essential to determine the absorption and scattering coefficients. However, measuring these coefficients separately is challenging due to the requirements of the measurement instruments, which include a perfectly collimated narrow beam and a narrow field-of-view detector, among others [81].

Nevertheless, both the absorption and scattering coefficients are considered in the attenuation coefficient, as described in Eq. (2.10). This parameter is commonly used to classify water types based on their turbidity. Therefore, the estimation of this parameter allows for an approximation of the water type emulated in the test-bed in terms of attenuation,

providing numerical information about its turbidity level that can be compared to standard water types, such as those described in Table 2.2.

The attenuation coefficient can be readily estimated from the Beer-Lambert's law described in Eq. (2.18) as follows

$$c = -\frac{1}{d} \log \left(\frac{\mathbb{E}[P_{rxu}]}{P_{tx}} \right). \quad (3.9)$$

Hence, by substituting Eq. (3.7) into (3.9), the attenuation coefficient can be determined as a function of the underwater path loss. However, the attenuation coefficient is an inherent optical property, meaning it depends solely on the intrinsic characteristics of the water's composition. This implies that external factors, such as the presence of air bubbles or other phenomena unrelated to the water's internal composition, should not influence this parameter. Consequently, the attenuation coefficient can be estimated exclusively based on the losses caused by particles in suspension as follows

$$c = -\frac{1}{d} \log(L_p). \quad (3.10)$$

Before each attenuation coefficient measurement with Maalox, a 5-minute waiting period is observed after introducing the compound into the water tank. This pause ensures the antacid homogenization throughout the tap water, aided by two propeller positioned at different heights and on opposite sides.

Scintillation index

Optical power fluctuations resulting from the stochastic behavior of the underwater channel are measured through the scintillation index described in Eq. (2.29).

Prior to analyzing the scintillation index, the received optical power, obtained as in Eq. (3.6), is normalized with respect to its mean value as follows

$$h_b[n] = \frac{P_{rxu}[n]}{\mathbb{E}[P_{rxu}[n]]}, \quad (3.11)$$

where $h_b[n] \triangleq H_b$ is the underwater channel gain representing the optical power fluctuations caused by air bubbles. As can be observed, these fluctuations are decoupled from the propagation losses introduced by the underwater channel, L_u , i.e., $\mathbb{E}[H_b] = 1$.

This normalization allows the optical power fluctuations to be quantified independently by computing the scintillation index given by

$$\sigma^2 = \frac{\mathbb{E}[H_b^2] - \mathbb{E}[H_b]^2}{\mathbb{E}[H_b]^2} = \frac{\mathbb{E}[H_b^2]}{\mathbb{E}[H_b]^2} - 1. \quad (3.12)$$

Probability density function

As mentioned in Section 3.1, one of the best statistical distributions to model the behavior of experimental measurements in relation to the goodness of fit is the generalized Gamma distribution [53]. The generalized Gamma distribution is a versatile statistical model that includes the Gamma distribution, the Chi and Chi-squared distribution, the Exponential distribution, and the Weibull distribution, which are usually employed in modeling power fluctuations in RF and optical wireless systems [53, 152, 153]. Hence, we propose the generalized Gamma distribution for small air bubbles-induced fading given by

$$f_{H_{\text{small}}}(h; a, d, p) = \frac{p}{a^d \Gamma(d/p)} h^{d-1} e^{-(h/a)^p}, \quad (3.13)$$

where h is the optical power fluctuation due to air bubbles and wind-generated currents, a is the scale parameter, d and p are the shape parameters.

The obstruction of the transmitted beam by a large bubble can induce total or partial light blockage at the receiver, which results in a bimodal distribution in the received optical power histogram [59]. Hence, we propose for the first time the use of a mixture distribution whose PDF is given as a sum of two generalized Gamma distributions when considering large air bubbles as follows

$$f_{H_{\text{large}}} = W \cdot f_{H_{\text{small}}}(h; a_1, d_1, p_1) + (1 - W) \cdot f_{H_{\text{small}}}(h; a_2, d_2, p_2), \quad (3.14)$$

where W is the proportion between the blockage effect, the first term, and the power fluctuation effect, the second term, such that $W \in [0, 1]$. Hence, we model the probability of total or partial blockages due to large bubbles and power fluctuations resulting from particles, wind-generated currents, and small bubbles that are formed through the collision of large bubbles.

Coherence time

Optical power fluctuation is a random phenomenon that varies over time and is characterized by a parameter known as coherence time, denoted by τ_0 . This parameter defines the time interval during which the variations in optical power are minimal, allowing the received signal to be considered approximately constant. When the coherence time is significantly greater than the symbol period of a communication system, the channel is classified as a slow fading channel, as multiple consecutive symbols are affected by a similar fade level. For instance, in a FSO communication system operating at a data rate of 500 Mbps, the symbol period is approximately 2 nanoseconds, which is much shorter than the typical coherence time of atmospheric turbulence, often on the order of several milliseconds [42, 154]. Conversely, if the symbol period is comparable to or longer than the coherence time, the channel is categorized as a fast fading channel, where fluctuations affect individual symbols more distinctly.

The coherence time, τ_0 , is related with the normalized temporal covariance function as [154]

$$\frac{B_\tau(\tau_0)}{B_\tau(0)} = \exp(-1), \quad (3.15)$$

where $B_\tau(t)$ is the temporal covariance function. The temporal covariance function is obtained as the autocovariance of the normalized received signal as

$$B_\tau(t) = \int_0^T \tilde{r}(t)\tilde{r}(t - \tau) dt, \quad t \geq 0 \quad (3.16)$$

where \tilde{r} is the normalized received signal, and T is the measurement period.

Average outage duration

To describe the time-varying behavior of an underwater channel affected by air bubble-induced fading, it is essential to analyze how these fades are distributed over time. The average outage duration (AOD), also known as average fade duration, is particularly useful in characterizing the received optical power fluctuations. This parameter quantifies the average time during which the received signal remains in an outage state [155]. Beyond providing insights into the statistical properties of the underwater channel, the AOD indirectly offers valuable information about its impact on the performance of UOWC systems operating under optical power fluctuations. Specifically, the AOD plays a vital role in cross-layer optimization, such as the design of adaptive transmission schemes, as regarding packet length, interleaver depth, and error control coding [156]. For example, by determining that the AOD has a specific average time, it becomes possible to design interleavers in error correction schemes with sufficient depth to cover the typical duration of fades. This ensures that data is distributed over intervals longer than each fade, enabling effective error correction. Additionally, the AOD provides critical guidance for adjusting packet sizes to ensure their transmission occurs within fading-free intervals, thereby minimizing both data loss and the need for retransmissions.

According to [155], the AOD (in seconds) is given by

$$AOD = \frac{OP}{N}, \quad (3.17)$$

where OP is the outage probability and N is the frequency of outages at a certain level, defined here as the 10% of the mean received power.

3.4.2 Channel measurements and calibration

The measurements conducted in this work were performed for a link distance of 3 meters and an operating current of 90 mA. These parameters have been carefully and deliberately

adjusted to emulate a wide range of underwater scenarios while maintaining experimental control. On one hand, the link distance of 3 meters was chosen to ensure greater interaction between the light beam and both air bubbles and antacid and tap water particles compared to a single-pass link in the 1.5-meter-long water tank. However, extending the link distance further would significantly increase the optical depth, which is defined as the product of the link distance and the attenuation coefficient, as described in Eq. (2.19). Although the antacid solution used in the experiments was kept minimal, a higher link distance would result in optical depths that do not accurately represent propagation through clear water at longer distances. In other words, a longer link distance would reduce experimental precision by limiting control over the impact of suspended particles on light propagation. Therefore, a link distance of 3 meters was selected as a balance: it enables multiple interactions of the light beam with air bubbles and in-suspension particles while maintaining precise control of the optical depth. This setup allows the gradual adjustment of the optical depth by introducing antacid in small and controlled increments. On the other hand, the operating current was set to 90 mA, corresponding to an optical output power P_{tx} of 12 mW. This value was chosen to prevent the saturation of the photodetector output voltage under conditions of low absorption and scattering, such as those observed in tap water without the presence of antacid particles. Simultaneously, this operating current ensures sufficient received optical power to overcome the inherent photodetection and ambient noise, even in highly turbid scenarios. This balance is critical for enabling precise statistical analysis in experimental conditions where severe attenuation occurs due to absorption and scattering effects caused by high concentrations of antacid particles in the water.

Regarding the sampling process, channel fluctuations are captured at a sampling rate of 25 kHz at 14 bits resolution for 5 minutes. The collected samples are analyzed in Matlab, where the received optical power is calculated and normalized to the mean of the received optical power in order to obtain the UOWC channel statistics. Finally, histograms and the fitted distributions are also obtained with the help of Wolfram Mathematica.

It should be noted that before conducting the experimental measurements, an in-depth calibration process was conducted for both the bubble generation device (the air pump) and the antacid solution utilized to modify the water turbidity. This procedure ensured the consistency of the random behavior of air bubbles across various time moments, leading to a consistent scintillation index for a given air bubble population. Likewise, it was confirmed that the turbidity level, as indicated by the attenuation coefficient for a specific concentration of Maalox per liter, remains reproducible across different time instants.

3.4.3 Numerical results and discussion

Firstly, we analyze the experimental measurements realized in tap water before adding the antacid solution. In Fig. 3.8, histograms of the received optical power fluctuations caused by the stochastic behavior of small and large bubbles with low and high density at link dis-

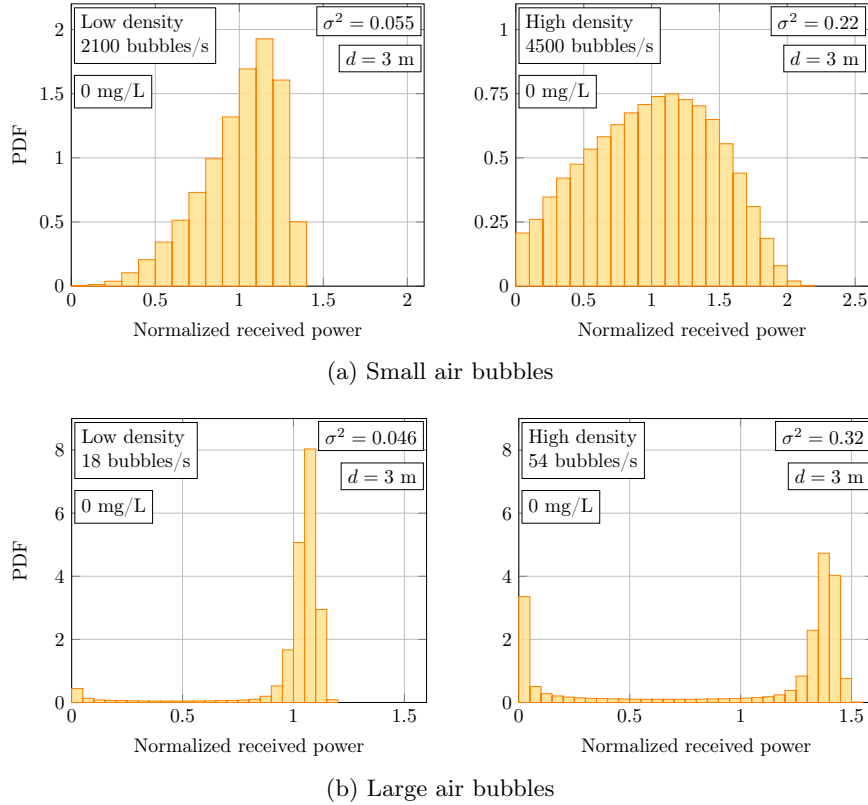


Figure 3.8: Histograms of channel fluctuations due to (a) small and (b) large air bubbles.

tances of 3 meters in tap water are represented. These experimental findings demonstrate that the formation of air bubbles clusters in a UOWC link leads to significant fluctuations. From Fig. 3.8, it can be also inferred that the density of air bubbles is a key parameter in the UOWC channel. These preliminary results are in line with previous studies: the bigger air bubbles population, the stronger intensity fluctuations, both in small and large air bubbles. As expected, the behavior of these fluctuations depends mainly on the size of the bubbles. On the one hand, fluctuations produced by small bubbles, as depicted in Fig. 3.8(a), exhibit a behavior similar to those induced by oceanic turbulence, showing fluctuations around the average received power [53]. On the other hand, Fig. 3.8(b) illustrates how large bubbles-induced fading also manifest a blockage component, which describes the partial or total obstruction of the transmitted optical beam. Additionally, bins nearby 0, which represent partial or total light blockages, also become more pronounced when the density of the bubbles cluster is getting bigger. These findings are also discernible by analyzing the footprints at the receiver plane. Fig. 3.9(a) illustrates the optical wavefront distortions induced by small bubbles, whereas Fig. 3.9(b) shows the blockage of the transmitted optical beam caused by large bubbles. Finally, it should be noted that low density scenarios induce very low intensity fluctuations, as reflected in the measured scintillation index value. This

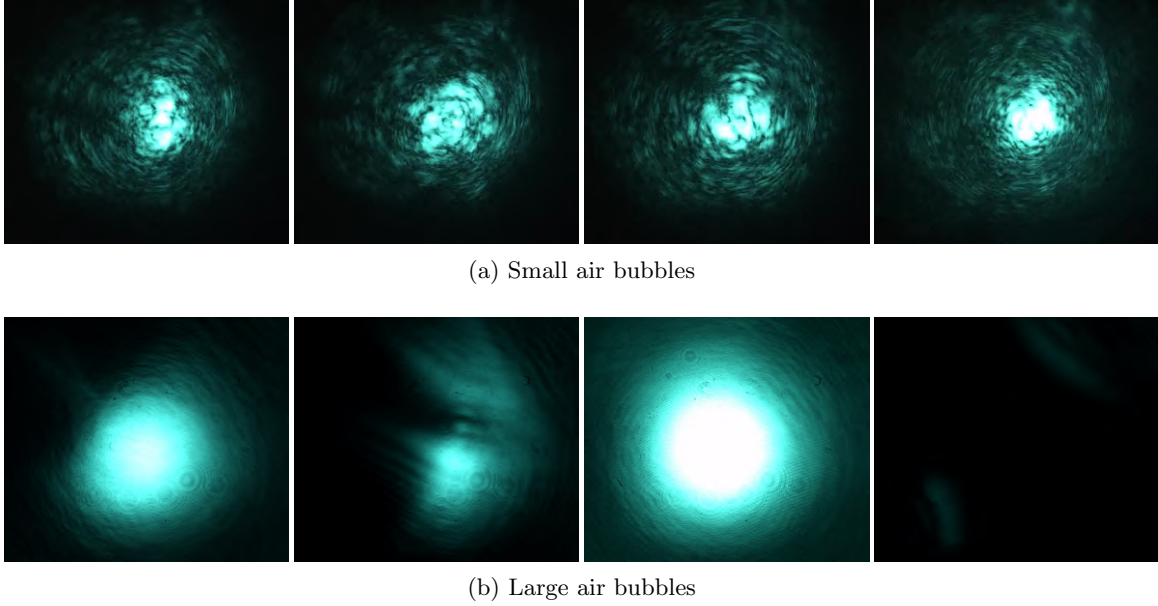


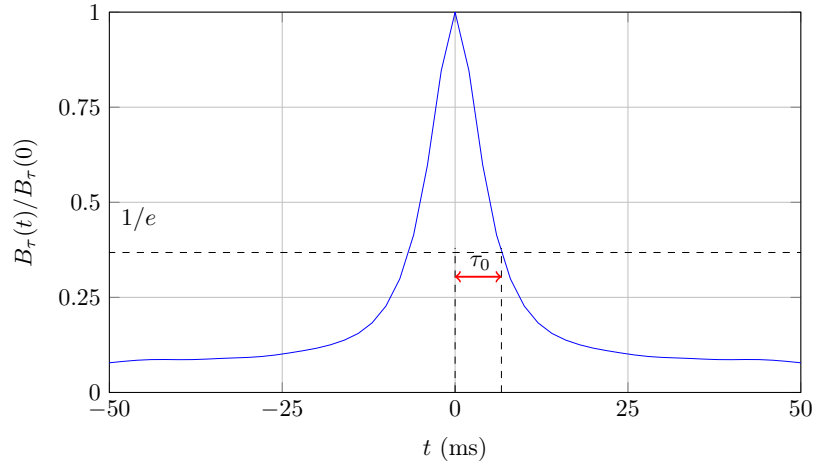
Figure 3.9: Received footprints of (a) small bubbles, and (b) large bubbles in consecutive frames at high density scenarios.

Table 3.2: Experimental results of the propagation losses, attenuation coefficient, coherence time, and AOD of the histograms in high density scenarios of small and large bubbles in Fig. 3.8(a) and Fig. 3.8(b), respectively.

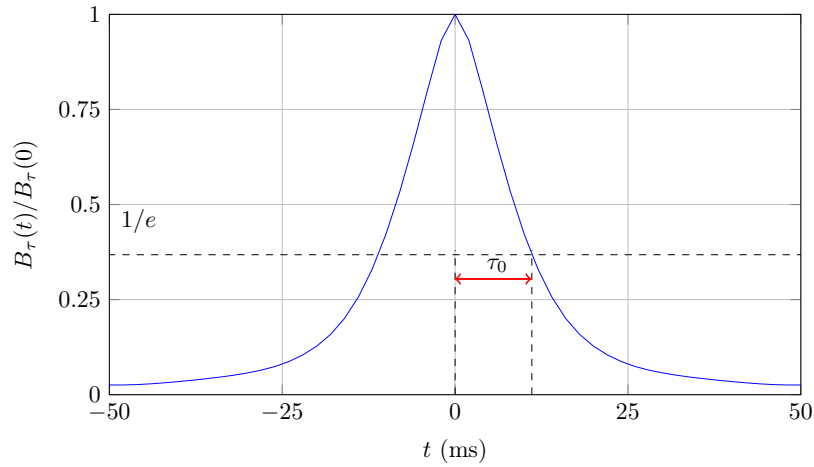
Channel	L_u (dB)	c (m^{-1})	τ_0 (ms)	AOD (ms)
No bubbles	2.1	0.16	-	-
Fig. 3.8(a)	6.8	0.16	6.7	2.04
Fig. 3.8(b)	5	0.16	11.1	9.54

is due to the minimal interaction between the light beam and the bubble column in these scenarios, which results in negligible impact on the received signal for both small and large bubbles. Hereinafter, all presented parameters will correspond to high density scenarios.

In Table 3.2, the statistical characterization parameters described in Section 3.4.1 for the high density scenarios are summarized. For comparison purposes, results of a measurement performed in the absence of air bubbles are included. The “Losses” column represents the total link losses, which are attributable to both in-suspension particles and air bubbles. As can be observed, an attenuation coefficient of 0.16 m^{-1} is obtained without air bubbles,



(a) Small air bubbles



(b) Large air bubbles

Figure 3.10: Normalized autocovariance of channel fluctuations when (a) small bubbles, and (b) large bubbles in high density scenario are considered.

which indicates that the employed tap water is similar to a clear ocean water type, as well as a Jerlov IB water type [19,157]. It should be noted that the attenuation coefficient remains constant for both small and large air bubble scenarios because it only accounts for losses attributable to particles, thereby ignoring any losses caused by air bubbles. Secondly, as can be seen in the AOD results, air bubbles produce light blockages of milliseconds on average, which can result in the loss of thousands of consecutive bits for high-data rates UOWC links operating in the order of Mbits/s, especially in the case of large bubbles. Finally, as expected, a slight difference exists in the coherence time between small and large bubbles. In Fig. 3.10, the normalized temporal autocovariance function, the mentioned threshold at e^{-1} , and the coherence time are depicted when small and large air bubbles are considered in tap

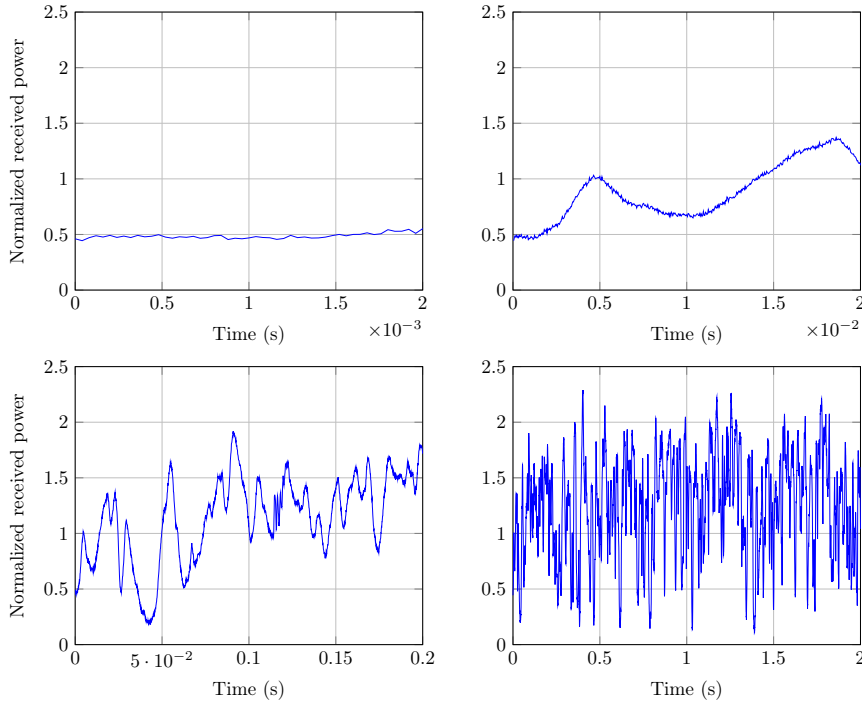


Figure 3.11: Normalized power fluctuations exclusively due to small air bubbles at different time scales.

water. As can be observed, small bubbles exhibit a slightly lower coherence time than large bubbles. While previous studies have analyzed coherence time in UOWC channel under oceanic turbulence [53], our findings extend previous reports. We demonstrate for the first time that the UOWC channel, influenced by bubbles-induced fading in tap water, represents a slow-fading channel even for UOWC systems operating at data rates of kbits/s, corresponding to a symbol period greater than 1 millisecond, because coherence time for both small and large bubbles exceeds 1 millisecond in empirical measurements. For the sake of illustration, Fig. 3.11 show the captured channel fluctuations at different time scales caused by the stochastic behavior of small bubbles with high density at a link distance of 3 meters in tap water. On a timescale of less than milliseconds, the received signal remains constant, indicating the slow-fading nature of air bubbles-induced fluctuations.

Pathloss analysis

As concluded above, the statistical behavior of both small and large bubbles differs qualitatively and quantitatively, as evidenced by the evaluation metrics. Therefore, understanding the impact of air bubbles in terms of propagation losses for the two analyzed bubble sizes is necessary before characterizing and analyzing the received optical power fluctuations under

Table 3.3: Experiment results of the losses due to particles and air bubbles in high density scenarios of small and large bubbles.

Channel	L_u (dB)	L_p (dB)	L_b (dB)
No bubbles	2.1	2.1	-
Fig. 3.8(a)	6.8	2.1	4.7
Fig. 3.8(b)	5	2.1	2.9

various turbidity levels. As mentioned in Section 3.4.1, the received optical power is obtained after compensate the responsivity of the photodiode, the reflectance of the dielectric mirror, the transmission coefficient of the plano-convex lens, and the refraction effect due to the medium changes.

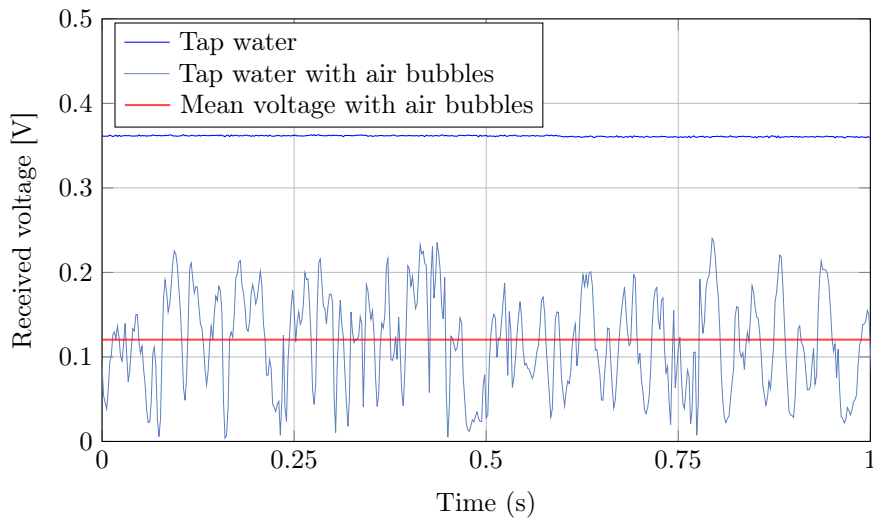
In Fig. 3.12, the received voltage when tap water and tap water with small and large air bubbles are represented. As can be observed, the mean value of the received voltage significantly decreases in the scenario with air bubbles, highlighting the presence of losses specifically attributable to air bubbles. Moreover, as illustrated in the figure, the impact of small and large air bubbles on losses exhibits notable differences. Although a direct comparison of the losses induced by small and large bubbles is not possible, Fig. 3.12 suggests that, on average, large bubbles result in a higher received voltage, i.e., lower losses, compared to small bubbles. This trend may be attributed to differences in the scattering properties of bubbles of varying sizes, as well as their impact on the propagation of the optical signal. To gain deeper insight into these effects, the underwater path loss is decomposed as in Eq. 3.8, distinguishing between losses due to air bubbles and losses due to particles in suspension.

For this purpose, a calibration measurement is first conducted without air bubbles to estimate the losses exclusively caused by in-suspension particles, i.e., Malloox antacid and tap water. These measurements are also used to calculate the attenuation coefficient using Eq. (3.10). Subsequently, as described in Eq. (3.7), a second set of measurements is performed in the presence of both air bubbles and in-suspension particles, allowing the total underwater path loss, L_u , to be estimated from the mean value of the received optical power.

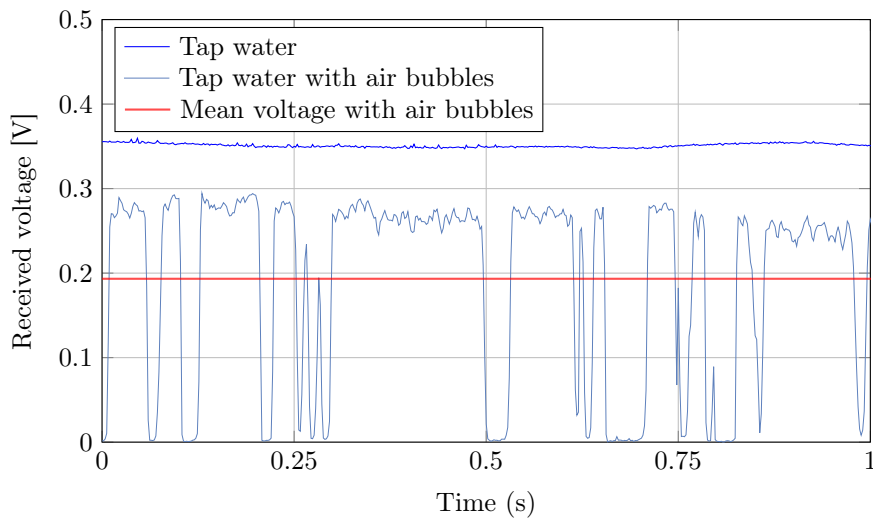
By comparing these results, the losses attributable to air bubbles can be isolated by subtracting the loss due to in-suspension particles from the total underwater losses as follows

$$L_b[dB] = L_u[dB] - L_p[dB]. \quad (3.18)$$

In Table 3.3, we present the losses attributable to particles as well as the losses attributable to air bubbles in the measurements of the respective histograms. Our experimental results



(a) Small air bubbles



(b) Large air bubbles

Figure 3.12: Received voltage when tap water and tap water with (a) small air bubbles and (b) large air bubbles are considered.

are consistent with simulation results obtained in [61], which conclude that small bubbles make the propagation losses greater than large bubbles.

Impact of water turbidity

In Figs. 3.13 and 3.14, the impact of particle-induced scattering on the histograms of the received optical power is illustrated for different concentrations of antacid solution, consider-

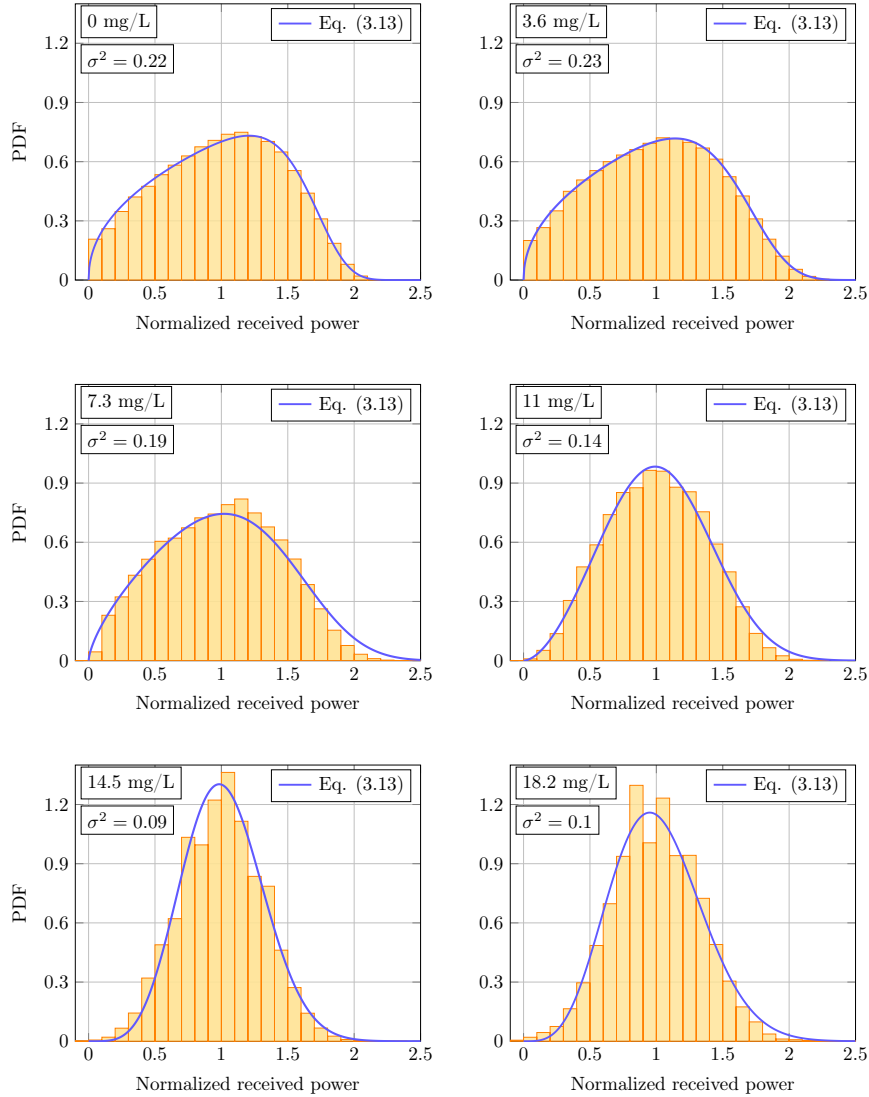


Figure 3.13: Statistical distribution model fitting under different levels of water turbidity when small air bubbles are considered.

ing small and large air bubbles, respectively. Furthermore, in Tables 3.4 and 3.5, we provide the fitting parameters for generalized Gamma and the mixture of generalized Gamma when considering the proposed scenarios for small and large bubbles, as well as the losses, coefficient of attenuation, and the coefficient of determination R^2 of each scenario. Both proposed models accurately show good fit with the measured data of small and large air bubbles with a coefficient of determination R^2 above 0.95 for all the considered scattering conditions. As expected, the path loss due to marine particles, L_p , increases quickly with the addition of the antacid. It should be noted that the presented scenarios cover a wide range of water types in terms of attenuation. Specifically, the emulated water environments cover from the

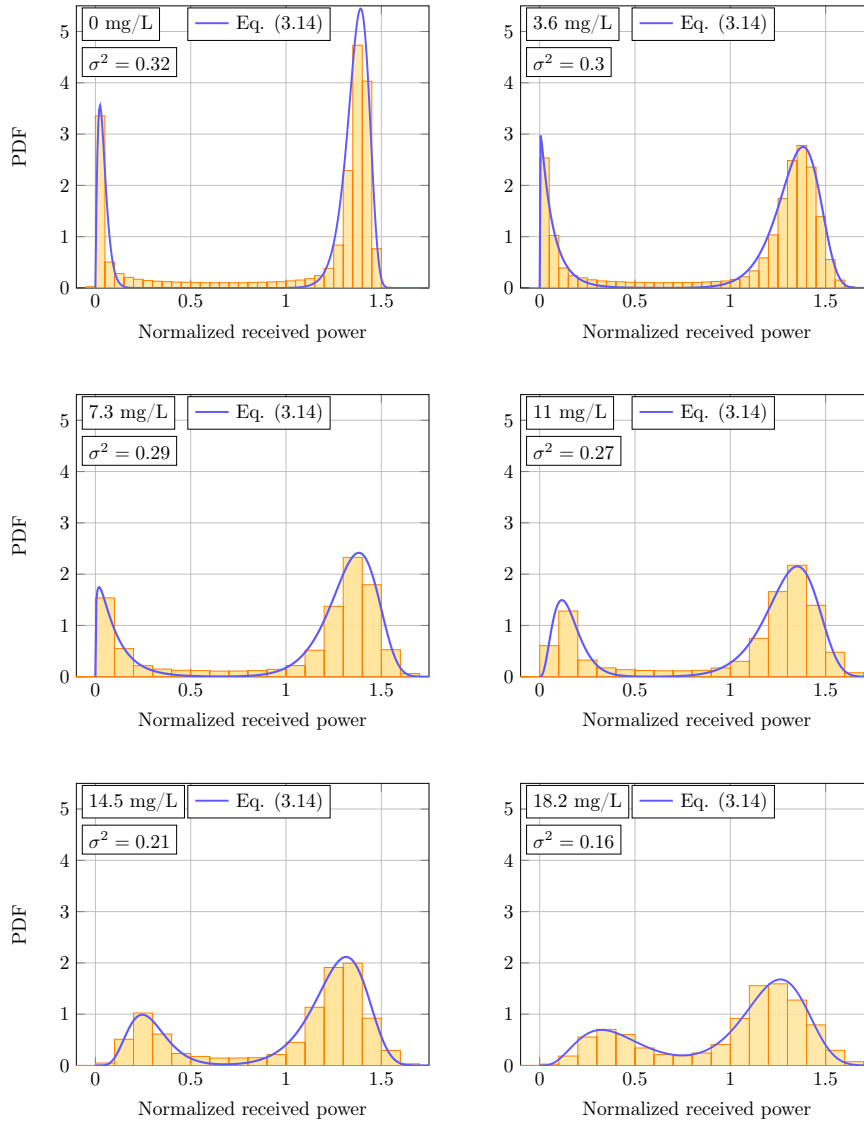


Figure 3.14: Statistical distribution model fitting under different levels of water turbidity when large air bubbles are considered.

Jerlov IB to 5C water type when a wavelength of 520 nm is considered [157].

Our results go beyond the current literature, as we have demonstrated for the first time that the scintillation index decreases with increasing water turbidity, as can be observed in Fig. 3.15 in both air bubble sizes. In addition, it is worth noting that the probability of blockage is dramatically reduced when increasing the antacid concentration per liter in the water tank. While this effect is observed in both sizes of air bubbles, it is particularly pronounced in larger bubbles. Physically, it appears that the fluctuations caused by air bubbles can be mitigated through a more significant collection of scattered photons resulting

Table 3.4: Experiment results of losses due to particles, attenuation coefficient, losses due to air bubbles, fitting parameters for generalized Gamma and R^2 of the histograms in Fig. 3.13.

Antacid [mg/L]	L_p [dB]	c [m^{-1}]	(a, d, p)	R^2
0	2.1	0.16	(1.73, 1.43, 7.95)	0.99
3.6	7	0.54	(1.72, 1.44, 6.28)	0.99
7.3	10	0.77	(1.59, 1.68, 4)	0.98
11	12.7	0.98	(1.19, 2.75, 3.05)	0.99
14.5	16.2	1.24	(0.79, 5.09, 2.41)	0.98
18.2	17.7	1.36	(0.75, 4.45, 2.1)	0.99

Table 3.5: Experiment results of losses due to particles, attenuation coefficient, losses due to air bubbles, fitting parameters for the mixture of generalized Gamma and R^2 of the histograms in Fig. 3.14.

Antacid [mg/L]	L_p [dB]	c [m^{-1}]	(a_1, d_1, p_1)	(a_2, d_2, p_2)	W	R^2
0	2.1	0.16	(0.028, 2, 1.2)	(1.38, 29.38, 22.7)	0.2	0.95
3.6	7	0.54	(0.05, 1.110, 0.85)	(1.38, 13.95, 12.8)	0.23	0.98
7.3	10	0.77	(0.06, 1.320, 0.85)	(1.39, 11.93, 11.7)	0.23	0.98
11	12.7	0.98	(0.047, 3.77, 1.06)	(1.36, 10.87, 10.55)	0.26	0.98
14.5	16.2	1.24	(0.037, 7.28, 0.98)	(1.33, 10.87, 10.2)	0.25	0.98
18.2	17.7	1.36	(0.09, 4.57, 1.03)	(1.26, 8.92, 7.65)	0.3	0.98

from the particle-induced scattering effect. Moreover, it is well known that increasing the level of scattering results in greater beam width broadening due to propagation through a more dispersive medium [141]. This results in a smaller relative size of the air bubble compared to the beam width, thereby reducing the likelihood of blockage. Therefore, while higher geometric and propagation losses are increases as the antacid concentration increases, a higher robustness to air bubble fading is achieved due to the beam expansion. This effect could similarly be achieved by employing UOWC systems with LD sources that have a larger beam width, as well as utilizing lenses with larger diameters at the receiver.

In line with the decrease in light blockage, the AOD represented in Fig. 3.16(a) is also

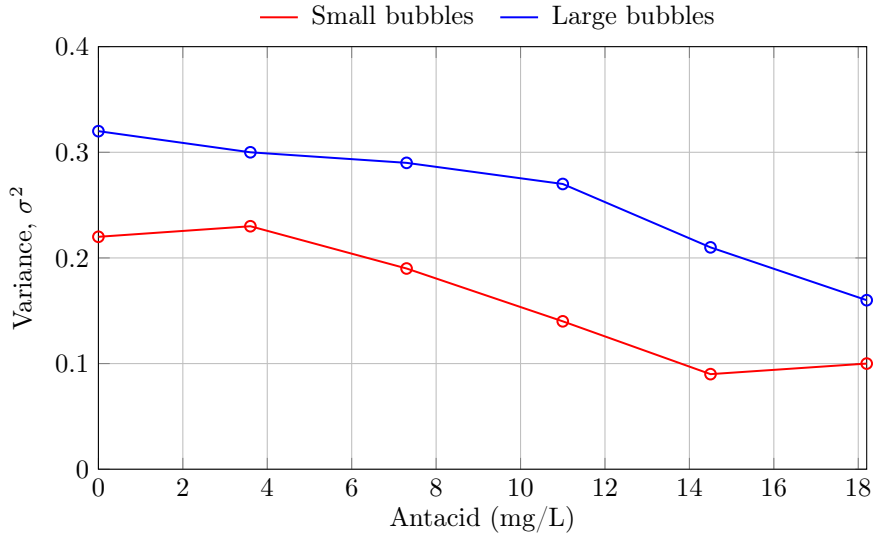


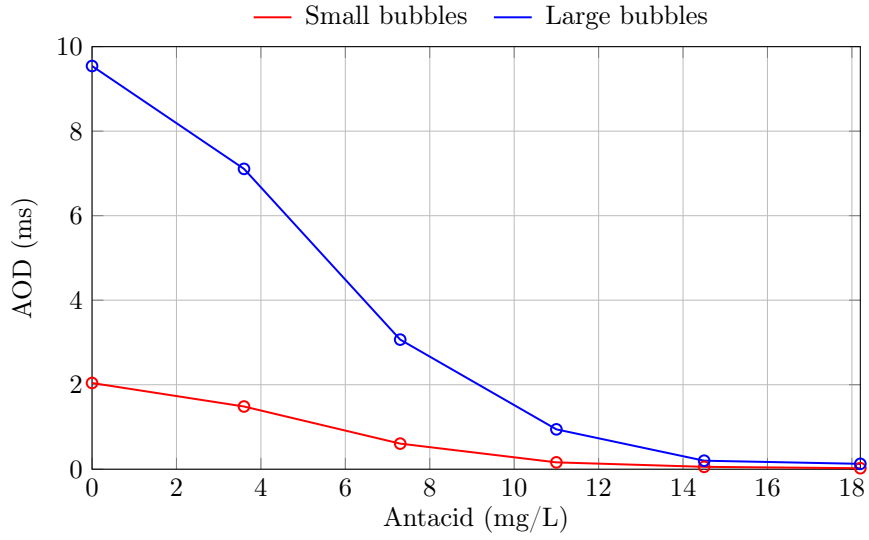
Figure 3.15: Scintillation index of small and large air bubbles under different levels of water turbidity.

significantly reduced due to water turbidity in both air bubbles cases. Most notably, this study presents compelling evidence for mitigating light blockage caused by air bubbles, thanks to the particle-induced scattering effect. Nevertheless, as depicted in Fig. 3.16(b), the coherence time remains constant for all the considered amounts of antacid, both small and large air bubbles. Thus, it can be concluded that water turbidity has no impact on the temporal correlation of UOWC channels under air bubbles-induced fading.

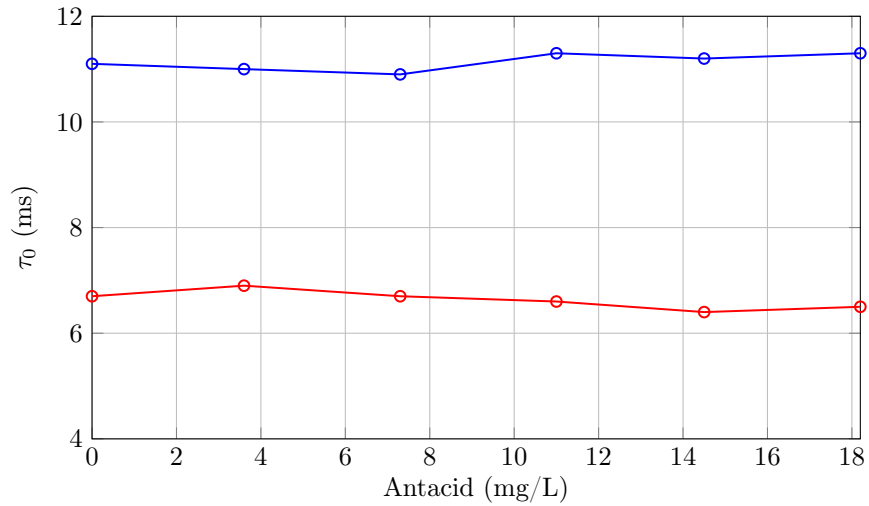
As far as we know, these findings have not been presented yet in the context of experimental UOWC channel characterization. Our current research contributes to the existing understanding of the impact of particle-induced scattering in UOWC systems affected by random variations in the refractive index due to air bubbles or oceanic turbulence. Consequently, our experiments can be used to accurately model natural waters bodies by considering the relationship between air bubbles and water turbidity.

3.5 UOWC system performance under proposed channel

In this section, the performance of a UOWC system is analyzed in terms of the average BER and the outage probability when considering small and large air bubbles under different levels of scattering following the empirical-based UOWC channel model in previous sections. Moreover, asymptotic expressions are obtained to shed light on the impact of the channel parameters on the system performance by revealing the diversity order and the coding gain.



(a) Average outage duration



(b) Coherence time

Figure 3.16: (a) Average outage duration and (b) coherence time of small and large air bubbles under different levels of water turbidity.

3.5.1 System and channel models

Consider a SISO UOWC system with an IM/DD scheme due to the lower complexity and low cost with respect to coherent schemes [41]. The received electrical signal for the proposed UOWC system is given by

$$Y = X L_u H_b + Z, \quad (3.19)$$

where L_u is the underwater path loss due to the water turbidity and air bubbles, H_b is the fading coefficient of the UOWC channel due to air bubbles, X is the transmitted optical power, and Z is additive white Gaussian noise with zero mean and variance $N_0/2$.

As mentioned before, air bubbles-induced fading is modeled using the generalized Gamma distribution of Eq. (3.13) and the mixture of two generalized Gamma distributions of Eq. (3.14) when considering small air bubbles and large air bubbles, respectively.

3.5.2 Bit error rate

Consider OOK signaling for the case of perfectly known channel state information (CSI) at the receiver. Hence, the conditional average BER at the receiver for the case of equally likely transmitted symbols is given by Eq. (2.44) as follows

$$P_b = \int_0^\infty Q\left(\sqrt{2\gamma} \cdot h\right) \cdot f_H(h) dh, \quad (3.20)$$

where H is a random variable that represents the underwater channel gain.

Hence, P_b in the small air bubble scenario is obtained by averaging over the PDF of small air bubbles defined in Eq. (3.13) as follows

$$P_{b_{\text{small}}} = \int_0^\infty Q\left(\sqrt{2\gamma} \cdot L_u \cdot h\right) \cdot f_{H_{\text{small}}}(h) dh. \quad (3.21)$$

By substituting Eq. (3.13) into Eq. (3.21), and making use of [158, Eq. (07.34.21.0012.01)] (see Appendix A.5), the exact closed-form expression for the average BER in the presence of small air bubbles can be obtained as follows

$$P_{b_{\text{small}}}(L_u, a, d, p) = \frac{p}{4\sqrt{\pi}(L_u a)^d \Gamma\left(\frac{d}{p}\right) L^d} \gamma^{-\frac{d}{2}} \times H_{2,2}^{1,2} \left[\frac{1}{(L_u a)^p} \gamma^{-\frac{p}{2}} \middle| \begin{matrix} (1 - \frac{d}{2}, \frac{p}{2}), (\frac{1-d}{2}, \frac{p}{2}) \\ (0, 1), (-\frac{d}{2}, \frac{p}{2}) \end{matrix} \right], \quad (3.22)$$

where $H_{p,q}^{m,n}(\cdot)$ is the H-Fox function (see Appendix A.4).

Similarly, the average BER when considering large air bubbles is obtained by averaging over the PDF of large air bubbles defined in Eq. (3.14) as follows:

$$P_{b_{\text{large}}} = \int_0^\infty Q\left(\sqrt{2\gamma} \cdot L_u \cdot h\right) \cdot f_{H_{\text{large}}}(h) dh. \quad (3.23)$$

From Eqs. (3.14) and (3.23) can be formulated as a weighted sum of integrals as follows

$$P_{b_{\text{large}}} = \int_0^\infty Q\left(\sqrt{2\gamma} \cdot L_u \cdot h\right) \cdot W \cdot f_{H_{\text{small}}}(h; a_1, d_1, p_1) dh + \int_0^\infty Q\left(\sqrt{2\gamma} \cdot L_u \cdot h\right) \cdot (1 - W) \cdot f_{H_{\text{small}}}(h; a_2, d_2, p_2) dh. \quad (3.24)$$

Thus, $P_{b_{\text{large}}}$ can be easily derived from Eq. (3.21) as a weighted sum of $P_{b_{\text{small}}}$ as follows

$$P_{b_{\text{large}}}(L_u, a_1, d_1, p_1, a_2, d_2, p_2, W) = W \cdot P_{b_{\text{small}}}(L_u, a_1, d_1, p_1) + (1 - W) \cdot P_{b_{\text{small}}}(L_u, a_2, d_2, p_2). \quad (3.25)$$

Since the obtained exact closed-form expressions could obscure the impact of PDF channel parameters on the UOWC system performance, more mathematically tractable expressions are obtained based on the asymptotic behavior at high SNR. As mentioned in Section 2.4.1, the asymptotic BER at high SNR can be derived with the behavior of the PDF of the considered random variable near the origin. Both PDFs expressed in Eqs. (3.13) and (3.14) can be approximated by a single polynomial term for $h \rightarrow 0$, i.e., near the origin, obtained from the Maclaurin series expansion as follows

$$f_{H_{\text{small}}}(h) \doteq \frac{p}{a^d \Gamma(d/p)} h^{d-1}, \quad (3.26a)$$

$$f_{H_{\text{large}}}(h) \doteq W \frac{p_1}{a_1^{d_1} \Gamma(d_1/p_1)} h^{d_1-1} + (1 - W) \frac{p_2}{a_2^{d_2} \Gamma(d_2/p_2)} h^{d_2-1}. \quad (3.26b)$$

Then, by substituting Eq. (3.26a) into Eq. (3.21), and making use of [158, Eq. (07.34.21.0009.01)] (see Appendix A.5), the asymptotic closed-form expression for the average BER when considering small air bubbles can be solved as follows

$$P_{b_{\text{small}}} \doteq \frac{p \Gamma\left(\frac{1+d}{2}\right)}{2 \sqrt{\pi} d (L_u a)^d \Gamma\left(\frac{d}{p}\right)} \gamma^{-\frac{d}{2}}. \quad (3.27)$$

Since the $P_{b_{\text{large}}}$ is a weighted sum of $P_{b_{\text{small}}}$, the asymptotic closed-form expression for the average BER can be easily solved as follows

$$P_{b_{\text{large}}} \doteq \frac{W}{2 \sqrt{\pi}} \frac{p_1 \Gamma\left(\frac{1+d_1}{2}\right)}{d_1 (L_u a_1)^{d_1} \Gamma\left(\frac{d_1}{p_1}\right)} \gamma^{-\frac{d_1}{2}} + \frac{1 - W}{2 \sqrt{\pi}} \frac{p_2 \Gamma\left(\frac{1+d_2}{2}\right)}{d_2 (L_u a_2)^{d_2} \Gamma\left(\frac{d_2}{p_2}\right)} \gamma^{-\frac{d_2}{2}}. \quad (3.28)$$

3.5.3 Outage probability

The outage probability is defined as the probability that the instantaneous SNR falls below a predefined threshold. By using the definition of Eq. (2.48), the outage probability can be obtained as follows

$$\text{OP} = P(\gamma_T \leq \gamma_{th}) = F_h \left(\sqrt{\frac{1}{4L_u^2 \gamma}} \right), \quad (3.29)$$

On the one hand, the corresponding CDF when considering small air bubbles is obtained as follows [159, Eq. (2)]

$$F_{H_{\text{small}}}(h; a, d, p) = \frac{\nu \left(\frac{d}{p}, (h/a)^p\right)}{\Gamma\left(\frac{d}{p}\right)}, \quad (3.30)$$

where $\nu(\cdot, \cdot)$ is the lower incomplete Gamma function (see Appendix A.2). By applying the decomposition formula of the Gamma function, $F_{H_{\text{small}}}(\cdot)$ can be easily derived, as follows

$$F_{H_{\text{small}}}(h; a, d, p) = 1 - \frac{\Gamma\left(\frac{d}{p}, (h/a)^p\right)}{\Gamma\left(\frac{d}{p}\right)}, \quad (3.31)$$

where $\Gamma(\cdot, \cdot)$ is the upper incomplete Gamma function (see Appendix A.2). Therefore, the corresponding outage probability when small air bubbles are considered can be easily derived by applying Eq. (3.31) into (3.29), as follows

$$\text{OP}_{\text{small}} = 1 - \frac{\Gamma\left(\frac{d}{p}, \frac{1}{(aL_u)^p} \bar{\gamma}^{-\frac{p}{2}}\right)}{\Gamma\left(\frac{d}{p}\right)}. \quad (3.32)$$

On the other hand, the CDF of large air bubbles-induced fading can be expressed as a weighted sum of two CDFs of small air bubbles-induced fading based on Eq. (3.14) as follows

$$F_{H_{\text{large}}}(h; a_1, d_1, p_1, a_2, d_2, p_2, W) = W \cdot F_{H_{\text{small}}}(h; a_1, d_1, p_1) + (1 - W) F_{H_{\text{small}}}(h; a_2, d_2, p_2). \quad (3.33)$$

Hence, the outage probability under large air bubbles is derived by applying Eq. (3.31) into Eq. (3.33) as follows

$$\text{OP}_{\text{large}} = W \left(1 - \frac{\Gamma\left(\frac{d_1}{p_1}, \frac{1}{(a_1 L_u)^{p_1}} \bar{\gamma}^{-\frac{p_1}{2}}\right)}{\Gamma\left(\frac{d_1}{p_1}\right)} \right) + (1 - W) \left(1 - \frac{\Gamma\left(\frac{d_2}{p_2}, \frac{1}{(a_2 L_u)^{p_2}} \bar{\gamma}^{-\frac{p_2}{2}}\right)}{\Gamma\left(\frac{d_2}{p_2}\right)} \right). \quad (3.34)$$

In the same way that the average BER, the outage probability at high SNR also tends to $\text{OP} \doteq (O_c \gamma)^{-O_d}$, where O_c is the coding gain, and O_d is the diversity order. Hence, by replacing Eq. (3.26a) into Eq. (3.29), we obtain the asymptotic behavior of the outage probability at high SNR for small air bubbles as follows

$$\text{OP}_{\text{small}} \doteq \frac{p}{(aL_u)^d \Gamma\left(\frac{d}{p}\right)} \bar{\gamma}^{-\frac{d}{2}}. \quad (3.35)$$

Finally, by applying Eq. (3.26b) into Eq. (3.29), we obtain the asymptotic of the outage probability at high SNR for large air bubbles as follows

$$\text{OP}_{\text{large}} \doteq W \frac{\left(\frac{1}{a_1 L_u}\right)^{d_1}}{\Gamma\left(\frac{d_1+p_1}{p_1}\right)} \bar{\gamma}^{-\frac{d_1}{2}} + (1 - W) \frac{\left(\frac{1}{a_2 L_u}\right)^{d_2}}{\Gamma\left(\frac{d_2+p_2}{p_2}\right)} \bar{\gamma}^{-\frac{d_2}{2}}. \quad (3.36)$$

3.5.4 Diversity order

As stated in Section 2.4.1, the BER and outage performance exhibit identical diversity orders for sufficiently large SNR. The resulting diversity order is useful for evaluating in a unifying manner and building insights about the impact of the underwater channel parameters on the UOWC system performance. From Eqs. (3.27) and (3.35), it can be shown that the diversity order, G_d , when considering small air bubbles is given by

$$G_{d_{\text{small}}} = \frac{d}{2}. \quad (3.37)$$

In the case of large bubbles, both the average BER and outage probability tend to $P_b \doteq (G_{c_1}\gamma)^{-G_{d_1}} + (G_{c_2}\gamma)^{-G_{d_2}}$ and $\text{OP} \doteq (O_{c_1}\bar{\gamma})^{-O_{d_1}} + (O_{c_2}\bar{\gamma})^{-O_{d_2}}$, where $G_{d_i} = O_{d_i}$. Therefore, the diversity order refers to the exponent of γ and $\bar{\gamma}$ in Eqs. (3.28) and (3.36), which determine the slope of the average BER and outage probability at high SNR, respectively. Mathematically, the smallest exponent dominates the behavior of these expressions. Thus, the diversity order can be expressed as the minimum of G_{d_1} and G_{d_2} . Consequently, the diversity order can be obtained from Eqs. (3.28) and (3.36) as follows

$$G_{d_{\text{large}}} = \frac{\min(d_1, d_2)}{2}. \quad (3.38)$$

3.5.5 Numerical results and discussion

In this section, the average BER and outage probability of UOWC links under air bubbles-induced scattering with different levels of water turbidity are evaluated. Furthermore, we provide Monte Carlo simulation results to verify the proposed analytical and asymptotic closed-form expressions. Due to the long simulation time involved, simulation results only up to 10^{-9} are included in this manuscript, which implies that the number of bits used in the Monte Carlo simulation is 10^{10} to ensure precision [136].

Concerning the empirical-based channel model, it must be noted that different channel conditions and fitted parameters are obtained from empirical measurements at a link distance of 3 m and a wavelength of 520 nm, which are summarized in Tables 3.4 and 3.5. Additionally, different levels of absorption and scattering were selected to represent a wide range of water types. For instance, for 0 mg/L of antacid, the extinction coefficient is $c = 0.16 \text{ m}^{-1}$, which can be compared to the extinction coefficient of clear ocean water or the Jerlov IB water type [19, 157]. In the case of the most turbid scenario, for 14.5 mg/L of antacid, $c = 1.24 \text{ m}^{-1}$, which is near the Jerlov 5C water type extinction coefficient [157].

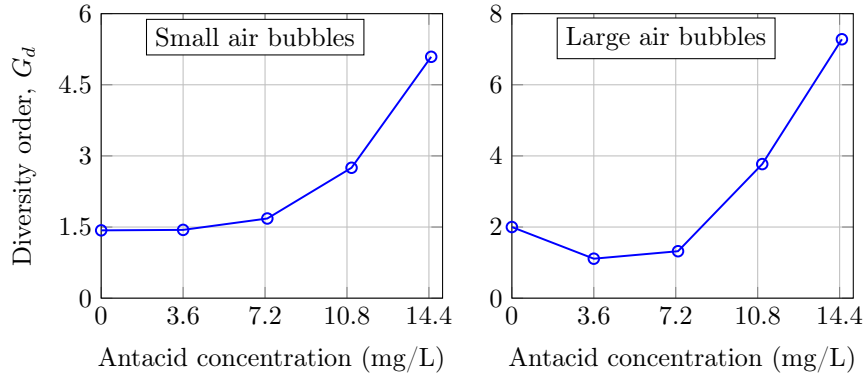


Figure 3.17: Diversity order when considering small air bubbles and large air bubbles for different levels of antacid in the experimental UOWC link.

Diversity order results

In Fig. 3.17, we show the diversity order of each level of water turbidity when considering small air bubbles and large air bubbles when considering the same UOWC system. Firstly, the diversity order exhibits an exponentially increasing trend as the concentration of antacid grows, demonstrating a proportional relationship between the two variables both in small and large bubbles scenario. However, we observe that at the lowest level of antacid, 3.6 mg/L, the diversity order of large air bubbles scenario decreases slightly compared with tap water, 0 mg/L. It may be attributed to the unique and singular impact of partial and total light blockages caused by large bubbles. This effect diminishes at higher antacid concentrations with a more significant collection of scattered photons, as detailed in Section 3.4.3. For this reason, after the initial singularity in the diversity order of the large air bubble scenario, both graphs provide a coherent and valuable insight into the exponential growth of diversity order in relation to water turbidity.

Small air bubbles

In Fig. 3.18, the average BER of a SISO UOWC system under small air bubbles for different levels of scattering are compared. As can be readily observed, the analytical and asymptotic results show an excellent agreement with Monte Carlo simulation results for all considered cases by validating the accuracy of the obtained expressions in Eqs. (3.22) and (3.27), respectively. Firstly, it is interesting to note that for scenarios with a low antacid concentration, the asymptotic expression approaches Monte Carlo and analytic results even at low SNR faster than higher antacid concentrations. Secondly, as one would expect, the high path loss due to increased antacid concentration deteriorates the average BER performance compared with the tap water case, as shown the 3.6 mg/L scenario, which shows a

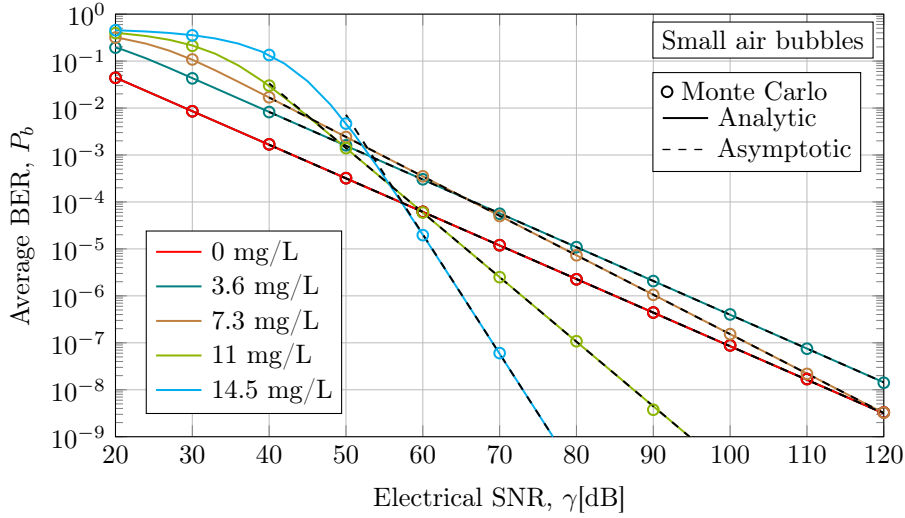


Figure 3.18: Average BER performance when considering an empirical UOWC channel in the presence of small air bubbles-induced fading under different levels of antacid concentration at a link distance of 3 m and a wavelength of 520 nm.

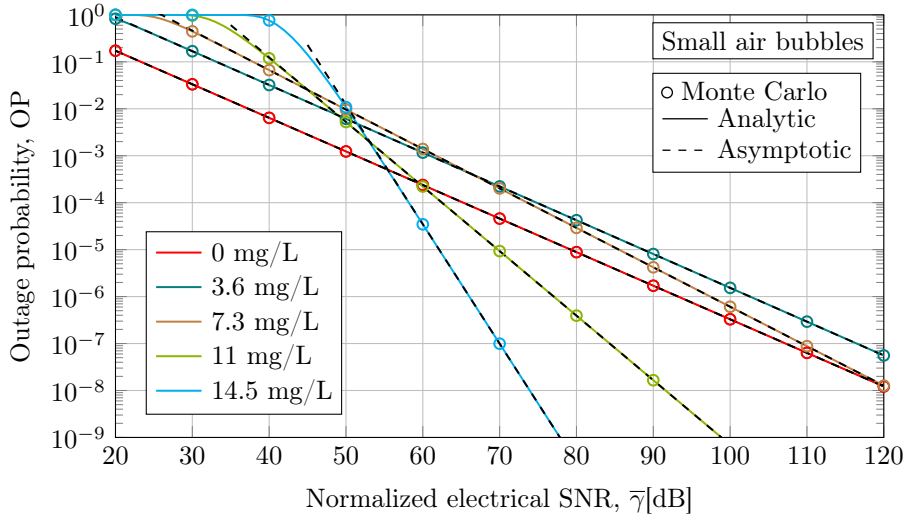


Figure 3.19: Outage performance when considering an empirical UOWC channel in the presence of small air bubbles-induced fading under different levels of antacid concentration at a link distance of 3 m and a wavelength of 520 nm.

higher average BER than the 0 mg/L scenario. However, the increase in diversity order due to higher water turbidity shown in Fig. 3.17, reverses this trend at high SNR regime, especially for more turbid scenarios. While the cases with 3.6 mg/L and 7.3 mg/L of antacid exhibit higher average BER than the 0 mg/L case within the presented SNR range, the

scenarios with the highest water turbidity, i.e., 11 mg/L and 14.5 mg/L of antacid concentration, significantly improve the performance of the UOWC system at high SNR under the same population of air bubbles. For instance, at 40 dB, the average BER for 14.5 mg/L is 1.35×10^{-1} , while for 0 mg/L, it is 1.7×10^{-3} . However, at 70 dB, the average BER for 14.5 mg/L is 6×10^{-6} , while for 0 mg/L, it is 1.2×10^{-5} . In practice, when the system is assured of having an SNR greater than 58 dB, the scenario with the highest turbidity will exhibit better performance in terms of average BER compared with the scenario with tap water. Thus, antacid-induced scattering mitigates the impact of air bubbles on the performance of UOWC systems. To illustrate this point, let us consider the natural optical beam spreading and geometric losses due to scattering. Hence, this effect can offer a great degree of robustness to air bubbles-induced scattering and light blocking. These findings are in line with previous simulation and experimental results reported in [141], where the impact of pointing error and scintillation index also decreases as the water gets more turbid, respectively. Therefore, we conclude that this change in trend can be perfectly attributable to an increase in the severity of scattering. However, this interpretation is limited to the 3 m experimental water tank from which fitted channel model parameters have been obtained. The impact of scattering over longer link distances may not be accurately reflected. For shorter distances, the attenuation effect of turbid waters might be less significant than the beam spreading effect, potentially improving BER performance, as mentioned above. Nevertheless, over longer distances, the path loss calculated from the Beer–Lambert law as e^{-cd} , where d is the link distance, becomes significantly greater in turbid waters, potentially resulting in higher BER performance. Therefore, beam spreading due to scattering can benefit short-range communication links by mitigating air bubble blockage, but overall performance can degrade over longer link distances due to increased path loss.

The outage probability for small air bubbles is represented in Fig. 3.19. As expected, the Monte Carlo simulation results agree with the analytical and asymptotic expression described in Eqs. (3.32) and (3.35), respectively. Note that the outage probability results reveal similar insights as the average BER into the impact of water turbidity on UOWC system performance.

Large air bubbles

In Fig. 3.20, we consider the average BER in the presence of large air bubbles-induced fading for different water turbidity levels. The considered antacid concentration levels are similar to small air bubble scenarios. Both analytic and asymptotic results demonstrate behavior similar to Monte Carlo simulation results, indicating the accuracy of the exact and asymptotic closed-form expressions obtained in Eqs. (3.25) and (3.28), respectively. In addition, Monte Carlo and analytic results support the convergence of the asymptotic solution, which is again faster for less turbid water cases. It can be observed that the asymptotic behavior of the scenario with a concentration of 14 mg/L of antacid does not fit as fast and accurately as

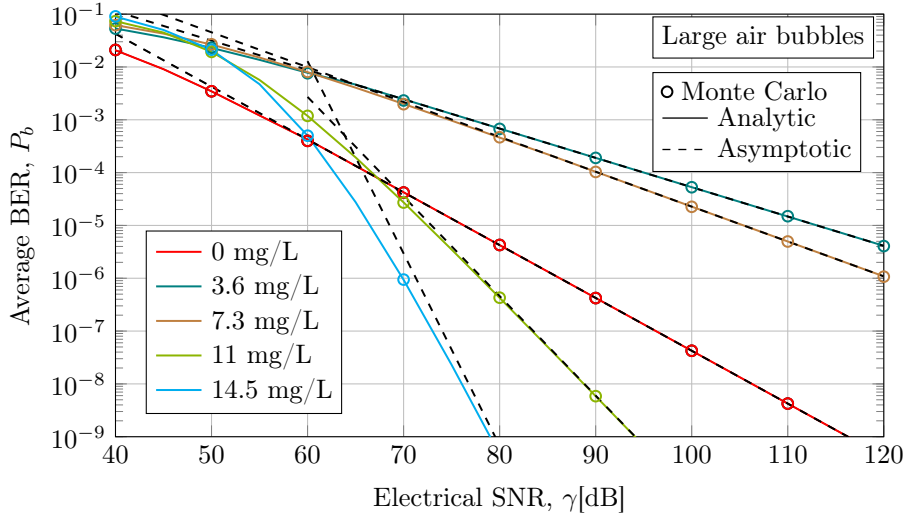


Figure 3.20: Average BER performance when considering an empirical UOWC channel in the presence of large air bubbles-induced fading under different levels of antacid concentration at a link distance of 3 m and a wavelength of 520 nm.

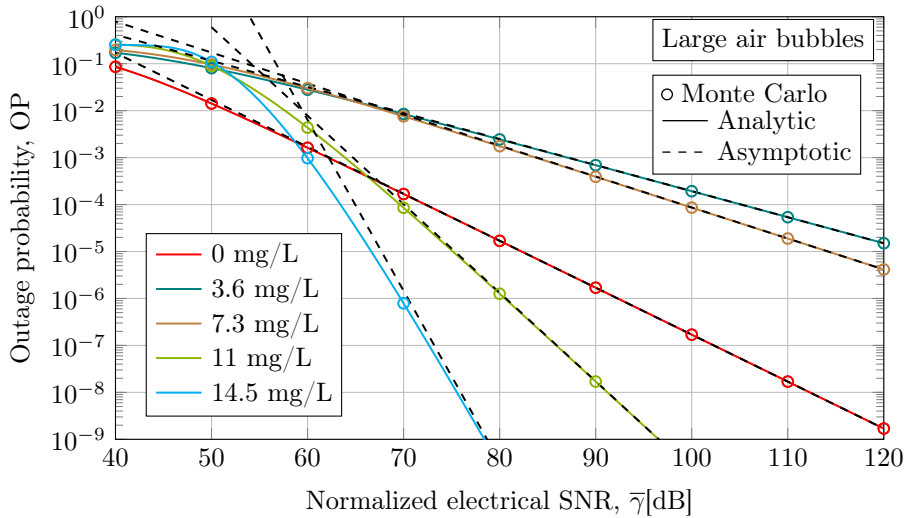


Figure 3.21: Outage performance when considering an empirical UOWC channel in the presence of large air bubbles-induced fading under different levels of antacid concentration at a link distance of 3 m and a wavelength of 520 nm.

the rest of the scattering scenarios. This is because this scenario exhibits a higher diversity order, i.e., a greater slope in the BER curve. Nonetheless, asymptotic results can be used as a tight upper bound across the presented SNR range.

As small air bubbles scenario performance results, the behavior of the average BER can be categorized into two regions. Before 60 dB, the average BER is lower when considering a tap water scenario, where the scattering effect is insignificant. However, after 60 dB, low average BER results are achieved in most turbid water scenarios. At 40 dB, the average BER for 14.5 mg/L is $9.1 \cdot 10^{-2}$, while for 0 mg/L, it is $2.1 \cdot 10^{-2}$. However, at 70 dB, the average BER for 14.5 mg/L is $9.4 \cdot 10^{-7}$, while for 0 mg/L, it is $4.2 \cdot 10^{-5}$. Although the scenarios with 3.6 mg/L and 7.3 mg/L of antacid show a higher average BER than the tap water scenario in all the evaluated SNR ranges, after 60 dB, the 7.3 mg/L scenario shows a lower average BER than the 3.6 mg/L scenario. This should be attributable to an increase in the absorption coefficient, i.e., a higher path loss, in 3.6 mg/L and 7.3 mg/L scenarios with respect to the clear water case. However, it seems that the scattering coefficient remains constant for both cases.

In Fig. 3.21, the outage performance results of the UOWC system under large air bubbles for different levels of water turbidity are plotted. Monte Carlo simulations results validate the analytic and asymptotic results obtained from Eqs. (3.34) and (3.36). The outage probability confirms the conclusions obtained from the average BER performance analyzed above.

3.6 Summary

An experimental underwater channel emulator has been developed to empirically model the stochastic behavior and the statistical distribution of optical power fluctuations induced exclusively by air bubbles in the presence of several water turbidity levels under laboratory conditions. Additionally, the proposed statistical models have been used to perform the BER and outage probability of a SISO UOWC system under the combined effects of air bubbles and scattering.

Firstly, the absorption and scattering coefficients of the tap water have been modified by spilling a commercial antacid which acts as a synthetic scattering agent with a volume scattering function similar to that of natural underwater particles. Regarding air bubbles generation, external air is introduced into the water tank employing an air pump, which is adjusted to manually regulate the airflow, allowing control over the volumetric flow rate, i.e., the bubble population, and the diameter of air bubbles. Then, two practical scenarios are analyzed: small and large air bubbles. To characterize the stochastic behavior of the emulated underwater channel and providing insights into the influence of turbidity in air bubbles-induced fading, a statistical analysis of the received optical power is conducted for various turbidity levels when small and large bubbles are considered. In addition, an analysis of the propagation losses, the coherence time, and the average outage duration is also obtained for all the proposed empirical scenarios. The key contributions of this study are summarized as follows

- The proposed generalized Gamma and the mixture of a weighted sum of two generalized Gamma distributions accurately model the stochastic behavior of the optical power fluctuations due to small and large bubbles, respectively. Notably, both distributions remain accurate under all the tested turbidity conditions.
- Experimental results demonstrate that bubbles-induced fluctuations are strongly influenced by particle-induced scattering, resulting in a significant reduction in light obstruction as the particle-induced scattering increases due to the capture of scattered photons.
- The scintillation index and the AOD decrease significantly as the antacid concentration increases. The slow-fading nature of fluctuations characterized by the coherence time of small and large bubbles remains constant under all the emulated water types and sizes of air bubbles.

To generalize previous studies of UOWC system performance in the presence of air bubbles, we propose to consider the impact of scattering on the air bubbles-induced fading in the UOWC system performance in terms of bit error rate and outage probability under the statistical framework fitted to the experimental measurements obtained in the underwater channel emulator. The main contributions of this analysis are summarized as follows

- Novel closed-form and asymptotic results of BER and outage probability are obtained from the empirical fitted statistical distribution, offering valuable insights into system performance in the presence of air bubbles under different water turbidity levels. Monte Carlo simulation results verify analytic and asymptotic expressions.
- Asymptotic expressions are used to analyze the diversity order of the BER and outage probability. Empirical results show that the diversity order exhibits an exponentially increasing trend at both bubble diameters as the concentration of antacid, i.e., the scattering coefficient, increases.
- Performance results show that the impact of air bubbles on BER performance becomes less significant for the most turbid waters with respect to the tap water scenario due to the higher diversity order at higher antacid concentrations. The natural optical beam spreading and geometric losses due to scattering act as inherent mechanisms of the underwater channel for mitigating air bubbles-induced fading and light obstruction.

Given the relevance of these results, this research need to be extended by thoroughly examining the influence of additional link parameters, such as transmission distance, on the fitted parameters of the proposed distribution and the probability of blockage. However, while this interpretation of the results is limited to the 3-meter experimental water tank from which the fitted channel model parameters are obtained, this study sheds light on the impact of scattering and attenuation on the deployment of UOWC transceivers on complex

underwater environments and underscores the necessity for further research into these factors over longer link distances to achieve a more thorough understanding of UOWC system performance. On the one hand, the proposed statistical models and performance expressions contribute to the study of more sophisticated transmission schemes, such as coherent modulation for UOWC systems, as well as spatial diversity techniques like MIMO-UOWC systems. On the other hand, the results presented in this chapter highlight the significant impact of scattering on the performance of UOWC systems when deployed in turbid underwater environments, such as coastal waters or Jerlov type 5C. There is a substantial need for UOWC systems to incorporate strategies and techniques specifically designed to mitigate scattering impairments in turbid waters, as well as to address optical fluctuations caused by oceanic turbulence and air bubbles in dynamic underwater scenarios.

Chapter 4

MISO UOWC systems

This chapter presents two MISO schemes designed to mitigate the impact of turbulence-induced fading, as well as the non-negligible absorption and scattering effects of underwater environments. Firstly, a novel spatial repetition coding scheme is presented based on a *per-source* power constraint. This allows each laser diode to operate at its maximum optical power, thus mitigating the absorption and scattering more directly than previous schemes presented in the literature, which consider *per-transmitter* power constraints. Moreover, the proposed mathematical model allows for the analysis of both power constraints, thus enabling the consideration of energy limitations in battery-powered UOWC systems. Furthermore, a tractable generalized transmit laser selection model is presented in order to consider the impact of erroneous selections of the best laser source due to imperfect channel state information at the transmitter. Additionally, analytical and asymptotic expressions are derived to evaluate the BER of both MISO UOWC systems operating over a Weibull salinity-induced oceanic turbulence and different types of waters, such as clear ocean and coastal waters.

4.1 Introduction

4.1.1 Motivation and related work

Previous chapters have demonstrated that the underwater channel significantly affects the performance of UOWC systems. This motivates the need to consider transmission schemes that minimize the impact of the underwater impairments on the received optical signal. Spatial diversity techniques have been usually proposed for terrestrial FSO communication links to improve the overall performance and reliability over turbulence-induced fading channels [160–164] (and references therein). Other techniques for mitigating fading in time-varying channels include the use of error control codes [165, 166]. However, high data rates

provided by optical systems require the use of large interleave lengths in order to achieve sufficient coding gains and effectively minimize the impact of turbulence [161,162]. Hence, considering the similarity of underwater optical turbulence and atmospheric optical turbulence, several works directly applied atmospheric spatial diversity techniques such as the spatial repetition coding (SRC) scheme at the transmitter side in UOWC systems [56,167–169]. In [56], the ergodic capacity and BER of UOWC SRC systems employing quadrature amplitude modulation are evaluated over a turbulent underwater channel characterized by a generalized gamma distribution. Similarly, in [167] the performance of a 2×2 UOWC MIMO system is investigated in terms of the BER under the presence of air bubbles for different bubbles sizes. These studies demonstrate an improvement in the performance of systems implementing SRC schemes. However, both works are limited to UOWC channels where absorption and scattering effects are ignored, as they do not account for the type of water. In [168], a comprehensive UOWC channel analysis under weak oceanic turbulence modeled as a lognormal distribution performs the efficacy of a SRC scheme in terms of BER over different types of water. The study demonstrates that under weak turbulence conditions, the proposed SRC scheme does not provide a significant performance enhancement with respect to SISO schemes, since the main impairments of the underwater environment are related to the scattering and absorption effects. Furthermore, it is shown that single-input/multiple-output (SIMO) and multiple-input/multiple-output (MIMO) configurations suffer greater performance degradation due to the ISI effect compared to the performance of MISO schemes. Nevertheless, no spatial diversity system is proposed that effectively mitigates the combined effects of scattering and oceanic turbulence. In [169], an adaptive power allocation algorithm with spatial modulation is proposed to mitigate the impact of the ISI on the BER of a UOWC MIMO system for different types of water. However, this study overlooks the fading effect that can be induced by oceanic turbulence or air bubbles.

In accordance with the antenna selection methodologies employed in RF systems, the optical community also proposes a straightforward alternative to the SRC scheme that is based on diversity selection [170]. This alternative, known as transmit laser selection (TLS) in FSO systems, relies on the selection of the optical sub-path with the highest channel gain by utilizing the knowledge of the channel state information of each light emitter at the transmitter side [171,172]. The receiver estimates the fading channel state using a CSI estimation technique, such as pilot-based, blind, or machine-learning methods. Pilot-based methods, widely used in optical wireless communication, are simple and accurate but reduce channel capacity [173,174]. Blind techniques avoid pilot overhead by relying on statistical properties, while machine-learning approaches enable real-time CSI estimation in dynamic environments at the cost of high computational resources [175,176]. In underwater environments, where oceanic turbulence varies slowly, any of these methods can provide a valid CSI estimate. Then, the estimated CSI is transmitted to the transmitter side via a low-rate feedback link, allowing the transmitter to select the light emitter with the optimal performance for data transmission. In the context of UOWC, some TLS configurations have been similarly proposed in order to extract channel full diversity and minimize the degrading

effects of oceanic turbulence [57, 58, 177]. In [177], authors analytically derives the BER expressions of a TLS UOWC system under the assumption of perfect CSI at the transmitter (CSIT) in weak oceanic turbulence modeled by a lognormal distribution. While this study considers propagation losses in coastal water scenarios, its analysis focuses exclusively on turbulence mitigation and does not extend its analysis to different turbidity levels. Furthermore, although perfect CSIT can be assumed feasible for both atmospheric and underwater optical channels given the slow time varying process of turbulence relative to the symbol rate, as noted in [177], earlier studies have proposed generalized TLS (GTLS) schemes to address situations where instantaneous CSI is unavailable at the transmitter. In [57], the outage probability of each emitter of a TLS scheme is calculated under oceanic turbulence modeled as a gamma-gamma fading channel. In [58], the effective secrecy throughput is obtained under the assumption that the transmitter has access to the average CSI, rather than the instantaneous CSI. As in previous studies, the results presented in [57, 58] are limited to a single type of water and lack a comprehensive analysis of the impact of absorption and scattering on system performance. Furthermore, neither of the two works investigates a GTLS UOWC system under an imperfect CSIT which is subject to fluctuations due to the inherent variability of the UOWC channel. Instead, their analyses focus on comparing the performance of individual fading channels corresponding to different light emitters. A realistic analysis of a GTLS UOWC system under imperfect CSI should consider the performance of a variable underwater channel, where the transmitter intermittently has access to CSI, with a probabilistic success rate for selecting the light emitter with the highest channel gain.

It is evident that the aforementioned analyses are not directly applicable to realistic underwater environments. Furthermore, the majority of MISO schemes utilized in UOWC performance analysis are employed exclusively as fading mitigation techniques, as they have been adapted from RF and FSO communication systems, which differ fundamentally from UOWC in their underlying physical principles and channel characteristics. As previously discussed in Chapter 2.2, the underwater channel exhibits higher absorption and scattering effects than the atmospheric channel due to the high concentration of chlorophyll and suspended particle concentration in natural waters. Considering the strong attenuation effect in realistic water bodies, it is imperative to propose alternative transmission schemes with the aim of enhancing the reliability of long UOWC links, as well as the UOWC system performance. Despite the incorporation of high optical power LD in UOWC transmitters, practical constraints on link budgets imposed by eye-safety standards prevent the transmission of the necessary powers in hostile underwater environments, leaving the link vulnerable to turbid waters and deep fades. Therefore, the use of multiple light emitters at the transmitter side, such as MISO schemes, can be exploited not only as a fading-mitigation tool, but also as a technique to remarkably increase the total transmitted optical power with the idea of mitigating the absorption and scattering effect, and support longer link distances in turbid environments. To do that without relaxing the optical power constraint, multiple light emitters not only need to be placed separately to assume independent channel fades

at the receiver but also to exceed the average optical power that can be transmitted in comparison to a SISO system.

Motivated by the above, it is clear that current literature has yet to address the practical implementation of MISO schemes in underwater environments. Firstly, the mitigation of underwater attenuation in realistic scenarios through SRC spatial diversity techniques should consider an increase in transmitter optical power achieved through an appropriate transmitter design that complies with the eye-safety standards. Furthermore, an in-depth analysis of various types of water is necessary for a complete implementation, considering the unique characteristics of realistic underwater environments. Secondly, the statistical distribution for oceanic turbulence considered in the majority of theoretical MISO analysis in the context of UOWC literature is limited to temperature-induced turbulence and air bubbles-induced fading phenomena, which are modeled as lognormal, generalized gamma, and gamma-gamma distributions [56, 57, 168, 177, 178]. This constraint reduces the scope of current studies, as salinity gradients are excluded from the analysis. To the best of our knowledge, only [58] has considered a MISO scheme under a Weibull fading channel to account for salinity-induced oceanic turbulence. Thirdly, regarding the deployment of GTLS systems in scenarios characterized by imperfect CSI or the absence of CSI at the transmitter, the optical community must address the necessity for a more realistic GTLS system that incorporates random erroneous channel selections. Although previous studies have assumed a GTLS scheme with unknown CSIT, the derived expressions do not account for the variability of the underwater channel. Therefore, it is necessary to propose a GTLS model that considers a CSIT available with varying degrees of probability, including instances where CSIT is unavailable and others where it is accessible due to the inherent instability of the underwater channel.

4.1.2 Structure

The remainder of this chapter is organized as follows. Section 4.2 introduces the theoretical principles of SRC and TLS schemes and the eye-safety power constraints assumed in this chapter. A novel compact transmitter design is proposed to assume different optical power constraints. In Section 4.3, the underwater channel model under oceanic turbulence-induced fading and absorption and scattering effect is introduced. Next, the system model of a novel SRC scheme that accounts for different optical power constraint approaches and a tractable GTLS model that considers different CSI conditions are presented. In Section 4.4, closed-form expressions for the BER of the proposed SRC and GTLS are obtained under the proposed UOWC channel. In Section 4.5, the BER performance of the proposed SRC, TLS, and GTLS systems is evaluated over different system configurations under salinity-induced oceanic turbulence, comparing system performance across various types of water. Finally, Section 4.6 summarizes the main findings and conclusions of the chapter.

4.2 MISO systems

Spatial diversity schemes enhance the overall system performance and reliability of UOWC systems by exploiting the multiple paths between the transmitter and receiver sides. The employment of multiple light emitters can mitigate the impact of the optical power fluctuations at the receiver by transmitting simultaneously multiple replicas of the same information signal through independent fading channels, which are much less likely to fade at the same time than each individual. It should be noted that the condition of independence between the different channels is ensured when the distance between transmitters is greater than the spatial coherence radius of a light beam after propagating through the oceanic turbulence assumed in this chapter. This form of diversity applies spatial redundancy along the underwater optical channel, which is used by SRC schemes.

An alternative approach to employing the multiple transmitters is selection diversity. The transmitter block can select a single emitter, i.e., a single path, based on the SNR of the received signals. In this technique, the transmitter requires the knowledge of the CSI of each path. This information is usually feedback from the receiver, and the channel state must remain constant over that period. This technique is known as a TLS scheme.

In addition to its function as a fading mitigation tool, multiple-transmitter designs can significantly mitigate the absorption and scattering process due to in-suspension particles, which is of particular importance in turbid underwater environments. In the case of a transmission scheme that allows for the use of multiple light sources simultaneously, an increase in the number of optical emitters results in an increase in the received optical power, which obviously enables the system to support longer link distances and achieve better performance under more turbid underwater scenarios. However, optical power constraints must be considered when designing an optical wireless transmitter, conforming to eye safety standards.

4.2.1 Eye safety considerations

Commercial OWC equipment are usually utilized in accordance with specific guidance provided by international committees for the safe use of laser products and FSO communication systems [79]. In this thesis, we assume the text of the International Electrotechnical Commission IEC60825-1 [78].

For a given LD beam, the maximum allowed average optical power is derived from the maximum permissible exposure (MPE), which is the level of laser radiation to which, under normal circumstances, persons can be exposed without suffering adverse effects. According to [78, Table 10], the values of MPEs in the range of 400 nm to 1400 nm are measured

over a $\phi_p = 7$ mm diameter aperture at a minimum distance of 100 mm ¹. For illustrative purposes, Fig. 4.1 depicts a scenario with two divergent LD sources separated by a distance of d_t and transmitting towards an eye located at a distance of 100 mm. As can be observed, the eye subtends only a single emitter because the pupil is exposed to only one light beam due to the distance between both LDs. Following a brief geometrical analysis, the minimum distance between emitters that ensures the aforementioned condition can be calculated as a function of the aperture dimension and the beam width of the laser beam at the measurement distance. The minimum distance between emitters is obtained as follows

$$d_{t_{\min}} = \phi_p + w_{\text{MPE}}, \quad (4.1)$$

where w_{MPE} is the beam width at 100 mm. The beam width can be approximated as $w_{\text{MPE}} \approx \theta \cdot 0.1$, where θ is the LD divergence angle in radians. Here, we assume a divergence angle of $\theta = 12$ mrad, so that $d_t \geq 8.2$ mm to ensure the eye safety under a *per-source* power constraint.

This new approach for MISO systems, where multiple LDs are transmitted simultaneously at a distance d_t from each other, guarantees that the eye safety constraint is satisfied at any location, allowing the average power, P_t , to be imposed *per-source*. This is in marked contrast to conventional MISO schemes adopted in RF systems and theoretical FSO system performance in which the constraint is always imposed *per-transmitter*. The obtained distance between emitters condition in the order of millimeters represents a coherent and realistic physical limitation in commercial UOWC systems with similar circular arrangements of emitters, such as the Sonardyne BlueComm 200 [48]. Furthermore, it should be noted that this procedure has been employed in commercial terrestrial FSO systems such as SONAbeam transceivers but has not yet been analyzed in the existing literature of UOWC MISO systems [44].

4.3 System and channel models

4.3.1 Underwater channel model

The corresponding underwater channel is mathematically described by a composed channel gain which accurately models the impact of the oceanic losses due to the light propagation, L , and the fading induced by oceanic turbulence, H_o . Firstly, the oceanic path loss includes the effect of the absorption and scattering, as well as the geometric losses for an LD. As demonstrated [25], a complete formula to compute it is given by

$$L = A_0 \times e^{-\alpha \cdot c \cdot d}, \quad (4.2)$$

¹The aperture of 7 mm represents the maximum dilation of the pupil in a young eye, and the 100 mm measurement distance corresponds to the shortest accommodation distance of the human eye [78].

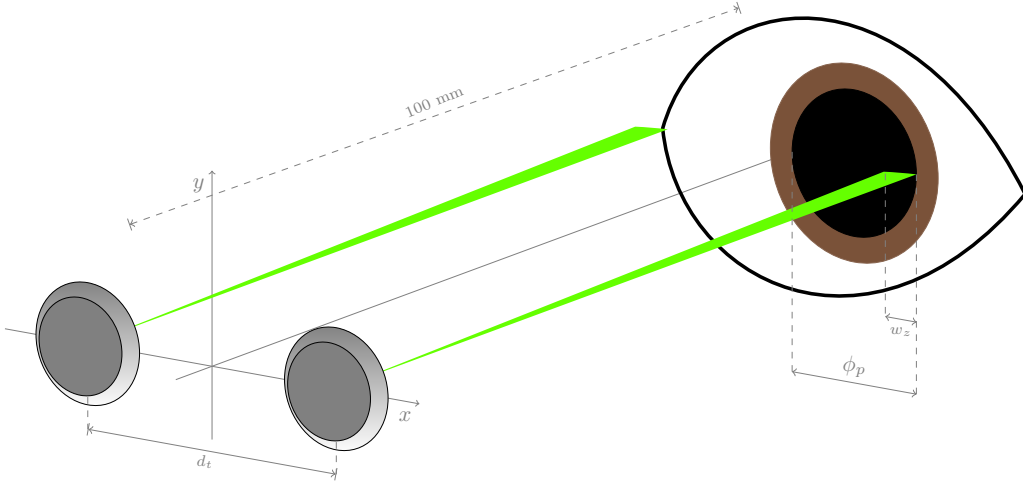


Figure 4.1: Geometric representation of a MISO system that guarantees the eye safety regulations when two emitters are simultaneously operating under a *per-source* power constraint.

where $A_0 = \left(\operatorname{erf} \left[\frac{\sqrt{\pi}}{\sqrt{2w_z}} \right] \right)^2$ is the fraction of the Gaussian beam geometric losses, $\bar{w}_z = w_z/a_r$ is the normalized beam width, a_r is the receiver radius, $\operatorname{erf}[\cdot]$ is the error function, α is a correcting factor in order to consider true received power due to scattering, and c is the extinction coefficient of the water [25, 179].

Secondly, as proposed in Chapter 2, the oceanic turbulence is statistically modeled using the Weibull probability distribution due to its high accuracy for different levels of salinity-induced oceanic turbulence in experimental measurement data [131]. The PDF of the considered turbulence-induced fading effect is presented in Eq. (2.31) as follows

$$f_{H_o}(h) = \frac{\beta_1}{\beta_2} \left(\frac{h}{\beta_2} \right)^{\beta_1 - 1} \times e^{-\left(\frac{h}{\beta_2} \right)^{\beta_1}}, \quad h \geq 0. \quad (4.3)$$

As mentioned in Chapter 2, to facilitate the analysis of fluctuations caused by oceanic turbulence, the PDF is normalized with respect to its mean value, i.e., $\mathbb{E}[H_o] = 1$, where $\mathbb{E}[H_o]$ is obtained in Eq. (2.32a). In this way, the Weibull parameters can be related as follows

$$\beta_2 = \frac{1}{\Gamma\left(1 + \frac{1}{\beta_1}\right)}. \quad (4.4)$$

Hence, β_1 can be approximated from the scintillation index $\sigma_{H_o}^2$ obtained in Eq. (2.32b) as in [141] as follows

$$\beta_1 \simeq (\sigma_{H_o}^2)^{-6/11}. \quad (4.5)$$

where σ_{H_o} is the scintillation index related to the oceanic turbulence-induced fading obtained in Eq. (2.30). However, Eq. (2.30) might be mathematically intractable. Therefore,

Table 4.1: Values of fitted parameters of Eq. (4.6) for different strengths of oceanic turbulence.

w	λ_1	λ_2	λ_3	λ_3
-1	6.54×10^{-6}	8.21×10^{-9}	-1.13×10^{-7}	2.34×10^{-7}
-3	2.9×10^{-6}	3.64×10^{-9}	-5.01×10^{-8}	1.04×10^{-8}

Table 4.2: Numerical values of oceanic turbulence parameters.

Parameter	Value
Dissipation of turbulent kinetic energy (ϵ)	$10^{-6} \text{ m}^2/\text{s}^3$
Dissipation of temperature (χ_T)	$10^{-4} \text{ K}^2/\text{s}$
Kolmogorov length scale (η)	10^{-3} m
A_T	1.863×10^{-2}
A_S	1.9×10^{-4}
A_{TS}	9.41×10^{-3}

the turbulence-induced fading scintillation index is approximated as a function of the link distance through polynomial interpolation given by [141] as follows

$$\sigma_{H_o}^2(d) \simeq \lambda_1 d^3 + \lambda_2 d^2 + \lambda_3 d + \lambda_4, \quad (4.6)$$

where $\lambda_1, \lambda_2, \lambda_3$ are computed via curve adjustment. In order to analyze different oceanic turbulence scenarios, several values of $\lambda_1, \lambda_2, \lambda_3$ are summarized in Table 4.1 for different temperature-salinity balance parameter w values within the interval $[-5, 0]$ and a receiver aperture of 10 cm, i.e., $D = 0.1$. The rest of the considered oceanic turbulence parameters are summarized in Table 4.2. In Fig. 4.2, the proposed fitted function of Eq. (4.6) is presented alongside the numerical results of Eq. (2.30) obtained using Monte Carlo simulations with the help of mathematical software packages such as Wolfram Mathematica. As observed, the proposed analytical fitting closely approximates the numerically obtained values within the distance range considered in this chapter, which represents a realistic interval for the various types of water analyzed.

4.3.2 Proposed MISO system models

Consider a MISO communication structure with an array of M laser diodes equally spaced a distance d_t on a circular arrangement at the transmitter and a single aperture of diameter D at the receiver separated by a link span of d , as illustrated by Fig. 4.3. IM/DD technique is assumed at the transmitter and receiver sides, respectively.

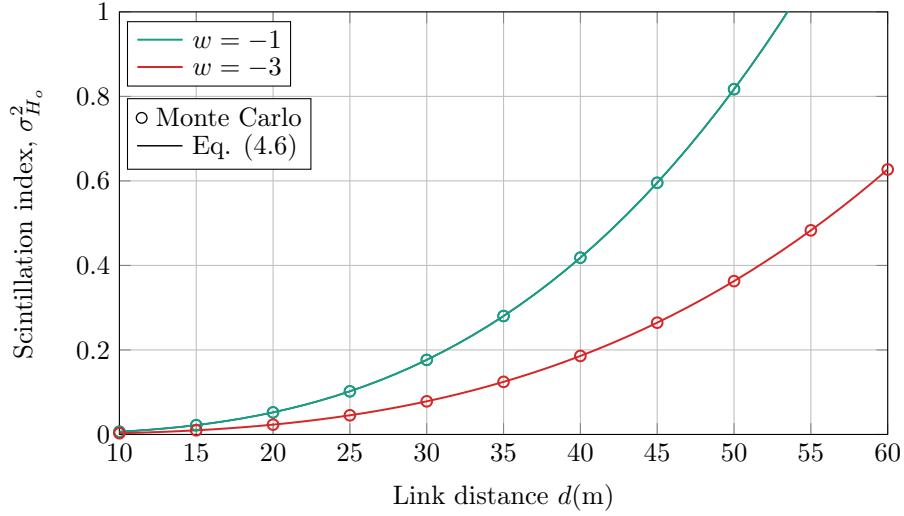


Figure 4.2: Scintillation index fitted function of Eq. (4.6) as a function of the link distance for different temperature-salinity ratios.

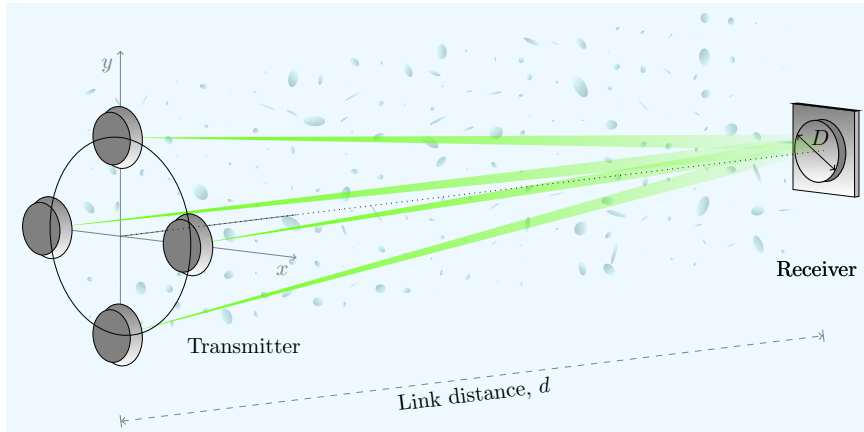


Figure 4.3: Diagram of the proposed underwater MISO system.

Before starting the analysis, it must be highlighted that we assume that d_t is larger than the spatial coherence radius of the oceanic turbulence, which is on the order of millimeters in the considered scenarios [180]. This condition also ensures the eye safety constraint for MISO systems that considers a *per-source* power constraint, as stated in Section 4.2.1. Hence, uncorrelated fading due to oceanic turbulence can be considered at the receiver. Furthermore, the underwater losses L can be considered identical for all emitters due to the ratio between d_t and the link distance.

Next, the mathematical models of SRC and TLS systems are derived in terms of the proposed channel attenuation model and the salinity-induced oceanic turbulence.

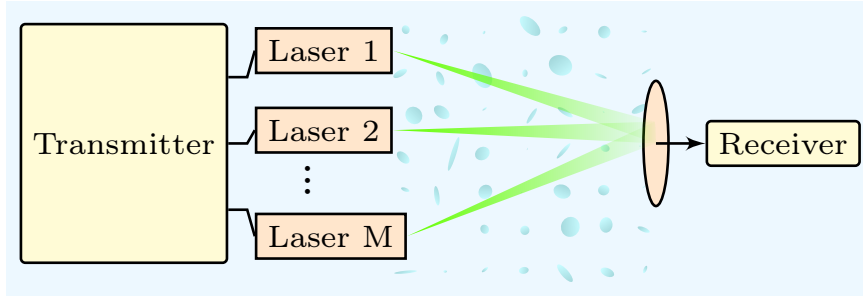


Figure 4.4: Block diagram of the proposed SRC system.

Spatial repetition coding

As illustrated in Fig. 4.4, a SRC scheme exploits the spatial redundancy by transmitting simultaneously through different independent fading channels. Traditionally, RF systems are subject to an average power constraint *per-transmitter*, i.e., a sum power constraint, due to safety radiation regulations [181]. However, by employing an appropriate transmitter design, the typical average power constraint *per-transmitter* can be adapted to increase the total emitted optical power and mitigate the severe impact of the absorption and scattering on UOWC systems in order to achieve higher performance by satisfying a *per-source* power constraint. Considering a suitable transmitter structure under the design assumption presented in Fig. 4.1, the photocurrent at the receiver for the proposed SRC system can be expressed as follows

$$y = x \frac{\rho}{M} \cdot L \cdot R \cdot \underbrace{\sum_{i=1}^M H_{o_i}}_{H_{\text{SRC}}} + z, \quad (4.7)$$

where $1 \leq \rho \leq M$, M is the total number of LD sources, x is the LD optical intensity, R is the photodetector responsivity which is assumed to be the unity, and H_{o_i} is the optical intensity fluctuation through the optical path between the i -th transmit LD source and the receiver. The noise at the receiver, z , is modeled as a statistically independent additive white Gaussian random process which is characterized by a variance $N_0/2$ and a zero mean.

Unlike current UOWC MISO literature, the proposed system allows for adjustment between a *per-source* power constraint and a *per-transmitter* power constraint by adjusting the value of the parameter ρ . Specifically, in the scenario where $\rho = 1$, the optical intensity at each source is restricted such that it is divided by the total number of LD sources, resulting in a transmitted optical intensity of $x \cdot \frac{1}{M}$. This configuration assumes an average power constraint *per-transmitter*. Conversely, when $\rho = M$, each LD operates at its maximum optical intensity, resulting in a transmitted optical intensity of $x \cdot \frac{M}{M} = x$, representing a power constraint *per-source*. Hence, the proposed SRC scheme can reduce the negative effect of

absorption and scattering as the leading adverse factor in hostile maritime environments by using the maximum power of each source when a power constraint *per-source* is considered. In this case, the resulting total transmitted optical power is $M \cdot P_t$, by increasing the maximum optical power with respect to the common approaches in theoretical analysis of SRC systems based on a power constraint *per-transmitter* considered in the literature. Furthermore, this approach also allows the transmitter to optimize the emitted power by modifying the value of ρ considering the inherent energy limitations of ROVs, or AUVs that are typically powered by batteries.

Regarding the closed-form of the composite PDF of $H_{\text{SRC}} = \sum_{i=1}^M H_{o_i}$, while an accurate similar PDF was obtained in [182] as an infinite summation, this form is not tractable for the performance analysis of SRC schemes in terms of the channel parameters, such as the severity of the oceanic turbulence and the link distance. In order to address this inconvenience, the Weibull PDF in Eq. (2.31) can be approximated by a more tractable single polynomial term using the Taylor expansion, such as $f_{H_o}(h) \doteq \frac{\beta_1}{\beta_2} \left(\frac{h}{\beta_2}\right)^{\beta_1-1}$. By assuming independent and identically distributed fading channels, the asymptotic PDF $f_{H_{\text{SRC}}}(h)$ can be obtained by using the moment generating function (MGF) and the Inverse Laplace Transform, which are fundamental statistical tools in the analysis of the distribution of sums of independent random variables [155]. Considering independent and identically distributed Weibull fading channels, the MGF of H_{SRC} can be expressed as follows

$$M_{H_{\text{SRC}}}(t) = \mathbb{E}[e^{t \cdot H_{\text{SRC}}}] = \mathbb{E}[e^{t \cdot \sum_{i=1}^M H_{o_i}}] = \mathbb{E}[e^{t \cdot H_{o_1}}] \cdot \mathbb{E}[e^{t \cdot H_{o_2}}] \cdots \mathbb{E}[e^{t \cdot H_{o_M}}]. \quad (4.8)$$

Based on the asymptotic behavior of the Weibull distribution, the MGF of H_{SRC} can be found as follows

$$M_{H_{\text{SRC}}}(t) \doteq \left(\frac{\beta_1 \Gamma(\beta_1)}{\beta_2^{\beta_1}} (-t)^{-\beta_1} \right)^M. \quad (4.9)$$

Then, since the MGF is the Laplace transform of the PDF with argument reversed in sign, i.e., $\mathcal{L}_Z(s) = M_z(-t)$, the asymptotic PDF of H_{SRC} can be obtained via inverse Laplace transform as follows

$$f_{H_{\text{SRC}}}(h) \doteq \mathcal{L}^{-1} \left[\left(\frac{\beta_1 \Gamma(\beta_1)}{\beta_2^{\beta_1}} s^{-\beta_1} \right)^M \right] = \left(\frac{\beta_1 \Gamma(\beta_1)}{\beta_2^{\beta_1}} \right)^M \frac{h^{M\beta_1-1}}{\Gamma(M\beta_1)}. \quad (4.10)$$

Generalized transmit laser selection

As previously stated, some optical MISO systems combat the effects of fading by employing selection diversity at the transmitter side, a technique known as TLS. A common TLS scheme with M emitters is depicted in Fig. 4.5. As can be observed, a TLS scheme transmits by utilizing a single light source at a given time instant, while the remaining sources remain idle. Considering perfect CSIT, the transmitter selects the channel with the highest received instantaneous SNR, i.e., the optical path with a greater value of scintillation.

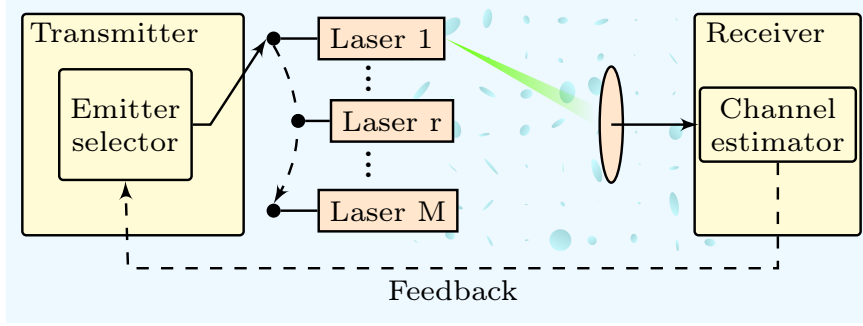


Figure 4.5: Block diagram of the proposed TLS system.

Hence, the TLS scheme can be rewritten as a SISO system where the gain channel is given by $H_{\text{TLS}} = L \cdot \max(H_{o_1}, \dots, H_{o_M})$. Since fading channels are assumed statistically independent, we can easily derive the CDF of H_{TLS} as $F_{H_{\text{TLS}}}(h) = [F_{H_o}(h)]^M$ [172, 183]. Hence, the PDF is obtained as $f_{H_{\text{TLS}}}(h) = M f_{H_o}(h) [F_{H_o}(h)]^{M-1}$ as follows

$$f_{H_{\text{TLS}}}(h) = \frac{M\beta_1}{\beta_2^{\beta_1}} h^{\beta_1-1} \sum_{k=0}^{M-1} (-1)^k \binom{M-1}{k} \left(e^{-\left(\frac{h}{\beta_2}\right)^{\beta_1}} \right)^{k+1}. \quad (4.11)$$

In practice, due to imperfect CSI knowledge, the transmitter eventually transmits with an LD from a set of available options. However, according to the existing UOWC literature, to the best of our knowledge, there is no work on realistic implementation of a TLS system in an underwater setting. In this regard, we consider imperfect CSI knowledge at the transmitter due to errors in the feedback link and/or outdated CSI.

From the perspective of the TLS system model illustrated in Fig. 4.5, a generalization of TLS scheme can be accomplished by considering that the transmitter selects the r -th smallest channel gain, where $1 \leq r \leq M$ and $r \in \mathbb{N}$. In this sense, the largest order statistic is represented by the M -th smallest channel gain. Consequently, the channel gains associated with each light emitter can be arranged in ascending order as $H_{o_1} < H_{o_2} < \dots < H_{o_M}$. Hence, the ideal TLS scheme is modeled as $r = M$, i.e., the channel with the largest gain is always selected. The PDF of H_o given the r -th smallest channel gain can be described as follows [183, Eq. (2.1.3)]

$$f_{H_{o_r}}(h | r) = \frac{M!}{(r-1)!(M-r)!} \frac{\beta_1}{\beta_2^{\beta_1}} h^{\beta_1-1} \times \sum_{k=0}^{r-1} (-1)^k \binom{r-1}{k} \left(e^{-\left(\frac{h}{\beta_2}\right)^{\beta_1}} \right)^{(k+1+M-r)}. \quad (4.12)$$

In order to shed light on what channel parameters determine the generalized TLS performance, we also obtain an asymptotic expression from the Taylor expansion of $f_{H_{o_r}}(h | r)$ as

follows

$$f_{H_{or}}(h | r) \doteq \frac{M!}{(r-1)!(M-r)!} \frac{\beta_1}{\beta_2^{r\beta_1}} \times \sum_{k=0}^{M-r} (-1)^k \binom{M-r}{k} \frac{1}{\beta_2^{k\beta_1}} h^{\beta_1(r+k)-1}. \quad (4.13)$$

Previous studies on GTLS UOWC schemes have utilized expressions similar to those derived in Eq. (4.12) for different PDFs which represent the stochastic fluctuations of the underwater channel [57,58]. These works have analyzed the performance in a GTLS system by evaluating the performance of the system based on the PDF in Eq. (4.12) for different values of r . However, these analyses do not account for a dynamic and realistic scenario where the transmitter intermittently has access to CSI and selects the light emitter with the highest channel gain based on a probabilistic success rate. To model a realistic scenario, we consider the possibility of random incorrect channel selections due to the degradation in the feedback channel or outdated CSI at the transmitter. Hence, r can be modeled as a discrete random variable that indicates the channel through which the GTLS system will transmit at each instant.

Upon initial examination, the behavior of the random variable r is not fully known beyond the fact that it is a non-negative discrete random variable with a finite number of probability mass points and a mean denoted as $\mathbb{E}[r]$. Moreover, it is known that the mean of this variable is related to the CSI. Specifically, if $\mathbb{E}[r] \rightarrow M$, it indicates that the GTLS system tends to select the light emitter with the highest channel gain, i.e., the CSIT is nearly perfect in the majority of instances. Conversely, it is reasonable to assume that if the transmitter has no channel information, it will select a light emitter with equal probability among all available emitters. In this case, r behaves as a uniformly distributed random variable with a mean given by $\frac{1}{M} \sum_{i=1}^M r_i$ [184]. Therefore, the degree of CSIT knowledge, that is, the accuracy of the CSI at the transmitter, can be determined from the mean of r .

According to the principle of maximum entropy, if there is no knowledge about the random variable r except the mean and non-negative constraints, the distribution of r , i.e., $f_r(r)$, should be a geometric distribution due to the fact that presents the maximum entropy under these constraints [185–187]. To the best of our knowledge, this approach has not yet been considered in OWC systems. As a result, the probability of selecting the r -th smallest channel gain can be calculated as follows

$$f_r(r) = \frac{e^{l \cdot r}}{\sum_{i=1}^M e^{l \cdot i}}, \quad (4.14)$$

where l is the growth constant. It should be noted that the normalization of the exponential ensures $\sum_{r=1}^M f_r(r) = 1$. Furthermore, although the simplicity of the exponential function, the inherent flexibility and versatility of the exponential function allows us to model a wide range of scenarios involving imperfect CSI at the transmitter with the help of a growth constant. On the one hand, scenarios where the CSI is rarely outdated at the transmitter and obtains a high likelihood of success are associated with a larger growth constant due to

the probability increases by a factor e . On the contrary, scenarios where the CSI is commonly outdated or unknown at the transmitter are described with a lower growth constant due to the fact that the whole of emitters presents a similar probability of being selected. A useful perspective is to consider a success probability p_M as the probability of selecting the best channel gain, i.e., the probability of $r = M$. We define the growth parameter l from a success probability p_M by performing the inversion of Eq. (4.14) when $r = M$. This can be numerically accomplished with the help of mathematical software packages such as Wolfram Mathematica. This correlation between the growth parameter and the success probability provides novel and valuable insights into the characteristics and implications of the CSI at the transmitter in the system performance. In Fig. 4.6, the proposed approach is computed for different success probabilities of obtaining a perfect CSI at the transmitter. As can be observed, our novel approach encompasses a spectrum of scenarios, covering the entire range between the two extreme cases. In the worst case of imperfect CSI, which is equivalent to an absence of CSI, the transmitter uniformly selects an emitter, i.e., $p_M = \frac{1}{M}$, which is described by $l = 0$. Otherwise, the case of having always perfect CSI at the transmitter (best case), i.e., $p_M = 100\%$, is described by $l \rightarrow \infty$. In practice, an l greater than 4.6 is enough to obtain a $p_M \geq 99\%$, as shown in Fig. 4.6. As mentioned above, $\mathbb{E}[r]$, p_M and l provide the same information regarding the CSI at the transmitter. However, for the reader's convenience, throughout the remainder of the chapter, only the probability of selecting the best channel gain p_M will be used. Hence, the PDF of the proposed GTLS with imperfect CSIT can be obtained by averaging Eq. (4.14) in Eq. (4.12) as follows

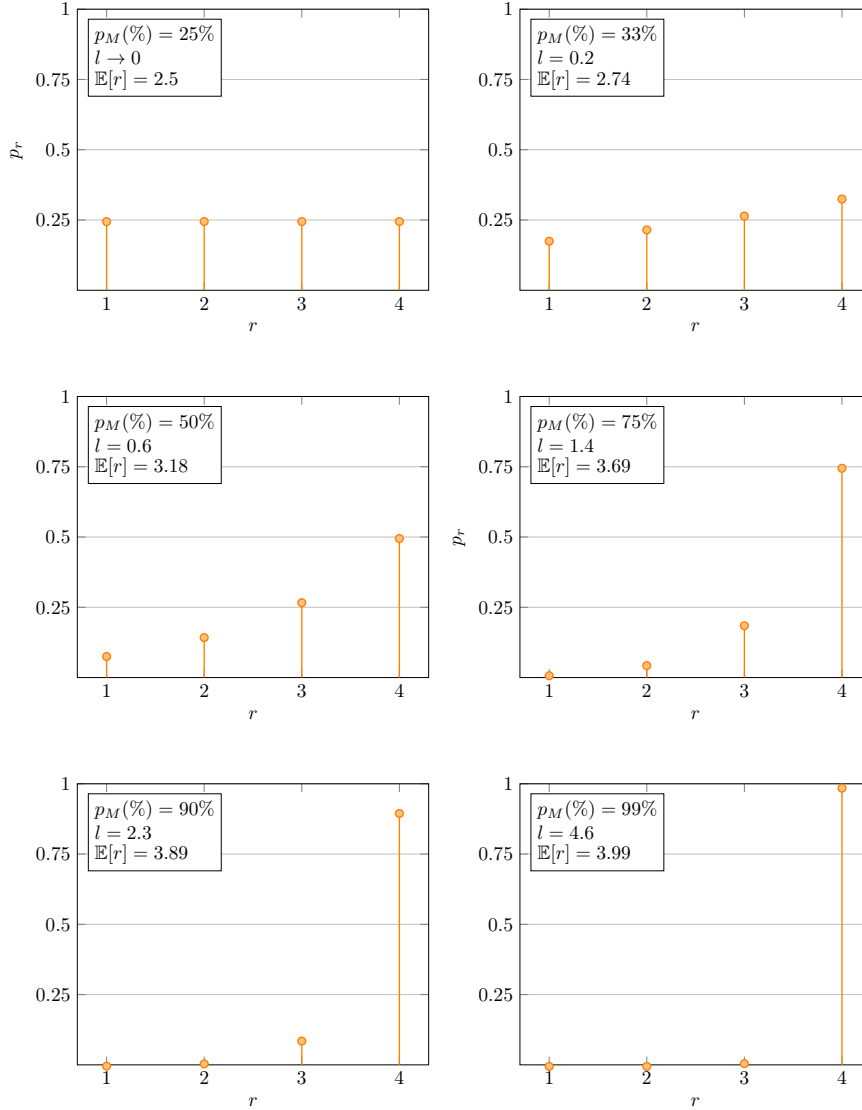
$$f_{H_{\text{GTLS}}}(h) = \sum_{r=1}^M f_r(r) \cdot f_{H_{o_r}}(h | r). \quad (4.15)$$

4.4 Performance analysis

In this section, the performance of both proposed MISO UOWC systems in terms of BER is analyzed when considering the underwater channel model described in Section 4.3, which accounts for the effect of the absorption and scattering and the geometric losses for an LD as well as salinity-induced turbulence effects.

Firstly, we consider IM/DD using OOK modulation. It is assumed that the CSI is perfectly known at the receiver. As stated in Eq. 2.44, the conditional average BER of a SISO for the case of equally likely transmitted symbols in the presence of oceanic turbulence and absorption and scattering is calculated as follows

$$P_b = \int_0^{\infty} Q(\sqrt{2}\gamma \cdot L \cdot h) \cdot f_{H_o}(h) dh. \quad (4.16)$$

Figure 4.6: Probability mass function of r with 4 laser sources.

4.4.1 Spatial repetition coding performance

The corresponding average BER of a MISO UOWC system with SRC scheme can be calculated as

$$P_{b\text{SRC}} = \underbrace{\int_0^\infty \cdots \int_0^\infty}_M Q \left(\sqrt{2\gamma} \cdot \frac{\rho L}{M} \sum_{i=1}^M h_i \right) \prod_{i=1}^M f_{H_o}(h_i) dh_i. \quad (4.17)$$

Unfortunately, as far as we know, Eq. (4.17) is mathematically intractable. Hence, the asymptotic average BER solution at high SNR can be derived by using Eq. (4.10) to gain

novel insights into the dominant factors that impact on the average BER performance when using the SRC system. As described in Section 2.4.1, the average BER behaves asymptotically as $P_b \doteq (G_c \gamma)^{-G_d}$ [135]. Hence, by substituting Eq. (4.10) into Eq. (4.17), a closed-form asymptotic expression can be easily derived as follows

$$P_{b_{\text{SRC}}} \doteq \frac{\left(\beta_1 \left(\frac{\beta_2 L \rho}{M} \right)^{-\beta_1} \Gamma(\beta_1) \right)^M}{2^{1+M\beta_1} \Gamma\left(\frac{M\beta_1}{2} + 1\right)} \gamma^{-\frac{\beta_1}{2}M}. \quad (4.18)$$

4.4.2 Generalized transmit laser selection performance

The corresponding average BER of the MISO UOWC channel with a GTLS scheme can be estimated as

$$P_{b_{\text{TLS}}} = \int_0^\infty Q\left(\sqrt{2\gamma} \cdot L \cdot h\right) f_{H_{or}}(h | r) dh. \quad (4.19)$$

By substituting Eq. (4.12) into Eq. (4.19) and using [158, Eq. (07.34.21.0012.01)] (see Appendix A.5) and [188, Eq. (8.4.14.1)] (see Appendix A.3.1), the average BER performance of a TLS system, which transmits through the r -th smallest channel gain, is obtained as follows

$$P_{b_{\text{TLS}}}(r) = \frac{\beta_1 M!}{(r-1)!(M-r)!} \frac{\sum_{k=0}^{r-1} (-1)^k \binom{r-1}{k}}{4\sqrt{\pi} (\beta_2 L \sqrt{\gamma})^{\beta_1}} \times H_{2,2}^{1,2} \left(\frac{k+M-r+1}{(\sqrt{\gamma} L \beta_2)^{\beta_1}} \middle| \begin{matrix} \left(\frac{1-\beta_1}{2}, \frac{\beta_1}{2}\right), \left(1 - \frac{\beta_1}{2}, \frac{\beta_1}{2}\right) \\ (0, 1), \left(\frac{-\beta_1}{2}, \frac{\beta_1}{2}\right) \end{matrix} \right). \quad (4.20)$$

Similarly to the SRC scheme, the corresponding asymptotic solution is calculated by replacing Eq. (4.13) into Eq. (4.19) as

$$P_{b_{\text{TLS}}}(r) \doteq \frac{M!}{r!(M-r)!} \frac{\Gamma\left(\frac{1}{2}(r\beta_1 + 1)\right)}{2\sqrt{\pi} (\beta_2 L)^{r\beta_1}} \gamma^{-\frac{\beta_1}{2}r}. \quad (4.21)$$

Based on the approach proposed in Eq. (4.14), the average BER performance of a GTLS system can be expressed as a function of the growth parameter l by averaging in r as follows

$$P_{b_{\text{GTLS}}} = \sum_{r=1}^M f_r(r) \cdot P_{b_{\text{TLS}}}(r). \quad (4.22)$$

In the same way, the asymptotic average BER performance of a GTLS system can be calculated by substituting the asymptotic expression of $P_{b_{\text{TLS}}}$ proposed in Eq. (4.21) into Eq. (4.22).

Table 4.3: UOWC system and channel parameters.

Parameter	Value
Wavelength	532 nm
LD divergence angle (θ)	12 mrad
Photodetector responsivity (R)	1
Photodetector surface diameter (D)	10 cm
Photodetector field-of-view	180°
Dissipation of turbulent kinetic energy (ϵ)	10^{-6} m ² /s ³
Dissipation of temperature (χ_T)	10^{-4} K ² /s
Kolmogorov length scale (η)	10^{-3} m
A_T	1.863×10^{-2}
A_S	1.9×10^{-4}
A_{TS}	9.41×10^{-3}

4.5 Numerical results and discussions

In this section, the performance in terms of average BER of the proposed MISO schemes under different configurations is evaluated in various realistic UOWC scenarios. Clear ocean and coastal water environments are considered to determine the benefits of these spatial diversity techniques under different scattering conditions. It is worth mentioning that harbor water scenarios have been excluded due to their high losses, which limit the maximum achievable distance to less than a few meters [25]. Therefore, we consider practical link spans such as $d = \{30, 40, 50\}$ m and $d = \{20, 30, 35\}$ m for clear ocean and coastal waters, respectively. Moreover, the oceanic turbulence parameters β_1 and β_2 are calculated via Eqs. (4.5) and (4.4), respectively. The scintillation index of Eq. (4.6) is computed for a salinity-balance parameter $w = \{-3, -1\}$. Additionally, average BER results of a SISO UOWC system are included in order to establish a baseline for comparison purposes. Monte Carlo simulation results up to 10^{-9} are included to verify the obtained expressions. The number of bits used in our simulations is 10^{10} to ensure precision in the Monte Carlo simulator [136]. The remainder of the configuration parameters are summarized in Table 4.3.

4.5.1 Impact of power constraint in SRC schemes

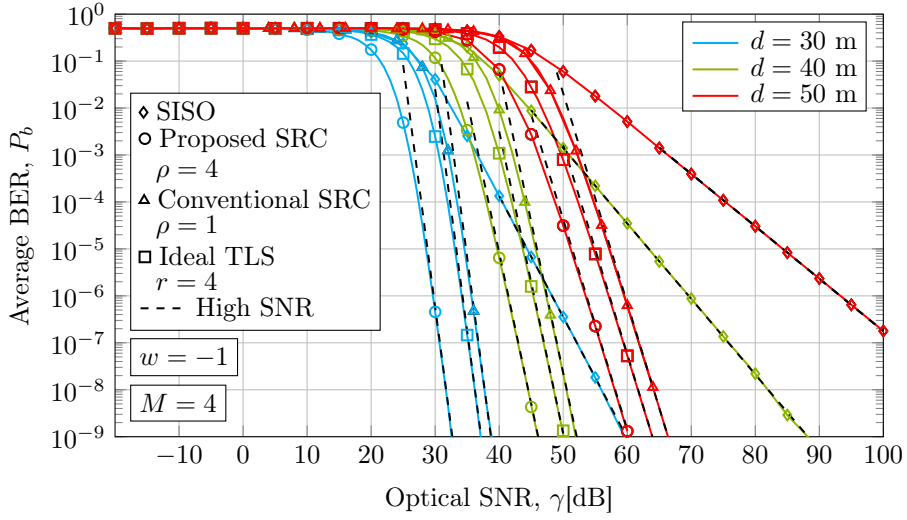
In Fig. 4.7, the average BER performance of the proposed SRC scheme when considering a *per-source* power constraint and $M = 4$ laser sources is compared with a conventional SRC scheme with a *per-transmitter* power constraint, an ideal TLS scheme, and a SISO scheme. The salinity-balance parameter $w = -1$ represents an hostile salinity-induced oceanic turbulence scenario.

Table 4.4: Values of scintillation index of Eq. (4.6) for different strengths of oceanic turbulence and link distances.

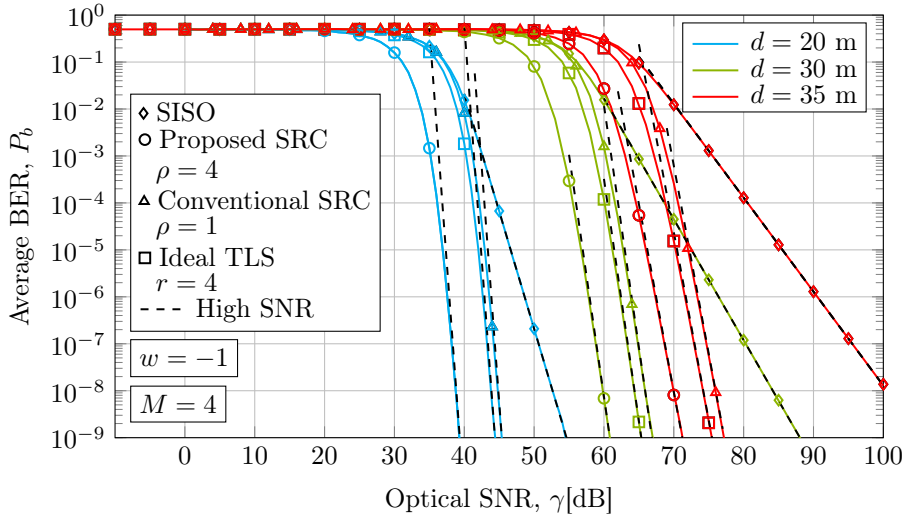
w	$d(\text{m})$	$\sigma_{H_o}^2$	w	$d(\text{m})$	$\sigma_{H_o}^2$
-1	20	0.05	-3	20	0.02
-1	30	0.18	-3	30	0.08
-1	35	0.28	-3	35	0.12
-1	40	0.42	-3	40	0.19
-1	50	0.82	-3	50	0.36

The proposed SRC scheme is applied in order to increase the total emitted optical power, so each LD source transmits an optical power of P_t , i.e., the maximum permissible average optical power, under the transmitter design assumption of Eq. (4.1). Mathematically, the average BER of the proposed SRC system is computed via Eq. (4.18) when $\rho = M$, while the average BER of an SRC under a *per-transmitter* power constraint is computed via Eq. (4.18) when $\rho = 1$. The comparison of both SRC schemes is based on the number of sources and the maximum transmitted optical power by each of them. The ideal TLS scheme is computed via Eq. (4.20) when $r = M$, i.e., with perfect CSIT during the transmission.

Firstly, as shown in Figs. 4.7(a), and 4.7(b), we demonstrate that the asymptotic expressions for average BER performance in Eqs. (4.18) and (4.21) for SRC and TLS systems, respectively, as well as the analytic BER performance expression for TLS scheme in Eq. (4.20), match closely with the Monte Carlo simulation results across the entire optical SNR regime. These results confirm the high accuracy of the proposed closed-form expressions in both clear ocean and coastal waters and different link distances. Secondly, it is important to mention the impact of path loss L on the overall performance. Despite the short range of the link, the high path loss in coastal water has a significant impact on the BER performance. In fact, at a link distance of $d = 30$ m and a SNR of 55 dB, the BER performance for a SISO system in clear ocean water is $P_b = 1.8 \times 10^{-8}$, while in coastal water is $P_b = 0.17$ when the same turbulence conditions are considered. Thus, it is remarked the dramatic impact of scattering, which represents the main impairment for UOWC links. In addition, the presented results illustrate that the proposed SRC technique under the *per-source* power constraint outperforms the ideal TLS scheme in both kinds of water, despite the unrealistic assumption of having perfect CSI knowledge at the transmitter. These results highlight for the first time the advantage of using the proposed SRC system over a TLS system due to the significant impact of scattering on the UOWC channel. This is because an SRC system properly designed according to Fig. 4.1 is capable of transmitting more optical power with the eye-safety constraint *per-source* by using the same number of transmitters sources, as illustrated in Eq. (4.7) when $\rho = M$. However, a conventional SRC system with *per-transmitter* power constraint, i.e., $\rho = 1$, obtains a higher BER than an ideal TLS system. At a link distance of $d = 30$ m and a SNR of 60 dB, the BER performance for the pro-



(a) Clear ocean water



(b) Coastal water

Figure 4.7: Average BER in UOWC links in clear ocean (a), and coastal waters (b), under oceanic turbulence, assuming a salinity-balance of $w = -1$ and several link distances when the SRC and GTLS schemes are used with 4 emitters when perfect CSIT is assumed.

posed SRC system in coastal water is reduced at $P_b = 7.5 \times 10^{-9}$, while in TLS scheme is $P_b = 1.19 \times 10^{-4}$ and in a conventional SRC system is $P_b = 0.012$.

As can be observed, SRC and TLS BER curves present asymptotically the same slope in a log-log scale, i.e., the same diversity order, G_d , at high SNR. Consequently, there is an horizontal gap in the abscissa-axis between the SRC and TLS BER curves, which represents the performance gain of using an SRC scheme. As shown in BER curves, as link distance

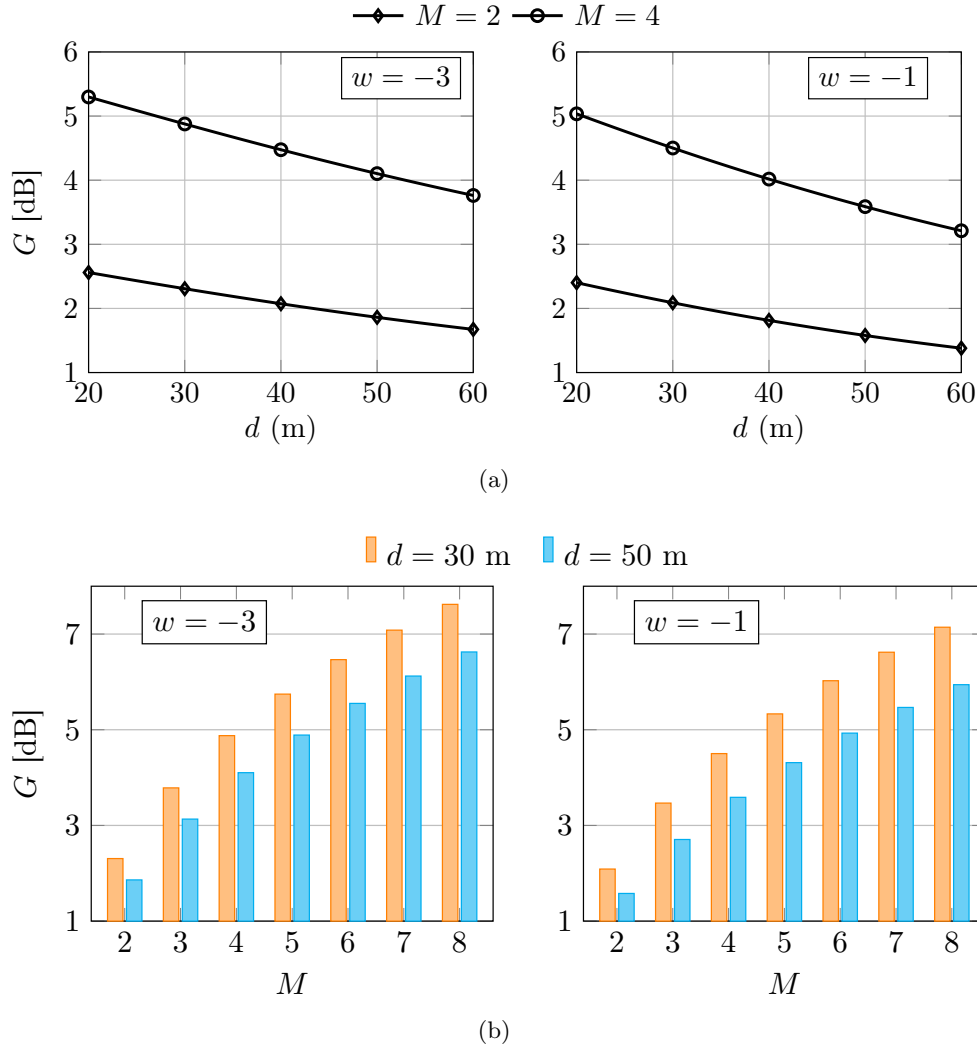


Figure 4.8: The gain G as a function of (a) the link span, and (b) the total number of transmitter sources M , assuming $\rho = M$ when different severity of oceanic turbulence are considered.

increases, the gap appears to diminish considerably. In order to gain further insight into the influence of the underwater channel on the performance for both schemes, the mathematical gain of the proposed SRC configuration compared to the TLS scheme can be calculated. This gap can be asymptotically obtained using Eq. (4.18) and (4.21) as follows

$$G = \frac{10}{M\beta_1} \log_{10} \left(\left(\frac{\rho}{M} \right)^{M\beta_1} \frac{\Gamma(1 + M\beta_1)}{\Gamma(1 + \beta_1)^M} \right). \quad (4.23)$$

In Fig. 4.8, the behavior of the optical gain is examined as a function of the link distance, and the number of light emitters. Firstly, in Fig. 4.8(a), the impact of the link distance on the gain of an SRC configuration relative to a TLS scheme is evaluated for different strengths of

turbulence based on the salinity-balance parameter w by assuming $w = \{-3, -1\}$ when 2 and 4 laser sources are considered. It can be observed that the coding gain of SRC with respect to TLS decreases, thereby demonstrating that the performance enhancement resulting from diversity techniques exhibits different behavior for the TLS and SRC schemes. Therefore, it can be inferred that the coding gain of the TLS scheme increases faster than the SRC coding gain as the link distance increases. These conclusions hold true for both salinity-balance parameters, corresponding to different oceanic turbulence channels. However, despite the fact that a TLS system tends to exhibit a better behavior than the SRC system at very long link distances, in none of the realistic analyzed scenarios does it manage to improve the coding gain of the proposed SRC system. Secondly, Fig. 4.8(b) highlights the advantage of using a larger number of light emitters in order to increase the total transmitted optical power. In this case, the performance enhancement of the SRC versus TLS is plotted as a function of the numbers of laser sources with a salinity-balance parameter of $w = \{-3, -1\}$ and a link distance $d = \{30, 50\}$ m. These results show an increase of the gain for SRC with respect to the TLS scheme as the number of emitters increases. By increasing the number of LDs, the proposed SRC scheme increases the total transmitted optical power by a factor M . In contrast, the TLS scheme primarily leverages the increased number of transmitters to better mitigate turbulence while maintaining a total transmitted optical power comparable to that of a SISO system. As mentioned before, this assertion maintains validity because the SRC system is designed according to Fig. 4.1. If the total emitted power of the source is subjected to a *per-transmitter* constraint, the SRC system would exhibit a higher BER than a TLS system. Unlike previous studies that neglect the importance of an appropriate transmitter structure design, our findings clearly illustrate that an alternative SRC system outperforms the TLS system in mitigating the dramatic underwater attenuation under realistic link distances and oceanic turbulence. Hence, in transmitter designs which allows for enough distance between sources and allows a *per-source* optical power constraint, the use of SRC emerges as the preferable option. Conversely, in situations characterized by compact transmitters mandating distance between sources constraints, it is recommended to use TLS schemes.

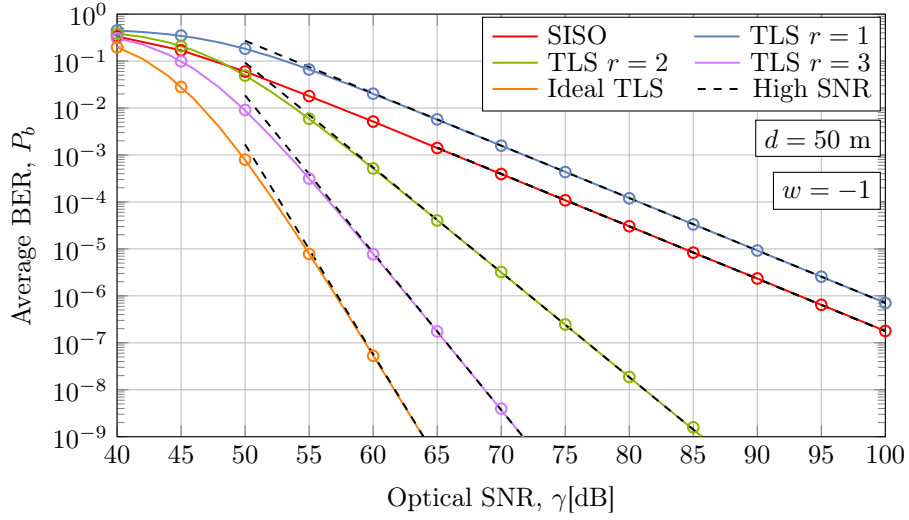
4.5.2 Impact of imperfect CSI in GTLS scheme

As stated in Section 4.3.2, a more realistic TLS scheme can be accomplished by considering that the transmitter randomly selects the r -th smallest channel gain, where $1 \leq r \leq M$, due to an imperfect or outdated CSIT.

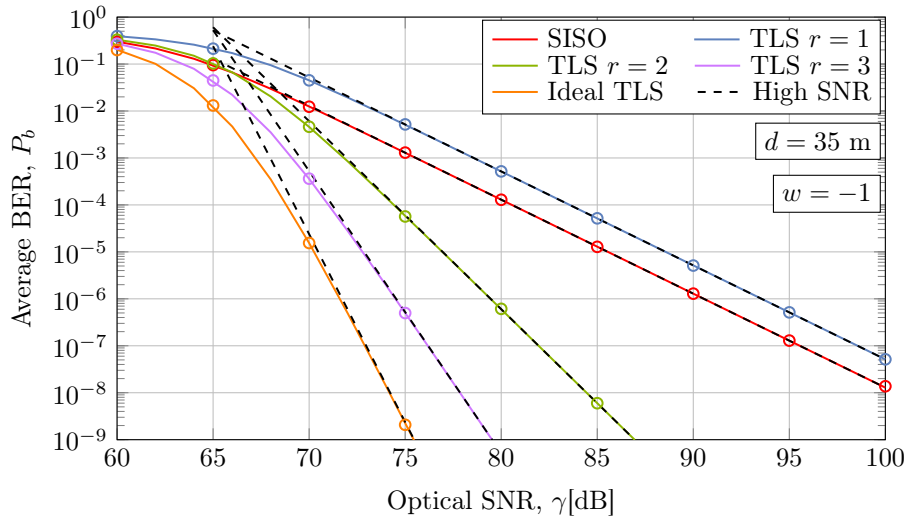
As a preliminary approach, we analyze the impact of selecting distinct transmitters during transmission on the performance of a TLS scheme in which the transmitter consistently selects the r -th smallest channel gain. Hence, the average BER of a TLS scheme that selects the r -th smallest channel gain is plotted in Figs. 4.9(a), and 4.9(b) for clear ocean and coastal waters, respectively. These results provide a lower and upper bounds for the

performance of a GTLS system which always selects the smallest channel gain and the best channel gain, respectively. It is essential to highlight that the average BER performance bounds in TLS systems has been studied in terrestrial FSO communication, but not in UOWC. Notably, the SISO system can provide better performance than a TLS configuration where the emitter selector always chooses the LD with the smallest fading coefficient in both types of water. In clear ocean water at a link distance of 50 m and an optical SNR of 60 dB, the UOWC SISO system achieves a BER of $P_b = 5.16 \times 10^{-3}$, while a TLS system with $r = 1$ achieves a BER performance of $P_b = 0.02$. By comparison, a TLS system with $r = 2$ achieves $P_b = 5 \times 10^{-4}$, a TLS system with $r = 3$ achieves $P_b = 7.8 \times 10^{-6}$, and an ideal TLS achieves $P_b = 5.3 \times 10^{-8}$.

After the comprehensive BER comparison above, we turn our attention to the performance of realistic and feasible TLS systems, in which the transmitter node randomly uses the LD with the r -th smallest channel gain due to imperfect CSI knowledge. As opposed to Figs. 4.9(a), and 4.9(b), where the transmitter consistently selects the r -th smallest channel gain due to imperfect CSI, the proposed generalization for the TLS scheme, i.e., the GTLS scheme, allows that the transmitter randomly transmits with an LD from a set of available options. Hence, in Figs. 4.10(a), and 4.10(b), we investigate more realistically the impact of potential errors in the emitter selector block on the average BER performance of a TLS system due to an imperfect CSI at the transmitter. We consider different scenarios for several probabilities of obtaining perfect CSI at the transmitter. Here, we show scenarios with a success probability of $p_M = \{50\%, 75\%, 90\%, 99\%\}$, which is defined in Eq. (4.14) when considering $r = M$. According to our results, the obtained BER results in Eq. (4.22), in both its analytical and asymptotic form, closely matches the Monte Carlo simulation results, validating the usefulness of these expressions. Furthermore, as anticipated, the performance of the GTLS system is highly susceptible to imperfection in the source selection process, despite the low probability of selecting incorrect laser sources. In order to achieve the forward-error-correction (FEC) threshold of 3.8×10^{-3} , the GTLS system with $p_M = 50\%$ requires an optical SNR of 56 dB when a link distance of 50 m and a salinity-balance parameter of $w = -1$ are considered in clear ocean water. This represents an improvement of only 4 dB compared to the 60 dB required for a SISO system under the same environmental conditions. As expected, as the probability of obtaining perfect CSI at the transmitter increases, the gain improvement becomes more significant, with improvements of 11 dB, 21 dB, and 29 dB computed for GTLS system with $p_M = 75\%$, $p_M = 90\%$, and $p_M = 99\%$, respectively. These results contribute significantly to exactly quantify the consequence of imperfect CSI at the transmitter in TLS systems, shedding light on the practical feasibility and performance limitations of such systems. Furthermore, the receiver can determine the degree of CSI knowledge at the transmitter by comparing the experimental BER of pilot signals with the theoretical BER. This capability can be particularly useful for optimizing the feedback link and dynamically enhancing the accuracy of the CSIT. Secondly, note that the diversity order, i.e., the asymptotic slope of the BER performance of GTLS systems, decreases as the SNR increases. Although the transmitter has a probability of obtaining the



(a) Clear ocean water



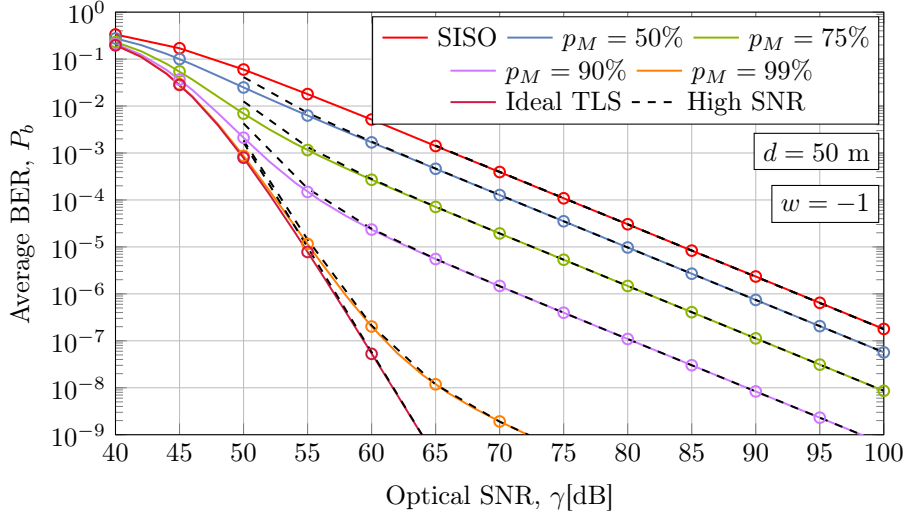
(b) Coastal water

Figure 4.9: Average BER in UOWC links in clear ocean (a), and coastal waters (b), under ocean turbulence, assuming a salinity-balance of $w = -1$ when an imperfect TLS scheme transmits through the r -th smallest channel gain.

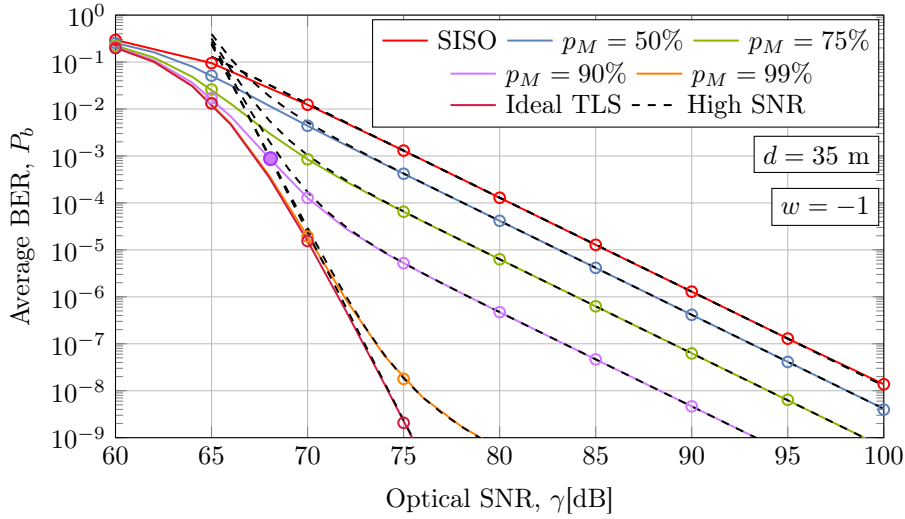
CSI exceeding 90%, the GTLS scheme exhibits a diversity order similar to that of a SISO system at high SNR.

To provide novel insights into the GTLS performance, we analyze the behavior of the diversity order as follows

$$G_d(l) = \frac{\partial P_{b\text{GTLS}}(l)}{\partial \gamma}. \quad (4.24)$$



(a) Clear ocean water



(b) Coastal water

Figure 4.10: Average BER in UOWC links in clear ocean (a), and coastal waters (b) when a GTLS scheme are used with 4 source lasers for several imperfect CSI at the transmitter scenarios, under salinity-induced turbulence with a salinity-balance of $w = -1$.

For the convenience of the reader, we do not include the non-tractable analytic expression due to its complexity. Asymptotically, we can also obtain a more tractable expression as follows

$$G_d(l) \doteq \frac{10^{\frac{\gamma}{5}} \beta_1}{2} \frac{\sum_{r=1}^M \frac{10^{-\frac{\gamma}{5}(1+\frac{r\beta_1}{2})} e^{l(r-1)} \Gamma(\frac{1}{2}(1+r\beta_1))}{(M-r)!(r-1)!(L\beta_2)^{r\beta_1}}}{\sum_{r=1}^M \frac{10^{-\frac{\gamma r\beta_1}{10}} e^{l(r-1)} \Gamma(\frac{1}{2}(1+r\beta_1))}{r!(M-r)!(L\beta_2)^{r\beta_1}}}. \quad (4.25)$$

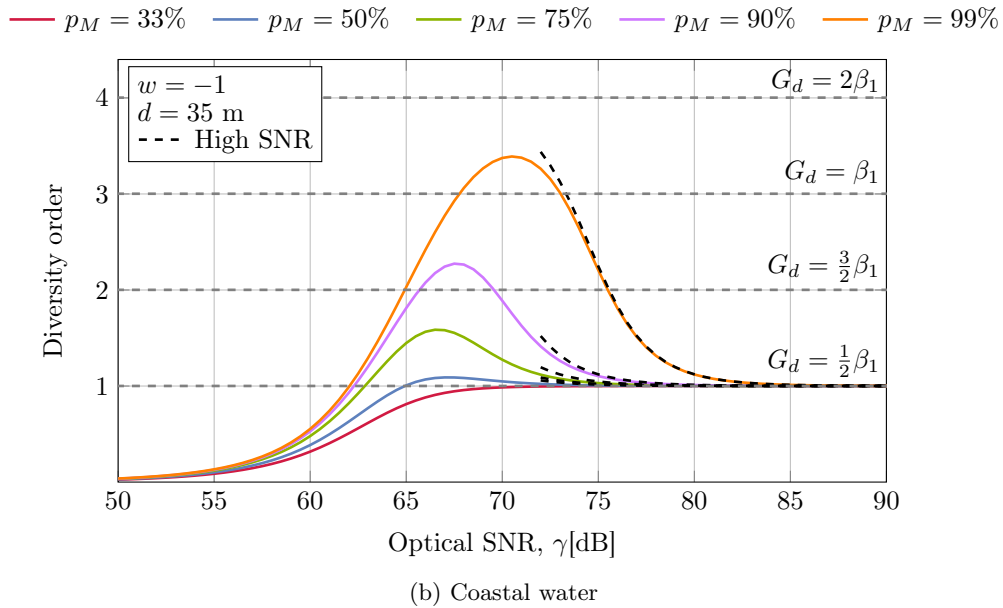
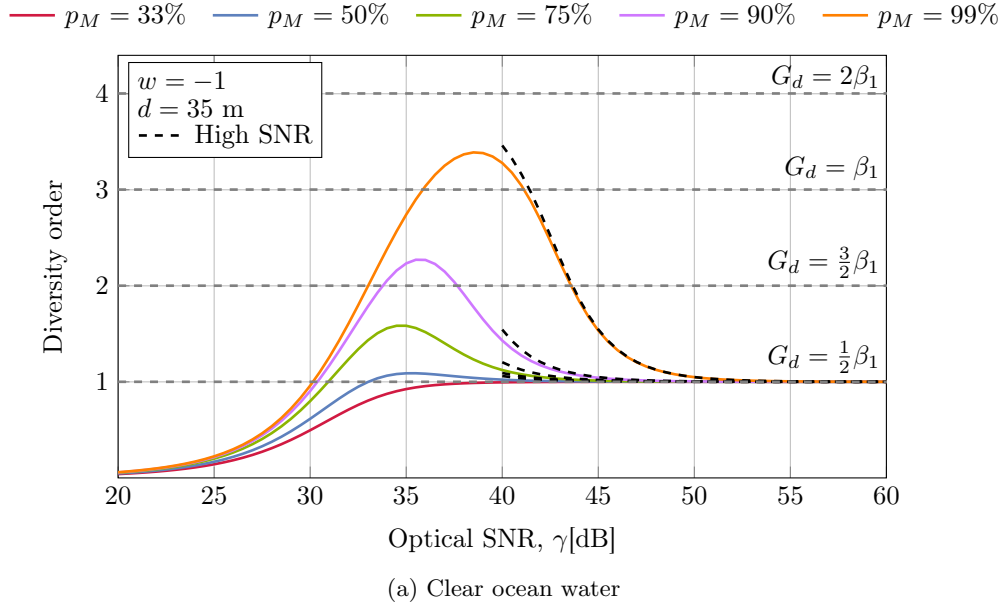


Figure 4.11: Diversity order of BER when a GTLS scheme are used with 4 source lasers for several imperfect CSI at the transmitter scenarios in clear ocean (a), and coastal waters (b), under salinity-induced turbulence, assuming a link distance of 35 m and a salinity-balance of $w = -1$.

Figs. 4.11(a), and 4.11(b) provide insights about the diversity order of the BER performance of the GTLS system with 4 laser sources for several probabilities of obtaining perfect CSI at the transmitter. We consider a salinity-balance parameter $w = -1$ and a link distance

of 35 m for clear ocean and coastal waters. As a reference, the diversity order of $P_{b_{\text{TLS}}}(r)$ in Eq. (4.21) is also plotted for $r = \{1, 2, 3, 4\}$. It should be noted that the asymptotic expression in Eq. (4.25) matches accurately with analytic results at high SNR in both kinds of water. Although the probability of obtaining a perfect CSI at the transmitter is 99%, the diversity order is far from what is obtained when a perfect TLS system is considered, i.e., $G_d = 2\beta_1$. For the first time, it can be concluded that the full diversity gain can not be achieved with a realistic TLS system when practical oceanic turbulence scenarios are supposed, even with a $p_M = 99\%$. Furthermore, the trend of the diversity order after the peak corroborates the results obtained in Figs. 4.10(a), and 4.10(b), where the slope of the imperfect GTLS tends to the SISO slope, i.e., $G_d = \beta_1/2$. As predicted in Fig. 4.10, the diversity order falls earlier when p_M is low. These results confirm that an imperfect TLS is susceptible to errors in the feedback link and outdated CSI at the transmitter. As can be seen, an additional SNR is required to achieve the same G_d diversity order in coastal water as in clear ocean water with the same oceanic turbulence, which is consistent with the previous results. The inflection point of the $p_M = 90\%$ scenario is achieved at 36 dB in clear ocean water, while the same peak is obtained at 68 dB. This point can be also observed in Fig. 4.10(b), where the purple circle indicates the maximum diversity order achieved for the $p_M = 90\%$ case in coastal water.

4.6 Summary

Spatial diversity techniques are commonly employed in OWC systems to mitigate the effect of turbulence-induced fading channels. In this chapter, novel MISO optical schemes are proposed to compensate for the effects of oceanic turbulence, as well as the inherent absorption and scattering in underwater environments. Two spatial diversity techniques at the transmitter have been examined: the SRC scheme, which implements spatial redundancy with the use of all the available emitters, and the TLS scheme, which transmits using solely the light source exhibiting the highest scintillation value. Both schemes are analyzed from a novel view of optical power constraints in MISO systems based on eye-safety regulations.

The proposed SRC technique incorporates a transmitter design with an appropriate emitter spacing in compact transceivers obtained from the divergence of the laser emitters and the international standard IEC60825-1, which ensures that an eye near the transmitter subtends only a single emitter. Regarding the TLS scheme, a generalized system model is proposed in order to consider an imperfect CSIT due to feedback link errors or outdated CSIT. In this way, the key contributions of the proposed MISO schemes are summarized as follows

- In contrast to previous SRC schemes described in the literature, the proposed SRC allows for adjustment under a *per-source* power constraint, thereby increasing the maximum optical power compared to conventional approaches, which typically as-

sume a power constraint *per-transmitter* in the theoretical analysis of SRC systems in terrestrial and underwater optical links.

- The developed SRC mathematical model can be used to optimize the total emitted power considering the energy limitations of battery-powered ROVs or AUVs.
- According to the principle of maximum entropy, a novel tractable exponential approach is presented for modeling random source selections in a TLS schemes based on the success probability of obtaining a perfect CSI at the transmitter.
- The proposed GTLS cover a wide range of imperfect or outdated CSIT scenarios by only modifying the success probability.

Thereafter, the average BER is studied for both developed SRC and GTLS system models over several underwater channel conditions in presence of Weibull oceanic turbulence and different types of waters, such as clear ocean and coastal waters. These findings offer novel insights for the underwater optics community. In this way, the key contributions and conclusions of this study are summarized as follows

- A new perspective on optical power constraints to consider a more reasonable adaptation of UOWC transceivers to turbid underwater environments in MISO systems.
- A novel asymptotic closed-form expression for the average BER of SRC UOWC systems over Weibull fading channels which allows for adjustment under a *per-source* and *per-transmitter* power constraint.
- The proposed SRC system under *per-source* power constraint outperforms the TLS system even when perfect CSI is assumed. This is due to the fact that the SRC system effectively reduces the negative impact of absorption and scattering by transmitting more optical power
- In underwater scenarios where the absorption and scattering effects represent the main impairment, such as coastal and harbor waters, a transmitter design that allows for sufficient distance between sources and a *per-source* optical power constraint makes the use of SRC the optimal choice.
- Analytic and asymptotic closed-form expressions for the average BER of GTLS UOWC systems over Weibull fading channels which consider imperfect CSIT by considering a certain success probability of obtaining perfect CSIT.
- TLS schemes are very susceptible to imperfect CSI at the transmitter side, showing similar diversity order to SISO at high SNR even with success probability of perfect CSIT above of 90%.

Chapter 5

Conclusions and Future Work

5.1 Conclusions

The complexity of the underwater environment highlights the need to develop channel models capable of accurately describing the phenomena associated with the water light propagation, taking into account water type and other fundamental characteristics. In this context, this thesis addresses the statistical modeling of various ocean light propagation impairments and their impact on the performance of UOWC systems under practical link configurations and realistic environmental conditions. Unlike previous UOWC system performance studies, this work focuses on the role of scattering as a main characteristic of an underwater optical channel, analyzing its various manifestations and its interplay with the rest of the oceanic effects, such as air bubbles and oceanic turbulence. Hence, all the considered performance metrics are evaluated under different turbidity levels, or types of waters. Finally, a performance comparison of two different MISO schemes has been addressed in the presence of oceanic turbulence under different types of waters. The most significant findings of this thesis are presented below.

One of the most significant challenges in underwater channel modeling is related to accurately derive empirical models derived from the experimental observations. In order to address this issue, in Chapter 3 an experimental UOWC test-bed is proposed and mounted to explore the impact of scattering in the presence of air bubbles and artificial water currents. The motivation for developing the test-bed is to emulate the underwater channel impairments on optical signal traversing it in a controlled environment. The proposed test-bed offers the advantage of repeatedly replicating several underwater conditions in a controlled manner without the need for a long observation period in complex and dynamic environment like the open sea. In the experimental setup, optical power fluctuations caused by partial and total light blockages due to air bubbles of different sizes and under varying water turbidity levels, are captured at the receiver. The scattering level, i.e., water turbidity, is modified

using a commercial antacid whose chemical components simulate the behavior of particles commonly found in underwater environments. Based on the experimental data collected at different scattering levels, a generalized Gamma distribution and a weighted mixture of two generalized Gamma distributions are proposed, capable of modeling fluctuations in scenarios with small and large bubbles, respectively. Both empirical models provide an accurate fit to the measured values for different turbidity levels. Furthermore, the resulting histograms show that the fluctuations induced by air bubbles and other phenomena in the experimental tank depend significantly on the water turbidity. Specifically, the scintillation index and average outage duration are reduced in more turbid waters. This effect is explained by a beam spreading induced by scattering, which provides greater robustness against light blockages caused by air bubbles due to the capture of scattered photons that are not blocked. On the other hand, experimental tests reveal that the coherence time remains constant, on the order of milliseconds to tens of milliseconds, for both small and large bubbles, despite variations in the scattering level.

In the light of the experimental results of Chapter 3, an analytical and asymptotic performance analysis is conducted in terms of BER and outage probability of a UOWC system under both empirical channel models fitted to the experimental data for small and large bubbles, as well as the experimental losses observed in each water type. Hence, closed-form and asymptotic expressions are derived based on the fitted statistical distributions. Additionally, the diversity order of the UOWC system is obtained as a function of turbidity levels for both bubble types. From the derived expressions, it is demonstrated that the diversity order of a UOWC system increases as water turbidity increases. This effect, not previously reported in the literature, reveals a new scattering behavior different from the commonly studied scattering-induced attenuation. The increase in diversity order is reflected in the performance results, which show that water turbidity mitigates the impact of air bubbles-induced power fluctuations as a natural mitigation mechanism due to the optical beam broadening induced by scattering. Therefore, more turbid waters present better results regarding BER and outage probability than tap water despite higher measured propagation losses of turbid waters under controlled laboratory conditions.

Furthermore, in order to provide a much deeper insight into advanced UOWC systems based on spatial diversity techniques adapted to underwater environments, a comparative analysis has been conducted between two different MISO schemes in Chapter 4. In particular, a novel SRC and a generalized TLS system have been evaluated under salinity-induced oceanic turbulence and different water turbidity, such as clear ocean and coastal waters. Both transmission systems have been designed following the international safety standards for optical radiation IEC60825-1. On the one hand, the design of the SRC scheme by appropriately spacing the LD emitters in accordance with the eye-safety regulation and the LD divergence allows for an increase in the total transmitted optical power with a *per-source* power constraint. Therefore, the proposed SRC design can optimize the total transmitted optical power by considering the impact of scattering in terms of attenuation as well as the

energy limitations of battery-powered transceivers. On the other hand, a more tractable exponential approach is presented for modeling random source selections in a non-ideal TLS, i.e., a generalized TLS scheme, where the transmitter has no knowledge of the CSI, or only partial knowledge during transmission. The proposed GTLS model offers greater analytical simplicity and mathematical tractability than proposed in the literature, as it allows for the study of a non-ideal TLS scheme based on a certain probability of successfully obtaining perfect CSI at the transmitter. Both developed MISO schemes are used to study the BER and provide fundamental insights on the practical design of UOWC systems for turbid environments.

From the analysis provided in Chapter 4, it is apparent that SRC schemes with a *per-source* power constraint significantly outperform ideal TLS schemes, particularly in scenarios with moderate to weak turbulence. It can be concluded that the SRC system is the optimal choice in environments where scattering represents a more significant challenge than oceanic turbulence. However, the performance gain of the SRC scheme is less pronounced for long-distance links or in strong turbulence conditions, which may not justify the increased optical power consumption for low-power or battery-operated devices. Additionally, the study highlights the significant vulnerability of a realistic TLS system under imperfect CSI at the transmitter, even when the success probability of perfect CSI exceeds 90%.

In summary, taking into account the diverse manifestations of scattering allows the design of optical wireless communication systems optimized for the unique characteristics of underwater environments. This thesis provides mathematical tools to evaluate the impact of scattering, as well as other underwater phenomena, on the propagation of light in underwater environments and its effect on the performance of a UOWC system. It is crucial to develop more advanced system designs capable of mitigating the adverse effects of the underwater channel, particularly high attenuation and scattering, given their impact in the most common underwater environments. This advancement will serve as a basis for developing optical wireless links that can transmit large volumes of data across short to moderate distances in challenging underwater conditions, addressing the current limitations of both acoustic and optical systems.

5.2 Future Work

This thesis has modeled and analyzed the impact of various phenomena induced by the dispersive behavior of oceans on the performance of UOWC systems. The following section outlines several future research directions to extend this work.

- **Analyze the propagation of OAM beams in turbid underwater environments**

Optical vortices carrying orbital angular momentum (OAM) modes can increase system capacity by transmitting multiple orthogonal spatial beams, each with an independent data channel [189, 190]. Although some studies demonstrate experimental links in underwater environments, only a few analyze the impact of scattering or their effectiveness depending on the water turbidity level [191, 192]. Therefore, a more in-depth evaluation of the feasibility of data transmission techniques in underwater environments using spatial multiplexing with OAM vortices is necessary. In particular, further investigation of OAM beams with higher tolerance to diffraction and partial obstructions, such as the Bessel-Gaussian beams, is needed due to the impact of scattering in turbid waters and links in the presence of air bubbles [193].

- **Characterize ultrashort pulse lasers in underwater environments**

Ultrashort pulse lasers (USPL) are a reality in several application areas [194, 195]. Consequently, some studies suggest their application in optical wireless communication systems [196]. USPLs seem to offer better performance in atmospheric FSO links under atmospheric turbulence compared to continuous wave (CW) lasers which have been considered in this thesis. This is due to the reduced probability of the signal being affected by atmospheric turbulence cells being lower, as the duration of the transmitted light pulse is extremely short, on the order of femtoseconds. This has been demonstrated in some experimental studies under laboratory conditions on short-distance links under atmospheric turbulence, where significantly reduced error rates and observed more consistent transmission compared to CW sources links [197–199]. However, USPL sources are affected by other channel phenomena, such as group velocity dispersion [200]. Therefore, it is of interest to assess whether the performance of USPL improves in comparison to CW lasers in underwater environments, where the dispersive nature of the medium, due to high levels of scattering, could negatively impact their performance.

- **Emulate temperature- and salinity-induced oceanic turbulence in the UOWC test-bed**

This thesis has presented a UOWC test-bed capable of emulating different types of water based on a commercial antacid, which modifies the turbidity level, as well as ocean currents and air bubbles of various sizes. However, a mechanism to emulate oceanic turbulence induced by temperature and salinity, which would simulate the Rayleigh–Bénard convection effect, has not been constructed due to the complexity of the system required at the time of this work. Therefore, it is proposed to implement a dynamic and continuous water inflow and outflow system, allowing for the continuous mixing of waters with different temperature and salinity levels during the channel measurement process.

- **Scattering compensation by adaptive optics in UOWC systems**

Wavefront reconstruction systems, such as adaptive optics systems, have been extensively investigated in the field of FSO systems and astronomy to mitigate optical

aberrations induced by atmospheric turbulence [201–203]. However, the effectiveness of these techniques in communication systems to reduce the dispersive effects of the medium, i.e., scattering, has not been explored. Nonetheless, adaptive optics and wavefront shaping techniques are already widely used in medical applications in the analysis of biological tissues, i.e., turbid samples, that show high levels of scattering for light propagation [204–206]. An important area for future research is to apply some of these techniques to reduce the impact of underwater scattering on the received wavefront, thereby decreasing beam dispersion and improving the UOWC system performance.

Appendices

Appendix A

Special Functions

A.1 Gamma Function

The Gamma function, $\Gamma(z)$, is a generalization of the factorial function to non-integer number arguments. If n is a positive integer

$$\Gamma(n) = (n - 1)!. \quad (\text{A.1.1})$$

The Gamma function is defined for all complex numbers except the non-positive integers. In this case, $\Gamma(z)$ is defined through the integral representation as in [207, Eq. (8.310)]

$$\Gamma(z) = \int_0^{\infty} x^{z-1} e^{-x} dx. \quad (\text{A.1.2})$$

An useful property of the Gamma function is given by [158, Eq. (06.05.25.0003.01)] as follows

$$\lim_{n \rightarrow \infty} \frac{\Gamma(a+n)}{\Gamma(b+n)} n^{b-a} = 1. \quad (\text{A.1.3})$$

A.2 Incomplete Gamma Function

The integral representation of the incomplete Gamma function can be expressed as in [207, Eq. (8.350)]

$$\nu(\alpha, z) = \int_0^z x^{\alpha-1} e^{-x} dx. \quad (\text{A.2.1a})$$

$$\Gamma(\alpha, z) = \int_z^{\infty} x^{\alpha-1} e^{-x} dx, \quad (\text{A.2.1b})$$

where $\nu(\alpha, z)$, and $\Gamma(\alpha, z)$ are the lower and upper incomplete gamma function, respectively. An useful property of the incomplete Gamma function known as decomposition formula is given by [208, Eq. (2.3)] as follows

$$\nu(\alpha, z) + \Gamma(\alpha, z) = \Gamma(z). \quad (\text{A.2.2})$$

A.3 Meijer's G-Function

A general definition of the Meijer's G-function $G_{p,q}^{m,n}(\cdot)$ is given by the following line integral in the complex plane as in [207, Eq. (9.301)]

$$G_{p,q}^{m,n} \left(z \left| \begin{matrix} (a_p) \\ (b_q) \end{matrix} \right. \right) = \frac{1}{2\pi i} \int_L \frac{\prod_{j=1}^m \Gamma(b_j - s) \prod_{j=1}^n \Gamma(1 - a_j + s)}{\prod_{j=m+1}^q \Gamma(1 - b_j + s) \prod_{j=n+1}^p \Gamma(a_j - s)} z^s ds, \quad (\text{A.3.1})$$

where $(a_p) = a_1, \dots, a_p$, $(b_q) = b_1, \dots, b_q$, and L denotes the path to be followed in the integration. For integers m, n, p, q such that $0 \leq m \leq q$, $0 \leq n \leq p$, and the poles of $\Gamma(b_j - s)$ must not coincide with the poles of $\Gamma(1 - a_k + s)$ for any j and k where $j = 1, \dots, m$ and $k = 1, \dots, n$. Moreover, the Meijer's G-function is a standard built-in function in most of the well-known mathematical software packages such as Maple[™] and Wolfram Mathematica[™]. The Meijer's G-function includes most of the special functions used in mathematics as particular cases.

A.3.1 Relation to Other Functions

The exponential function can be expressed in terms of the Meijer's G-function as follows [188, Eq. (8.4.3.1)]

$$e^{-x} = G_{0,1}^{1,0} \left(x \left| \begin{matrix} \cdot \\ 0 \end{matrix} \right. \right) \quad (\text{A.3.2})$$

The natural logarithm can be expressed in terms of the Meijer's G-function as follows [188, Eq. (8.4.6.5)]

$$\log(1+x) = G_{2,2}^{1,2} \left(x \left| \begin{matrix} 1, 1 \\ 1, 0 \end{matrix} \right. \right) \quad (\text{A.3.3})$$

The complementary error function can be expressed in terms of the Meijer's G-function as follows [188, Eq. (8.4.14.1)]

$$\operatorname{erfc}(\sqrt{x}) = \frac{1}{\sqrt{\pi}} G_{1,2}^{2,0} \left(x \left| \begin{matrix} 1 \\ 0, \frac{1}{2} \end{matrix} \right. \right) \quad (\text{A.3.4})$$

A.4 H-Fox Function

The H-Fox function $H_{p,q}^{m,n}[\cdot]$ is a generalization of the Meijer's G-function (see Appendix A.3) and is defined via a Mellin Barnes type integral [209, Eq. (1.1)] as follows

$$\begin{aligned} H_{p,q}^{m,n} \left(z \left| \begin{array}{c} (a_p, A_p) \\ (b_q, B_q) \end{array} \right. \right) & \\ = \frac{1}{2\pi i} \int_L \frac{\prod_{j=1}^m \Gamma(b_j + B_j s) \prod_{j=1}^n \Gamma(1 - a_j - A_j s)}{\prod_{j=m+1}^q \Gamma(1 - b_j - B_j s) \prod_{j=n+1}^p \Gamma(a_j + A_j s)} z^s ds, & \end{aligned} \quad (\text{A.4.1})$$

where $(a_p, A_p) = (a_1, A_1), \dots, (a_p, A_p)$, $(b_q, B_q) = (b_1, B_1), \dots, (b_q, B_q)$, and L denotes the path to be followed in the integration. The special case for which the H-Fox function reduces to the Meijer's G-function is $A_j = B_k = C$, $C > 0$ for $j = 1, \dots, p$ and $k = 1, \dots, q$.

$$H_{p,q}^{m,n} \left(z \left| \begin{array}{c} (a_1, C), \dots, (a_p, C) \\ (b_1, C), \dots, (b_q, C) \end{array} \right. \right) = \frac{1}{C} G_{p,q}^{m,n} \left(z^{1/C} \left| \begin{array}{c} a_1, \dots, a_p \\ b_1, \dots, b_q \end{array} \right. \right). \quad (\text{A.4.2})$$

A.5 Other Definite Integrals

$$1. \int_0^\infty x^{\alpha-1} G_{p,q}^{m,n} \left(xz \left| \begin{array}{c} a_1, \dots, a_n, a_{n+1}, \dots, a_p \\ b_1, \dots, b_m, b_{m+1}, \dots, b_q \end{array} \right. \right) dx = \frac{\prod_{k=1}^m \Gamma(\alpha + b_k) \prod_{k=1}^n \Gamma(1 - \alpha - a_k)}{\prod_{k=n+1}^p \Gamma(\alpha + a_k) \prod_{k=m+1}^q \Gamma(1 - \alpha - b_k)} z^{-\alpha} \quad [158, \text{Eq. (07.34.21.0009.01)}]$$

$$\begin{aligned} 2. \int_0^\infty x^{\alpha-1} G_{u,v}^{s,t} \left(\sigma x \left| \begin{array}{c} c_1, c_2, \dots, c_u \\ d_1, d_2, \dots, d_v \end{array} \right. \right) G_{p,q}^{m,n} \left(\omega x \left| \begin{array}{c} a_1, a_2, \dots, a_p \\ b_1, b_2, \dots, b_q \end{array} \right. \right) dx = \\ \sigma^{-\alpha} H_{p+v+q+u}^{m+t, n+s} \left(\frac{\omega}{\sigma} \left| \begin{array}{c} (a_1, 1), \dots, (a_n, 1), (1 - \alpha - d_1, r), \dots, (1 - \alpha - d_v, r), (a_{n+1}, 1), \dots, (a_p, 1) \\ (b_1, 1), \dots, (b_m, 1), (1 - \alpha - c_1, r), \dots, (1 - \alpha - c_u, r), (b_{m+1}, 1), \dots, (b_q, 1) \end{array} \right. \right) \end{aligned} \quad [158, \text{Eq. (07.34.21.0012.01)}]$$

Appendix B

Publications and Projects

B.1 Publications

In this section, a complete list of all the publications derived from the research conducted during this thesis are presented.

Journal papers

- **P. Salcedo-Serrano**, R. Boluda-Ruiz, J.M. Garrido-Balsells, and A. García-Zambrana, “On the scattering-induced fading for optical wireless links through seawater: statistical characterization and its applications,” *Opt. Express* **29**(23), 37101-37116 (2021).
- R. Boluda-Ruiz, **P. Salcedo-Serrano**, B. Castillo-Vázquez, A. García-Zambrana, and J.M. Garrido-Balsells, “Capacity of underwater optical wireless communication systems over salinity-induced oceanic turbulence channels with ISI,” *Opt. Express* **29**(15), 23142-23158 (2021)
- **P. Salcedo-Serrano**, C. Gómez-García, J. Iamaguti-Debessa, R. Boluda-Ruiz, J.M. Garrido-Balsells, B. Castillo-Vázquez, A. Puerta-Notario, A. García-Zambrana, “On the Effect of Air Bubbles-Induced Scattering on Turbid Waters: An Experimental UOWC Channel Modeling Approach,” *IEEE Access*, **12**, pp. 75888-75898 (2024).
- R. Boluda-Ruiz, **P. Salcedo-Serrano**, B. Castillo-Vázquez, A. García-Zambrana and J.M. Garrido-Balsells, “Impact of Scattering on Secrecy Outage Probability of Underwater Optical Wireless Links,” in *IEEE Journal of Oceanic Engineering*, **48**(4), pp. 1362-1372 (2023)
- **P. Salcedo-Serrano**, R. Boluda-Ruiz, J.M. Garrido-Balsells, B. Castillo-Vázquez, A. Puerta-Notario, A. García-Zambrana, “Performance Evaluation of UOWC Systems

from an Empirical Channel Model Approach for Air Bubble-Induced Scattering,” *Sensors* **24**(16), 5232 (2024).

- **P. Salcedo-Serrano**, R. Boluda-Ruiz, J.M. Garrido-Balsells, B. Castillo-Vázquez, A. Puerta-Notario, A. García-Zambrana, and S. Hranilovic “UOWC spatial diversity techniques over hostile maritime environments: a new approach under imperfect CSI and per-source power constraints,” *Opt. Express* **32**(24), 42347-42367 (2024). (2024).

Conference papers

- **P. Salcedo-Serrano**, R. Boluda-Ruiz, J.M. Garrido-Balsells, and A. García-Zambrana, “On scattering-induced fading in underwater FSO links for clear ocean and coastal waters,” in *Conference on Lasers and Electro-Optics (CLEO)*, OSA Technical Digest (Optical Society of America, 2021), paper JTu3A.166.
- R. Boluda-Ruiz, **P. Salcedo-Serrano**, B. Castillo-Vázquez, A. García-Zambrana and J.M. Garrido-Balsells, ”On the effect of inter-symbol interference on mutual information of undersea optical wireless links,” *2021 IEEE Photonics Conference (IPC)*, 2021, pP. 1-2.
- **P. Salcedo-Serrano**, R. Boluda-Ruiz, J.M. Garrido-Balsells, and A. García-Zambrana, “Outage capacity of underwater FSO systems over scattering-induced fading channels,” in *OSA Imaging and Applied Optics Congress 2021 (3D, COSI, DH, ISA, pcAOP)*, OSA Technical Digest (Optical Society of America, 2021), paper PM2G.2.
- **P. Salcedo-Serrano**, R. Boluda-Ruiz, J.M. Garrido-Balsells, and A. García-Zambrana, “Ergodic capacity analysis of underwater FSO systems over scattering-induced fading channels in the presence of Weibull oceanic turbulence,” *IEEE International Conference on Communications (ICC)*, Seoul, Republic of Korea, 2022, pp. 3814-3819
- **P. Salcedo-Serrano**, R. Boluda-Ruiz, J.M. Garrido-Balsells, A. García-Zambrana and S. Hranilovic, “Underwater Optical Wireless Channel Capacity Under Oceanic Turbulence Using Spatial Diversity Techniques,” *IEEE International Conference on Communications (ICC)*, Rome, Italy, 2023, pp. 1162-1168
- **P. Salcedo-Serrano**, R. Boluda-Ruiz, J.M. Garrido-Balsells, and A. Garcia-Zambrana, “Caracterización estadística del desvanecimiento inducido por dispersión en sistemas de comunicación óptica inalámbrica subacuática,” *XXXVI Simposio Nacional URSI Spain*, September 20-24, 2021, Vigo, Spain.
- **P. Salcedo-Serrano**, R. Boluda-Ruiz, J.M. Garrido-Balsells, and A. Garcia-Zambrana, “Incremento de la capacidad del canal óptico submarino mediante técnicas

MISO en presencia de dispersión y turbulencia oceánica,” XXXVII Simposio Nacional URSI Spain, September 5-7, 2022, Málaga, Spain.

- **P. Salcedo-Serrano**, J.M. Garrido-Balsells, A. García-Zambrana, A. Puerta-Notario, B. Castillo-Vázquez, R. Boluda-Ruiz, “Análisis de técnicas de diversidad espacial adaptadas al canal óptico submarino en presencia de dispersión y turbulencia oceánica,” XXXVIII Simposio Nacional URSI Spain, September 13-15, 2023, Cáceres, Spain.
- C. Gómez-García, J. Iamaguti-Debessa, **P. Salcedo-Serrano**, R. Boluda-Ruiz, J.M. Garrido-Balsells, B. Castillo-Vázquez, A. Puerta-Notario, A. García-Zambrana, ”Modelado estadístico del efecto de burbujas de aire en sistemas de comunicaciones ópticos inalámbricos submarinos”, XXXVIII Simposio Nacional URSI Spain, September 13-15, 2023, Cáceres, Spain.

B.2 Funding and projects

This thesis has been funded by the Spanish Ministerio de Ciencia, Innovación y Universidades under the grant FPU22/02183. Furthermore, all the publications above have been developed in the framework of the below research projects

- P18-RTJ-3343 funded by the Programa Operativo I+D+i FEDER Andalucía 2014-2020.
- PID2019-107792GB-I00 funded by the Spanish Ministerio de Ciencia, Innovación y Universidades.
- P21_00390 funded by the Plan Andaluz de Investigación, Desarrollo e Innovación (PAIDI) 2021.

B.3 Research Fellowship

A research stay at McMaster University (Hamilton, Ontario, Canada) was conducted for a period of three months under the supervision of Prof. Steve Hranilovic.

Appendix C

Summary (Spanish)

De acuerdo con el Artículo 54 del Reglamento 4/2022 de la Universidad de Málaga, se incluye un resumen en español del trabajo realizado en esta tesis doctoral. En primer lugar, se presenta una introducción al tema de estudio, junto con una breve descripción del estado actual del campo de investigación, que justifica la relevancia de este estudio así como sus objetivos principales. A continuación, se resume el contenido de cada capítulo, incluyendo los resultados, la discusión y las conclusiones más relevantes de cada apartado. Por último, se destacan las principales contribuciones originales de este trabajo, así como una lista de las líneas futuras de investigación que han surgido del desarrollo de esta tesis.

C.1 Introducción a las comunicaciones inalámbricas ópticas submarinas

C.1.1 Antecedentes y motivación

En la actualidad, la industria marítima representa un 2.5% del total del valor añadido bruto mundial, abarcando multitud de sectores tales como la pesca, el transporte de mercancías, parques eólicos marinos, la extracción de petróleo y gas en alta mar, las telecomunicaciones o el turismo [1]. Estas actividades se han desarrollado de acuerdo con diferentes planes estratégicos de organizaciones internacionales como la Organización de las Naciones Unidas, como por ejemplo el *Decenio de las ciencias oceánicas para el desarrollo sostenible 2021-2030*, comúnmente conocido como el Decenio del océano [8]. Dicho documento recoge nuevas iniciativas y aplicaciones relacionadas con la industria oceánica para el desarrollo sostenible de la economía marítima y la lucha contra el cambio climático. Muchas de estas nuevas aplicaciones integran sistemas de recolección masiva de datos (*big data*) a través de dispositivos del “Internet de las cosas submarinas” (*Internet of Underwater Things*, IoUT) [9–11]. Para el correcto despliegue de estos dispositivos, es necesario implementar redes de comu-

nicación capaces de transmitir y recibir en tiempo real dichas cantidades de datos a través de enlaces robustos de alta velocidad. Por un lado, los sistemas de comunicación guiados, a través de redes de fibra óptica, o par de cobre, proveen enlaces robustos y de velocidades altas y moderadas, respectivamente. Sin embargo, estos sistemas requieren altos costes de mantenimiento, sobre todo en localizaciones remotas de difícil acceso. En este tipo de localizaciones se despliegan redes de sensores inalámbricos submarinos (*underwater wireless sensor networks*, UWSNs), los cuales hacen uso de sistemas de comunicación inalámbricos para la transmisión de la información recolectada en el suelo marino. Por otro lado, los sistemas guiados presentan menor flexibilidad para el control y conducción de dispositivos móviles como los vehículos operados a distancia (*remotely operated vehicles*, ROV) o vehículos autónomos submarinos (*autonomous underwater vehicles*, AUV). En aras de facilitar y mejorar el rendimiento de estas nuevas aplicaciones, es necesario el desarrollo de sistemas de comunicación inalámbricos que permitan una comunicación efectiva con un menor coste y mayor flexibilidad que los sistemas actuales.

Actualmente, los dispositivos de comunicación inalámbricos submarinos más usados emplean sistemas de transmisión acústicos, los cuales permiten desplegar enlaces de hasta varios kilómetros. Sin embargo, la reducida velocidad de propagación de las ondas acústicas en el medio oceánico provoca retardos en la comunicación incompatibles con aplicaciones que requieran de datos en tiempo real, como por ejemplo, la transmisión de vídeo para la conducción de un ROV. Además, el escaso ancho de banda que presentan los sistemas acústicos no permite tasas de transmisión elevadas, limitando los enlaces a velocidades por debajo de las decenas de kbps [13–15]. En interés de incrementar las velocidades de transmisión, se ha propuesto el uso del espectro de radiofrecuencia (*Radio-Frequency*, RF), de uso extendido en las aplicaciones terrestres. Sin embargo, el medio acuático presenta una absorción muy elevada en el rango de VHF y UHF (*Very- y Ultra-High Frequency*, respectivamente), lo que limita las comunicaciones vía RF a enlaces del orden de centímetros de distancia [13, 16]. Si bien es posible utilizar rangos de frecuencia menores para los cuales la atenuación submarina no es tan crítica, las dimensiones y el coste de las antenas de dichos sistemas hacen impracticable su uso en aplicaciones móviles [17]. La necesidad de disponer de enlaces no guiados de alta velocidad en ambientes submarinos ha propiciado un mayor interés en las comunicaciones ópticas submarinas inalámbricas (*underwater optical wireless communication*, UOWC), dado que el espectro óptico en el rango de 400 a 700 nm, correspondiente a las longitudes de onda del azul y el verde, presenta una absorción suficientemente baja para permitir enlaces a distancias moderadas en determinadas aplicaciones. A diferencia de los sistemas acústicos, el espectro óptico ofrece un ancho de banda significativamente amplio, alcanzando tasas de transmisión de hasta varios Gbps con una latencia mínima en condiciones de laboratorio [20–22]. Además, el bajo consumo de energía y el menor coste de implementación de los sistemas ópticos facilitan su integración en dispositivos submarinos portátiles alimentados por baterías.

Sin embargo, los enlaces UOWC presentan inconvenientes derivados de la propagación de

la luz por el canal submarino que limitan las prestaciones totales de los sistemas UOWC. El canal óptico submarino es un medio altamente dispersivo en comparación con el medio atmosférico dada su alta concentración de partículas en suspensión que conforman la composición del agua. La interacción de los fotones con las partículas del medio se refleja en un proceso de absorción y dispersión. Estos procesos dan lugar a la atenuación del haz de luz transmitido y al esparcimiento temporal y espacial debido a la luz dispersada por la interacción con las partículas [85]. Ambos efectos dependerán del nivel de turbidez del agua, es decir, de la concentración de partículas del medio acuático. Otra limitación de los sistemas UOWC son las turbulencias oceánicas inducidas por microvariaciones en la temperatura y salinidad del agua que provocan fluctuaciones de carácter aleatorio en el índice de refracción del agua. Estas pequeñas variaciones en el medio durante la propagación del haz provocan fluctuaciones aleatorias en intensidad y fase de la señal óptica recibida, efecto denominado como *fading*. Por último, las burbujas de aire generadas por procesos biológicos inherentes al medio submarino, así como actividades artificiales externas pueden producir bloqueos parciales o totales del haz de luz transmitido y reducir las prestaciones del sistema.

Estas limitaciones inherentes al medio submarino han impulsado a la industria y a las instituciones de investigación a explorar y analizar el canal óptico submarino para la mejora y el diseño de sistemas UOWC capaces de mitigar dichos efectos y aumentar las distancias de enlace y las velocidades de transmisión ofrecidas por los dispositivos actuales. En este contexto, el modelado del canal óptico submarino ha sido un foco central de investigación durante los últimos años [56, 141, 145, 168] (y sus referencias). Inspirados por los avances en el campo de la comunicación óptica en espacio libre (*free-space optical*, FSO) para abordar los efectos de la turbulencia atmosférica, algunos estudios han aplicado enfoques estadísticos similares para analizar la influencia de la turbulencia oceánica y las burbujas de aire en los canales submarinos.

A pesar de ello, pocos trabajos han abordado la interacción entre la turbulencia oceánica y las burbujas de aire con el fenómeno de la dispersión. Esta ausencia de conocimiento es particularmente relevante, dado que uno de los principales factores limitantes para el despliegue de sistemas UOWC es la corta distancia de enlace provocada por los efectos de absorción y dispersión, lo que dificulta el establecimiento de enlaces en entornos submarinos no ideales, como aguas costeras o cercanas a zonas portuarias con alta presencia de materia orgánica. Además, muchos de los modelos estadísticos utilizados para evaluar el rendimiento de los sistemas UOWC en presencia de turbulencia oceánica y burbujas de aire se basan en herramientas de simulación. Si bien las simulaciones ofrecen ventajas en términos de accesibilidad y costos, la falta de modelos experimentales limita la aplicabilidad práctica de estos enfoques. Este es el caso del diseño de sistemas UOWC adaptados a entornos marinos hostiles, donde los efectos combinados de la turbulencia oceánica, las burbujas de aire y la dispersión inducida por partículas son determinantes. Por lo tanto, es esencial realizar análisis experimentales que evalúen el impacto de las perturbaciones oceánicas y su variación con diferentes niveles de turbidez del agua.

C.1.2 Objetivos

A partir de lo expuesto en el apartado anterior, se evidencia la necesidad de llevar a cabo un estudio experimental del canal óptico submarino con el propósito de evaluar con precisión el comportamiento de la propagación de la luz en presencia de diferentes niveles de dispersión. En concreto, esta tesis se enmarca en el análisis y modelado del canal submarino, con especial interés en el efecto de la dispersión, y su interacción con otros efectos submarinos, como las burbujas de aire y la turbulencia oceánica. Así pues, el objetivo de este trabajo es doble: por un lado, desarrollar un marco estadístico que describa los fenómenos asociados a la dispersión y su interacción con otros efectos submarinos a partir de mediciones experimentales. Para ello, se construye un banco de pruebas experimental capaz de emular diferentes fenómenos oceánicos asociados a las UOWC, como burbujas de aire, corrientes marinas y diferentes niveles de turbidez, es decir, niveles de absorción y dispersión, de forma controlable y reproducible. Por otro lado, se propone estudiar diseños avanzados de transmisores, como esquemas MISO (*Multiple-Input/Single-Output*), para mitigar de forma conjunta los efectos de absorción, dispersión y turbulencia oceánica en el entorno submarino.

C.2 Fundamentos de las comunicaciones inalámbricas ópticas submarinas

C.2.1 Absorción y dispersión

La señal óptica que se propaga por el medio oceánico es susceptible de sufrir alteraciones que puedan llegar a degradar notablemente las prestaciones de un sistema UOWC.

En primer lugar, los rayos que se propagan por el medio oceánico interactúan con las partículas que constituyen el medio submarino, provocando una transferencia de energía ligada al haz de luz a energía calorífica de la partícula con la que impacta [85]. Este proceso determina la absorción que sufre la señal óptica a medida que se propaga por el medio submarino. Por ello, la absorción es mayor cuando el medio acuático tiene una concentración de partículas muy alta, como por ejemplo las aguas costeras o aguas de puerto.

Además de la pérdida de potencia debido a la transferencia de energía, la interacción del rayo de luz con la partícula provoca que una parte de la energía del haz de luz se transmita en una dirección diferente a la dirección de propagación inicial [95]. Este efecto se denomina como dispersión, y depende en gran medida de la geometría de las partículas con las que interactúa el haz de luz. Caben destacar los fenómenos de dispersión de Rayleigh o dispersión de Mie dada su generalidad en la propagación de la luz en medios como la atmósfera cuando la luz interactúa con partículas homogéneas y esféricas de un tamaño menor o comparable a la longitud de onda, respectivamente. Sin embargo, dada la geometría de las partículas en suspensión más comunes en el agua, ninguno de estos dos tipos de dispersión pueden

Table C.1: Coeficientes de absorción, dispersión y extinción para diferentes tipos de agua considerando una longitud de onda $\lambda = 532$ nm [19].

Tipo de agua	a [m^{-1}]	b [m^{-1}]	c [m^{-1}]
Agua de océano claro	0.114	0.037	0.151
Agua de costa	0.179	0.219	0.398
Agua de puerto	0.295	1.875	2.17

aplicarse a la propagación de la luz a través del medio submarino. El esparcimiento de la luz debido a la dispersión por partículas se describe a través de la función de dispersión volumétrica (*Volume Scattering Function*, VSF), la cual indica la distribución angular de la potencia esparcida.

Los fenómenos de absorción y dispersión de un medio de propagación son descritos matemáticamente por los coeficientes de absorción y dispersión, $a(\lambda)$ y $b(\lambda)$, respectivamente, los cuales depende del medio, así como de la longitud de onda. A partir de dichos coeficientes, es posible definir el coeficiente de atenuación, también conocido como coeficiente de extinción, como [19]

$$c(\lambda) = a(\lambda) + b(\lambda) \quad (\text{m}^{-1}). \quad (\text{C.2.1})$$

De acuerdo con la literatura, es posible clasificar los diferentes tipos de agua presentes en la Tierra en función de sus propiedades ópticas. En esta tesis, se consideran los tres tipos de agua más utilizados en el estudio del canal UOWC, presentados en la Tabla C.1 junto con sus respectivos coeficientes de absorción, dispersión y extinción [19].

Desde un punto de vista analítico, la propagación de la luz en un medio submarino con partículas en suspensión puede describirse mediante la ecuación de transferencia radiativa (*Radiative Transfer Equation*, RTE). No obstante, hasta donde se tiene conocimiento, esta ecuación carece de una solución exacta en forma cerrada. Bajo la suposición de que el transmisor y el receptor están perfectamente alineados y que todos los fotones dispersados se pierden, es posible derivar una solución analítica basada en la ley de Beer-Lambert. Este modelo caracteriza las pérdidas de camino que sufre el haz óptico tras recorrer una distancia d en un medio submarino descrito a través del coeficiente de extinción como

$$L = e^{-c(\lambda) \cdot d}. \quad (\text{C.2.2})$$

Aunque este enfoque permite describir la atenuación óptica en términos del coeficiente de extinción, cabe señalar que subestima la potencia óptica recibida con respecto a los resultados obtenidos en medidas experimentales. Esto se debe a la hipótesis de que los fotones dispersados en una dirección diferente a la dirección de propagación no contribuyen a la señal óptica recibida en el fotodetector. En un escenario real, una proporción significativa de los fotones

dispersados en ángulos pequeños puede alcanzar el fotodetector, incrementando la potencia óptica recibida. Este fenómeno es particularmente relevante en aguas turbias, donde la dispersión es el factor predominante en la propagación de la luz [25]. Para abordar las limitaciones de este modelo simplificado, se emplean herramientas de simulación basadas en el trazado de rayos, técnica también conocida como simulación Monte Carlo. Este método simula las trayectorias de los rayos emitidos, teniendo en cuenta las múltiples interacciones con las partículas presentes en el medio submarino [93].

C.2.2 Turbulencia oceánica

La propagación de un haz de luz también sufre alteraciones derivadas de las turbulencias oceánicas. El fenómeno de la turbulencia en un medio submarino se origina por microvariaciones de temperatura y salinidad en un cuerpo de agua, lo que provoca diferencias en el índice de refracción a lo largo de la dirección de propagación de los fotones. En términos de propagación de un haz de luz, la potencia óptica recibida experimenta desvanecimientos aleatorios debido a dichas variaciones del índice de refracción. Este fenómeno ha sido ampliamente estudiado en la bibliografía relativa a los sistemas FSO atmosféricos [42]. Sin embargo, el proceso de generación de turbulencias en el océano es significativamente distinto al de las turbulencias atmosféricas. Esta diferencia se refleja en la densidad espectral de potencia asociada a las variaciones del índice de refracción. En el estudio de prestaciones de sistemas UOWC, el espectro más utilizado es el espectro de Nikishov dada su simplicidad y adaptabilidad bajo la condición de aguas homogéneas e isotrópicas en términos de temperatura y salinidad [29, 30]. En este trabajo se adopta dicho espectro dada su facilidad matemática y adaptabilidad a los diferentes escenarios de turbulencias oceánicas, y por ende, a su utilidad para estudiar de forma amplia y general el impacto que pueden llegar a provocar en las prestaciones de un sistema UOWC.

C.2.3 Burbujas de aire

Por último, esta tesis también considera el posible impacto de la interacción del haz de luz con burbujas de aire a lo largo del medio submarino. Las burbujas de aire se originan por diversos fenómenos naturales, tales como la ruptura de olas impulsadas por el viento, que forma nubes de burbujas con tamaños que varían desde fracciones de milímetro hasta varios milímetros, o las producidas por organismos acuáticos como el fitoplancton para ajustar su flotabilidad. Por otro lado, las actividades humanas, como la propulsión de vehículos submarinos o el uso de sistemas de buceo, también contribuyen a la formación de burbujas. Desde el punto de vista óptico, una burbuja de aire se puede analizar como un cambio de medio local entre agua y aire, y viceversa. Las interacciones entre la luz y estas burbujas dependen de su tamaño relativo a la longitud de onda de la luz, pudiendo describirse mediante teorías como la dispersión de Rayleigh o Mie, o utilizando leyes ópticas

como la refracción y reflexión si el tamaño de la burbuja es mucho más grande que la longitud de onda. Estas interacciones provocan una transmisión parcial de la luz al interactuar con la burbuja, provocando pérdidas de potencia óptica durante la propagación. Además, la generación y el movimiento aleatorio de las burbujas de aire en el conjunto del medio submarino provoca un efecto de fluctuación de la potencia óptica recibida similar al inducido por las turbulencias oceánicas.

C.2.4 Modelo de sistema UOWC

A continuación, se presenta el modelo de sistema UOWC adoptado a lo largo de esta tesis. Los sistemas UOWC propuestos y evaluados en este trabajo están basados en modulación de intensidad y detección directa (*Intensity Modulation and Direct Detection*, IM/DD) con línea de visión directa (*line-of-sight*, LOS) entre transmisor y receptor.

Así, el modelo matemático en banda base para dicho canal viene dado por

$$Y = R X H + Z, \quad (\text{C.2.3})$$

donde X es la potencia óptica transmitida, R es la responsividad del fotodetector, Y es la corriente de salida del fotodetector, H es la ganancia del canal óptico submarino que representa los efectos debidos a la dispersión, las turbulencias oceánicas y las burbujas de aire, y Z es el ruido aditivo blanco y Gaussiano (*Additive White Gaussian Noise*, AWGN) de media cero y varianza $\sigma_Z^2 = N_0/2$, donde N_0 es la densidad espectral de potencia del ruido. Sin pérdida de generalidad, en lo sucesivo se asume que la responsividad del fotodetector es igual a la unidad.

Como se ha indicado arriba, H representa la ganancia del canal submarino, que incluye las pérdidas de camino, o pérdidas de propagación, L , y las fluctuaciones de potencia normalizadas debido a variaciones en el índice de refracción, H_i , pudiendo descomponerse como

$$H = L \cdot H_i, \quad (\text{C.2.4})$$

donde H_i describe las fluctuaciones de potencia causadas por burbujas de aire (H_b) o turbulencias oceánicas (H_o).

C.3 Modelado de canal UOWC experimental

En esta sección, se propone un modelo de canal UOWC empírico basado en mediciones experimentales con el objetivo de analizar el impacto de las burbujas de aire en las prestaciones del sistema bajo diferentes niveles de dispersión. Para ello, se desarrolla un emulador de canal óptico submarino que permite obtener mediciones precisas y reproducibles en diferentes instantes de tiempo en condiciones de laboratorio. A partir de estas mediciones, se analiza el

comportamiento estadístico de las fluctuaciones en la potencia óptica recibida considerando distintos diámetros de burbujas de aire y niveles de turbidez del agua. Además, se derivan nuevas expresiones analíticas y asintóticas para estudiar la tasa de error de bit (*Bit Error Rate*, BER) de un sistema SISO (*Single-Input/Single-Output*) UOWC, empleando el marco analítico desarrollado a partir de los datos experimentales obtenidos.

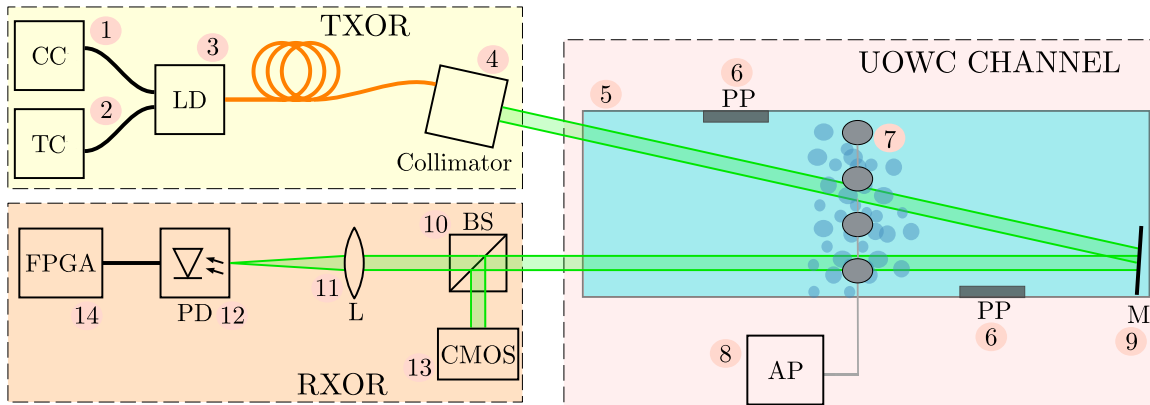
C.3.1 Motivación

En los últimos años, el modelado del canal óptico submarino ha despertado un notable interés en la comunidad científica. Diversas investigaciones se han centrado en medir y modelar las fluctuaciones de potencia óptica bajo diferentes configuraciones de enlace UOWC, considerando factores como las turbulencias oceánicas inducidas por gradientes de temperatura y salinidad, la presencia de burbujas de aire o la combinación simultánea de ambos fenómenos [53–55, 131, 137–139] (y sus referencias). No obstante, no tenemos conocimiento del análisis y el modelado del índice de centelleo para distintos niveles de turbidez del agua y su variación con éste de manera experimental, a pesar de la importancia de la absorción y la dispersión en los enlaces UOWC.

C.3.2 Emulador de canal UOWC

En la Fig. C.1, se muestra el diagrama de bloques del banco de pruebas experimental de UOWC para emular el canal óptico submarino, así como una fotografía de la implementación final de éste en el laboratorio junto con todos los dispositivos empleados. El sistema propuesto emplea un diodo láser (*Laser Diode*, LD) verde de 520 nm en transmisión con control de temperatura y corriente. En recepción, un divisor de haz, o *beam splitter*, divide de manera equitativa la luz recibida hacia una cámara de alta resolución y una lente plano-convexa que converge la luz en una fotodetector que consta de un fotodiodo PIN y un módulo de amplificación. La señal eléctrica de salida del fotodetector se muestrea mediante una placa FPGA (*Field Programmable Gate Array*) Red Pitaya STEMLab. Finalmente, los datos obtenidos son procesados para realizar su caracterización estadística en un ordenador a través de los programas MATLAB y Wolfram Mathematica.

El emulador de canal submarino consta de un tanque de vidrio de $1.5 \times 0.2 \times 0.3$ m llenado con agua de grifo. Con el objetivo de emular el movimiento del agua debido a las corrientes marinas, se instalan ventiladores controlados por motores de corriente continua ajustables en velocidad y patrón de movimiento. Un espejo situado en un extremo del tanque permite extender la distancia del enlace UOWC, que será establecido en 3 metros para este estudio. Las burbujas de aire se generan mediante una bomba externa que expulsa aire dentro del tanque de agua a través de unos tubos conectados a unas piedras porosas que actúan de difusores de aire, pudiendo controlar algunas características de las burbujas de aire. Las burbujas pequeñas tienen diámetros de 1 a 4 mm, mientras que las grandes, generadas sin



(a) Diagrama de bloques del banco de pruebas de UOWC experimental.



(b) Implementación final en el laboratorio del banco de pruebas de UOWC experimental.

Figure C.1: (1) Controlador de corriente (CC). (2) Controlador de temperatura (TC). (3) Diodo láser. (4) Colimador. (5) Tanque de agua. (6) Ventiladores (PP). (7) Difusores de aire. (8) Bomba de aire (AP). (9)Espejo dieléctrico. (10) Beamsplitter (BS). (11) Lente plano-convexa (L). (12) Fotodetector (PD). (13) Cámara CMOS. (14) RedPitaya STEMLab.

los difusores de aire, es decir, expulsando el aire directamente desde los tubos de salida, alcanzan un diámetro de aproximadamente 1 cm. Para emular distintos niveles de turbidez, se emplea el antiácido comercial Maalox, compuesto principalmente por hidróxido de magnesio e hidróxido de aluminio. Este producto presenta una VSF similar a la observada en entornos oceánicos reales, lo que lo convierte en una herramienta ampliamente utilizada en la comunidad científica para emular diversos ambientes marinos [148–150].

C.3.3 Análisis de las fluctuaciones inducidas por las burbujas de aire

El proceso aleatorio de generación y movimiento de las burbujas de aire provoca fluctuaciones en la señal óptica recibida durante la transmisión de un haz de luz de potencia constante. Con el fin de analizar en detalle los fenómenos emulados en el banco de pruebas, se realiza una caracterización estadística de la señal recibida. En este análisis, se estiman las pérdidas de potencia debido a las partículas y burbujas de aire, el coeficiente de atenuación del medio, el índice de centelleo y la función de densidad de probabilidad (*Probability Density Function*, PDF) de las fluctuaciones. Además, se calculan otros parámetros relacionados con el comportamiento estocástico de la señal, como el tiempo de coherencia de las fluctuaciones, τ_0 , y el tiempo medio de *outage* (*Average Outage Duration*, AOD) de la señal.

Para medir las pérdidas de potencia causadas por el canal submarino, es necesario compensar las pérdidas adicionales que no están relacionadas con el canal submarino en sí mismo, como los efectos de refracción provocados por las transiciones aire-cristal y cristal-agua, la reflectividad de los espejos utilizados para extender la distancia del enlace y la transmitancia de la lente empleada en el montaje experimental. Posteriormente, para analizar las contribuciones de las partículas suspendidas y las burbujas de aire sobre las pérdidas totales del canal acuático, éstas se descomponen en dos componentes: las pérdidas causadas por las burbujas de aire, L_b , y las debidas a las partículas en suspensión, como el Maalox y las moléculas del agua de grifo, L_p . Así, las pérdidas totales debido al canal submarino pueden ser calculadas como

$$L_u[dB] = L_b[dB] + L_p[dB]. \quad (\text{C.3.1})$$

Para realizar esta descomposición, se realiza una estimación de las pérdidas para medidas en presencia de burbujas y sin burbujas de aire para las mismas condiciones de turbidez.

Una aproximación del coeficiente de atenuación se puede estimar fácilmente a partir de la ley de Beer-Lambert y las pérdidas causadas por partículas en suspensión como

$$c = -\frac{1}{d} \log(L_p). \quad (\text{C.3.2})$$

El índice de centelleo se calcula a partir del análisis de la varianza de la señal capturada. Antes de calcular este parámetro, la señal recibida se normaliza respecto a su valor medio, lo que permite separar las fluctuaciones de potencia causadas por las burbujas de aire de las pérdidas de propagación introducidas por el canal submarino. Así, el índice de centelleo puede ser calculado como

$$\sigma^2 = \frac{\mathbb{E}[H_b^2] - \mathbb{E}[H_b]^2}{\mathbb{E}[H_b]^2} = \frac{\mathbb{E}[H_b^2]}{\mathbb{E}[H_b]^2} - 1. \quad (\text{C.3.3})$$

donde H_b fluctuación de potencia óptica normalizada y $\mathbb{E}(\cdot)$ es la esperanza matemática.

Para modelar el comportamiento estadístico de las fluctuaciones de potencia causadas por burbujas pequeñas y grandes, se parte de la distribución de probabilidad Gamma generalizada, que ha demostrado un gran nivel de precisión para mediciones experimentales de

fluctuaciones de potencia en canales UOWC. Así, para las burbujas pequeñas, se emplea la distribución Gamma generalizada descrita como

$$f_{H_{\text{small}}}(h; a, d, p) = \frac{p}{a^d \Gamma(d/p)} h^{d-1} e^{-(h/a)^p}, \quad (\text{C.3.4})$$

donde h es la fluctuación de potencia óptica normalizada debida a las burbujas de aire y las corrientes generadas por el viento, a es el parámetro de escala, y d y p son los parámetros de forma. En el caso de las burbujas grandes, que pueden obstruir parcial o totalmente el haz de luz en el receptor, se propone el uso de una distribución que combina dos distribuciones Gamma generalizadas como

$$f_{H_{\text{large}}} = W \cdot f_{H_{\text{small}}}(h; a_1, d_1, p_1) + (1 - W) \cdot f_{H_{\text{small}}}(h; a_2, d_2, p_2), \quad (\text{C.3.5})$$

donde W es la proporción entre el efecto de obstrucción (primer término) y el efecto de fluctuación de potencia (segundo término), tal que $W \in [0, 1]$.

Resultados numéricos

A continuación se presentan algunos resultados numéricos de los parámetros mencionados anteriormente, obtenidos para diferentes niveles de turbidez y tamaños de burbujas de aire. La señal recibida se captura a una frecuencia de muestreo de 25 kHz y una resolución de 14 bits durante 5 minutos.

En las Figs. C.2 y C.3, se muestra el impacto del efecto de dispersión inducido por partículas en los histogramas de la potencia óptica recibida para diferentes concentraciones de solución de antiácido, considerando burbujas de aire pequeñas y grandes, respectivamente. Como se puede observar, los dos modelos propuestos en las Ecs. (C.3.4) y (C.3.5) se ajustan de manera precisa a los histogramas experimentales, logrando un coeficiente de determinación R^2 superior a 0.95 en todas las condiciones de dispersión evaluadas. Además, se puede observar como la pérdida de potencia atribuida a las partículas, L_p , aumenta rápidamente con la adición de antiácido, al igual que el coeficiente de extinción, abarcando así una amplia variedad de tipos de agua en términos de absorción y dispersión. Asimismo, cabe destacar que la probabilidad de bloqueo de la señal disminuye de forma significativa al incrementar la concentración de antiácido. Aunque este efecto se observa en ambos tamaños de burbujas, resulta más visible en el caso de burbujas grandes. Este fenómeno también se refleja en la reducción del índice de centelleo con el aumento de la turbidez del agua para ambos tamaños de burbujas de aire.

Por otro lado, en la Fig. C.4 también se muestra la drástica disminución del AOD debido al incremento de la turbidez del agua en ambos casos de burbujas de aire. Estos resultados respaldan la evidencia observada en los histogramas, mostrando que el efecto de dispersión inducido por partículas puede mitigar eficazmente el bloqueo de luz causado por las burbujas de aire. Por último, se observa que el tiempo de coherencia permanece constante para todas

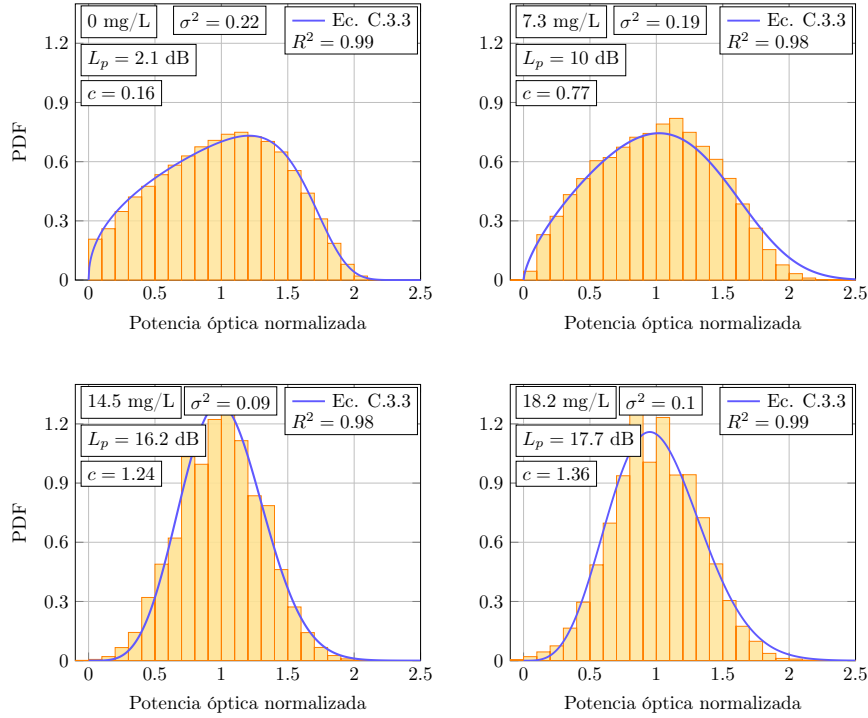


Figure C.2: Ajuste del modelo de distribución estadística propuesto bajo diferentes niveles de turbidez cuando se consideran burbujas de aire pequeñas.

las concentraciones de antiácido analizadas, tanto en el caso de burbujas pequeñas como grandes. Por lo tanto, se concluye que la turbidez del agua no tiene un impacto significativo en la correlación temporal de las fluctuaciones de potencia inducidas por burbujas de aire.

C.3.4 Rendimiento de sistemas UOWC bajo el canal empírico propuesto

Análisis de prestaciones, BER

Asumiendo CSI (*Channel State Information*) instantáneo en el receptor, y un sistema de modulación en transmisión OOK (*On-Off Keying*), la tasa de error de bit de un sistema SISO UOWC puede ser descrita como

$$P_{b_{\text{small}}} = \int_0^{\infty} Q\left(\sqrt{2\gamma} \cdot L_u \cdot h\right) \cdot f_H(h) dh. \quad (\text{C.3.6})$$

donde H es la variable aleatoria que representa la fluctuación de potencia óptica normalizada del canal UOWC, f_H es la PDF de dicha variable, y γ es el SNR (*Signal-to-Noise Ratio*) eléctrico. Así, sustituyendo la PDF empírica asociada al comportamiento de las fluctuaciones de potencia en presencia de burbujas de aire pequeñas descrita en la Ec. (C.3.4), la integral de Ec. (C.3.6) se puede resolver con la ayuda de [158, Ec. (07.34.21.0012.01)] (véase

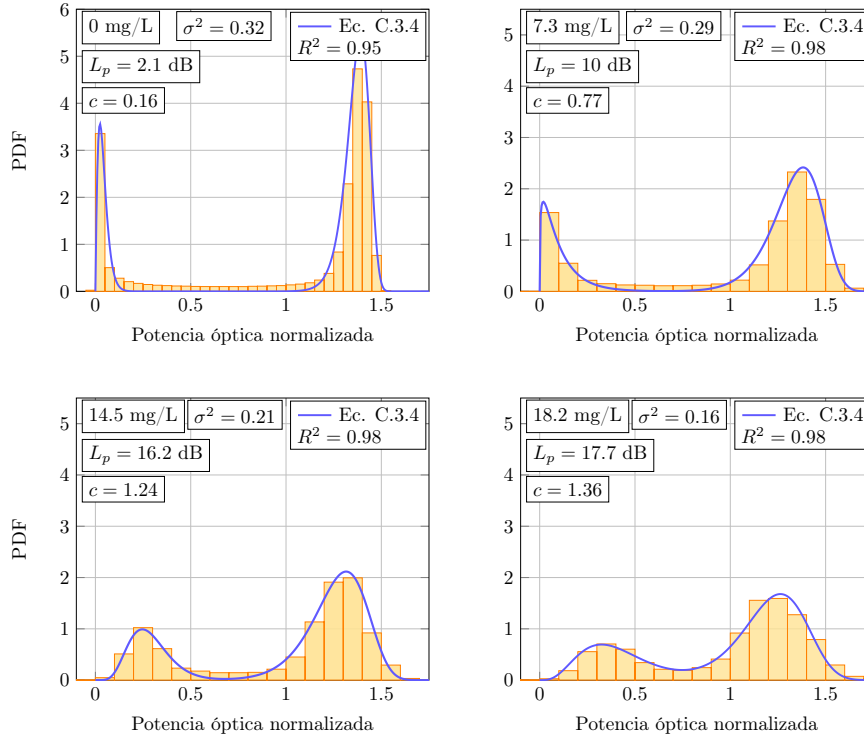


Figure C.3: Ajuste del modelo de distribución estadística propuesto bajo diferentes niveles de turbidez cuando se consideran burbujas de aire grandes.

Apéndice A.5), obteniendo una expresión analítica para evaluar la BER de un sistema SISO UOWC en presencia de burbujas de aire pequeñas

$$P_{b_{\text{small}}}(L, a, d, p) = \frac{p}{4\sqrt{\pi}(La)^d \Gamma\left(\frac{d}{p}\right) L^d} \gamma^{-\frac{d}{2}} \times H_{2,2}^{1,2} \left[\frac{1}{(La)^p} \gamma^{-\frac{p}{2}} \left| \begin{array}{c} \left(1 - \frac{d}{2}, \frac{p}{2}\right), \left(\frac{1-d}{2}, \frac{p}{2}\right) \\ (0, 1), \left(-\frac{d}{2}, \frac{p}{2}\right) \end{array} \right. \right], \quad (\text{C.3.7})$$

donde $H_{p,q}^{m,n}(\cdot)$ es la función H-Fox (véase Apéndice A.4).

De la misma forma, sustituyendo la PDF empírica asociada a las burbujas de aire grandes descrita en la Ec. (C.3.5) en la Ec. (C.3.6), es posible obtener la expresión analítica para evaluar la BER de un sistema SISO UOWC en presencia de burbujas de aire grandes. En este sentido, la BER de un sistema en presencia de burbujas grandes se puede obtener a partir de la suma ponderada de $P_{b_{\text{small}}}$ en Ec. (C.3.7) como

$$P_{b_{\text{large}}}(L, a_1, d_1, p_1, a_2, d_2, p_2, W) = W \cdot P_{b_{\text{small}}}(L, a_1, d_1, p_1) + (1 - W) \cdot P_{b_{\text{small}}}(L, a_2, d_2, p_2). \quad (\text{C.3.8})$$

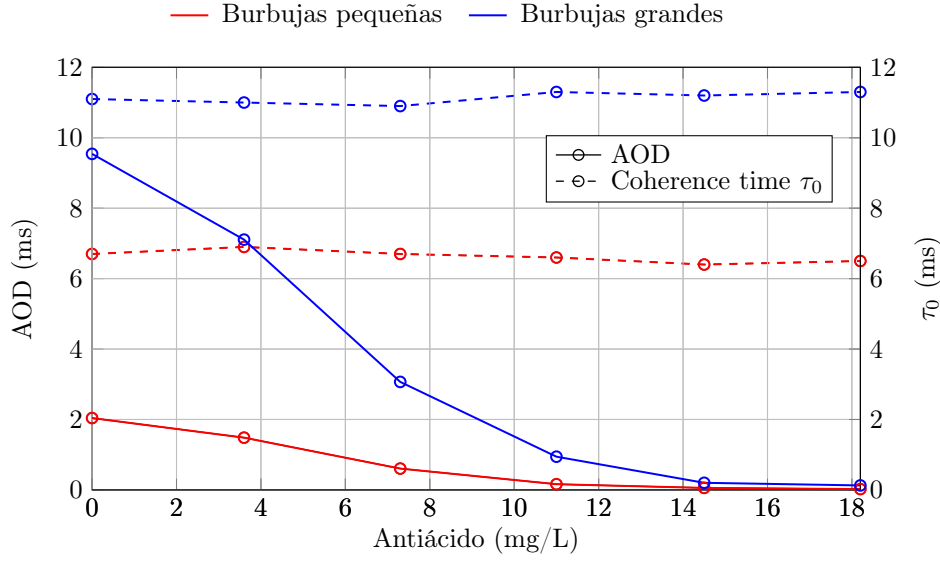


Figure C.4: Índice de centelleo, AOD, y tiempo de coherencia de las fluctuaciones bajo diferentes niveles de turbidez cuando se consideran burbujas de aire pequeñas y grandes.

Debido a que las expresiones exactas en forma cerrada pueden complicar la interpretación del impacto de los fenómenos físicos en las prestaciones del sistema UOWC, se derivan expresiones matemáticamente más simples basadas en el comportamiento asintótico en condiciones de alta SNR. En términos generales, la BER asintótica en este régimen puede obtenerse analizando el comportamiento de la PDF de la variable aleatoria cerca del origen (véase Capítulo 2.4.1) [135]. Para el caso de burbujas de aire pequeñas, se obtiene la expresión en forma cerrada asintótica para la BER promedio como

$$P_{b_{\text{small}}} \doteq \frac{p, \Gamma\left(\frac{1+d}{2}\right)}{2, \sqrt{\pi}, d(L_u, a)^d, \Gamma\left(\frac{d}{p}\right)} \gamma^{-\frac{d}{2}}. \quad (\text{C.3.9})$$

En el caso de burbujas de aire grandes, dado que $P_{b_{\text{large}}}$ es una suma ponderada de $P_{b_{\text{small}}}$, la expresión asintótica en forma cerrada para la BER promedio se obtiene fácilmente

$$P_{b_{\text{large}}} \doteq \frac{W}{2\sqrt{\pi}} \frac{p_1 \Gamma\left(\frac{1+d_1}{2}\right)}{d_1 (L_u a_1)^{d_1} \Gamma\left(\frac{d_1}{p_1}\right)} \gamma^{-\frac{d_1}{2}} + \frac{1-W}{2\sqrt{\pi}} \frac{p_2 \Gamma\left(\frac{1+d_2}{2}\right)}{d_2 (L_u a_2)^{d_2} \Gamma\left(\frac{d_2}{p_2}\right)} \gamma^{-\frac{d_2}{2}}. \quad (\text{C.3.10})$$

Resultados numéricos

A continuación se muestran algunos resultados numéricos con el objetivo de evaluar las expresiones matemáticas obtenidas a partir del modelo estadístico empírico para la BER

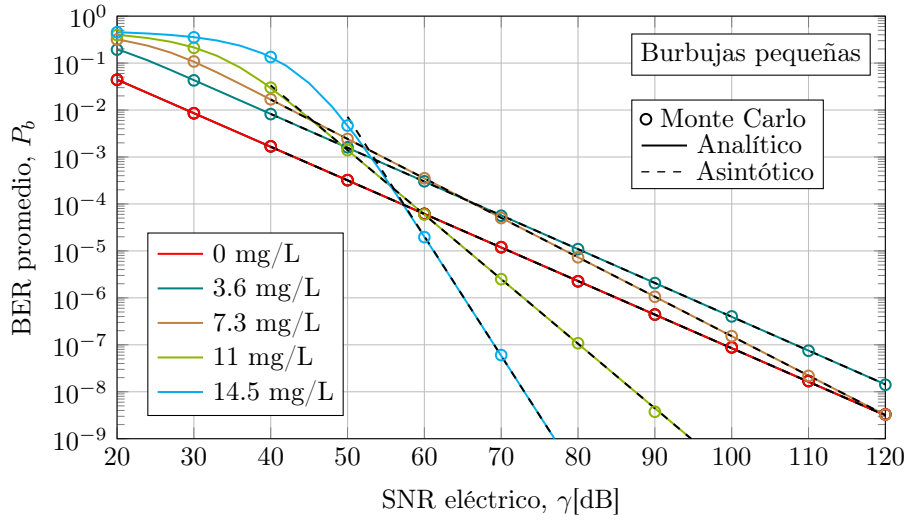


Figure C.5: BER promedio cuando se considera un modelo de canal UOWC empírico en presencia de burbujas de aire pequeñas para diferentes niveles de turbidez a una distancia de enlace de 3 metros y $\lambda = 520$ nm.

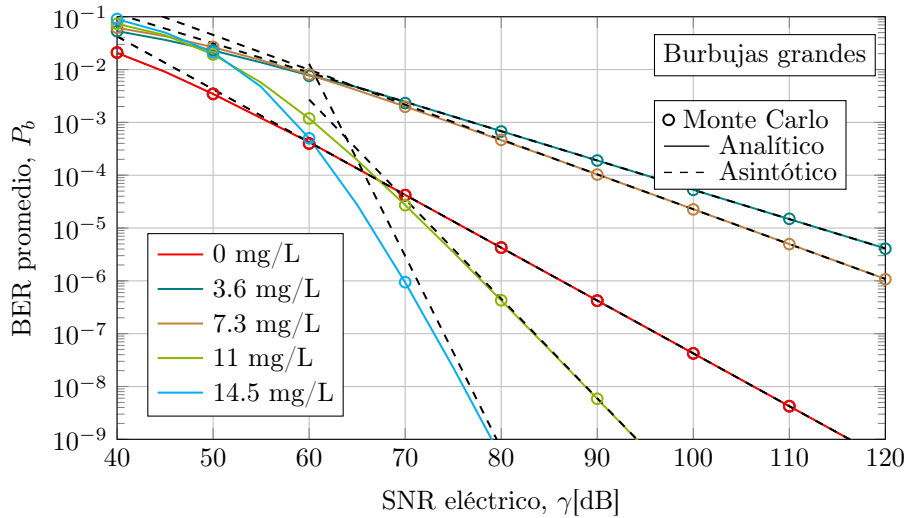


Figure C.6: BER promedio cuando se considera un modelo de canal UOWC empírico en presencia de burbujas de aire grandes para diferentes niveles de turbidez a una distancia de enlace de 3 metros y $\lambda = 520$ nm.

correspondiente a sistemas SISO UOWC en presencia de burbujas de aire. Además, se han incluido las correspondientes simulaciones de Monte Carlo con el objetivo de validar dichas expresiones matemáticas.

En las Figs. C.5 y C.6 se muestra la BER promedio de un sistema SISO UOWC bajo la influencia de burbujas de aire pequeñas y grandes, respectivamente, para diferentes niveles de dispersión. Los resultados analíticos y asintóticos obtenidos muestran una excelente concordancia con los valores obtenidos mediante simulaciones Monte Carlo, lo que valida la precisión de las expresiones propuestas. Además, se puede observar que los resultados obtenidos a partir de los datos experimentales en escenarios de mayor turbidez presentan una pendiente mayor en la curva, lo que implica un descenso mayor de la BER con el incremento del SNR. Esta pendiente se relaciona con el orden de diversidad del sistema, el cual se puede demostrar que está directamente afectado por la dispersión del canal UOWC [135].

En este sentido, es posible analizar el comportamiento de la BER promedio del sistema en dos regiones diferenciadas según el nivel de SNR. En condiciones de baja SNR, el rendimiento del sistema en términos de BER es superior en el escenario de agua de grifo. Sin embargo, a alta SNR, los escenarios con mayor turbidez muestran un mejor desempeño en términos de BER promedio. Este cambio de tendencia se debe a que la dispersión inducida por partículas mitiga los efectos negativos de las burbujas de aire al ensanchar naturalmente el haz de luz y reducir la probabilidad de bloqueo, como se discutió previamente en la Sección C.3.3.

Es importante destacar que estas conclusiones están limitadas a los datos experimentales obtenidos en el tanque de agua con una distancia de enlace de 3 m, a partir de los cuales se obtiene tanto el modelo empírico de canal, como las pérdidas debido al canal submarino. En distancias más largas, las pérdidas por absorción y dispersión, caracterizadas de manera aproximada por la ley de Beer-Lambert, aumentan exponencialmente, lo que podría revertir las ventajas observadas en escenarios con alta turbidez. Por lo tanto, aunque la dispersión inducida por partículas beneficia a los enlaces de corto alcance al mitigar el bloqueo causado por burbujas de aire, en distancias mayores las pérdidas acumuladas podrían deteriorar el rendimiento de la BER, superando incluso el obtenido en agua de grifo.

C.4 Análisis de sistemas MISO UOWC

C.4.1 Motivación

En esta sección, se presenta un análisis teórico de las prestaciones en términos de BER de dos sistemas MISO: un primer sistema con un esquema de repetición de código espacial (*Spatial Repetition Coding*, SRC) y un segundo sistema con un esquema de selección de láser en transmisión (*Transmit Laser Selection*, TLS). Ambos sistemas son evaluados sobre un canal UOWC en presencia de absorción, dispersión y turbulencias oceánicas modeladas a partir de la distribución de probabilidad Weibull.

Tras revisar la literatura existente sobre sistemas de transmisión y recepción basados en diversidad espacial en canales UOWC, se puede observar que dichos estudios han centrado el

análisis dichos esquemas para mitigar el efecto de las turbulencias oceánicas. En este sentido, la gran mayoría de los trabajos no analizan las prestaciones de los esquemas propuestos en entornos submarinos realistas donde se considere el tipo de agua, distancias de enlace realistas, o el impacto de la atenuación del canal. Esto resulta particularmente relevante, dado que el principal factor limitante en el despliegue de enlaces UOWC en escenarios reales es la corta distancia de enlace, causada por los elevados niveles de absorción y dispersión inherentes al canal submarino.

En este contexto, se propone, en primer lugar, un nuevo diseño de esquema SRC que sea capaz de mitigar tanto los efectos significativos de absorción y dispersión como los de las turbulencias oceánicas. Este diseño contempla un transmisor en el que las fuentes emisoras de luz están separadas por una distancia suficiente que permita que cada emisor opere dentro de la restricción de potencia máxima por fuente establecida por la normativa IEC60825-1 [78] de la *International Electrotechnical Commission* (IEC). En segundo lugar, se introduce un modelo generalizado del sistema TLS, denominado como GTLS, que incorpora el impacto de selecciones erróneas de la fuente láser más óptima en transmisión debido a una información del estado del canal (*Channel State Information*, CSI) imperfecta en el transmisor.

C.4.2 Consideraciones de seguridad ocular

La máxima potencia óptica permitida en un diodo láser está regulada por el límite de exposición máxima permisible (*Maximum Permissible Exposure*, MPE), que establece los niveles de exposición máximos de un ojo a una fuente de luz sin que se produzca daño ocular [78]. Según la normativa, el MPE debe medirse en una apertura de 7 mm, que representa el diámetro promedio de una pupila dilatada, a una distancia de 100 mm, correspondiente a la distancia mínima de acomodación ocular. Así, en el caso de que un ojo humano se exponga a la luz proveniente de múltiples emisores LD, la potencia máxima de cada emisor debe limitarse para cumplir con los requisitos de seguridad ocular.

Sin embargo, mediante un análisis geométrico que considera la divergencia angular del haz de un LD, se puede calcular la distancia mínima entre emisores que permita a cada uno operar a la potencia máxima permitida por el MPE. Dicho de otro modo, separando lo suficientes los emisores LD, se puede asegurar que un ojo que observe un transmisor con varios emisores LD a 100 mm de distancia, solo reciba luz de un único emisor. Esta distancia mínima, $d_{t_{\min}}$, se expresa como $d_{t_{\min}} = \phi_p + w_z$, donde ϕ_p es el diámetro de la pupila y $w_z = \theta \cdot 100$ es el ancho del haz a una distancia de 100 mm, siendo θ la divergencia angular del LD. Por ejemplo, para $\theta = 12$ mrad, se obtiene $d_{t_{\min}} = 8.2$ mm, lo cual resulta en una configuración física coherente y aplicable a sistemas comerciales, como el Sonardyne BlueComm 200 [48]. La Fig. C.7 ilustra un sistema MISO que garantiza la seguridad ocular bajo estas condiciones de operación.

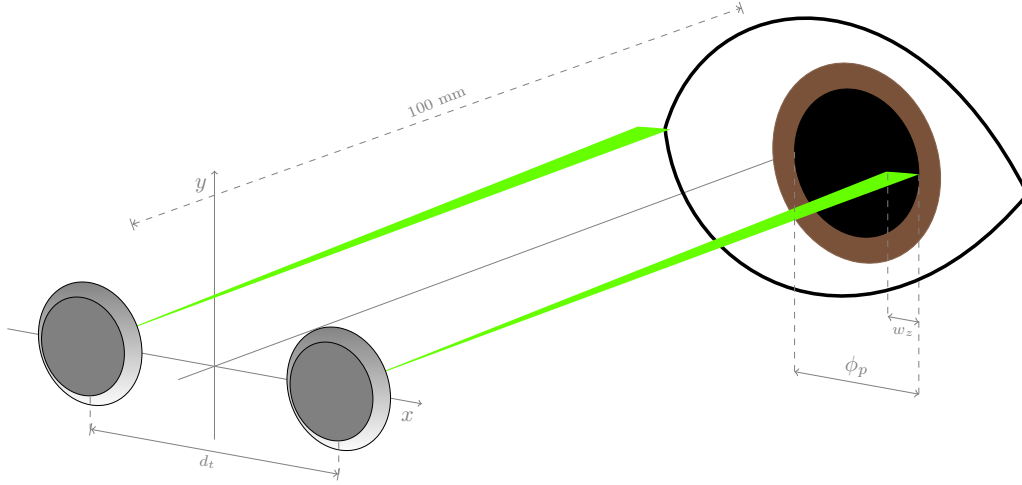


Figure C.7: Representación geométrica de un sistema MISO que cumple con las regulaciones de seguridad ocular cuando dos emisores operan simultáneamente bajo una restricción de potencia por fuente.

C.4.3 Modelo de canal óptico submarino

El canal óptico submarino se modela mediante una ganancia de canal compuesta que incluye las pérdidas oceánicas debidas a la propagación de la luz, L , y el desvanecimiento inducido por la turbulencia oceánica, H_o . Las pérdidas oceánicas se obtienen como

$$L = A_0 \times e^{-\alpha \cdot c \cdot d}, \quad (\text{C.4.1})$$

donde $A_0 = \left(\text{erf} \left[\frac{\sqrt{\pi}}{\sqrt{2}w_z} \right] \right)^2$ representa las pérdidas geométricas de un haz gaussiano normalizado con respecto al radio del receptor, y α es un factor de corrección que considera los fotones dispersos recibidos que no son contabilizados en la ley de Beer-Lambert [25].

Por otro lado, las fluctuaciones de potencia aleatorias inducidas por la turbulencia oceánica se modela estadísticamente mediante una distribución Weibull, cuya PDF se define como

$$f_{H_o}(h) = \frac{\beta_1}{\beta_2} \left(\frac{h}{\beta_2} \right)^{\beta_1 - 1} e^{-\left(\frac{h}{\beta_2} \right)^{\beta_1}}, \quad (\text{C.4.2})$$

donde β_1 y β_2 son los parámetros característicos de la distribución. Estos parámetros se calculan a partir del índice de centelleo $\sigma_{H_o}^2$, obtenido a partir de la densidad espectral de potencia asociada a las variaciones del índice de refracción de Nikishov [29, 30] (véase Sección 2.3.1). En particular, β_1 se aproxima como [141]

$$\beta_1 \simeq (\sigma_{H_o}^2)^{-6/11}, \quad (\text{C.4.3})$$

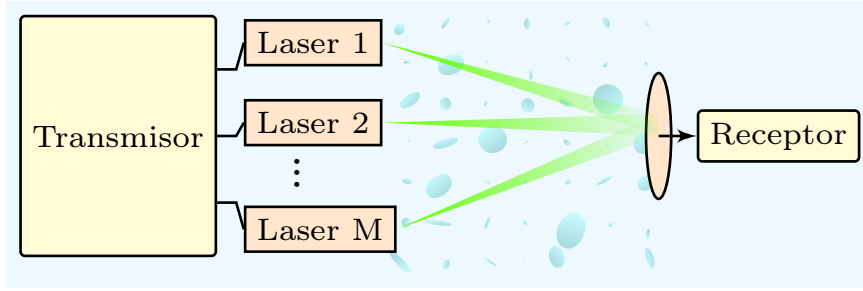


Figure C.8: Diagrama de bloques del sistema SRC propuesto.

y β_2 se define como

$$\beta_2 = \frac{1}{\Gamma\left(1 + \frac{1}{\beta_1}\right)}. \quad (\text{C.4.4})$$

C.4.4 Esquema SRC

En la Fig. C.8 se muestra el diagrama de bloques del esquema SRC propuesto. Los sistemas de RF tradicionales están sujetos a una restricción de potencia promedio por transmisor, impuesta por regulaciones de radiación, lo que implica que la potencia máxima de cada emisor se divide entre todos los emisores. En cambio, el esquema SRC propuesto permite una restricción de potencia por fuente, lo que significa que cada emisor opera con su potencia óptica máxima, aumentando la potencia óptica total enviada sin sobrepasar la MPE dada la distancia mínima entre emisores previamente definida. Esto facilita un aumento en la potencia óptica total emitida y ayuda a mitigar los efectos adversos de la absorción y la dispersión.

El sistema propuesto modela la fotocorriente generada en el receptor como

$$y = x \frac{\rho}{M} \cdot L \cdot R \cdot \sum_{i=1}^M H_{o_i} + z, \quad (\text{C.4.5})$$

donde M es el número de fuentes láser y H_{o_i} representa la fluctuación de intensidad óptica en el i -ésimo canal. Si $\rho = 1$, el sistema SRC adopta una restricción de potencia por fuente, mientras que si $\rho = M$, adopta una restricción de potencia por emisor. Para analizar el canal compuesto $H_{\text{SRC}} = \sum_{i=1}^M H_{o_i}$, donde H_{o_i} es la ganancia de canal de cada emisor, se propone una aproximación del PDF de Weibull mediante expansión de Taylor para simplificar su representación matemática. A través de la función generadora de momentos y la transformada inversa de Laplace (véase Capítulo 4), la PDF asintótica de H_{SRC} se obtiene como

$$f_{H_{\text{SRC}}}(h) \doteq \left(\frac{\beta_1 \Gamma(\beta_1)}{\beta_2^{\beta_1}} \right)^M \frac{h^{M\beta_1-1}}{\Gamma(M\beta_1)}. \quad (\text{C.4.6})$$

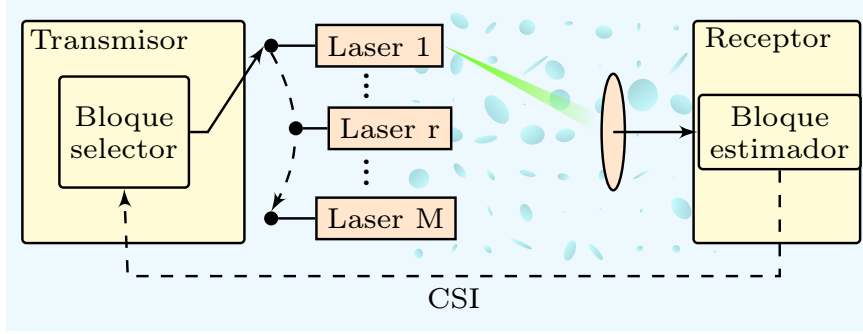


Figure C.9: Diagrama de bloques del sistema TLS propuesto.

Con la expresión C.4.6, podemos obtener el comportamiento asintótico de la BER como

$$P_{b_{\text{SRC}}} \doteq \frac{\left(\beta_1 \left(\frac{\beta_2 L \rho}{M} \right)^{-\beta_1} \Gamma(\beta_1) \right)^M}{2^{1+M\beta_1} \Gamma\left(\frac{M\beta_1}{2} + 1\right)} \gamma^{-\frac{\beta_1}{2} M}. \quad (\text{C.4.7})$$

C.4.5 Esquema TLS

En la Fig. C.9 se muestra el diagrama de bloques del esquema TLS propuesto. En este esquema, solo el LD que presenta el canal con mayor SNR transmite la información, mientras los demás permanecen inactivos. Si el transmisor cuenta con información perfecta del estado del canal (CSIT), el canal de un sistema TLS se describe como $H_{\text{TLS}} = L \cdot \max(H_{o_1}, \dots, H_{o_M})$. La función de distribución acumulativa (*Cumulative Density Function*, CDF) asociada a H_{TLS} puede derivarse asumiendo la independencia estadística de los canales, tal que $F_{H_{\text{TLS}}}(h) = [F_{H_o}(h)]^M$ [172, 183]. Así, la PDF se deriva como $f_{H_{\text{TLS}}}(h) = M f_{H_o}(h) [F_{H_o}(h)]^{M-1}$ tal que

$$f_{H_{\text{TLS}}}(h) = \frac{M\beta_1}{\beta_2^{\beta_1}} h^{\beta_1-1} \sum_{k=0}^{M-1} (-1)^k \binom{M-1}{k} \left(e^{-\left(\frac{h}{\beta_2}\right)^{\beta_1}} \right)^{k+1}. \quad (\text{C.4.8})$$

Generalización del sistema TLS

El esquema TLS puede generalizarse a un modelo más realista suponiendo que el transmisor seleccione el r -ésimo peor canal (el canal con la ganancia de canal menor), donde $1 \leq r \leq M$, debido a errores en el enlace de *feedback* que provoquen un CSI imperfecto en el transmisor.

La PDF del canal del r -ésimo peor canal se obtiene como [183, Eq. (2.1.3)]

$$f_{H_{or}}(h | r) = \frac{M!}{(r-1)!(M-r)!} \frac{\beta_1}{\beta_2^{\beta_1}} h^{\beta_1-1} \times \sum_{k=0}^{r-1} (-1)^k \binom{r-1}{k} \left(e^{-\left(\frac{h}{\beta_2}\right)^{\beta_1}} \right)^{(k+1+M-r)}. \quad (\text{C.4.9})$$

Así, el comportamiento de la BER de un sistema TLS que transmite por el r -ésimo peor canal viene dado por

$$P_{b_{\text{TLS}}}(r) = \frac{\beta_1 M!}{(r-1)!(M-r)!} \frac{\sum_{k=0}^{r-1} (-1)^k \binom{r-1}{k}}{4\sqrt{\pi} (\beta_2 L \sqrt{\gamma})^{\beta_1}} \times H_{2,2}^{1,2} \left(\frac{k+M-r+1}{(\sqrt{\gamma} L \beta_2)^{\beta_1}} \left| \begin{array}{c} \left(\frac{1-\beta_1}{2}, \frac{\beta_1}{2}\right), \left(1-\frac{\beta_1}{2}, \frac{\beta_1}{2}\right) \\ (0, 1), \left(\frac{-\beta_1}{2}, \frac{\beta_1}{2}\right) \end{array} \right. \right), \quad (\text{C.4.10})$$

El correspondiente comportamiento asintótico puede ser obtenido a través de la aproximación de la PDF de H_{TLS} a través del primer coeficiente de la expansión de Taylor de la Ec. C.4.7 como

$$P_{b_{\text{TLS}}}(r) \doteq \frac{M!}{r!(M-r)!} \frac{\Gamma\left(\frac{1}{2}(r\beta_1 + 1)\right)}{2\sqrt{\pi}(\beta_2 L)^{r\beta_1}} \gamma^{-\frac{\beta_1}{2}r}. \quad (\text{C.4.11})$$

Para modelar la aleatoriedad del canal y su impacto en la variabilidad del CSI en el transmisor, se asume que la selección del canal (r) es una variable aleatoria discreta. En situaciones ideales el transmisor selecciona siempre el mejor canal, mientras que en condiciones de completa incertidumbre, la selección es uniforme entre todos los emisores disponibles. Aplicando el principio de máxima entropía, la distribución de r se modela como una distribución geométrica, descrita como

$$f_r(r) = \frac{e^{l \cdot r}}{\sum_{i=1}^M e^{l \cdot i}}, \quad (\text{C.4.12})$$

donde l es una constante de crecimiento de la exponencial que se puede utilizar para describir la precisión de la CSIT. En aras de manejar un parámetro más intuitivo para describir el conocimiento del CSI en el transmisor, se define el parámetro p_M como la probabilidad de seleccionar el mejor canal (p_M). Para una CSIT perfecta, $p_M \rightarrow 100\%$, y para incertidumbre completa, $p_M = \frac{1}{M}$. La PDF del esquema GTLS se obtiene ponderando la probabilidad de cada emisor de ser seleccionado como

$$f_{H_{\text{GTLS}}}(h) = \sum_{r=1}^M f_r(r) \cdot f_{H_{or}}(h | r). \quad (\text{C.4.13})$$

En la Figura C.10, se muestra como este enfoque abarca un amplio espectro de escenarios, desde el caso más desfavorable, en el que la CSI es completamente imperfecta o inexistente y el transmisor selecciona de forma uniforme entre los emisores ($p_M = \frac{1}{M}$, correspondiente

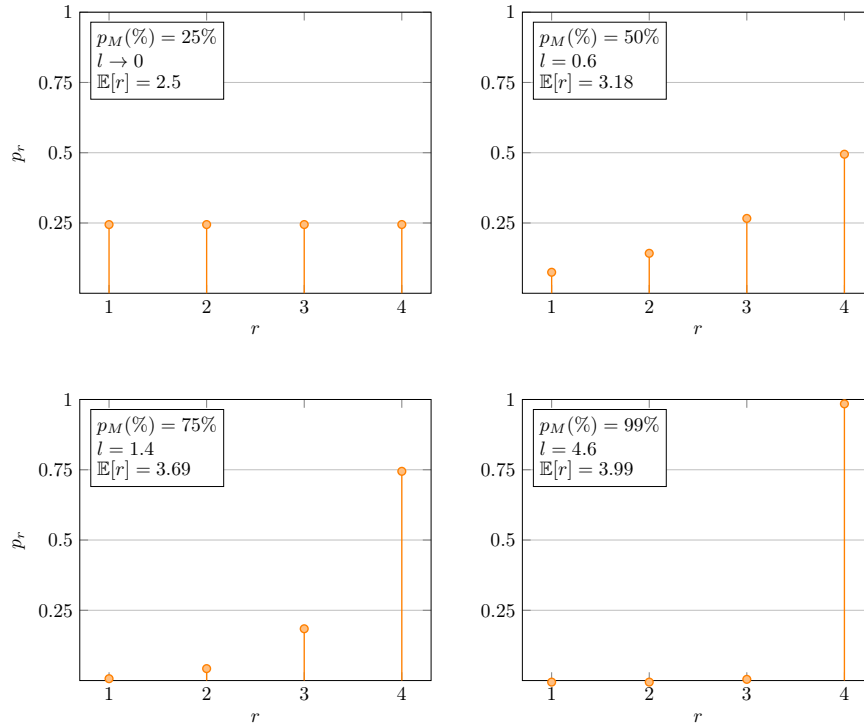


Figure C.10: Función de densidad de probabilidad de r para 4 emisores.

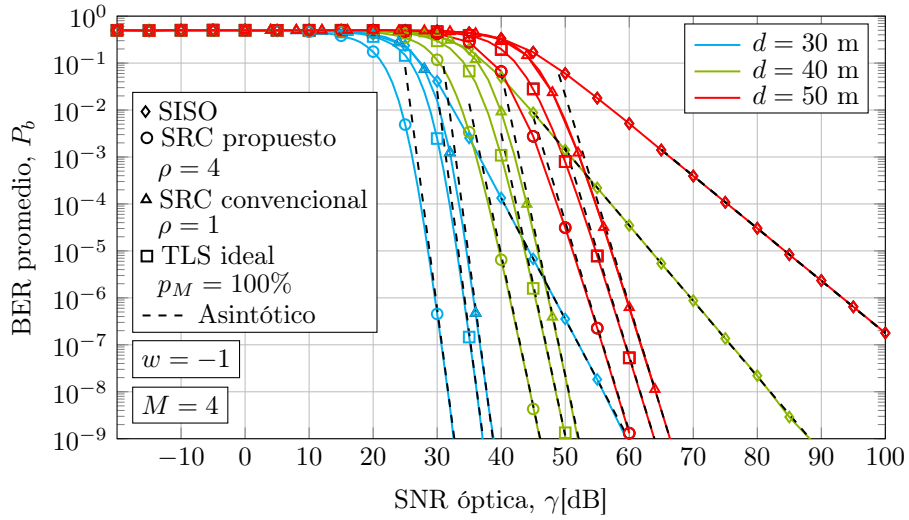
a $l = 0$), hasta el caso ideal en el que se dispone siempre de CSI perfecta ($p_M = 100\%$, representado por $l \rightarrow \infty$).

A través de este modelo, el comportamiento de la BER de un sistema TLS generalizado se puede obtener promediando la Ec. C.4.10 con la PDF propuesta en Ec. C.4.12 como

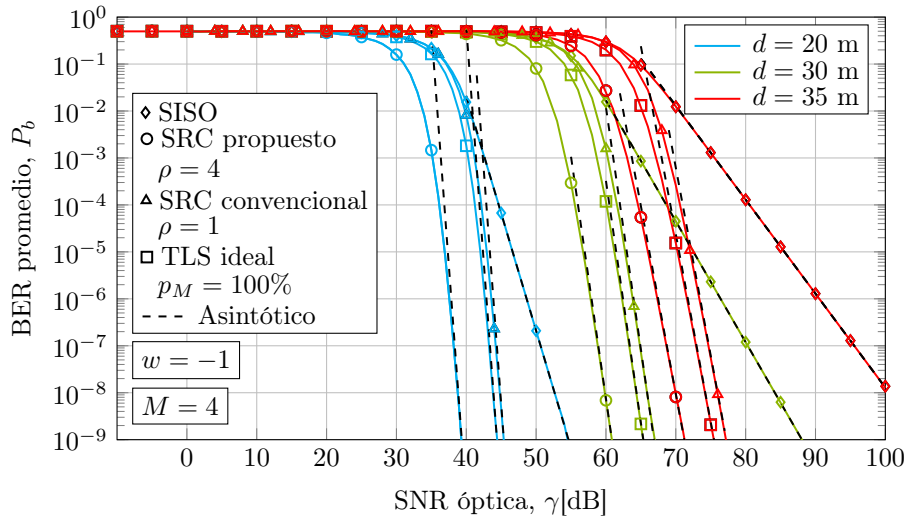
$$P_{b_{\text{GTLS}}} = \sum_{r=1}^M f_r(r) \cdot P_{b_{\text{TLS}}}(r). \quad (\text{C.4.14})$$

C.4.6 Resultados numéricos

En la Fig. C.11, se muestra la BER promedio de los sistemas MISO UOWC propuestos en presencia de turbulencias oceánicas con $w = -1$ y varias distancias de enlace, utilizando los esquemas SRC y GTLS con 4 emisores y CSI en el transmisor perfecto. Los resultados demuestran que las expresiones analíticas propuestas para el desempeño promedio de BER en sistemas UOWC son muy precisas, ya que se ajustan a los resultados obtenidos vía simulación Monte Carlo en diferentes tipos de agua y distancias de enlace. Además, se destaca el impacto crítico de la dispersión y la pérdida de camino, especialmente en aguas costeras, donde la BER se deteriora significativamente en comparación con aguas claras.



(a) Clear ocean water

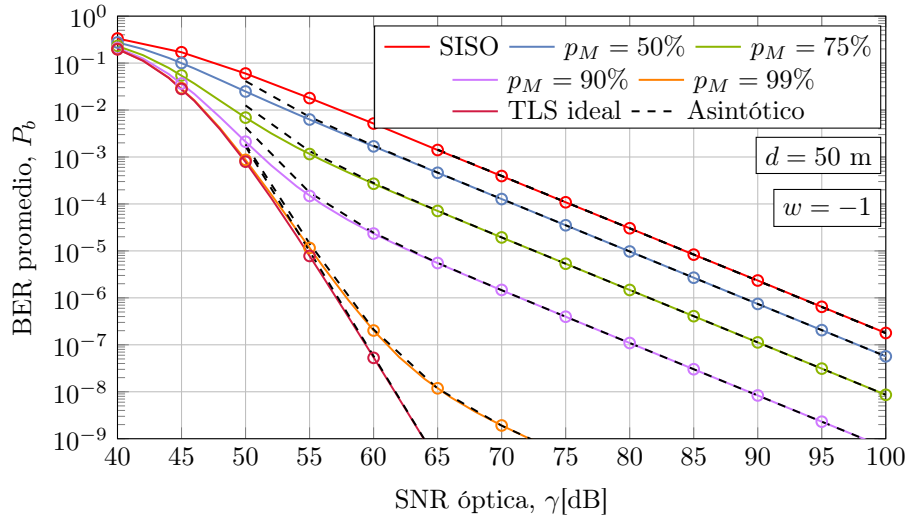


(b) Coastal water

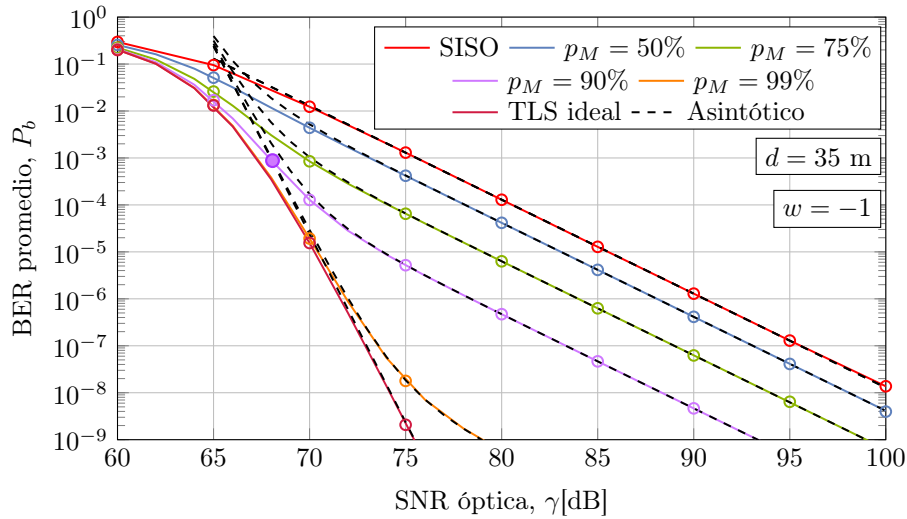
Figure C.11: BER promedio de sistemas MISO UOWC en océano claro (a) y agua de costa (b) en presencia de turbulencias oceánicas con $w = -1$ y varias distancias de enlace, utilizando los esquemas SRC y GTLS con 4 emisores y CSI en el transmisor perfecto.

Por último, se confirma que la técnica SRC propuesta, donde se aumenta la potencia óptica total transmitida, supera al esquema TLS ideal en ambos tipos de agua, subrayando su ventaja como solución eficiente para canales UOWC donde la absorción y la dispersión son el principal inconveniente, y las turbulencias oceánicas un efecto de menor importancia.

En la Fig. C.12 se analiza el impacto de errores en la selección de emisores debido a una CSI imperfecto en el transmisor en sistemas TLS, considerando distintas probabilidades de



(a) Clear ocean water



(b) Coastal water

Figure C.12: BER promedio de sistemas GTLS UOWC en océano claro (a), y agua de costa (b), en presencia de turbulencias oceánicas con $w = -1$ para diferentes escenarios de CSI imperfecto en el transmisor.

obtener una CSI perfecta. Los resultados, tanto analíticos como asintóticos, coinciden estrechamente con simulaciones Monte Carlo, validando las expresiones propuestas. Se observa que, aunque la probabilidad de seleccionar emisores incorrectos sea baja, las prestaciones del sistema GTLS es altamente sensible con respecto al conocimiento del CSI en el transmisor. Sin embargo, se destaca que, a medida que aumenta la probabilidad de obtener CSI perfecto en el transmisor, la mejora en las prestaciones del sistema es muy notable. Estos hallazgos

cuantifican el impacto de una CSI imperfecta y subrayan las limitaciones prácticas de los sistemas TLS. Asimismo, se resalta que el receptor puede estimar el nivel de conocimiento de CSI en el transmisor al comparar la BER experimental con la obtenida teóricamente para dicho escenario. Esto permitiría optimizar dinámicamente el enlace de retroalimentación y mejorar el estado del CSI en el transmisor.

C.5 Conclusiones y líneas futuras

C.5.1 Conclusiones

En esta tesis se abordan algunos de los desafíos clave en el modelado estadístico del canal óptico submarino, debido a la complejidad de los fenómenos que afectan la propagación de la luz en el agua y su interrelación. Así, se propone el desarrollo de modelos estadísticos del canal UOWC que describan de manera más realista el efecto de la dispersión y otros efectos oceánicos. A diferencia de trabajos previos, se enfatiza el papel central de la dispersión como característica del canal óptico submarino, evaluando las métricas de rendimiento para distintos niveles de turbidez y tipos de agua.

Para ello, se desarrolla un modelo empírico de canal UOWC en base a medidas experimentales obtenidas en un banco de pruebas experimental UOWC desarrollado en esta tesis. El emulador de canal UOWC emula diversos efectos del canal submarino como burbujas de aire y corrientes de agua. Además, se modifica el nivel de turbidez del agua a partir de un antiácido comercial que modifica las propiedades de absorción y dispersión del agua. Las fluctuaciones de potencia óptica obtenidas para las diferentes configuraciones del emulador se modelan mediante la distribución Gamma generalizada. Los resultados muestran que, en escenarios con mayor turbidez, la obstrucción de luz debido a las burbujas disminuye significativamente por la captura de luz dispersa que llega al fotodetector. El índice de centelleo y la duración promedio de bloqueos disminuyen con la concentración de partículas, mientras que el tiempo de coherencia de las fluctuaciones se mantiene constante, independientemente de la turbidez. A partir del modelo empírico, se derivan expresiones analíticas y asintóticas para la BER y la probabilidad de *outage*. Los resultados muestran que el orden de diversidad de un sistema UOWC bajo este canal aumenta conforme se incrementa la turbidez. Además, se confirma que el esparcimiento natural del haz óptico, inducido por las partículas submarinas, actúa como un mecanismo inherente para mitigar las fluctuaciones y obstrucciones de luz causadas por las burbujas, mejorando significativamente el rendimiento del sistema UOWC.

Asimismo, se presentan nuevas perspectivas sobre las restricciones de potencia óptica para la adaptación de transceptores UOWC en entornos subacuáticos turbios en sistemas MISO. En este sentido, se desarrolla un esquema SRC que permite operar bajo una restricción de potencia por fuente incrementando la potencia óptica máxima en comparación con los

enfoques convencionales, así como una restricción de potencia por transmisor, lo que permite optimizar las limitaciones energéticas del sistema MISO de forma dinámica. Además, se introduce un nuevo esquema generalizado basado en un sistema MISO TLS que permite modelar de manera más realista los errores en la selección del emisor de luz con mejor canal debido a un conocimiento imperfecto del CSI en el transmisor. En primer lugar, los resultados muestran que el sistema SRC supera al sistema TLS incluso en escenarios donde se considera CSI perfecto, ya que reduce el impacto negativo de la absorción y dispersión mediante la transmisión de mayor potencia óptica. En entornos con efectos significativos de absorción y dispersión, como aguas costeras y de puerto, el diseño de transmisores con restricción de potencia por fuente hace que el SRC sea la opción óptima. Finalmente, se destaca que los esquemas TLS son muy sensibles a la CSI imperfecta en el lado del transmisor.

C.5.2 Líneas futuras

A continuación, se muestran algunas líneas futuras de investigación las cuales han sido derivadas de las investigaciones realizadas en esta tesis, que profundizan en el ámbito del modelado de canal óptico submarino y el estudio de sistemas UOWC más complejos que permitan el despliegue de redes UOWC de mayor distancia y velocidades de transmisión.

- **Análisis de haces con momento angular orbital (*Orbital Angular Momentum, OAM*):** Evaluar el uso de haces OAM en entornos submarinos, especialmente en aguas turbias, para aumentar la capacidad del sistema mediante multiplexación espacial.
- **Caracterización de láseres de pulsos ultracortos (*Ultrashort Pulse Lasers, USPL*):** Investigar su desempeño frente a láseres de onda continua en entornos submarinos, considerando fenómenos como la dispersión del grupo de velocidad.
- **Emulación de turbulencia oceánica:** Mejorar el banco de pruebas para simular turbulencia inducida por temperatura y salinidad mediante sistemas dinámicos de mezcla de agua.
- **Compensación de dispersión con óptica adaptativa:** Aplicar técnicas de reconstrucción de frente de onda, utilizadas en astronomía y medicina, para mitigar los efectos de la dispersión del medio submarino y mejorar el desempeño de sistemas UOWC.

References

- [1] Organisation for Economic Co-operation and Development (OECD), *The Ocean Economy in 2030*. OECD Publishing, Apr. 2016.
- [2] E. Commission, D.-G. for Maritime Affairs, Fisheries, and J. R. Centre, *The EU Blue Economy Report 2024*. Publications Office of the European Union, 2024.
- [3] K. Koutsopoulos and J. H. Stel, *Ocean Literacy: Understanding the Ocean*. Springer, 2021.
- [4] E. E. Cordes and L. A. Levin, “Exploration before exploitation,” *Science*, vol. 359, no. 6377, pp. 719–719, 2018.
- [5] N. R. Council, D. on Earth, L. Studies, O. S. Board, and C. on Exploration of the Seas, *Exploration of the Seas: Voyage into the Unknown*. National Academies, 2003.
- [6] Intergovernmental Oceanographic Commission, *The International Decade of Ocean Exploration (IDOE), 1971-1980*. United Nations Educational, Scientific and Cultural Organisation (UNESCO), 1975.
- [7] J.-B. Jouffray, R. Blasiak, A. V. Norström, H. Österblom, and M. Nyström, “The blue acceleration: the trajectory of human expansion into the ocean,” *One Earth*, vol. 2, no. 1, pp. 43–54, 2020.
- [8] United Nations Decade of Ocean Science for Sustainable Development (2021-2030), “Ocean Decade,” [Accessed 27-09-2024]. [Online]. Available: <https://oceandecade.org>
- [9] M. Jahanbakht, W. Xiang, L. Hanzo, and M. R. Azghadi, “Internet of underwater things and big marine data analytics—a comprehensive survey,” *IEEE Communications Surveys & Tutorials*, vol. 23, no. 2, pp. 904–956, 2021.
- [10] Y. Guo, M. Kong, O. Alkhazragi, M. A. Sait, C. H. Kang, I. Ashry, Q. Yang, T. K. Ng, and B. S. Ooi, “Current trend in optical internet of underwater things,” *IEEE Photon. J.*, vol. 14, no. 5, pp. 1–14, 2022.

- [11] C. T. Nguyen, M. T. Nguyen, and V. V. Mai, "Underwater optical wireless communication-based IoUT networks: MAC performance analysis and improvement," *Optical Switching and Networking*, vol. 37, p. 100570, 2020.
- [12] Y. Lou and N. Ahmed, *Underwater Communications and Networks*. Springer, 2022.
- [13] M. F. Ali, D. N. K. Jayakody, Y. A. Chursin, S. Affes, and S. Dmitry, "Recent advances and future directions on underwater wireless communications," *Archives of Computational Methods in Engineering*, vol. 27, pp. 1379–1412, 2020.
- [14] M. Stojanovic, "On the relationship between capacity and distance in an underwater acoustic communication channel," *ACM SIGMOBILE Mobile Computing and Communications Review*, vol. 11, no. 4, pp. 34–43, 2007.
- [15] I. F. Akyildiz, D. Pompili, and T. Melodia, "Underwater acoustic sensor networks: research challenges," *Ad hoc networks*, vol. 3, no. 3, pp. 257–279, 2005.
- [16] C. M. Gussen, P. S. Diniz, M. L. Campos, W. A. Martins, F. M. Costa, and J. N. Gois, "A survey of underwater wireless communication technologies," *J. Commun. Inf. Sys.*, vol. 31, no. 1, pp. 242–255, 2016.
- [17] R. K. Moore, "Radio communication in the sea," *IEEE Spectrum*, vol. 4, no. 11, pp. 42–51, 1967.
- [18] F. Hanson and S. Radic, "High bandwidth underwater optical communication," *Applied Optics*, vol. 47, no. 2, pp. 277–283, 2008.
- [19] Z. Zeng, S. Fu, H. Zhang, Y. Dong, and J. Cheng, "A survey of underwater optical wireless communications," *IEEE Commun. Surv. & Tut.*, vol. 19, no. 1, pp. 204–238, 2017.
- [20] C. Lu, J. Wang, S. Li, and Z. Xu, "60m/2.5 Gbps underwater optical wireless communication with NRZ-OOK modulation and digital nonlinear equalization," in *2019 Conference on Lasers and Electro-Optics (CLEO)*. IEEE, 2019, pp. 1–2.
- [21] X. Chen, W. Lyu, Z. Zhang, J. Zhao, and J. Xu, "56-m/3.31-Gbps underwater wireless optical communication employing nyquist single carrier frequency domain equalization with noise prediction," *Opt. Express*, vol. 28, no. 16, pp. 23 784–23 795, 2020.
- [22] T. Zhang, C. Fei, Y. Wang, J. Du, Y. Xie, F. Zhang, J. Tian, G. Zhang, G. Wang, X. Hong *et al.*, "4-Gbps low-latency FPGA-based underwater wireless optical communication," *Opt. Express*, vol. 32, no. 21, pp. 36 207–36 222, 2024.
- [23] G. Schirripa Spagnolo, L. Cozzella, and F. Leccese, "Underwater optical wireless communications: Overview," *Sensors*, vol. 20, no. 8, p. 2261, 2020.

- [24] B. Cochenour, L. Mullen, and J. Muth, “Temporal response of the underwater optical channel for high-bandwidth wireless laser communications,” *IEEE Journal of Oceanic Engineering*, vol. 38, no. 4, pp. 730–742, 2013.
- [25] R. Boluda-Ruiz, P. Rico-Pinazo, B. Castillo-Vázquez, A. García-Zambrana, and K. Qaraqe, “Impulse response modeling of underwater optical scattering channels for wireless communication,” *IEEE Photonics Journal*, vol. 12, no. 4, pp. 1–14, 2020.
- [26] B. M. Cochenour, L. J. Mullen, and A. E. Laux, “Characterization of the beam-spread function for underwater wireless optical communications links,” *IEEE Journal of Oceanic Engineering*, vol. 33, no. 4, pp. 513–521, 2008.
- [27] R. J. Hill, “Models of the scalar spectrum for turbulent advection,” *Journal of Fluid Mechanics*, vol. 88, no. 3, pp. 541–562, 1978.
- [28] ———, “Optical propagation in turbulent water,” *JOSA*, vol. 68, no. 8, pp. 1067–1072, 1978.
- [29] V. V. Nikishov and V. I. Nikishov, “Spectrum of turbulent fluctuations of the sea - water refraction index,” *International Journal of Fluid Mechanics Research*, vol. 27, no. 1, 2000.
- [30] O. Korotkova, N. Farwell, and E. Shchepakina, “Light scintillation in oceanic turbulence,” *Waves in Random and Complex Media*, vol. 22, no. 2, pp. 260–266, 2012.
- [31] J. R. Waaland and D. Branton, “Gas vacuole development in a blue-green alga,” *Science*, vol. 163, no. 3873, pp. 1339–1341, 1969.
- [32] S. Thorpe and P. Humphries, “Bubbles and breaking waves,” *Nature*, vol. 283, no. 5746, pp. 463–465, 1980.
- [33] S. Ling and H. Pao, “Study of micro-bubbles in the north sea,” in *Sea Surface Sound: Natural Mechanisms of Surface Generated Noise in the Ocean*. Springer, 1988, pp. 197–210.
- [34] S. Arnon and D. Kedar, “Non-line-of-sight underwater optical wireless communication network,” *JOSA A*, vol. 26, no. 3, pp. 530–539, 2009.
- [35] C. Fang, S. Li, Y. Wang, and K. Wang, “Investigation of non-line-of-sight underwater optical wireless communications with wavy surface,” *Opt. Express*, vol. 32, no. 4, pp. 4799–4815, 2024.
- [36] P. Samaniego-Rojas, R. Boluda-Ruiz, J. M. Garrido-Balsells, B. Castillo-Vázquez, A. Puerta-Notario, and A. García-Zambrana, “Exploring the effect of a wavy sea surface on NLOS-UOWC systems: A novel deterministic approach,” *Sensors*, vol. 25, no. 3, p. 695, 2025.

- [37] H. Kaushal and G. Kaddoum, “Underwater optical wireless communication,” *IEEE Access*, vol. 4, pp. 1518–1547, 2016.
- [38] A. G. Bell, “The photophone,” *Science*, no. 11, pp. 130–134, 1880.
- [39] F. E. Goodwin, “A review of operational laser communication systems,” *Proceedings of the IEEE*, vol. 58, no. 10, pp. 1746–1752, 1970.
- [40] M. A. Khalighi and M. Uysal, “Survey on free space optical communication: A communication theory perspective,” *IEEE Commun. Surv. & Tut.*, vol. 16, no. 4, pp. 2231–2258, 2014.
- [41] J. R. Barry, *Wireless infrared communications*. Springer Science & Business Media, 1994, vol. 280.
- [42] L. C. Andrews, R. L. Phillips, and C. Y. Hopen, *Laser beam scintillation with applications*. SPIE press, 2001, vol. 99.
- [43] S. Karmous, N. Adem, M. Atiquzzaman, and S. Samarakoon, “How can optical communications shape the future of deep space communications? A survey,” *IEEE Commun. Surv. & Tut.*, 2024.
- [44] “The fSONA Networks, Inc.” [Online]. Available: <http://www.fsona.com>
- [45] T. Wiener and S. Karp, “The role of blue/green laser systems in strategic submarine communications,” *IEEE Trans. Commun.*, vol. 28, no. 9, pp. 1602–1607, 1980.
- [46] S. Zhu, X. Chen, X. Liu, G. Zhang, and P. Tian, “Recent progress in and perspectives of underwater wireless optical communication,” *Progress in Quantum Electronics*, vol. 73, p. 100274, 2020.
- [47] Underwater Optical Wireless Communication MC500. [Online]. Available: <https://www.shimadzu.com/industry/products/underwater/mc500.html>
- [48] Sonardyne, BlueComm 200. [Online]. Available: <https://www.sonardyne.com/products/bluecomm-200-wireless-underwater-link/>
- [49] Hydromea, LUMA. [Online]. Available: <https://www.hydromea.com/underwater-wireless-communication>
- [50] Dat Light S.L. [Online]. Available: <https://www.datlight.es/>
- [51] Andalus Sea Robótica Submarina. [Online]. Available: <https://andalu-sea.com/>
- [52] Blue Float Energy: Energía Eólica Marina. [Online]. Available: <https://www.bluefloat.com/>

- [53] M. V. Jamali, A. Mirani, A. Parsay, B. Abolhassani, P. Nabavi, A. Chizari, P. Khorramshahi, S. Abdollahramezani, and J. A. Salehi, "Statistical studies of fading in underwater wireless optical channels in the presence of air bubble, temperature, and salinity random variations," *IEEE Trans. Commun.*, vol. 66, no. 10, pp. 4706–4723, 2018.
- [54] X. Ke, J. Bao, and J. Liang, "Experimental study of underwater wireless optical channel model," *Optical Engineering*, vol. 62, no. 12, pp. 124 103–124 103, 2023.
- [55] H. Qiu, Z. Huang, J. Xu, W. Zhai, Y. Gao, and Y. Ji, "Unified statistical thermocline channel model for underwater wireless optical communication," *Opt. Letters*, vol. 48, no. 3, pp. 636–639, 2023.
- [56] H. Jiang, H. Qiu, N. He, W. Popoola, Z. Ahmad, and S. Rajbhandari, "Ergodic capacity and error performance of spatial diversity UWOC systems over generalized gamma turbulence channels," *Optics communications*, vol. 505, p. 127476, 2022.
- [57] Q. Zhang, D. Yue, and X. Xu, "Generalized transmit laser selection for vertical underwater wireless optical communications over gamma-gamma turbulence channels," *Opt. Express*, vol. 31, no. 23, pp. 37 943–37 958, 2023.
- [58] B. Zhou, P. Wang, W. Pang, H. Jiang, and G. Li, "Effective secrecy throughput optimization for GTLS-based UWOC systems with eavesdropper outage constraint," *Opt. Express*, vol. 32, no. 18, pp. 32 079–32 093, 2024.
- [59] M. Shin, K.-H. Park, and M.-S. Alouini, "Statistical modeling of the impact of underwater bubbles on an optical wireless channel," *IEEE Open J. of the Commun. Soc.*, vol. 1, pp. 808–818, 2020.
- [60] C. T. Geldard, J. S. Thompson, and W. O. Popoola, "On the relative effect of underwater optical turbulence in different channel conditions," *IEEE Access*, 2024.
- [61] L. Kou, J. Zhang, P. Zhang, Y. Yang, and F. He, "Composite channel modeling for underwater optical wireless communication and analysis of multiple scattering characteristics," *Opt. Express*, vol. 31, no. 7, pp. 11 320–11 334, 2023.
- [62] Y. Ata and K. Kiasaleh, "Analysis of optical wireless communication links in turbulent underwater channels with wide range of water parameters," *IEEE Transactions on Vehicular Technology*, vol. 72, no. 5, pp. 6363–6374, 2023.
- [63] P. Salcedo-Serrano, C. Gómez-García, J. Iamaguti-Debessa, R. Boluda-Ruiz, J. M. Garrido-Balsells, B. Castillo-Vázquez, A. Puerta-Notario, and A. García-Zambrana, "On the effect of air bubbles-induced scattering on turbid waters: an experimental UOWC channel modeling approach," *IEEE Access*, 2024.

- [64] P. Salcedo-Serrano, R. Boluda-Ruiz, J. M. Garrido-Balsells, B. Castillo-Vázquez, A. Puerta-Notario, and A. García-Zambrana, “Performance evaluation of UOWC systems from an empirical channel model approach for air bubble-induced scattering,” *Sensors*, vol. 24, no. 16, p. 5232, 2024.
- [65] P. Salcedo-Serrano, R. Boluda-Ruiz, J. M. Garrido-Balsells, A. García-Zambrana, B. Castillo-Vázquez, A. Puerta-Notario, and S. Hranilovic, “UOWC spatial diversity techniques over hostile maritime environments: an approach under imperfect CSI and per-source power constraints,” *Opt. Express*, vol. 32, no. 24, pp. 42 347–42 367, Nov 2024.
- [66] P. Salcedo-Serrano, R. Boluda-Ruiz, J. M. Garrido-Balsells, A. García-Zambrana, and S. Hranilovic, “Underwater optical wireless channel capacity under oceanic turbulence using spatial diversity techniques,” in *ICC 2023-IEEE International Conference on Communications*. IEEE, 2023, pp. 1162–1168.
- [67] P. Salcedo-Serrano, R. Boluda-Ruiz, J. M. Garrido-Balsells, and A. García-Zambrana, “On the scattering-induced fading for optical wireless links through seawater: statistical characterization and its applications,” *Opt. Express*, vol. 29, no. 23, pp. 37 101–37 116, 2021.
- [68] R. Boluda-Ruiz, P. Salcedo-Serrano, B. Castillo-Vázquez, A. García-Zambrana, and J. M. Garrido-Balsells, “Capacity of underwater optical wireless communication systems over salinity-induced oceanic turbulence channels with isi,” *Opt. Express*, vol. 29, no. 15, pp. 23 142–23 158, 2021.
- [69] —, “Impact of scattering on secrecy outage probability of underwater optical wireless links,” *IEEE Journal of Oceanic Engineering*, 2023.
- [70] P. Salcedo-Serrano, R. Boluda-Ruiz, J. M. Garrido-Balsells, and A. García-Zambrana, “On scattering-induced fading in underwater FSO links for clear ocean and coastal waters,” in *CLEO: Science and Innovations*. Optica Publishing Group, 2021, pp. JTu3A–166.
- [71] R. Boluda-Ruiz, P. Salcedo-Serrano, B. Castillo-Vázquez, A. García-Zambrana, and J. M. Garrido-Balsells, “On the effect of inter-symbol interference on mutual information of undersea optical wireless links,” in *2021 IEEE Photonics Conference (IPC)*. IEEE, 2021, pp. 1–2.
- [72] P. Salcedo-Serrano, R. Boluda-Ruiz, J. M. Garrido-Balsells, and A. García-Zambrana, “Outage capacity of underwater FSO systems over scattering-induced fading channels,” in *Propagation Through and Characterization of Atmospheric and Oceanic Phenomena*. Optica Publishing Group, 2021, pp. PM2G–2.

- [73] ———, “Ergodic capacity analysis of underwater FSO systems over scattering-induced fading channels in the presence of weibull oceanic turbulence,” in *ICC 2022-IEEE International Conference on Communications*. IEEE, 2022, pp. 3814–3819.
- [74] Z. Ghassemlooy, W. Popoola, and S. Rajbhandari, *Optical wireless communications: system and channel modelling with Matlab®*. CRC, 2019.
- [75] B. Cochenour, L. Mullen, and A. Laux, “Phase coherent digital communications for wireless optical links in turbid underwater environments,” in *OCEANS 2007*. IEEE, 2007, pp. 1–5.
- [76] E. Zedini, Y. Ata, F. M. Al-Sallami, and S. Rajbhandari, “Evaluation of underwater optical wireless channels over f turbulence for different detection types,” *IEEE Transactions on Communications*, 2024.
- [77] S. Hranilovic, *Wireless optical communication systems*. Springer Science & Business Media, 2006.
- [78] IEC, “Safety of laser products - Part 1: Equipment classification and requirements IEC 60825-1:2014,” 2014.
- [79] M. Dehghani Soltani, E. Sarbazi, N. Bamiedakis, P. d. Souza, H. Kazemi, J. M. H. Elmighani, I. H. White, R. V. Penty, H. Haas, and M. Safari, “Safety analysis for laser-based optical wireless communications: A tutorial,” *Proceedings of the IEEE*, vol. 110, no. 8, pp. 1045–1072, 2022.
- [80] P. Pandey, G. Matta, and M. Aggarwal, “Performance comparisons between Avalanche and PIN photodetectors for use in underwater optical wireless communication systems,” in *OCEANS 2021: San Diego – Porto*. San Diego, CA, USA: IEEE, Sep. 2021, pp. 1–8.
- [81] M. Curtis, *The Oceanic Optics Book*. International Ocean Colour Coordinating Group (IOCCG), 2022. [Online]. Available: <https://repository.oceanbestpractices.org/handle/11329/1853>
- [82] X. Zhang, M. Lewis, and B. Johnson, “Influence of bubbles on scattering of light in the ocean,” *Applied Optics*, vol. 37, no. 27, pp. 6525–6536, 1998.
- [83] W. S. Pegau, D. Gray, and J. R. V. Zaneveld, “Absorption and attenuation of visible and near-infrared light in water: dependence on temperature and salinity,” *Applied optics*, vol. 36, no. 24, pp. 6035–6046, 1997.
- [84] R. Röttgers, D. McKee, and C. Utschig, “Temperature and salinity correction coefficients for light absorption by water in the visible to infrared spectral region,” *Optics Express*, vol. 22, no. 21, pp. 25 093–25 108, 2014.

- [85] M. Curtis, *Light and water: radiative transfer in natural waters*. Academic Press, 1994.
- [86] NASA Image and Video Library. [Online]. Available: <https://images.nasa.gov/>
- [87] M. G. Solonenko and C. D. Mobley, "Inherent optical properties of Jerlov water types," *Appl. Opt.*, vol. 54, no. 17, pp. 5392–5401, Jun 2015. [Online]. Available: <https://opg.optica.org/ao/abstract.cfm?URI=ao-54-17-5392>
- [88] L. Prieur and S. Sathyendranath, "An optical classification of coastal and oceanic waters based on the specific spectral absorption curves of phytoplankton pigments, dissolved organic matter, and other particulate materials 1," *Limnology and oceanography*, vol. 26, no. 4, pp. 671–689, 1981.
- [89] V. I. Haltrin, "Chlorophyll-based model of seawater optical properties," *Appl. Opt.*, vol. 38, no. 33, pp. 6826–6832, Nov 1999. [Online]. Available: <https://opg.optica.org/ao/abstract.cfm?URI=ao-38-33-6826>
- [90] T. J. Petzold, *Volume scattering functions for selected ocean waters*. Scripps Institution of Oceanography La Jolla, CA, USA, 1972.
- [91] H. C. Hulst and H. C. van de Hulst, *Light scattering by small particles*. Courier Corporation, 1981.
- [92] Y. I. Kopilevich, M. E. Kononenko, and E. I. Zadorozhnaya, "The effect of the forward-scattering index on the characteristics of a light beam in sea water," *J. Opt. Technol.*, vol. 77, no. 10, pp. 598–601, Oct 2010. [Online]. Available: <https://opg.optica.org/jot/abstract.cfm?URI=jot-77-10-598>
- [93] C. Gabriel, M.-A. Khalighi, S. Bourennane, P. Léon, and V. Rigaud, "Monte-carlo-based channel characterization for underwater optical communication systems," *Journal of Optical Communications and Networking*, vol. 5, no. 1, pp. 1–12, 2013.
- [94] V. I. Haltrin, "Two-term henry-greenstein light scattering phase function for seawater," in *IEEE 1999 International Geoscience and Remote Sensing Symposium. IGARSS'99 (Cat. No. 99CH36293)*, vol. 2. IEEE, 1999, pp. 1423–1425.
- [95] C. D. Mobley, "Radiative transfer in the ocean," *Encyclopedia of ocean sciences*, vol. 4, pp. 2321–2330, 2001.
- [96] H. R. Gordon, "Modeling and simulating radiative transfer in the ocean," in *Ocean Optics*. Oxford University, 1994.
- [97] R. E. Walker, *Marine light field statistics*. Wiley-Interscience, 1994.
- [98] C. D. Mobley, B. Gentili, H. R. Gordon, Z. Jin, G. W. Kattawar, A. Morel, P. Reinersman, K. Stamnes, and R. H. Stavn, "Comparison of numerical models for computing underwater light fields," *Applied Optics*, vol. 32, no. 36, pp. 7484–7504, 1993.

- [99] L. Wang, S. L. Jacques, and L. Zheng, “MCML—monte carlo modeling of light transport in multi-layered tissues,” *Computer methods and programs in biomedicine*, vol. 47, no. 2, pp. 131–146, 1995.
- [100] S. Arnon, D. Sadot, and N. Kopeika, “Simple mathematical models for temporal, spatial, angular, and attenuation characteristics of light propagating through the atmosphere for space optical communication: Monte carlo simulations,” *Journal of Modern Optics*, vol. 41, no. 10, pp. 1955–1972, 1994.
- [101] M. Xu, “Electric field monte carlo simulation of polarized light propagation in turbid media,” *Opt. Express*, vol. 12, no. 26, pp. 6530–6539, 2004.
- [102] R. X. Huang, *Ocean circulation: wind-driven and thermohaline processes*. Cambridge University Press, 2010.
- [103] A. Jurado-Navas, J. M. Garrido-Balsells, J. F. Paris, A. Puerta-Notario, and J. Awrejcewicz, “A unifying statistical model for atmospheric optical scintillation,” in *Numerical simulations of physical and engineering processes*. Intech Rijeka, Croatia, 2011, vol. 181, no. 8, pp. 181–205.
- [104] A. N. Kolmogorov, “Dissipation of energy in the locally isotropic turbulence,” *Proceedings: Mathematical and Physical Sciences*, vol. 434, no. 1890, pp. 15–17, 1991.
- [105] ———, “The local structure of turbulence in incompressible viscous fluid for very large reynolds numbers,” *Proceedings: Mathematical and Physical Sciences*, vol. 434, no. 1890, pp. 9–13, 1991.
- [106] R. Hill, “Spectra of fluctuations in refractivity, temperature, humidity, and the temperature-humidity cospectrum in the inertial and dissipation ranges,” *Radio Science*, vol. 13, no. 6, pp. 953–961, 1978.
- [107] O. Korotkova, “Light propagation in a turbulent ocean,” in *Progress in Optics*. Elsevier, 2019, vol. 64, pp. 1–43.
- [108] Y. Baykal, “Expressing oceanic turbulence parameters by atmospheric turbulence structure constant,” *Applied Optics*, vol. 55, no. 6, pp. 1228–1231, 2016.
- [109] X. Luan, P. Yue, and X. Yi, “Scintillation index of an optical wave propagating through moderate-to-strong oceanic turbulence,” *JOSA A*, vol. 36, no. 12, pp. 2048–2059, 2019.
- [110] J.-R. Yao, H.-J. Zhang, R.-N. Wang, J.-D. Cai, Y. Zhang, and O. Korotkova, “Wide-range prandtl/schmidt number power spectrum of optical turbulence and its application to oceanic light propagation,” *Opt. Express*, vol. 27, no. 20, pp. 27 807–27 819, 2019.

- [111] J.-R. Yao, M. Elamassie, and O. Korotkova, "Spatial power spectrum of natural water turbulence with any average temperature, salinity concentration, and light wavelength," *JOSA A*, vol. 37, no. 10, pp. 1614–1621, 2020.
- [112] A. P. Trujillo and H. V. Thurman, *Essentials of oceanography*. PHI Learning Private Limited, 2012.
- [113] Y. Baykal, Y. Ata, and M. C. Gökçe, "Underwater turbulence, its effects on optical wireless communication and imaging: A review," *Optics & Laser Technology*, vol. 156, p. 108624, 2022.
- [114] S. A. Thorpe, "On the clouds of bubbles formed by breaking wind-waves in deep water, and their role in air-sea gas transfer," *Philosophical Transactions of the Royal Society of London. Series A, Mathematical and Physical Sciences*, vol. 304, no. 1483, pp. 155–210, 1982.
- [115] D. Farmer, C. McNeil, and B. Johnson, "Evidence for the importance of bubbles in increasing air-sea gas flux," *Nature*, vol. 361, no. 6413, pp. 620–623, 1993.
- [116] E. R. Lewis and S. E. Schwartz, *Sea salt aerosol production: mechanisms, methods, measurements, and models*. American geophysical union, 2004, vol. 152.
- [117] A. E. Walsby, "Gas vesicles," *Microbiological reviews*, vol. 58, no. 1, pp. 94–144, 1994.
- [118] D. Selivanovsky, P. Stunzhas, and I. Didenkulov, "Acoustical investigation of phytoplankton," *ICES Journal of Marine Science*, vol. 53, no. 2, pp. 313–316, 1996.
- [119] S. Vahaji, L. Chen, S. C. Cheung, and J. Tu, "Numerical investigation on bubble size distribution around an underwater vehicle," *Applied Ocean Research*, vol. 78, pp. 254–266, 2018.
- [120] D. L. Kingsbury and P. L. Marston, "Mie scattering near the critical angle of bubbles in water," *JOSA*, vol. 71, no. 3, pp. 358–361, 1981.
- [121] Q. Fu and W. Sun, "Mie theory for light scattering by a spherical particle in an absorbing medium," *Applied Optics*, vol. 40, no. 9, pp. 1354–1361, 2001.
- [122] D. Meschede, *Optics, light and lasers: the practical approach to modern aspects of photonics and laser physics*. John Wiley & Sons, 2017.
- [123] G. P. Agrawal, *Fiber-optic communication systems*. John Wiley & Sons, 2012.
- [124] D. Chen, J. Wang, S. Li, and Z. Xu, "Effects of air bubbles on underwater optical wireless communication. invited," *Chin. Opt. Lett.*, vol. 17, no. 10, p. 100008, Oct 2019.
- [125] Y. Ata and Y. Baykal, "Scintillations of optical plane and spherical waves in underwater turbulence," *JOSA A*, vol. 31, no. 7, pp. 1552–1556, 2014.

- [126] L. C. Andrews, R. L. Phillips, and C. Y. Hopen, "Aperture averaging of optical scintillations: power fluctuations and the temporal spectrum," *Waves in Random Media*, vol. 10, no. 1, p. 53, 2000.
- [127] M. C. Gökçe and Y. Baykal, "Aperture averaging in strong oceanic turbulence," *Optics Communications*, vol. 413, pp. 196–199, 2018.
- [128] Y. Fu, Q. Duan, C. Huang, Y. Du, and L. Zhou, "Average BER performance of rectangular QAM-UWOC over strong oceanic turbulence channels with pointing error," *Optics Communications*, vol. 476, p. 126362, 2020.
- [129] Y. Ata and I. Toselli, "Aperture-averaged scintillation for a weak underwater turbulence-affected gaussian beam using the OTOPS model," *JOSA A*, vol. 40, no. 3, pp. 492–501, 2023.
- [130] H. Wang, F.-Z. Kang, X. Wang, W. Zhao, and S.-W. Sun, "Aperture-averaged scintillation index and fade statistics in weak oceanic turbulence," *Chinese Physics B*, vol. 30, no. 6, p. 064207, 2021.
- [131] H. M. Oubei, E. Zedini, R. T. ElAfandy, A. Kammoun, T. K. Ng, M.-S. Alouini, and B. S. Ooi, "Efficient Weibull channel model for salinity induced turbulent underwater wireless optical communications," in *2017 Opto-Electronics and Communications Conference (OECC) and Photonics Global Conference (PGC)*. IEEE, 2017, pp. 1–2.
- [132] M.-A. Khalighi, C. Gabriel, T. Hamza, S. Bourennane, P. Leon, and V. Rigaud, "Underwater wireless optical communication; recent advances and remaining challenges," in *2014 16th international conference on transparent optical networks (ICTON)*. IEEE, 2014, pp. 1–4.
- [133] M. Shangguan, Z. Weng, Z. Lin, Z. Lee, M. Shangguan, Z. Yang, J. Sun, T. Wu, Y. Zhang, and C. Wen, "Day and night continuous high-resolution shallow-water depth detection with single-photon underwater lidar," *Opt. Express*, vol. 31, no. 26, pp. 43 950–43 962, 2023.
- [134] J. G. Proakis and M. Salehi, *Digital communications*. McGraw-Hill., 2008.
- [135] Z. Wang and G. B. Giannakis, "A simple and general parameterization quantifying performance in fading channels," *IEEE Trans. Commun.*, vol. 51, no. 8, pp. 1389–1398, 2003.
- [136] M. C. Jeruchim, P. Balaban, K. S. Shanmugan, M. C. Jeruchim, P. Balaban, and K. S. Shanmugan, "Modeling of communication systems," *Simulation of Communication Systems*, pp. 303–462, 1992.
- [137] H. M. Oubei, E. Zedini, R. T. ElAfandy, A. Kammoun, M. Abdallah, T. K. Ng, M. Hamdi, M.-S. Alouini, and B. S. Ooi, "Simple statistical channel model for weak

- temperature-induced turbulence in underwater wireless optical communication systems,” *Opt. Letters*, vol. 42, no. 13, pp. 2455–2458, 2017.
- [138] E. Zedini, H. M. Oubei, A. Kammoun, M. Hamdi, B. S. Ooi, and M.-S. Alouini, “Unified statistical channel model for turbulence-induced fading in underwater wireless optical communication systems,” *IEEE Trans. Commun.*, vol. 67, no. 4, pp. 2893–2907, 2019.
- [139] M. Yousefi, F. D. Kashani, A. Aghajani, and M. R. H. Rad, “Experimental study of the effects of thermally induced optical turbulence on underwater wireless optical communication link parameters,” *Journal of Optics*, vol. 22, no. 2, p. 025702, 2020.
- [140] A. Jurado-Navas, N. G. Serrato, J. Garrido-Balsells, and M. Castillo-Vázquez, “Error probability analysis of OOK and variable weight MPPM coding schemes for underwater optical communication systems affected by salinity turbulence,” *OSA Continuum*, vol. 1, no. 4, pp. 1131–1143, 2018.
- [141] R. Boluda-Ruiz, A. García-Zambrana, B. Castillo-Vázquez, and S. Hranilovic, “Impact of angular pointing error on BER performance of underwater optical wireless links,” *Opt. Express*, vol. 28, no. 23, pp. 34 606–34 622, 2020.
- [142] R. Boluda-Ruiz, P. Salcedo-Serrano, B. Castillo-Vázquez, A. García-Zambrana, and J. M. Garrido-Balsells, “Capacity of underwater optical wireless communication systems over salinity-induced oceanic turbulence channels with ISI,” *Opt. Express*, vol. 29, no. 15, pp. 23 142–23 158, Jul 2021.
- [143] A. Samir, M. Elsayed, A. A. A. El-Banna, I. Shafique Ansari, K. Rabie, and B. M. ElHalawany, “Performance analysis of dual-hop hybrid RF-UOWC noma systems,” *Sensors*, vol. 22, no. 12, 2022.
- [144] Z. Rahman, M. Z. Hassan, and G. Kaddoum, “Ergodic capacity optimization for RSMA-based UOWC systems over EGG turbulence channel,” *IEEE Commun. Lett.*, vol. 28, no. 3, pp. 587–591, 2024.
- [145] G. Ding, X. Du, H. Du, S. Wang, H. Feng, G. Xu, Z. Xiong, Z. Jia, and Y. Li, “Performance analysis of OSSK-UWOC systems considering pointing errors and channel estimation errors,” *Opt. Express*, vol. 32, no. 3, pp. 3606–3618, Jan 2024. [Online]. Available: <https://opg.optica.org/oe/abstract.cfm?URI=oe-32-3-3606>
- [146] Thorlabs, PDA10A2. [Online]. Available: <https://www.thorlabs.com/thorproduct.cfm?partnumber=LP520-SF15&pn=LP520-SF15>
- [147] “STEMlab 125-14 - Red Pitaya,” Jun. 2021. [Online]. Available: <https://redpitaya.com/stemlab-125-14/>

- [148] B. Cochenour, L. Mullen, and J. Muth, "Effect of scattering albedo on attenuation and polarization of light underwater," *Opt. Lett.*, vol. 35, no. 12, pp. 2088–2090, Jun 2010.
- [149] L. Mullen, D. Alley, and B. Cochenour, "Investigation of the effect of scattering agent and scattering albedo on modulated light propagation in water," *Applied Optics*, vol. 50, no. 10, pp. 1396–1404, 2011.
- [150] A. Laux, R. Billmers, L. Mullen, B. Concannon, J. Davis, J. Prentice, and V. Con-tarino, "The a, b, cs of oceanographic lidar predictions: a significant step toward closing the loop between theory and experiment," *Journal of Modern Optics*, vol. 49, no. 3-4, pp. 439–451, 2002.
- [151] Thorlabs, PDA10A2. [Online]. Available: <https://www.thorlabs.com/thorproduct.cfm?partnumber=PDA10A2>
- [152] V. A. Aalo, T. Piboongunon, and C.-D. Iskander, "Bit-error rate of binary digital modulation schemes in generalized gamma fading channels," *IEEE Commun. Lett.*, vol. 9, no. 2, pp. 139–141, 2005.
- [153] H. AlQuwaiee, I. S. Ansari, and M.-S. Alouini, "On the performance of free-space optical communication systems over double generalized gamma channel," *IEEE J. Select. Areas Commun.*, vol. 33, no. 9, pp. 1829–1840, 2015.
- [154] A. Mostafa and S. Hranilovic, "Channel measurement and markov modeling of an urban free-space optical link," *Journal of Optical Communications and Networking*, vol. 4, no. 10, pp. 836–846, 2012.
- [155] M. K. Simon and M.-S. Alouini, *Digital communications over fading channels*, 2nd ed. New Jersey: Wiley-IEEE Press, 2005.
- [156] L. Yang and M.-S. Alouini, "On the average outage rate and average outage dura-tion of wireless communication systems with multiple cochannel interferers," *IEEE Transactions on Wireless Communications*, vol. 3, no. 4, pp. 1142–1153, 2004.
- [157] C. A. Williamson and R. C. Hollins, "Measured IOPs of Jerlov water types," *Applied Optics*, vol. 61, no. 33, pp. 9951–9961, 2022.
- [158] Wolfram Research, Inc., "The Wolfram functions site." [Online]. Available: <http://functions.wolfram.com>
- [159] E. W. Stacy, "A generalization of the gamma distribution," *The Annals of mathemat-ical statistics*, pp. 1187–1192, 1962.
- [160] E. J. Lee and V. W. Chan, "Part 1: Optical communication over the clear turbulent atmospheric channel using diversity," *IEEE J. Select. Areas Commun.*, vol. 22, no. 9, pp. 1896–1906, 2004.

- [161] S. M. Navidpour, M. Uysal, and M. Kavehrad, "Ber performance of free-space optical transmission with spatial diversity," *IEEE Trans. Wir. Commun.*, vol. 6, no. 8, pp. 2813–2819, 2007.
- [162] T. A. Tsiftsis, H. G. Sandalidis, G. K. Karagiannidis, and M. Uysal, "Optical wireless links with spatial diversity over strong atmospheric turbulence channels," *IEEE Transactions on Wireless Communications*, vol. 8, no. 2, pp. 951–957, 2009.
- [163] A. A. Farid and S. Hranilovic, "Diversity gain and outage probability for MIMO free-space optical links with misalignment," *IEEE Trans. Commun.*, vol. 60, no. 2, pp. 479–487, 2011.
- [164] R. Boluda-Ruiz, A. García-Zambrana, B. Castillo-Vázquez, and C. Castillo-Vázquez, "Impact of nonzero boresight pointing error on ergodic capacity of MIMO FSO communication systems," *Opt. Express*, vol. 24, no. 4, pp. 3513–3534, 2016.
- [165] X. Zhu and J. M. Kahn, "Performance bounds for coded free-space optical communications through atmospheric turbulence channels," *IEEE Trans. Commun.*, vol. 51, no. 8, pp. 1233–1239, 2003.
- [166] M. Uysal, S. M. Navidpour, and J. Li, "Error rate performance of coded free-space optical links over strong turbulence channels," *IEEE Commun. Lett.*, vol. 8, no. 10, pp. 635–637, 2004.
- [167] X. Chen, Y. Dai, Z. Tong, X. Yang, X. Li, G. Song, H. Zou, B. Jia, S. Qin, Z. Zhang *et al.*, "Demonstration of a 2×2 MIMO-UWOC system with large spot against air bubbles," *Applied Optics*, vol. 61, no. 1, pp. 41–48, 2021.
- [168] M. V. Jamali, J. A. Salehi, and F. Akhouni, "Performance studies of underwater wireless optical communication systems with spatial diversity: MIMO scheme," *IEEE Trans. Commun.*, vol. 65, no. 3, pp. 1176–1192, 2017.
- [169] A. Huang, L. Tao, and Y. Niu, "Underwater wireless optical MIMO system with spatial modulation and adaptive power allocation," *Optics Communications*, vol. 412, pp. 21–27, 2018.
- [170] S. Sanayei and A. Nosratinia, "Antenna selection in MIMO systems," *IEEE Commun. Mag.*, vol. 42, no. 10, pp. 68–73, 2004.
- [171] A. García-Zambrana, C. Castillo-Vázquez, B. Castillo-Vázquez, and A. Hiniesta-Gómez, "Selection transmit diversity for FSO links over strong atmospheric turbulence channels," *IEEE Photon. Technol. Lett.*, vol. 21, no. 14, pp. 1017–1019, 2009.
- [172] A. García-Zambrana, B. Castillo-Vázquez, and C. Castillo-Vázquez, "Asymptotic error-rate analysis of FSO links using transmit laser selection over gamma-gamma atmospheric turbulence channels with pointing errors," *Opt. Express*, vol. 20, no. 3, pp. 2096–2109, 2012.

- [173] J. H. Manton, "On optimal channel identification by use of training sequences and pilot tones," in *Proceedings of the Sixth International Symposium on Signal Processing and its Applications (Cat. No. 01EX467)*, vol. 2. IEEE, 2001, pp. 599–602.
- [174] I.-Y. Choi, W.-H. Shin, and S.-K. Han, "CSI estimation with pilot tone for scintillation effects mitigation on satellite optical communication," *Optics Communications*, vol. 435, pp. 88–92, 2019.
- [175] A. Aboutaleb, W. Fatnassi, M. Soltani, and Z. Rezki, "Symbol detection and channel estimation using neural networks in optical communication systems," in *ICC 2019-2019 IEEE International Conference on Communications (ICC)*. IEEE, 2019, pp. 1–6.
- [176] A. Elfikky and Z. Rezki, "Symbol detection and channel estimation for space optical communications using neural network and autoencoder," *IEEE Transactions on Machine Learning in Communications and Networking*, 2023.
- [177] M. Elamassie, M. Al-Nahhal, R. C. Kizilirmak, and M. Uysal, "Transmit laser selection for underwater visible light communication systems," in *2019 IEEE 30th Annual International Symposium on Personal, Indoor and Mobile Radio Communications (PIMRC)*. IEEE, 2019, pp. 1–6.
- [178] M. V. Jamali, P. Nabavi, and J. A. Salehi, "MIMO underwater visible light communications: Comprehensive channel study, performance analysis, and multiple-symbol detection," *IEEE Trans. Veh. Technol.*, vol. 67, no. 9, pp. 8223–8237, 2018.
- [179] A. A. Farid and S. Hranilovic, "Outage capacity optimization for free-space optical links with pointing errors," *Journal of Lightwave technology*, vol. 25, no. 7, pp. 1702–1710, 2007.
- [180] L. Lu, X. Ji, and Y. Baykal, "Wave structure function and spatial coherence radius of plane and spherical waves propagating through oceanic turbulence," *Opt. Express*, vol. 22, no. 22, pp. 27 112–27 122, 2014.
- [181] Y.-W. P. Hong, W.-J. Huang, and C.-C. J. Kuo, *Cooperative communications and networking: technologies and system design*. Springer Science & Business Media, 2010.
- [182] F. D. A. García, F. R. A. Parente, G. Fraidenraich, and J. C. S. Santos Filho, "Light exact expressions for the sum of Weibull random variables," *IEEE Wir. Commun. Lett.*, vol. 10, no. 11, pp. 2445–2449, 2021.
- [183] H. A. David and H. N. Nagaraja, *Order statistics*, 3rd ed. John Wiley and Sons Inc., 2003.
- [184] H. P. Hsu, *Theory and problems of probability, random variables, and random processes*. McGraw-hill, 1997.

- [185] J. Lisman and M. Van Zuylen, “Note on the generation of most probable frequency distributions,” *Statistica Neerlandica*, vol. 26, no. 1, pp. 19–23, 1972.
- [186] J. Shore and R. Johnson, “Axiomatic derivation of the principle of maximum entropy and the principle of minimum cross-entropy,” *IEEE Trans. Inf. Theory*, vol. 26, no. 1, pp. 26–37, 1980.
- [187] J. Van Campenhout and T. Cover, “Maximum entropy and conditional probability,” *IEEE Trans. Inf. Theory*, vol. 27, no. 4, pp. 483–489, 1981.
- [188] A. P. Prudnikov, Y. A. Brychkov, and O. I. Marichev, *Integrals and series Volume 3: More Special Functions*. Gordon and Breach Science Publishers, 1999, vol. 3.
- [189] J. Wang, J.-Y. Yang, I. M. Fazal, N. Ahmed, Y. Yan, H. Huang, Y. Ren, Y. Yue, S. Dolinar, M. Tur *et al.*, “Terabit free-space data transmission employing orbital angular momentum multiplexing,” *Nature photonics*, vol. 6, no. 7, pp. 488–496, 2012.
- [190] A. Forbes, M. De Oliveira, and M. R. Dennis, “Structured light,” *Nature Photonics*, vol. 15, no. 4, pp. 253–262, 2021.
- [191] J. Baghdady, K. Miller, K. Morgan, M. Byrd, S. Osler, R. Ragusa, W. Li, B. M. Cochenour, and E. G. Johnson, “Multi-gigabit/s underwater optical communication link using orbital angular momentum multiplexing,” *Opt. Express*, vol. 24, no. 9, pp. 9794–9805, 2016.
- [192] Y. Ren, L. Li, Z. Wang, S. M. Kamali, E. Arbabi, A. Arbabi, Z. Zhao, G. Xie, Y. Cao, N. Ahmed *et al.*, “Orbital angular momentum-based space division multiplexing for high-capacity underwater optical communications,” *Scientific Reports*, vol. 6, no. 1, p. 33306, 2016.
- [193] Y. Zhao, A. Wang, L. Zhu, W. Lv, J. Xu, S. Li, and J. Wang, “Performance evaluation of underwater optical communications using spatial modes subjected to bubbles and obstructions,” *Opt. Letters*, vol. 42, no. 22, pp. 4699–4702, 2017.
- [194] J. Lee, K. Lee, Y.-S. Jang, H. Jang, S. Han, S.-H. Lee, K.-I. Kang, C.-W. Lim, Y.-J. Kim, and S.-W. Kim, “Testing of a femtosecond pulse laser in outer space,” *Scientific Reports*, vol. 4, no. 1, p. 5134, 2014.
- [195] H. Shi, Y. Song, F. Liang, L. Xu, M. Hu, and C. Wang, “Effect of timing jitter on time-of-flight distance measurements using dual femtosecond lasers,” *Opt. Express*, vol. 23, no. 11, pp. 14 057–14 069, 2015.
- [196] E. Weiss, D. Bykhovsky, and S. Arnon, “Symbol error rate model for communication using femtosecond pulses for space applications,” *IEEE Photon. Technol. Lett.*, vol. 28, no. 12, pp. 1286–1289, 2016.

- [197] N. A. M. Nor, M. Komanec, J. Bohata, Z. Ghassemlooy, M. R. Bhatnagar, and S. Zvánovec, “Experimental all-optical relay-assisted FSO link with regeneration and forward scheme for ultra-short pulse transmission,” *Opt. Express*, vol. 27, no. 16, pp. 22 127–22 137, 2019.
- [198] E. Wohlgemuth, R. Lesnik, R. Cohen, I. Attia, F. Emaury, T. Michel, O. Jacques-Sermet, P. Jian, R. Vered, and D. Sadot, “Robust coherent FSO using ultrashort pulses,” in *2024 24th International Conference on Transparent Optical Networks (ICTON)*. IEEE, 2024, pp. 1–4.
- [199] W. H. Knox, A. LeBon, T. Colangelo, B. Gregory, and T. Chaffee, “Atmospheric propagation of femtosecond optical pulses: Gaussian beamlet model of coherence effects,” in *Laser Communication and Propagation through the Atmosphere and Oceans XII*, vol. 12691. SPIE, 2023, pp. 175–183.
- [200] A. Stassinakis, H. Nistazakis, K. Peppas, and G. Tombras, “Improving the availability of terrestrial FSO links over log normal atmospheric turbulence channels using dispersive chirped gaussian pulses,” *Optics & Laser Technology*, vol. 54, pp. 329–334, 2013.
- [201] J. W. Hardy, *Adaptive optics for astronomical telescopes*. Oxford University, USA, 1998, vol. 16.
- [202] A. K. Majumdar, J. C. Ricklin, T. Weyrauch, and M. A. Vorontsov, “Free-space laser communications with adaptive optics: Atmospheric compensation experiments,” *Free-space laser communications: principles and advances*, pp. 247–271, 2008.
- [203] K. M. Hampson, R. Turcotte, D. T. Miller, K. Kurokawa, J. R. Males, N. Ji, and M. J. Booth, “Adaptive optics for high-resolution imaging,” *Nature Reviews Methods Primers*, vol. 1, no. 1, p. 68, 2021.
- [204] J. M. Wanek, M. Mori, and M. Shahidi, “Effect of aberrations and scatter on image resolution assessed by adaptive optics retinal section imaging,” *JOSA A*, vol. 24, no. 5, pp. 1296–1304, 2007.
- [205] B. Mastiani, G. Osnabrugge, and I. M. Vellekoop, “Wavefront shaping for forward scattering,” *Opt. Express*, vol. 30, no. 21, pp. 37 436–37 445, 2022.
- [206] S. Gigan, O. Katz, H. B. De Aguiar, E. R. Andresen, A. Aubry, J. Bertolotti, E. Bossy, D. Bouchet, J. Brake, S. Brasselet *et al.*, “Roadmap on wavefront shaping and deep imaging in complex media,” *Journal of Physics: Photonics*, vol. 4, no. 4, p. 042501, 2022.
- [207] I. S. Gradshteyn and I. M. Ryzhik, *Table of integrals, series, and products*. Academic press, 2007.

- [208] M. A. Chaudhry and S. M. Zubair, *On a class of incomplete gamma functions with applications*. Chapman and Hall/CRC, 2001.
- [209] A. A. Kilbas, *H-transforms: Theory and Applications*. CRC Press, 2004.